Improving NMR Sensitivity: The Synthesis and SABRE Evaluation of Nicotine Isotopologues

William Hugh Duckworth

Doctor of Philosophy

University of York

Chemistry

December 2018

Abstract

This thesis describes the development of a range of isotopically-labelled derivatives of (−)-nicotine, their subsequent hyperpolarisation by SABRE, their characterisation and the evaluation of their performance. Hyperpolarisation is a method of generating significantly enhanced magnetic resonance signals without increased sample size, scan time or prohibitively expensive improvements in equipment.

The primary aim of this thesis was to develop a family of (−)-nicotine derivatives as potent SABRE substrates with a view unlocking their future biological applications in areas such as MRI. (−)-Nicotine is an important biological compound of great interest, with potent and well-documented psychoactivity. Initial results in Chapter 2 focuses on the isotopic labelling of (−)-nicotine through regioselective lithiation-trapping and subsequent catalytic deuterodehalogenation.

Chapter 3 discusses the hyperpolarisation of (−)-nicotine and its isotopologues derivatives by SABRE. The relationship between signal enhancement, signal lifetime and a range of dependencies such as temperature, field and substrate choice are examined in detail. Results show that the interdependencies of such conditions are highly complex but follow logical patterns.

The results shown in Chapter 4 highlight the efforts made to understand the SABRE process itself, specifically the impact of the rate of exchange of substrate molecules onto and from the SABRE catalyst. Kinetic models are developed to more accurately describe the intricacies of the resulting chiral (−)-nicotine-based complexes, and they shed light on significant flaws in existing SABRE exchange models.

Collectively, the synthetic ^{2}H-labelling developments and SABRE evaluation involved no less than 23 materials, unlocking ^{1}H enhancement levels of up to ~2700-fold (equivalent to 9 % polarisation) with magnetic state lifetimes of up to 37 seconds. The previously overlooked effects of chirality are identified and rates of ligand loss robustly quantified as 3.08 ± 0.07 s^{-1}. In addition, our understanding of the role ^{2}H labelling plays in SABRE is secured.

Contents

Abstract 3

Contents 5

List of figures 9

List of tables 21

List of equations 28

Acknowledgements 29

Declaration 31

1: Introduction 33

1.1 NMR spectroscopy, MRI and their limitations 33

1.2 Signal enhancement and hyperpolarisation 35

1.2.1 Brute force 36

1.2.2 Optical pumping of gases 36

1.2.3 Dynamic Nuclear Polarisation 38

1.3 *para*-Hydrogen 42

1.3.1 *para*-Hydrogen Induced Polarisation (PHIP) 44

1.3.2 Signal Amplification By Reversible Exchange (SABRE) 49

1.4 Project outline 54

2: Synthesis of isotopically-labelled nicotines 57

2.1 Synthetic strategy and design 57

2.2 Synthesis of halonicotines 58

2.3 Synthesis of deuteronicotines 69

3: NMR spectroscopic studies on nicotine isotopologues 77

3.1 SABRE substrate screen 77

3.1.1 Screen for enhancement 77

3.1.2 Screen for T_1 magnetic lifetime 83

3.2 Only *Para*-hydrogen Spectroscopy (OPSY) 90
3.3 Optimisation overview 93
3.4 Kinetics optimisation 95
3.4.1 Alternative SABRE catalysts 96
3.4.2 Variable-temperature SABRE studies 97
3.4.3 Concentration of substrate vs. concentration of catalyst 100
3.4.4 Variable-pressure SABRE studies 109
3.5 Polarisation transfer optimisation 110
3.5.1 Varied PTF 110
3.5.2 Varied shake/bubble time 113
3.6 Mixing optimisation 115
3.7 'Doping' studies with fully-deuterated co-ligand 118
3.8 Imaging experiments 122
3.8.1 Rapid Acquistion with Relaxation Enhancement (RARE) studies 124
3.8.2 Fast Imaging with Steady-state free Precession (FISP) studies 127
3.9 Conclusions 130
4: SABRE exchange kinetics and modelling 131
4.1 The nicotine-iridium complex and Exchange Spectroscopy (EXSY) 131
4.1.1 Complex characterisation 131
4.1.2 Exchange Spectroscopy (EXSY) 134
4.2 Kinetic model improvements 141
4.2.1 Models 2 and 3 141
4.2.2 Model 4 151
4.3 Summary/Conclusions 157
5: Future work 159
6: Experimental 161
6.1 Standard/general methods 161
6.2 Specialised approaches 162

Preparation of *para*-hydrogen 162
Standard sample preparation and activation (Method 1) 162
Achieving SABRE (shake-and-drops in stray field) (Method 2) 162
Achieving SABRE (shake-and-drops with magnetic shaker) (Method 3) 163
Calculation of signal enhancement 163
Flow methodology (Method 4) 163
^{1}H T_1 relaxation time measurement via inversion-recovery (Method 5) 165
^{1}H T_1 relaxation time measurement via saturation-recovery (Method 6) 165
Exchange Spectroscopy (EXSY) (Method 7) 166
Error calculation 167
6.3 Synthetic results 167
6.4 SABRE and other NMR results 178
6.4.1 Varied substrate concentration – enhancements 178
6.4.2 Varied substrate concentration studies – T_1 179
6.4.2 Variable temperature SABRE – enhancements 181
6.4.3 Variable pressure SABRE 182
6.4.4 Flow experiments 183
6.4.5 Mixing studies results 185
6.5 EXSY results 185
(−)-nicotine 1, IMes 18 185
(−)-nicotine 1, d_{22}-IMes 19 186
4,6-nicotine-d_2 9, IMes 18 186
4,6-nicotine-d_2 9, d_{22}-IMes 19 187
7: Appendices 189
7.1 Model 1 EXSY plots and rate constant tables 189
7.1.1 Model 1 (−)-nicotine 1, IMes 18 189
7.1.2 Model 1 (−)-nicotine 1, d_{22}-IMes 19 197
7.1.3 Model 1 4,6-nicotine-d_2 9, IMes 18 204

7.1.4 Model 1 4,6-nicotine-d_2 9, d_{22}-IMes 19 211
7.2 Model 4 EXSY plots and rate constant tables 218
7.2.1 Model 4 (−)-nicotine 1, IMes 18 218
7.2.2 Model 4 (−)-nicotine 1, d_{22}-IMes 19 227
7.2.3 Model 4 4,6-nicotine-d_2 9, IMes 18 236
7.2.4 Model 4 4,6-nicotine-d_2 9, d_{22}-IMes 19 246
7.3 EXSY Eyring error estimates 255
7.3.1 Model 1 errors 255
7.3.2 Model 4 errors 255
7.3.3 Comparison 256
7.4 SABRE error estimates 256
7.4.1 Varied substrate concentration 256
7.4.2 Substrate screen 266
7.4.3 Alternative catalysts 267
7.4.4 Mixing studies 268
7.4.5 Co-ligand ‘doping’ studies 269
7.4.6 Variable pressure studies 270
7.4.7 Variable temperature studies 273
8: Abbreviations 276
9: References 279

List of figures

Figure 1: Populations of nuclear spin energies at thermal equilibrium for I = ½..... 33

Figure 2: Hyperpolarised populations of nuclear spin energies for I = ½ 35

Figure 3: Apparatus for polarizing gas (in this case ^{3}He) outside the body..... 37

Figure 4: Hyperpolarised 129Xe MRI images (red) overlaid with the corresponding ^{1}H MRI images of the thoracic cavity. 38

Figure 5: differences in polarisation between electrons (green) and proton nuclei (black) in a 14 T magnetic field and the temperature dependence of each. 39

Figure 6: *In vivo* angiographic images in a rat after a tail vein injection of hyperpolarised water. 40

Figure 7: Data from abdominal ^{13}C CSI acquisition of pyruvate metabolite maps in a rat. 41

Figure 8: Distribution of hyperpolarised pyruvate in a pig heart, via multiple slices through the short axis. 41

Figure 9: the four spin isomers of hydrogen. 42

Figure 10: schematic representation of a para-hydrogen generator as used by the Duckett group. Taken from Duckett *et al.* website[51]..... 44

Figure 11: Schematic representation of nuclear spin states in natural abundance hydrogen (left) and para-hydrogen (right) derived hydrogenation products and the corresponding NMR spectra of the labelled transitions between states. 45

Figure 12: First demonstration that hydrogenation with para-hydrogen yields significantly stronger NMR signals. 46

Figure 13: Schematic representation of reaction product nuclear spin states using para-hydrogen under PASADENA and ALTADENA conditions and the corresponding NMR spectra of the labelled transitions between states. 47

Figure 14: Reaction between acetylenedicarboxylic acid dimethyl ester with parahydrogen in the presence of a rhodium catalyst to give maleic acid dimethyl ester. 48

Figure 15: MRI images of a rat (generated at 2.4 T). 48

Figure 16: Schematic representation of the magnetisation transfer process in SABRE. 50

Figure 17: SABRE precatalyst acitvation and subsequent hyperpolarisation of substrate. 50

Figure 18: ^{1}H NMR spectra of pyridine, 7 – 9 ppm region shown only. 51

Figure 19: Methyl nicotinate and isotopologues methyl 4,6-nicotinate-d2 comparisons of T_1 relaxation times and polarisation by SABRE. 53

Figure 20: pulse sequence used to create, maintain and observe singlet states. 54

Figure 21: examples of molecules successfully hyperpolarised with SABRE and subsequently converted to a pseudo-singlet state 54

Figure 22: Chemical shifts and splitting patterns in the ^{1}H NMR spectra for 6-chloronicotine *2* and 2-chloronicotine *3* 59

Figure 23: major and minor pathways for lithiation adjacent to nitrogen in (−)-nicotine *1* 60

Figure 24: Chemical shifts and splitting patterns in the ^{1}H NMR spectrum for 5,6-dichloronicotine *5* 64

Figure 25: steric clashing between the bulky base and pyrrolidinyl ring combines with coordination to chlorine to effect DoM 64

Figure 26: Chemical shifts and splitting patterns in the ^{1}H NMR spectrum for 4,6-dichloronicotine *6* 65

Figure 27: comparison of effects of $CHNR_2$ and Cl as *ortho*-directing functional groups 66

Figure 28: Chemical shifts and splitting patterns in the ^{1}H NMR spectrum for 2,6-dichloronicotine *7* 67

Figure 29: general method for production of deuteronicotines from halonicotines 69

Figure 30: deuterodehalogenation catalytic cycle for conversion of halonicotines to the corresponding deuteronicotines 70

Figure 31: Chemical shifts and splitting patterns in the ^{1}H NMR spectrum for 6-deuteronicotine *4* 71

Figure 32: Chemical shifts and splitting patterns in the ^{1}H NMR spectrum for 5,6-nicotine-d_2 *8* 72

Figure 33: Chemical shifts and splitting patterns in the ^{1}H NMR spectrum for 4,6-nicotine-d_2 *9*..... 74

Figure 34: Chemical shifts and splitting patterns in the ^{1}H NMR spectrum for 2,6-nicotine-d_2 10..... 75

Figure 35: nicotine isotopologues produced in the project..... 75

Figure 36: thermal (a) and hyperpolarised (b) ^{1}H NMR spectra of (−)-nicotine *1* in the presence of the active form of IMes precatalyst species *18*..... 79

Figure 37: SABRE hyperpolarised signal enhancements per proton for (−)-nicotine *1* with IMes *18* precatalyst, relative to thermal signal..... 80

Figure 38: SABRE hyperpolarised signal enhancements per proton for 6-nicotine-d_1 *4* with IMes *18* precatalyst, relative to thermal signal..... 80

Figure 39: SABRE hyperpolarised signal enhancements per proton for 5,6-nicotine-d_2 *8* with IMes *18* precatalyst, relative to thermal signal..... 81

Figure 40: SABRE hyperpolarised signal enhancements per proton for 4,6-nicotine-d_2 *9* with IMes *18* precatalyst, relative to thermal signal..... 81

Figure 41: SABRE hyperpolarised signal enhancements per proton for 2,6-nicotine-d_2 *10* with IMes *18* precatalyst, relative to thermal signal..... 82

Figure 42: saturation-recovery of equilibrium magnetisation M_z/decay of observable signal by T_1 a.k.a spin-lattice relaxation..... 84

Figure 43: Major through-bond coupling relaxation pathways in (−)-nicotine *1* under both unactivated and activated conditions..... 85

Figure 44: (−)-nicotine *1* T_1 relaxation times, both under unactivated and activated conditions..... 86

Figure 45: 6-nicotine-d_1 *4* T_1 relaxation times under unactivated and activated conditions..... 86

Figure 46: 5,6-nicotine-d_2 *8* T_1 relaxation times under unactivated and activated conditions..... 87

Figure 47: 4,6-nicotine-d_2 *9* T_1 relaxation times under unactivated and activated conditions in methanol-d_4 and associated coupling mechanisms to explain T_1 performance..... 88

Figure 48: 2,6-nicotine-d_2 *10* T_1 relaxation times under unactivated and activated conditions in methanol-d_4 89

Figure 49: 4,6-nicotine-d_2 *9* T_1 relaxation times under unactivated and activated conditions in ethanol-d_6 89

Figure 50: OPSY-*d* experimental protocol. 91

Figure 51: Thermal ^{1}H NMR spectrum of (−)-nicotine *1* for direct comparison to OPSY spectra, focused on the pyrrolidyl proton signals at ~1.5-3.5 ppm 92

Figure 52: OPSY-*d* of (−)-nicotine *1*. 93

Figure 53: summary of the factors affecting SABRE 94

Figure 54: substrate and hydrogen exchange mechanism for $[Ir(H)_2(IMes)(NIC)_3]$ Cl (A) in methanol-d_4. 95

Figure 55: alternative SABRE catalysts in order of increasing typical exchange rates .. 96

Figure 56: signal enhancement vs. precatalyst for 'shake-and-drop' experiments on 4,6-nicotine-d_2 *9*. 97

Figure 57: signal enhancement vs. temperature for (−)-nicotine *1* and 4,6-nicotine-d_2 *9*. 98

Figure 58: activated conditions proton T_1 relaxation time vs. temperature for 4,6-nicotine-d_2 *9* using precatalyst IMes *18*. 100

Figure 59: signal enhancement vs. substrate concentration @ 298 K for (−)-nicotine *1* and 4,6-nicotine-d_2 *9* using precatalyst IMes *18*. 101

Figure 60: potential through-bond couplings from substrate to catalyst as relaxation pathways for (−)-nicotine *1* and 4,6-nicotine-d_2 *9* 102

Figure 61: activated conditions proton T_1 relaxation time vs. substrate concentration @ 298 K for (−)-nicotine *1* using precatalyst IMes *18*. 102

Figure 62: activated conditions proton T_1 relaxation time vs. substrate concentration @ 298 K for 4,6-nicotine-d_2 *9* using precatalyst IMes *18*. 103

Figure 63: signal-to-noise ratio vs. substrate concentration @ 298 K for (−)-nicotine *1* and 4,6-nicotine-d_2 *9* using precatalyst *18*. 104

Figure 64*:* signal enhancement vs. substrate concentration @ 298 K for (−)-nicotine *1* and 4,6-nicotine-d_2 *9* using precatalyst d_{22}-IMes *19*. 105

Figure 65: Activated conditions proton T_1 relaxation time vs. substrate concentration @ 298 K for (−)-nicotine *1* using precatalyst d_{22}-IMes *19*. 106

Figure 66: activated-conditions proton T_1 relaxation time vs. substrate concentration @ 298 K for 4,6-nicotine-d_2 *9* using precatalyst d_{22}-IMes *19*. 106

Figure 67: signal-to-noise ratio vs. substrate concentration @ 298 K for (−)-nicotine *1* and 4,6-nicotine-d_2 *9* using precatalyst d_{22}-IMes *19*. 107

Figure 68: comparison of signal-to-noise ratio calculations using the SINO function for different iterations of the same 'shake-and-drop' experiment. 108

Figure 69 (repeat of Figure 54): substrate and hydrogen exchange mechanism for $[Ir(H)_2(IMes)(NIC)_3]$ Cl (A) in methanol-d_4. 109

Figure 70: signal enhancement vs. para-hydrogen pressure for (−)-nicotine *1* and 4,6-nicotine-d_2 *9*. 110

Figure 71: Signal enhancement vs. polarisation transfer field for (−)-nicotine *1* and 4,6-nicotine-d_2 *9* using the automated flow setup. 111

Figure 72: Different possible polarisation transfers from catalyst hydrides to (-)-nicotine *1* and 4,6-nicotine-d_2 *9*. 113

Figure 73: Signal enhancement vs. bubble time for (-)-nicotine *1* and 4,6-nicotine-d_2 *9* using the automated flow setup. 114

Figure 74: Schematic and photographic representation of the SABRE magnetic shaker. 116

Figure 75: signal enhancement obtained in stray magnetic field versus with the magnetic shaker @ 298 K for 4,6-nicotine-d_2 *9* using precatalyst IMes *18*. 117

Figure 76: signal enhancement vs. para-hydrogen pressure for 4,6-nicotine-d_2 *9* with differing experimental mixing/PTF protocol. 118

Figure 77: use of a fully-deuterated co-ligand (Co-D) in conjunction with the desired substrate (Sub) to reduce dilution of polarisation between multiple bound substrate molecules. 119

Figure 78: signal enhancement for various substrate, catalyst and co-ligand combinations. 120

Figure 79: signal-to-noise ratio for various substrate, catalyst and co-ligand combinations. 121

Figure 80: the spin-echo experiment, the basis of most imaging techniques. 122

Figure 81: the filling of *k*-space with data points using field gradients.[116] 123

Figure 82: lens analogy for the process of imaging from a spin-echo experiment..... 124

Figure 83: comparison of the RARE sequence to a conventional spin-echo. 125

Figure 84: One-shot 2D ^{1}H MRI RARE results 126

Figure 85: establishment of a magnetic steady-state (M'_{ss}), viewed in terms of magnetisation, from spin-echo experiments with short repetition times ($TR<<T_2$). 127

Figure 86: establishment of magnetic steady-state, viewed in terms of signal, from spin-echo experiments with short repetition times ($TR<<T_2$). 128

Figure 87: One-shot 2D ^{1}H hyperpolarised MRI FISP results of 4,6-nicotine-d_2 *9* in conjunction with the d_{22}-IMes precatalyst *19* 128

Figure 88: ^{1}H MRI signal decay expressed as a function of time as a fraction of the initial maximum signal, derived from low flip-angle FISP images 129

Figure 89: ^{1}H NMR spectrum showing two distinct hydride signals when (−)-nicotine *1* and IMes precatalyst *18* react in methanol-d_4 at 298 K with 4 bar of hydrogen... 131

Figure 90: the arrangement of substrate (NIC) molecules around the iridium centre in a typical SABRE catalyst. 132

Figure 91: assignment of (−)-nicotine *1* ^{1}H NMR peaks at 243 K to specific resonances in specific binding sites on the IMes *18* iridium centre, assigned using COSY and NOESY experiments. 133

Figure 92: COSY of (−)-nicotine *1* with IMes *18* at 243 K with colour labels matching Figure 91. 133

Figure 93: The *selnogp* pulse sequence..... 134

Figure 94: a) Model 1, the initial kinetic model b) raw real and simulated data for observed exchange of (−)-nicotine *1* molecules with precatalyst IMes *18* using Model 1, following selective excitation of the 'Bound 1' resonance at 298 K. ... 135

Figure 95: observed rate constants for dissociation of substrate molecules at 298 K using Model 1. 136

Figure 96: observed rate constants for dissociation of substrate molecules at 303 K using Model 1. 138

Figure 97: Enthalpies of activation for the dissociation of bound substrate molecules from iridium using data from Model 1. Error bars are the standard deviation of the mean (n=8) 139

Figure 98: Entropies of activation for the dissociation of bound substrate molecules from iridium using Model 1 140

Figure 99: Gibbs free energies of activation for the dissociation of bound substrate molecules from iridium using Model 1 140

Figure 100: Model 2 – a kinetic model of the SABRE substrate exchange process for nicotines that considers intermediates and other species. 142

Figure 101: raw real and simulated data for observed exchange of (−)-nicotine *1* molecules with precatalyst IMes *18* using Model 2, following selective excitation of Bound 1 (species A) resonance at 298 K. 143

Figure 102: raw real and simulated data for observed exchange of (−)-nicotine *1* molecules with precatalyst IMes *18* using Model 2, following selective excitation of Bound 1 (species F) resonance at 298 K. 144

Figure 103: raw real and simulated data for observed exchange of (−)-nicotine *1* molecules with precatalyst IMes *18* using Model 2, following selective excitation of Bound 1 (species F) resonance at 298 K. 147

Figure 104: raw real and simulated data for observed exchange of (−)-nicotine *1* molecules with precatalyst IMes *18* using Model 3, following selective excitation of Bound 1 (species A) resonance at 298 K. 148

Figure 105: raw real and simulated data for observed exchange of (−)-nicotine *1* molecules with precatalyst IMes *18* using Model 3, following selective excitation of Bound 1 (species F) resonance at 298 K. 148

Figure 106: raw real and simulated data for observed exchange of (−)-nicotine *1* molecules with precatalyst IMes *18* using Model 2, following selective excitation of ligand ‘free’ in solution (species E) resonance at 298 K. 149

Figure 107: observed rate constants for dissociation of substrate molecules at 298 K using Model 3. 150

Figure 108: raw real and simulated data for observed exchange of 4,6-nicotine-d_2 *9* molecules with precatalyst IMes *18* using Model 4, following selective excitation of Bound 1 (species A) resonance at 298 K. 152

Figure 109: raw real and simulated data for observed exchange of 4,6-nicotine-d_2 *9* molecules with precatalyst IMes *18* using Model 4, following selective excitation of Bound 2 (species F) resonance at 298 K. 153

Figure 110: raw real and simulated data for observed exchange of 4,6-nicotine-d_2 *9* molecules with precatalyst IMes *18* using Model 4, following selective excitation of ligand 'free' in solution (species E) resonance at 298 K. 153

Figure 111: observed rate constants for dissociation of substrate molecules at 298 K using Model 4. 155

Figure 112: enthalpies of activation for ligand dissociation for a range of substrate/precatalyst combinations using Model 4. Error bars are the standard deviation of all results (n=8) 155

Figure 113: entropies of activation for ligand dissociation for a range of substrate/precatalyst combinations. 156

Figure 114: Gibbs free energies of activation for the dissociation of bound substrate molecules from iridium using Model 4 157

Figure 115: Depiction of automated flow setup for SABRE 164

Figure 116: inversion-recovery pulse sequence to derive T_1 relaxation times 165

Figure 117: saturation-recovery pulse sequence to derive T_1 relaxation times. 166

Figure 118: 'Bound 1' (A+G/2) excitation @ 288 K. 189

Figure 119: 'Bound 2' (F+G/2) excitation @ 288 K 190

Figure 120: 'Bound 1' (A+G/2) excitation @ 293 K. 191

Figure 121: 'Bound 2' (F+G/2) excitation @ 293 K 191

Figure 122: 'Bound 1' (A+G/2) excitation @ 298 K. 192

Figure 123: 'Bound 2' (A+G/2) excitation @ 298 K. 193

Figure 124: 'Bound 1' (A+G/2) excitation @ 303 K. 194

Figure 125: 'Bound 2' (F+G/2) excitation @ 303 K 194

Figure 126: Eyring plot of Bound 1 for (−)-nicotine *1*, IMes *18*. 195

Figure 127: Eyring plot of Bound 2 for (−)-nicotine *1*, IMes *18* 196
Figure 128: 'Bound 1' (A+G/2) excitation @ 288 K 197
Figure 129: 'Bound 2' (F+G/2) excitation @ 288 K 197
Figure 130: 'Bound 1' (A+G/2) excitation @ 293 K 198
Figure 131: 'Bound 2' (F+G/2) excitation @ 293 K 199
Figure 132: 'Bound 1' (A+G/2) excitation @ 298 K 200
Figure 133: 'Bound 2' (F+G/2) excitation @ 298 K 200
Figure 134: 'Bound 1' (A+G/2) excitation @ 303 K 201
Figure 135: 'Bound 2' (F+G/2) excitation @ 303 K 202
Figure 136: Eyring plot of Bound 1 for (−)-nicotine *1*, d_{22}-IMes *19* 203
Figure 137: Eyring plot of Bound 2 for (−)-nicotine *1*, d_{22}-IMes *19* 203
Figure 138: kinetic parameters for (−)-nicotine *1*, d_{22}-IMes *19* 203
Figure 139: 'Bound 1' (A+G/2) excitation @ 288 K 204
Figure 140: 'Bound 2' (F+G/2) excitation @ 288 K 204
Figure 141: 'Bound 1' (A+G/2) excitation @ 293 K 205
Figure 142: 'Bound 2' (F+G/2) excitation @ 293 K 206
Figure 143: 'Bound 1' (A+G/2) excitation @ 298 K 207
Figure 144: 'Bound 2' (F+G/2) excitation @ 298 K 207
Figure 146: 'Bound 1' (A+G/2) excitation @ 303 K 208
Figure 147: 'Bound 2' (F+G/2) excitation @ 303 K 209
Figure 148: Eyring plot of Bound 1 for 4,6-nicotine-d_2 *9*, IMes *18* 210
Figure 149: Eyring plot of Bound 2 for 4,6-nicotine-d_2 *9*, IMes *18* 210
Figure 150: kinetic parameters for 4,6-nicotine-d_2 *9*, IMes *18* 210
Figure 151: 'Bound 1' (A+G/2) excitation @ 288 K 211
Figure 152: 'Bound 2' (F+G/2) excitation @ 288 K 211
Figure 153: 'Bound 1' (A+G/2) excitation @ 293 K 212
Figure 154: 'Bound 2' (F+G/2) excitation @ 293 K 213

Figure 155: ‘Bound 1’ (A+G/2) excitation @ 298 K..... 214

Figure 156: ‘Bound 2’ (F+G/2) excitation @ 298 K 214

Figure 157: ‘Bound 1’ (A+G/2) excitation @ 303 K..... 215

Figure 158: ‘Bound 2’ (F+G/2) excitation @ 303 K 216

Figure 159: Eyring plot of Bound 1 for 4,6-nicotine-d_2 *9*, d_{22}-IMes *19* 217

Figure 160: Eyring plot of Bound 2 for 4,6-nicotine-d_2 *9*, d_{22}-IMes *19* 217

Figure 161: kinetic parameters for 4,6-nicotine-d_2 *9*, d_{22}-IMes *19*..... 217

Figure 162: ‘Bound 1’ (A+G/2) excitation @ 288 K..... 218

Figure 163: ‘Bound 2’ (F+G/2) excitation @ 288 K 218

Figure 164: ‘Free’ (E) excitation @ 288 K 219

Figure 165: ‘Bound 1’ (A+G/2) excitation @ 293 K..... 220

Figure 166: ‘Bound 2’ (F+G/2) excitation @ 293 K 220

Figure 167: ‘Free’ (E) excitation @ 293 K 221

Figure 168: ‘Bound 1’ (A+G/2) excitation @ 298 K..... 222

Figure 169: ‘Bound 2’ (A+G/2) excitation @ 298 K..... 222

Figure 170: ‘Free’ (E) excitation @ 298 K 223

Figure 171: ‘Bound 1’ (A+G/2) excitation @ 303 K..... 224

Figure 172: ‘Bound 2’ (F+G/2) excitation @ 303 K 224

Figure 173: ‘Free’ (E) excitation @ 303 K 225

Figure 174: Eyring plot of Bound 1 for (−)-nicotine *1*, IMes *18*..... 226

Figure 175: Eyring plot of Bound 2 for (−)-nicotine *1*, IMes *18*..... 226

Figure 176: ‘Bound 1’ (A+G/2) excitation @ 288 K..... 227

Figure 177: ‘Bound 2’ (F+G/2) excitation @ 288 K 228

Figure 178: ‘Free’ (E) excitation @ 288 K 228

Figure 179: ‘Bound 1’ (A+G/2) excitation @ 293 K..... 229

Figure 180: ‘Bound 2’ (F+G/2) excitation @ 293 K 230

Figure 181: ‘Free’ (E) excitation @ 293 K 230

Figure 182: ‘Bound 1’ (A+G/2) excitation @ 298 K 231
Figure 183: ‘Bound 2’ (F+G/2) excitation @ 298 K 232
Figure 184: ‘Free’ (E) excitation @ 298 K 232
Figure 185: ‘Bound 1’ (A+G/2) excitation @ 303 K 233
Figure 186: ‘Bound 2’ (F+G/2) excitation @ 303 K 234
Figure 187: ‘Free’ (E) excitation @ 303 K 234
Figure 188: Eyring plot of Bound 1 for (−)-nicotine *1*, d_{22}-IMes *19* 235
Figure 189: Eyring plot of Bound 2 for (−)-nicotine *1*, d_{22}-IMes *19* 236
Figure 190: kinetic parameters for (−)-nicotine *1*, d_{22}-IMes *19* 236
Figure 191: ‘Bound 1’ (A+G/2) excitation @ 288 K 237
Figure 192: ‘Bound 2’ (F+G/2) excitation @ 288 K 237
Figure 193: ‘Free’ (E) excitation @ 288 K 238
Figure 194: ‘Bound 1’ (A+G/2) excitation @ 293 K 239
Figure 195: ‘Bound 2’ (F+G/2) excitation @ 293 K 239
Figure 196: ‘Free’ (E) excitation @ 293 K 240
Figure 197: ‘Bound 1’ (A+G/2) excitation @ 298 K 241
Figure 198: ‘Bound 2’ (F+G/2) excitation @ 298 K 241
Figure 199: ‘Free’ (E) excitation @ 298 K 242
Figure 200: ‘Bound 1’ (A+G/2) excitation @ 303 K 243
Figure 201: ‘Bound 2’ (F+G/2) excitation @ 303 K 243
Figure 202: ‘Free’ (E) excitation @ 303 K 244
Figure 203: Eyring plot of Bound 1 for 4,6-nicotine-d_2 *9*, IMes *18* 245
Figure 204: Eyring plot of Bound 2 for 4,6-nicotine-d_2 *9*, IMes *18* 245
Figure 205: kinetic parameters for 4,6-nicotine-d_2 *9*, IMes *18* 245
Figure 206: ‘Bound 1’ (A+G/2) excitation @ 288 K 246
Figure 207: ‘Bound 2’ (F+G/2) excitation @ 288 K 246
Figure 208: ‘Free’ (E) excitation @ 288 K 247

Figure 209: ‘Bound 1’ (A+G/2) excitation @ 293 K..... 248

Figure 210: ‘Bound 2’ (F+G/2) excitation @ 293 K 248

Figure 211: ‘Free’ (E) excitation @ 293 K 249

Figure 212: ‘Bound 1’ (A+G/2) excitation @ 298 K..... 250

Figure 213: ‘Bound 2’ (F+G/2) excitation @ 298 K 250

Figure 214: ‘Free’ (E) excitation @ 298 K 251

Figure 215: ‘Bound 1’ (A+G/2) excitation @ 303 K..... 252

Figure 216: ‘Bound 2’ (F+G/2) excitation @ 303 K 252

Figure 217: ‘Free’ (E) excitation @ 303 K 253

Figure 218: Eyring plot of Bound 1 for 4,6-nicotine-d_2 *9*, d_{22}-IMes *19* 254

Figure 219: Eyring plot of Bound 2 for 4,6-nicotine-d_2 *9*, d_{22}-IMes *19* 254

Figure 220: kinetic parameters for 4,6-nicotine-d_2 *9*, d_{22}-IMes *19*..... 254

List of tables

Table 1: variation in hydrogen isomer populations with temperature, adapted from Duckett *et al.*, 1999[9] 43

Table 2: signal-to-noise ratios calculated for one-shot 2D ^{1}H MRI rare results 126

Table 3: effective T_1 relaxation times calculated..... 130

Table 4: (observed) rate constants generated by Model 2 for (−)-nicotine *1* molecules with precatalyst IMes *18* at 298 K. 145

Table 5: EXSY fitting least squares errors using Model 2 for (−)-nicotine *1* molecules with precatalyst IMes *18* at 298 K with all rate constants artificially set to 2.5 s^{-1}. 146

Table 6: (observed) rate constants generated by Model 4 for 4,6-nicotine-d_2 *9* and IMes *18* at 298 K..... 154

Table 7: Model 1 observed rate constants for (−)-nicotine *1*, IMes *18* @ 288 K..... 190

Table 8: sum of least squares for each plot 190

Table 9: Model 1 observed rate constants for (−)-nicotine *1*, IMes *18* @ 293 K. Rate constants are read as k_{XY}, *i.e.* k_{AB} is row A, column B 192

Table 10: sum of least squares for each plot 192

Table 11: Model 1 observed rate constants for (−)-nicotine *1*, IMes *18* @ 298 K..... 193

Table 12: sum of least squares for each plot 193

Table 13: Model 1 observed rate constants for (−)-nicotine *1*, IMes *18* @ 303 K..... 195

Table 14: sum of least squares for each plot 195

Table 15: kinetic parameters for (−)-nicotine *1*, IMes *18* 196

Table 16: Model 1 observed rate constants for (−)-nicotine *1*, d_{22}-IMes *19* @ 288 K. 198

Table 17: sum of least squares for each plot 198

Table 18: Model 1 observed rate constants for (−)-nicotine *1*, d_{22}-IMes *19* @ 293 K. 199

Table 19: sum of least squares for each plot 199

Table 20: Model 1 observed rate constants for (−)-nicotine *1*, d_{22}-IMes *19* @ 298 K. 201

Table 21: sum of least squares for each plot 201

Table 22: Model 1 observed rate constants for (−)-nicotine *1*, d_{22}-IMes *19* @ 303 K. 202

Table 23: sum of least squares for each plot 202

Table 24: Model 1 observed rate constants for 4,6-nicotine-d_2 *9*, IMes *18* @ 288 K. . 205

Table 25: sum of least squares for each plot and the modelled T_1 relaxation parameters (in seconds) used 205

Table 26: Model 1 observed rate constants for 4,6-nicotine-d_2 *9*, IMes *18* @ 293 K. . 206

Table 27: sum of least squares for each plot 206

Table 28: Model 1 observed rate constants for 4,6-nicotine-d_2 *9*, IMes *18* @ 298 K. . 208

Table 29: sum of least squares for each plot 208

Table 30: Model 1 observed rate constants for 4,6-nicotine-d_2 *9*, IMes *18* @ 303 K. . 209

Table 31: sum of least squares for each plot and the modelled T_1 relaxation parameters (in seconds) used 209

Table 32: Model 1 observed rate constants for 4,6-nicotine-d_2 *9*, d_{22}-IMes *19* @ 288 K. 212

Table 33: sum of least squares for each plot 212

Table 34: Model 1 observed rate constants for 4,6-nicotine-d_2 *9*, d_{22}-IMes *19* @ 293 K. 213

Table 35: sum of least squares for each plot 213

Table 36: Model 1 observed rate constants for 4,6-nicotine-d_2 *9*, d_{22}-IMes *19* @ 298 K. 215

Table 37: sum of least squares for each plot 215

Table 38: Model 1 observed rate constants for 4,6-nicotine-d_2 *9*, d_{22}-IMes *19* @ 303 K. 216

Table 39: sum of least squares for each plot 216

Table 40: Model 4 observed rate constants for (−)-nicotine *1*, IMes *18* @ 288 K..... 219

Table 41: sum of least squares for each plot and the modelled T_1 relaxation parameters (in seconds) used 219

Table 42: Model 4 observed rate constants for (−)-nicotine *1*, IMes *18* @ 293 K..... 221

Table 43: sum of least squares for each plot and the modelled T_1 relaxation parameters (in seconds) used 221

Table 44: Model 4 observed rate constants for (−)-nicotine *1*, IMes *18* @ 298 K..... 223

Table 45: sum of least squares for each plot and the modelled T_1 relaxation parameters (in seconds) used 224

Table 46: Model 4 observed rate constants for (−)-nicotine *1*, IMes *18* @ 303 K..... 225

Table 47: sum of least squares for each plot and the modelled T_1 relaxation parameters (in seconds) used 226

Table 48: kinetic parameters for (−)-nicotine *1*, IMes *18* 227

Table 49: Model 4 observed rate constants for (−)-nicotine *1*, d_{22}-IMes *19* @ 288 K. 229

Table 50: sum of least squares for each plot and the modelled T_1 relaxation parameters (in seconds) used 229

Table 51: Model 4 observed rate constants for (−)-nicotine *1*, d_{22}-IMes *19* @ 293 K. 231

Table 52: sum of least squares for each plot and the modelled T_1 relaxation parameters (in seconds) used 231

Table 53: Model 4 observed rate constants for (−)-nicotine *1*, d_{22}-IMes *19* @ 298 K. 233

Table 54: sum of least squares for each plot and the modelled T_1 relaxation parameters (in seconds) used 233

Table 55: Model 4 observed rate constants for (−)-nicotine *1*, d_{22}-IMes *19* @ 303 K. 235

Table 56: sum of least squares for each plot and the modelled T_1 relaxation parameters (in seconds) used 235

Table 57: Model 4 observed rate constants for 4,6-nicotine-d_2 *9*, IMes *18* @ 288 K. . 238

Table 58: sum of least squares for each plot and the modelled T_1 relaxation parameters (in seconds) used 238

Table 59: Model 4 observed rate constants for 4,6-nicotine-d_2 *9*, IMes *18* @ 293 K. . 240

Table 60: sum of least squares for each plot and the modelled T_1 relaxation parameters (in seconds) used 240

Table 61: Model 4 observed rate constants for 4,6-nicotine-d_2 *9*, IMes *18* @ 298 K. . 242

Table 62: sum of least squares for each plot and the modelled T_1 relaxation parameters (in seconds) used 242

Table 63: Model 4 observed rate constants for 4,6-nicotine-d_2 *9*, IMes *18* @ 303 K. . 244

Table 64: sum of least squares for each plot and the modelled T_1 relaxation parameters (in seconds) used 244

Table 65: Model 4 observed rate constants for 4,6-nicotine-d_2 *9*, d_{22}-IMes *19* @ 288 K. 247

Table 66: sum of least squares for each plot and the modelled T_1 relaxation parameters (in seconds) used 247

Table 67: Model 4 observed rate constants for 4,6-nicotine-d_2 *9*, d_{22}-IMes *19* @ 293 K. 249

Table 68: sum of least squares for each plot and the modelled T_1 relaxation parameters (in seconds) used 249

Table 69: Model 4 observed rate constants for 4,6-nicotine-d_2 *9*, d_{22}-IMes *19* @ 298 K. 251

Table 70: sum of least squares for each plot and the modelled T_1 relaxation parameters (in seconds) used 251

Table 71: Model 4 observed rate constants for 4,6-nicotine-d_2 *9*, d_{22}-IMes *19* @ 303 K. 253

Table 72: sum of least squares for each plot and the modelled T_1 relaxation parameters (in seconds) used 253

Table 73: Model 1 EXSY data combined, with standard deviation errors. 255

Table 74: Model 4 EXSY data combined, with standard deviation errors. 255

Table 75: comparison of data from Models 1 and 4, with errors 256

Table 76: ‘shake and drop’ errors for 4 equivalents (−)-nicotine *1* with IMes *18*, shaken in stray field. 256

Table 77: ‘shake and drop’ errors for 5 equivalents (−)-nicotine *1* with IMes *18*, shaken in stray field. 257

Table 78: ‘shake and drop’ errors for 6 equivalents (−)-nicotine *1* with IMes *18*, shaken in stray field. 257

Table 79: ‘shake and drop’ errors for 10 equivalents (−)-nicotine *1* with IMes *18*, shaken in stray field. 258

Table 80: ‘shake and drop’ errors for 15 equivalents (−)-nicotine *1* with IMes *18*, shaken in stray field. 258

Table 81: ‘shake and drop’ errors for 4 equivalents (−)-nicotine *1* with d_{22}-IMes *19*, shaken in stray field..... 259

Table 82: ‘shake and drop’ errors for 6 equivalents (−)-nicotine *1* with d_{22}-IMes *19*, shaken in stray field..... 259

Table 83: ‘shake and drop’ errors for 8 equivalents (−)-nicotine *1* with d_{22}-IMes *19*, shaken in stray field..... 260

Table 84: ‘shake and drop’ errors for 10 equivalents (−)-nicotine *1* with d_{22}-IMes *19*, shaken in stray field..... 260

Table 85: ‘shake and drop’ errors for 15 equivalents (−)-nicotine *1* with d_{22}-IMes *19*, shaken in stray field..... 261

Table 86: ‘shake and drop’ errors for 4 equivalents 4,6-nicotine-d_2 *9* with IMes *18*, shaken in stray field. 261

Table 87: ‘shake and drop’ errors for 5 equivalents 4,6-nicotine-d_2 *9* with IMes *18*, shaken in stray field. 262

Table 88: ‘shake and drop’ errors for 6 equivalents 4,6-nicotine-d_2 *9* with IMes *18*, shaken in stray field. 262

Table 89: ‘shake and drop’ errors for 10 equivalents 4,6-nicotine-d_2 *9* with IMes *18*, shaken in stray field..... 262

Table 90: ‘shake and drop’ errors for 15 equivalents 4,6-nicotine-d_2 *9* with IMes *18*, shaken in stray field..... 263

Table 91: ‘shake and drop’ errors for 4 equivalents 4,6-nicotine-d_2 *9* with d_{22}-IMes *19*, shaken in stray field..... 263

Table 92: ‘shake and drop’ errors for 6 equivalents 4,6-nicotine-d_2 *9* with d_{22}-IMes *19*, shaken in stray field..... 264

Table 93: ‘shake and drop’ errors for 8 equivalents 4,6-nicotine-d_2 *9* with d_{22}-IMes *19*, shaken in stray field..... 264

Table 94: ‘shake and drop’ errors for 10 equivalents 4,6-nicotine-d_2 *9* with d_{22}-IMes *19*, shaken in stray field. 265

Table 95: ‘shake and drop’ errors for 15 equivalents 4,6-nicotine-d_2 *9* with d_{22}-IMes *19*, shaken in stray field. 265

Table 96: ‘shake and drop’ errors for 5 equivalents 6-nicotine-d_1 *4* with IMes *18*, shaken in stray field. 266

Table 97: ‘shake and drop’ errors for 5 equivalents 5,6-nicotine-d_2 *8* with IMes *18*, shaken in stray field. 266

Table 98: ‘shake and drop’ errors for 5 equivalents 2,6-nicotine-d_2 *10* with IMes *18*, shaken in stray field. 267

Table 99: ‘shake and drop’ errors for 5 equivalents 4,6-nicotine-d_2 *9* with I^{t}Bu *20*, shaken in stray field. 267

Table 100: ‘shake and drop’ errors for 5 equivalents 4,6-nicotine-d_2 *9* with ICl *21*, shaken in stray field. 268

Table 101: ‘shake and drop’ errors for 5 equivalents 6-nicotine-d_1 *4* with IMes *18*, shaken in a 60 G magnetic shaker assembly. 268

Table 102: ‘shake and drop’ errors for 5 equivalents 4,6-nicotine-d_2 *9* with d_{22}-IMes *19*, shaken in a 60 G magnetic shaker assembly for six seconds. 269

Table 103: ‘shake and drop’ errors for 2.5 equivalents 4,6-nicotine-d_2 *9* with 2.5 equivalents coligand py-d_5 23 and d_{22}-IMes *19*, shaken in a 60 G magnetic shaker assembly for six seconds. 269

Table 104: ‘shake and drop’ errors for 5 equivalents (−)-nicotine *1* with IMes *18*, with 5 bar *p*-H_2 shaken in stray field. 270

Table 105: ‘shake and drop’ errors for 5 equivalents (−)-nicotine *1* with IMes *18*, with 6 bar *p*-H_2 shaken in stray field. 270

Table 106: ‘shake and drop’ errors for 5 equivalents 4,6-nicotine-d_2 *1* with IMes *18*, with 5 bar *p*-H_2 shaken in stray field. 271

Table 107: ‘shake and drop’ errors for 5 equivalents 4,6-nicotine-d_2 *1* with IMes *18*, with 6 bar *p*-H_2 shaken in stray field. 271

Table 108: ‘shake and drop’ errors for 5 equivalents 4,6-nicotine-d_2 *1* with IMes *18*, with 5 bar *p*-H_2 shaken in a 60 G magnetic shaker assembly. 272

Table 109: ‘shake and drop’ errors for 5 equivalents 4,6-nicotine-d_2 *1* with IMes *18*, with 6 bar *p*-H_2 shaken in a 60 G magnetic shaker assembly. 272

Table 110: ‘shake and drop’ errors for 5 equivalents 4,6-nicotine-d_2 *1* with d_{22}-IMes *19*, with 6 bar *p*-H_2 shaken in a 60 G magnetic shaker assembly. 273

Table 111: ‘shake and drop’ errors for 4 equivalents (−)-nicotine *1* with IMes *18*, shaken in stray field at 303 K. 273

Table 112: ‘shake and drop’ errors for 4 equivalents (−)-nicotine *1* with IMes *18*, shaken in stray field at 308 K. 274

Table 113: ‘shake and drop’ errors for 4 equivalents (−)-nicotine *1* with IMes *18*, shaken in stray field at 308 K. 274

Table 114: ‘shake and drop’ errors for 4 equivalents 4,6-nicotine-d_2 *9* with IMes *18*, shaken in stray field at 303 K. 274

Table 115: ‘shake and drop’ errors for 4 equivalents 4,6-nicotine-d_2 *9* with IMes *18*, shaken in stray field at 308 K. 275

Table 116: ‘shake and drop’ errors for 4 equivalents 4,6-nicotine-d_2 *9* with IMes *18*, shaken in stray field at 313 K. 275

List of equations

Equation 1: components of a molecular wavefunction[46] 43

Equation 2: T_1 decay constant equation for MRI data 130

Equation 3: the Eyring equation and its rearrangement to derive enthalpy and entropy of activation. 138

Equation 4: simulated relaxation term for kinetic modelling. 151

Equation 5: equation for calculation of signal enhancement 163

Equation 6: equation for standard error (S.E.), where σ is the standard deviation and *n* is the number of entries in the data series 167

Acknowledgements

I would like to thank my two supervisors; Professor Simon Duckett and Professor Peter O'Brien for their guidance and support through this work. Secondly, I would like to thank the entirety of both research groups I have been part of, including the Taylor research group also in D-block. Extra thanks should go to the PDRAs Pete Rayner, Phil Norcott and Mike Burns, who helped immensely with developing the synthetic methodology and setup, as well as transitioning a synthetic chemist to the analytical world of SABRE, Pete Richardson for development of new and innovative equipment, Alexandra Olaru for facilitating imaging experiments and Masakazu Atobe and James Firth for substantial synthetic assistance and encouragement. PhD student friends and colleagues Adam Islip and Chris Lancaster deserve special credit for being the nearest on-hand day-to-day for ideas to bounce off, general advice and help, a good laugh and for being the two who had to put up with me the most throughout the project, especially when writing TAP reports!

My fellow students and those who have completed during the course of the project also deserve thanks - from the SBD group Amy, Liz, Jenny, Olga, Emma, Rhianna, Kate, Allistair, Ben and my late good friend and colleague Robin, who is sorely missed. Mary, Mickey, Sarah, Alice, Paul, Nico and Tom from the PAOB group deserve thanks also. Even Joe from the Parsons group, who made my first year so entertaining and because I promised I would give him an acknowledgement if I could borrow his measuring cylinder one time in D215. I would also like to thank Vicky, Richard, Denise and Lyndsay from CHyM, Graeme, Karl and Heather in D-block and all the rest of the technical and administrative staff for their tireless and invaluable efforts to fix, build and organise things.

Thanks should be given to my friends in the world of historic re-enactment, who have provided me with welcome distractions throughout my research. I thank my friends and housemates, Jacob, Vytautas, Hannah, James, Rob, Jess, Catherine, Catherine and Grace. Finally I wish to thank my family Colin, Julia and Emma for their continued support and reassurance.

Declaration

I confirm that this thesis is a presentation of original work and I am the sole author. If any passage(s) or diagram(s) have been copied from academic papers, books, the internet or any other sources these are clearly identified and the reference(s) is fully cited. I certify that, other than where indicated and to the very best of my knowledge, this work does not breach the regulations of the University of York regarding plagiarism or academic conduct in examinations. This work has not previously been presented for an award at this, or any other, University. All sources are acknowledged as references.

1: Introduction

1.1 NMR spectroscopy, MRI and their limitations

Nuclear Magnetic Resonance (NMR) spectroscopy is amongst the most important and widely used procedures in science. Magnetic Resonance Imaging (MRI), a biological application of NMR, is one of the most prominent procedures in healthcare. However, the relative insensitivity inherent to all NMR techniques severely restricts their diagnostic potential.

Signal strength in an NMR experiment is dependent on the bulk magnetic moment (often also known as the nuclear spin polarisation, *P*) of all the nuclei in the sample when a magnetic field is applied. This is in turn derived from the Boltzmann population of nuclear spin energy levels, specifically the population difference between them. For the I = ½ nuclear spin system (to which ^{1}H, ^{13}C, ^{15}N, ^{31}P, ^{19}F and many others belong), the nuclear spins can either align with the applied magnetic field (I = + ½) or against it (I = − ½) (Figure 1).

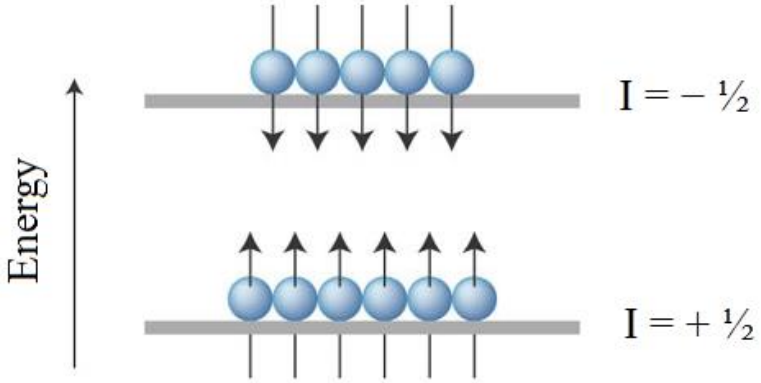

Figure 1: Populations of nuclear spin energies at thermal equilibrium for I = ½

The difference in energy between each of these spin energy levels for spin I = ½ is given by $\Delta E = \gamma \hbar B_0$, ie. it is proportional to the strength of the magnetic field. At field strengths possible for an NMR magnet, this energy difference is very small, far smaller than the ambient thermal energy (*kT*, the energy of molecules colliding with each other) and hence the levels are almost equally populated. Indeed, in a normal 400 MHz spectrometer, with a field strength of 9.4 T, the population difference between the two levels for ^{1}H is only 31 nuclei per million, *i.e.* there are only thirty-one more nuclei in the lower energy level

than the higher out of every million observed. This also means that there are only thirty-one nuclei per million that can be spin-flipped to the higher energy level and thus produce a signal when the RF pulse of an NMR experiment is applied.[1-3] The problem is exacerbated enormously for other even less sensitive nuclei, with ^{13}C having one quarter ($\gamma/2\pi$ = 10.708 MHz•T^{-1}) of the nuclear spin polarisation as its ^{1}H equivalent ($\gamma/2\pi$ = 42.577 MHz•T^{-1}), and ^{15}N having one tenth ($\gamma/2\pi$ = −4.316 MHz•T^{-1}), the vastly reduced natural abundances of these isotopes compared to ^{1}H notwithstanding.[1,3] Thus, the signal intensity produced is comparatively weak compared to that of optical spectroscopy, where nearly every atom/molecule observed will contribute to a signal.

Since it can be derived that the population difference $P \approx \Delta E/2kT \equiv \frac{\gamma\hbar B_0}{2kT}$, then there are several ways that the thermal equilibrium population difference can be enhanced.[2] The most obvious method is to simply increase the strength of the applied field with a more powerful magnet, giving a greater difference between the nuclear spin energy levels and reducing the likelihood that the ambient thermal energy of the molecules will promote them into the higher energy level. However, increasingly powerful magnets rise dramatically in cost and can only improve *P* so much – indeed, even with a very strong (and very expensive) 21 T magnet, the population difference at equilibrium will still only be 70 ppm.[3]

Alternatively, a lowered temperature will reduce the ambient thermal energy and result in a stronger population bias towards the lower spin energy level for similar reasons as above. Unfortunately, whilst this has been used successfully with NMR experiments already (although gains are still fairly minor), *in vivo* experiments such as MRI will always be limited to around biological temperatures, a minimum of around 300 K.

The third, and easiest, solution to the weak population difference is simply to increase the number of nuclei observed so that their net signal is stronger. In practical terms, this only means increasing the concentration of the sample and/or increasing the number of scans performed (which achieves the same result). Regrettably, there are once again practical limits to what these approaches can achieve. There is only a finite quantity of substrate that can be dissolved in a given amount of solvent, so increased concentration can only offer a finite improvement. It would also be totally impractical for research and diagnosis if every NMR experiment and MRI scan ever performed took hours or days rather than

minutes because of the increased number of scans needed. More importantly for biological applications, there is a limited timeframe before an injected contrast agent will be excreted from the body by the kidneys and so waiting hours to collect a great number of scans is not feasible. There is also the problem of how harmful these contrast agents are for the body: for example, the existing agents are based on the extremely toxic heavy metal gadolinium – while ionic cyclic gadolinium (III) chelates are relatively safe compared to other forms,[4] it would be ill-advised to inject more harmful material than absolutely necessary into a patient to achieve a better signal.

With these problems, it is obvious that an alternative approach is needed to improve the sensitivity of NMR and, by extension, the sensitivity of MRI.

1.2 Signal enhancement and hyperpolarisation

Signal enhancement is the production of a non-Boltzmann distribution of spins, i.e. selectively populating certain spin-states (Figure 2) and thereby increasing the number of spin-flips possible in an NMR experiment. As the NMR signal for a given sample is derived from the sum of these observable transitions, this *hyperpolarised* state will result in significantly increased signal strength.

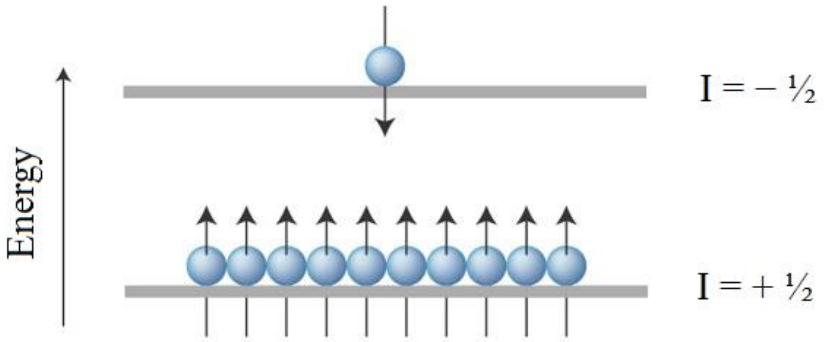

Figure 2: Hyperpolarised populations of nuclear spin energies for I = ½

There are several methods for available for production of a hyperpolarised state, including 'brute force'[5,6], optical pumping of gases[7], Dynamic Nuclear Polarisation[8] and the use of a material called *para*-hydrogen.[9] These will be discussed in detail below.

1.2.1 Brute force

Brute force is a simple hyperpolarisation method, originally proposed in the 1960s but now considered antiquated.[5,6] It is essentially a more-extreme version of the physical improvements described in Chapter 1.1 – a sample is exposed to a strong magnetic field and ultra-low temperatures, the former increasing the energy gap between spin states and the latter reducing/eliminating transitions via ambient thermal energy. Over time, a hyperpolarised state is very gradually produced.[7] An increase in polarisation of 1000-fold was observed by cooling a sample to 4 K in a 20 T field.[10] An extremely low temperature of 7 milli-kelvin and a magnetic field of 16 T was reported by Owers-Bradley *et al.* to yield a signal enhancement of ~200,000 fold versus the same sample at 310 K and 3 T, although the enhancement needed to be mediated by nanoparticles.[11]

Such enormous signal comes at a price, the cost of such powerful magnets notwithstanding. Firstly, the hyperpolarised state only exists at super-low temperatures, degrading rapidly back to Boltzmann equilibrium when warmed to temperatures more useful for diagnostic purposes. Secondly, the hyperpolarised state takes an inordinate amount of time to form, as the T_1 relaxation times of samples become extremely long at low temperatures. As transitions between spin states are either an excitation or relaxation (in this case the latter), the gradual production of a hyperpolarised state by long relaxation will invariably be very slow. Due to the demanding conditions required, there has been minimal research done into a practicable application for brute force and other methods are far more prominent. However, recent work by Hirsch *et al.* with new protocols for the polarisation and subsequent warming of samples with minimal loss of polarisation indicates brute force may become a relevant technique again.[12]

1.2.2 Optical pumping of gases

Optical pumping is a technique first developed for medical imaging by Albert et al., in 1994.[13] A noble gas, typically ^{129}Xe or ^{3}He, is combined with alkali metal vapour (typically rubidium) and nitrogen in a gas cell. Circularly polarised light of a specific wavelength is produced by a laser shining through a quarter-wavelength metal plate and passed through the mixture. The gas is hyperpolarised by spin exchange from the alkali metal in a Helmholtz coil-generated magnetic field – the alkali metal is itself polarised by absorbing the angular momentum of the laser light. A small sense coil monitors

completion of the hyperpolarisation process, subsequently the alkali metal is condensed and the hyperpolarised gas extracted to a gas bag for diagnostic use (Figure 3).[5,14]

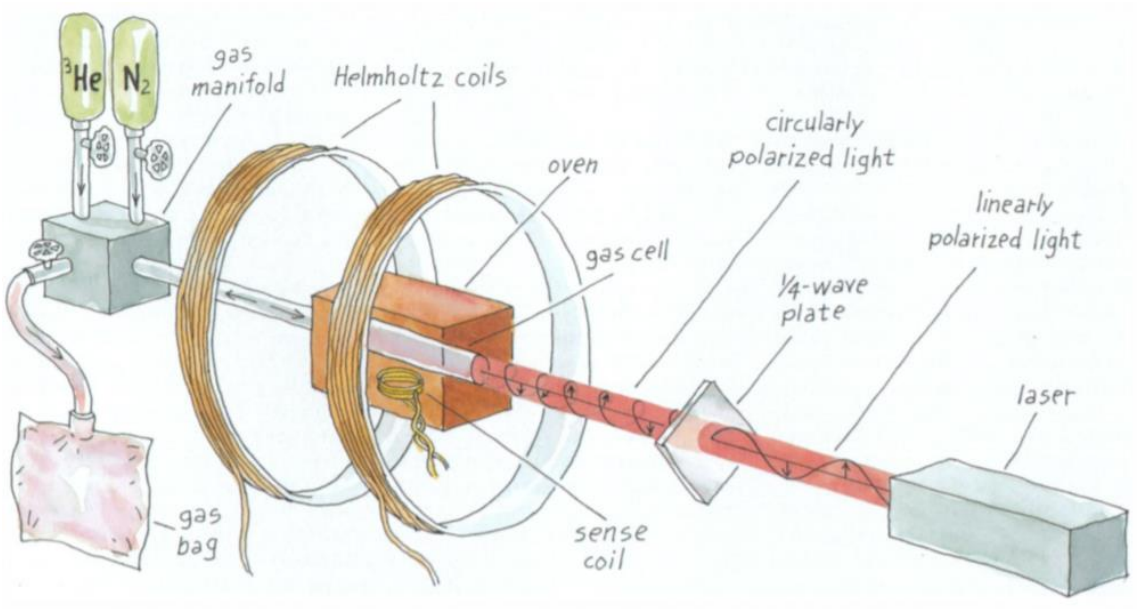

Figure 3: Apparatus for polarizing gas (in this case ^{3}He) outside the body. Figure taken from Kadlecek et al., 2002[14]

Hyperpolarised gases have primarily been used for the imaging of the lungs. Normal proton MRI of the lungs is very difficult, as they are predominantly filled with gas spaces and devoid of the blood (i.e. water) needed for proton MRI to work. There are also susceptibility issues encountered with air/tissue interfaces, where gradual magnetisation of the lung membranes generates image artefacts.[15] However , ^{129}Xe has shown much diagnostic promise beyond lung imaging, as its lipophilic nature allows it to dissolve in both fatty tissues and blood.[16] The technique has developed to allow full imaging of human lungs,[17] the human oral cavity[18] and easy distinction between healthy lungs and those with asthma, cystic fibrosis or chronic obstructive pulmonary disease (COPD).[19] In the latter study, overlay of ^{1}H and ^{129}Xe MRI spectra allowed for a complete picture of the lungs to be obtained (Figure 4).

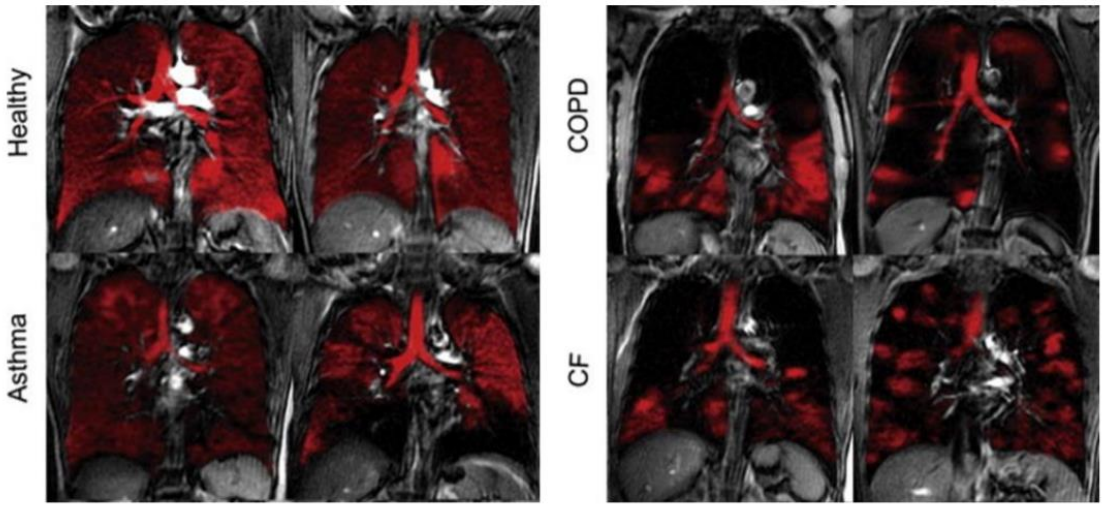

Figure 4: Hyperpolarised 129Xe MRI images (red) overlaid with the corresponding ^{1}H MRI images of the thoracic cavity. Images are from healthy participants and those with asthma, chronic obstructive pulmonary disease (COPD) and cystic fibrosis (CF). Image taken from Shukla *et al.*[19]

The chief flaw in the use of hyperpolarised gases is generally poor signal intensity compared to other hyperpolarisation techniques.[20] Research has therefore focused on applications for which non-gaseous agents would be ill-suited, such as perfusion of gas into tissues[21-24] and studies into brain function by perfusion tracking.[16]

1.2.3 Dynamic Nuclear Polarisation

Dynamic Nuclear Polarisation (DNP) is a method that transfers polarisation from lone electron pairs to create a non-Boltzmann distribution of nuclear spins.[7] Such a transfer is affected by applying GHz-wavelength microwave radiation at very low temperatures (1-2 K) and in a relatively high magnetic field (~3 T). Electrons have a much higher gyromagnetic ratio (1.76×10^{11} rad T s^{-1}) than typical nuclei (2.68×10^{8} rad T s^{-1} for a hydrogen nucleus),[25] hence polarisation of an electron spin is 657 times greater magnitude than proton spin under the same conditions.[26]

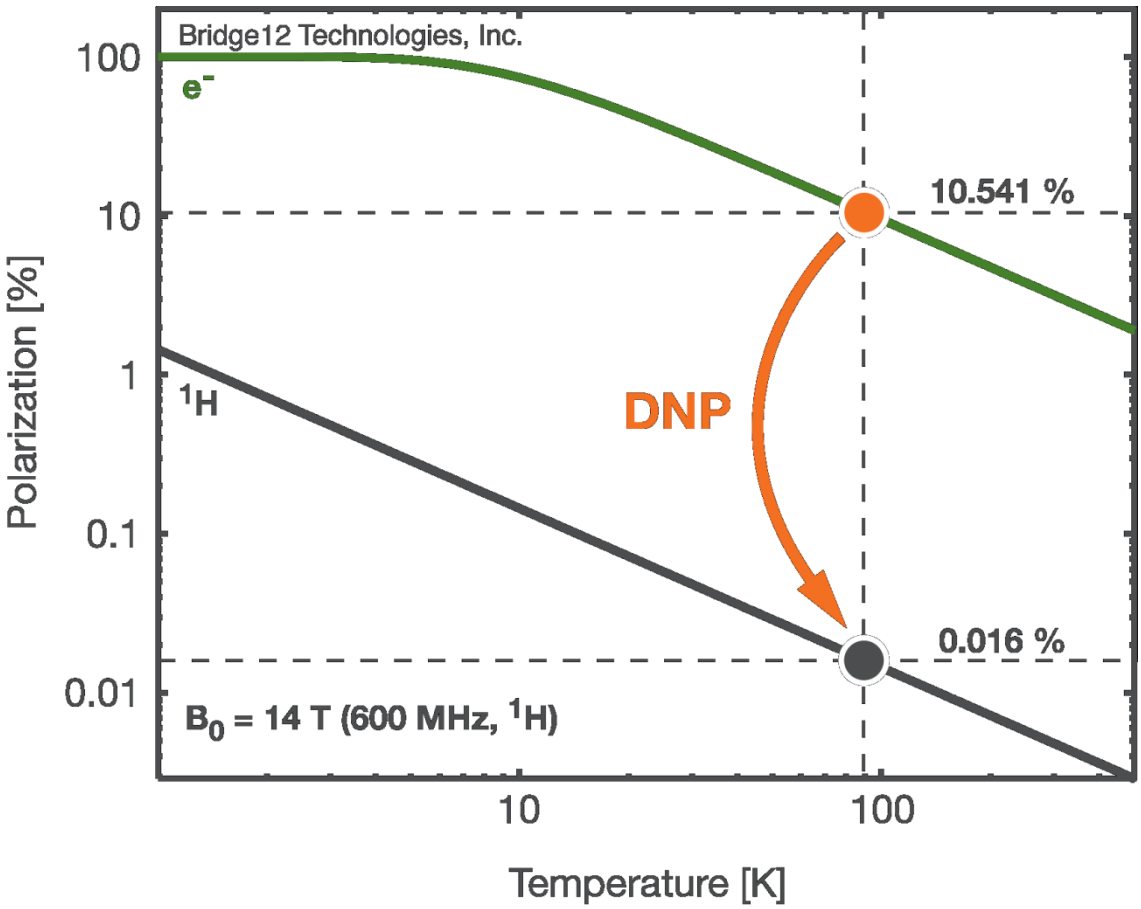

Figure 5: differences in polarisation between electrons (green) and proton nuclei (black) in a 14 T magnetic field and the temperature dependence of each. DNP is the process of transferring polarisation from electrons to nuclei, as indicated by the orange arrow. Image taken from Bridge12 Technologies[27]

The microwave polarisation transfer in DNP can be effected in four different methods - solid-effect (SE), the cross-effect (CE), thermal-mixing (TM) and the Overhauser effect (OE).[28] The first three methods have been predominantly used to hyperpolarise in the solid state, with notable research including ribosome structural biology[29] and bacterial cell interactions.[3,30] The chief limitation of solid-state DNP is that it is difficult to utilise low-temperature solids in *in vivo* or *in vitro* applications.

Dissolved-phase or dissolution DNP is a more promising method, in which nuclear spins are still hyperpolarised in the solid state at very low temperature but are then warmed within seconds to a liquid with minimal loss of polarisation. This method was first successfully completed for a urea sample with a resulting polarisation of 37% for ^{13}C and 7.8% for ^{15}N.[3]

An important development in recent years has been the successful hyperpolarisation of water. Water is an appealing target, as protons can yield high levels of magnetisation due to one of the highest gyromagnetic ratios of all nuclei. Secondly, water is not only completely biocompatible, but also crucial in a wide variety of metabolic processes.[31] Water hyperpolarisation has been achieved using both Overhauser-effect solid-state[32] and dissolution DNP[33], with the latter exhibiting greater and longer-lived enhancement. An example of hyperpolarised water used in imaging is shown in Figure 6.

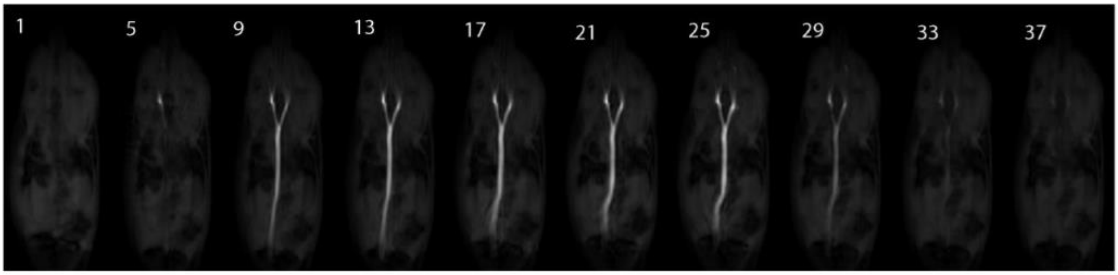

Figure 6: *In vivo* angiographic images in a rat after a tail vein injection of hyperpolarised water. The numbers represent time after injection in seconds. Image taken from Ardenkjær-Larsen et al., 2011[33]

However, DNP hyperpolarisation of water has significant limitations. The hyperpolarised water relaxes back to thermal equilibrium very quickly, as the T_1 relaxation time of water is only 3.7 seconds. Secondly, creation of the hyperpolarised sample in the first place is very slow, typically taking an hour or more.[34] The fast relaxation can be alleviated somewhat by addition of D_2O, although this creates complications as D_2O in large volumes is considered toxic.

Pyruvate is the other molecule of most interest to DNP studies, with several ideal properties for diagnostic imaging. This sample molecule is highly solubility in water, exhibits rapid distribution and metabolism *in vivo*, shows different metabolism in tumour cells versus healthy cells and has a relatively long T_1 relaxation time when labelled with ^{13}C.[35] In addition, there is highly efficient transport of pyruvate into cells through dedicated transport proteins.[36]

Pyruvate is metabolised to form lactate, alanine and bicarbonate, each which have a distinct ^{13}C chemical shift. Tumour cells have been shown to produce more lactate than healthy cells, which means a hyperpolarised injection of pyruvate can be used to determine the success of chemotherapy in a non-invasive manner. Chemical Shift Imaging (CSI) is an imaging technique whereby maps can be produced of the location of

each individual pyruvate metabolite signal.[37] CSI has been successfully combined with DNP for a range of organs in a range of species. Some examples of the images produced are shown in Figures 7 and 8.

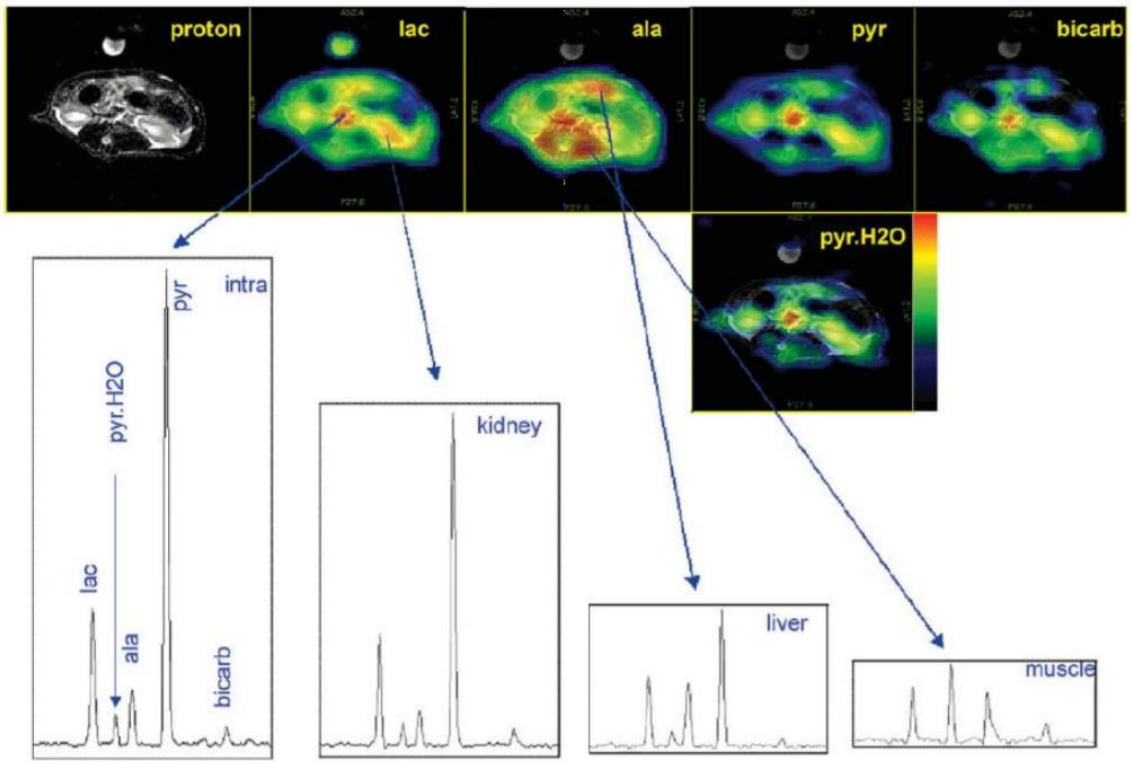

Figure 7: Data from abdominal ^{13}C CSI acquisition of pyruvate metabolite maps in a rat. Different metabolites are shown to become concentrated in different tissue. Image taken from Kohler et al., 2007[38] 'Intra' refers to the intracellular spaces

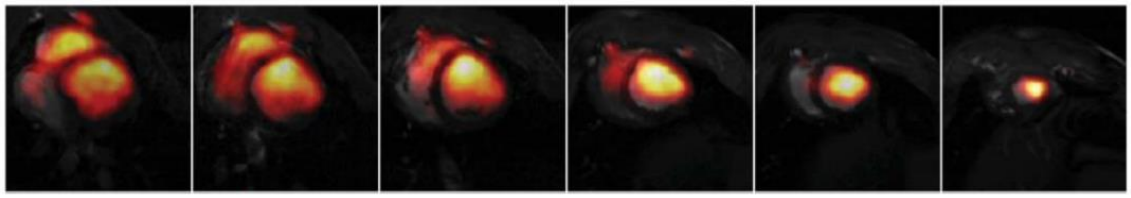

Figure 8: Distribution of hyperpolarised pyruvate in a pig heart, via multiple slices through the short axis. Image taken from Lau et al., 2010[39]

DNP has become a well-established hyperpolarisation technique, although it is not without its problems. Details of the complex polarisation transfer between electrons and nuclei are still not fully understood, and several papers have been published by Vega *et al.* trying to more fully eleucidate the mechanisms.[40-42] Diagnostic use requires long relaxation times for the hyperpolarised agent to both be injected and reach the site of interest without signal intensity diminishing significantly. Slow relaxation has so far been

achieved with ^{13}C-labelling of compounds, which adds extra time and cost to the sample preparation and also adds requirements to the MRI facility. Using DNP in a clinical environment therefore requires the MRI facility to have access to dual tuned ($^{1}H/^{13}C$) coils and a dedicated clean room to house the bulky DNP instrument. The extra equipment and facilities required come both at considerable financial cost as well as demanding significant space.

1.3 *para*-Hydrogen

The most recent (and perhaps most promising) source of non-equilibrium polarisation is a material known as *para*-hydrogen (*p*-H_2), a form of molecular hydrogen gas. This gas can be employed hydrogenatively in a technique called *para*-Hydrogen Induced Polarisation (PHIP) or non-hydrogenatively in a technique known as Signal Amplification By Reversible Exchange (SABRE).

A (di)hydrogen molecule (H_2) consists of two covalently-bonded hydrogen atoms, each of which possess a nuclear spin angular quantum number of ½.[43] In an external magnetic field, these spin numbers will take the values of + ½ or - ½, typically referred to as α or β states respectively, where α is a spin parallel to the magnetic field and β is antiparallel (in-line with but opposite to the field). Therefore, a hydrogen molecule has four possible spin configurations, αα, αβ, βα and ββ. As αβ and βα are energetically identical (the individual spins are indistinguishable and so cannot be separated), a linear combination of addition and subtraction is used to instead give two new terms, (αβ + βα) and (αβ - βα). αα, ββ and αβ+βα are symmetric with respect to inversion (exchange of nuclei) and form the triplet spin isomers collectively known as *ortho*-hydrogen. The fourth configuration (αβ - βα) is anti-symmetric with respect to inversion and forms a singlet state known as *para*-hydrogen (Figure 9).[44,45]

Figure 9: the four spin isomers of hydrogen. The three isomers in green are known as *ortho*-hydrogen, whereas the isomer in blue is known as *para*-hydrogen

The Pauli exclusion principle requires the overall wave function (Ψ) of H_2 to be antisymmetric. The wave function is a combination of translational, electronic, vibrational, rotational and nuclear contributions (Equation 1).[46]

$$\Psi = \Psi_{translational} \cdot \Psi_{electron} \cdot \Psi_{nuclear} \cdot \Psi_{rotation} \cdot \Psi_{vibration}$$

Equation 1: components of a molecular wavefunction[46]

The translational, electronic and vibrational wavefunctions are *always* symmetrical, hence one of the nuclear and rotational components must be antisymmetric (and the other symmetric) for the overall wavefunction to be antisymmetric as required. Therefore, *ortho*-hydrogen symmetric nuclear spin states have an antisymmetric rotational state (J = 1, 3, 5…). In contrast, the *para*-hydrogen isomer that has an antisymmetric nuclear spin configuration (αβ – βα) occupies symmetric rotational states (J = 0, 2, 4…). At room temperature all four spin combinations are equally populated (*i.e.* 75% *ortho*-hydrogen and 25% *para*-hydrogen), as the energy differences between each form are very small. As it can occupy the lowest-energy rotational state (J = 0), the percentage of *para*-hydrogen increases as temperature decreases. At 20 K, the proportion of *para*-hydrogen is greater than 99.8 %.[9]

Temperature (K)	% *ortho*-hydrogen	% *para*-hydrogen
>273	75.00	25.00
273	74.87	25.13
150	71.46	28.54
75	48.14	51.86
20	0.18	99.82
0	0.00	100.00

Table 1: variation in hydrogen isomer populations with temperature, adapted from Duckett *et al.*, 1999[9]

The interconversion between the two isomers is formally spin-forbidden, therefore a paramagnetic catalyst is required to produce *para*-hydrogen[2,47-50] Charcoal, iron (III) oxide and iron (III) hydroxide have proven suitable catalysts for interconversion, over which ultra-pure hydrogen gas is passed at 20 K or less to produce pure *para*-hydrogen (Figure 10).

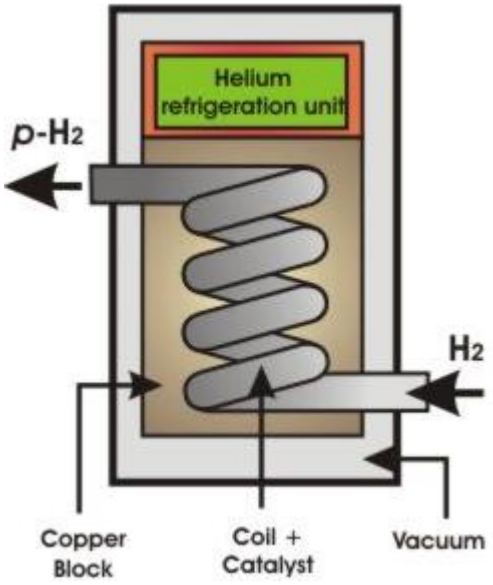

Figure 10: schematic representation of a para-hydrogen generator as used by the Duckett group. Taken from Duckett *et al.* website[51]

The upside to the difficulties associated with production of *para*-hydrogen is that the formally forbidden interconversion makes the pure *para*-hydrogen very stable even when warmed back to ambient temperatures. Therefore, it is relatively easy to store for extended periods without loss of purity.

1.3.1 *para*-Hydrogen Induced Polarisation (PHIP)

Para-hydrogen itself is completely NMR silent, as the antiparallel nuclear spins cancel each other out and the molecule has no net spin angular momentum. However, reaction of *para*-hydrogen with other molecules typically result in non-Boltzmann nuclear spin state populations when the (anti)symmetry of the *para*-hydrogen is broken. *Para*-Hydrogen Induced Polarisation (PHIP) is a technique where *para*-hydrogen is added across unsaturated bonds in a hydrogenation reaction, thereby breaking the hydrogen molecule's symmetry and creating a strong non-equilibrium spin population.[47,48] Only the the αβ and βα configurations are populated in *para*-hydrogen derived hydrogenation products, hence transitions between energy levels are not cancelled out and significantly stronger NMR signals result. (Figure 11) Because transitions from the αβ and βα states can be either in absorption or emission, a characteristic pair of antiphase doublets are observed in the associated NMR spectra.

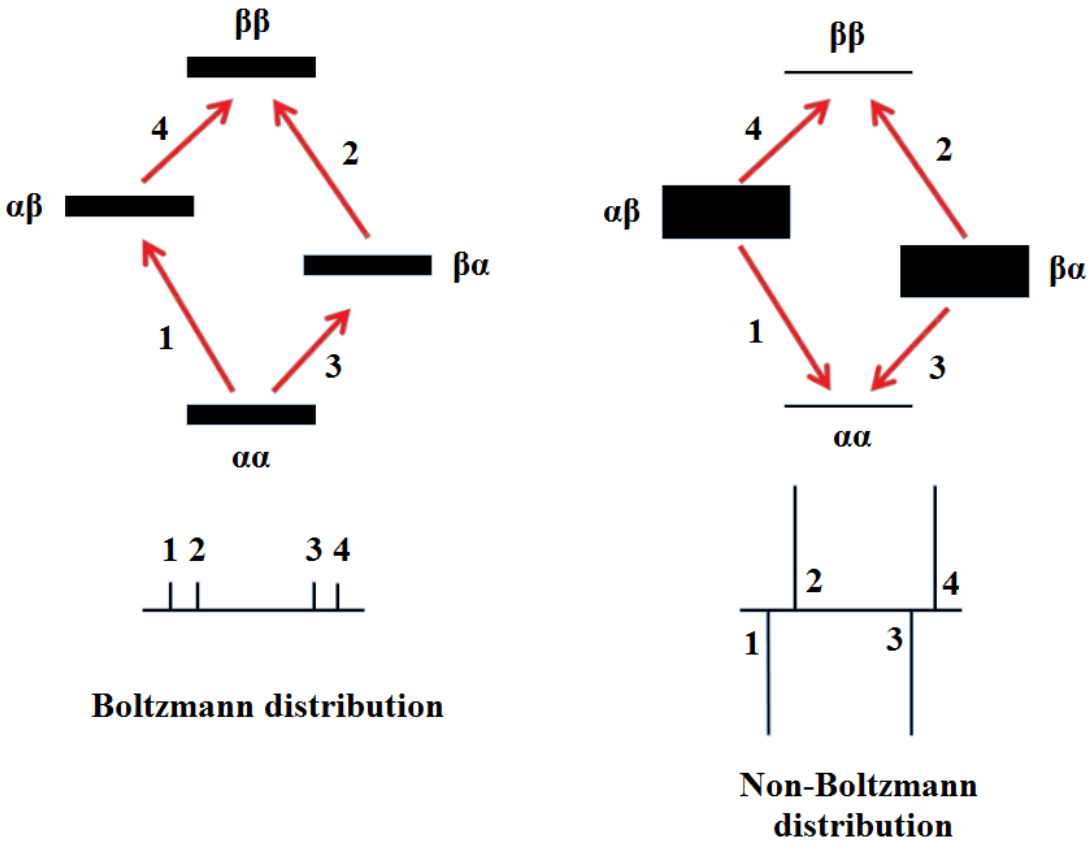

Figure 11: Schematic representation of nuclear spin states in natural abundance hydrogen (left) and para-hydrogen (right) derived hydrogenation products and the corresponding NMR spectra of the labelled transitions between states. The thickness of the lines in the top images reflect the population of that spin state. Adapted from Duckett *et al.*, 2012 [47]

The first instances of successful PHIP were reported by Bowers and Weitekamp in 1987, in which *para*-hydrogen and Wilkinson's catalyst (tris(triphenylphosphine)rhodium (I) chloride) were used to hydrogenate acrylonitrile (CH_2CHCN) to propionitrile (CH_3CH_2CN).[52,53] The ^1H NMR spectrum acquired of the product showed significantly enhanced signals for new propionitrile C-H resonances and in the hydride region of the hydrogenated catalyst (Figure 12).

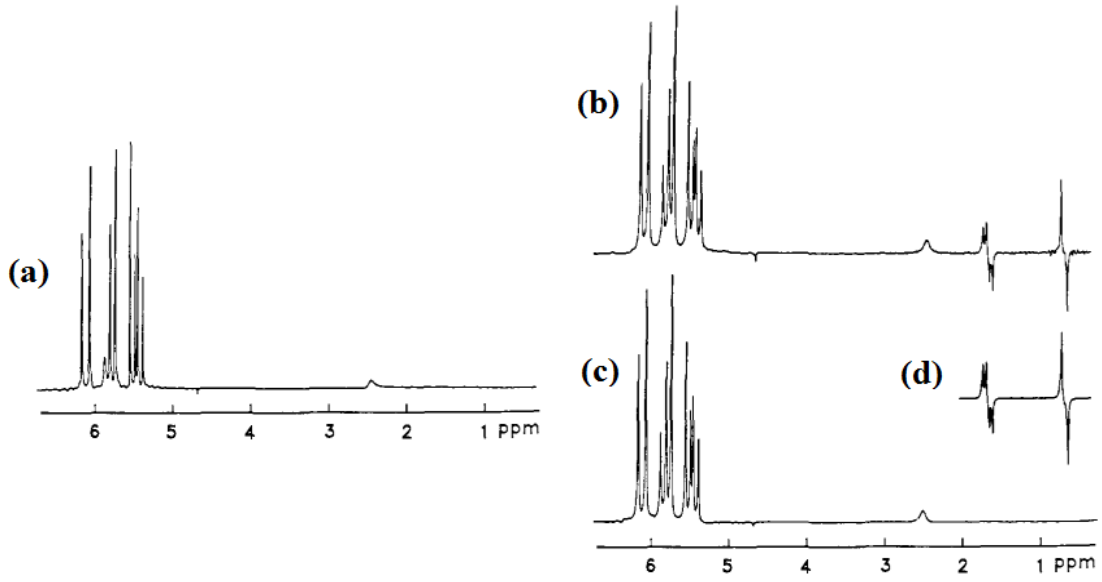

Figure 12: First demonstration that hydrogenation with para-hydrogen yields significantly stronger NMR signals. (a) is immediately prior to *para*-hydrogen addition (*i.e.* acrylonitrile starting material), (b) is immediately after parahydrogen addition, (c) is the spectrum of the sample left to equilibrate and (d) is the predicted line shape according to theory, which closely matches that in (b). Images taken from Bowers and Weitekamp, 1987[53]

These first PHIP experiments by Bowers and Weitekamp were performed in a relatively strong magnetic field inside the NMR magnet at ~200 MHz[53] and they coined the name Parahydrogen And Synthesis Allow Dramatically Enhanced Nuclear Alignment (PASADENA) for such *para*-hydrogen hydrogenation experiments in high field. However, Weitekamp went on to prove with Pravica *et al.* that incorporation of parahydrogen into the sample can still occur in the absence of a strong magnetic field (*e.g.* in Earth's relatively weak magnetic field).[54] This variation of PHIP was named Adiabatic Longitudinal Transport After Dissociation Engenders Net Alignment (ALTADENA) due to the adiabatic transfer of the sample from a weak to a strong magnetic field *after* the addition of *para*-hydrogen. When the hydrogenation occurs in a weak magnetic field, *para*-hydrogen remains in the singlet state, despite breaking the physical symmetry of the molecule. Subsequent transfer into a high field full breaks the nuclear spin symmetry but only the lower-energy βα spin state is populated and the resulting NMR signals therefore appear as a single line in absorption and a single line in emission of equal intensity (Figure 13).[55]

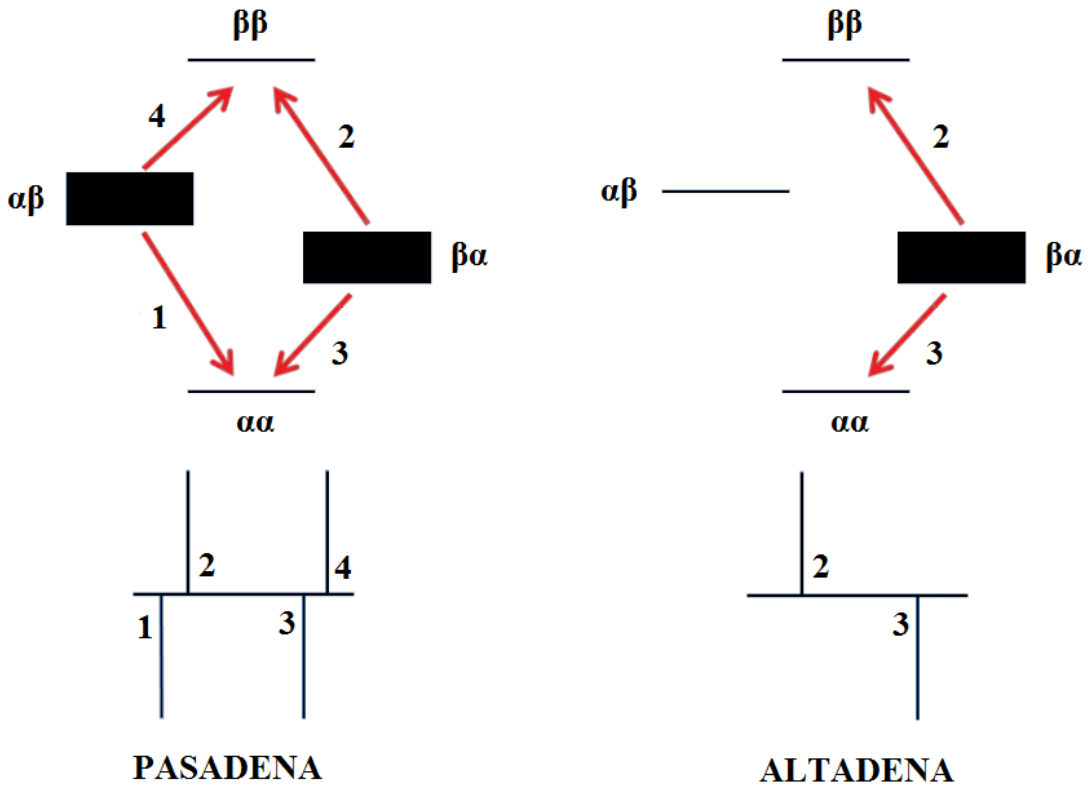

Figure 13: Schematic representation of reaction product nuclear spin states using para-hydrogen under PASADENA and ALTADENA conditions and the corresponding NMR spectra of the labelled transitions between states. The thickness of the lines in the top images reflect the population of that spin state. Adapted from Natterer *et al.*, 1997[55]

While there has been work using PHIP to investigate reaction intermediates[56-58], the most significant use of the technique so far has been hyperpolarised *in vivo* signals in MRI. These studies have typically focused on ^{13}C nuclei to take advantage of its significantly longer hyperpolarisation lifetimes (usually in the tens of seconds) when compared to most ^{1}H nuclei (a few seconds) and to take advantage of no observable background signal in the body. The first example of *in vivo* PHIP imaging was the (*para*)-hydrogenation of acetylenedicarboxylic acid dimethyl ester to maleic acid dimethyl ester, with a ^{13}C-labelled carbonyl group and a rhodium catalyst (Figure 14).[59]

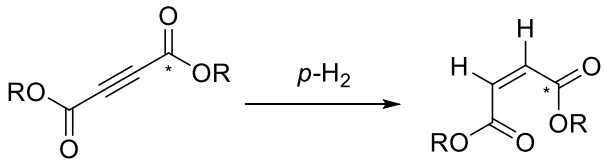

Figure 14: Reaction between acetylenedicarboxylic acid dimethyl ester with parahydrogen in the presence of a rhodium catalyst to give maleic acid dimethyl ester. The * represents a ^{13}C isotope. Adapted from Golman *et al.*, 2001[59]

Proton images were taken of an anaesthetised rat with a scan time of 5.4 minutes. Subsequently, 3 mL of hyperpolarised maleic acid dimethyl ester solution was injected into the tail vein and a ^{13}C single-shot sequence was used to generate an image one second after injection (Figure 15).

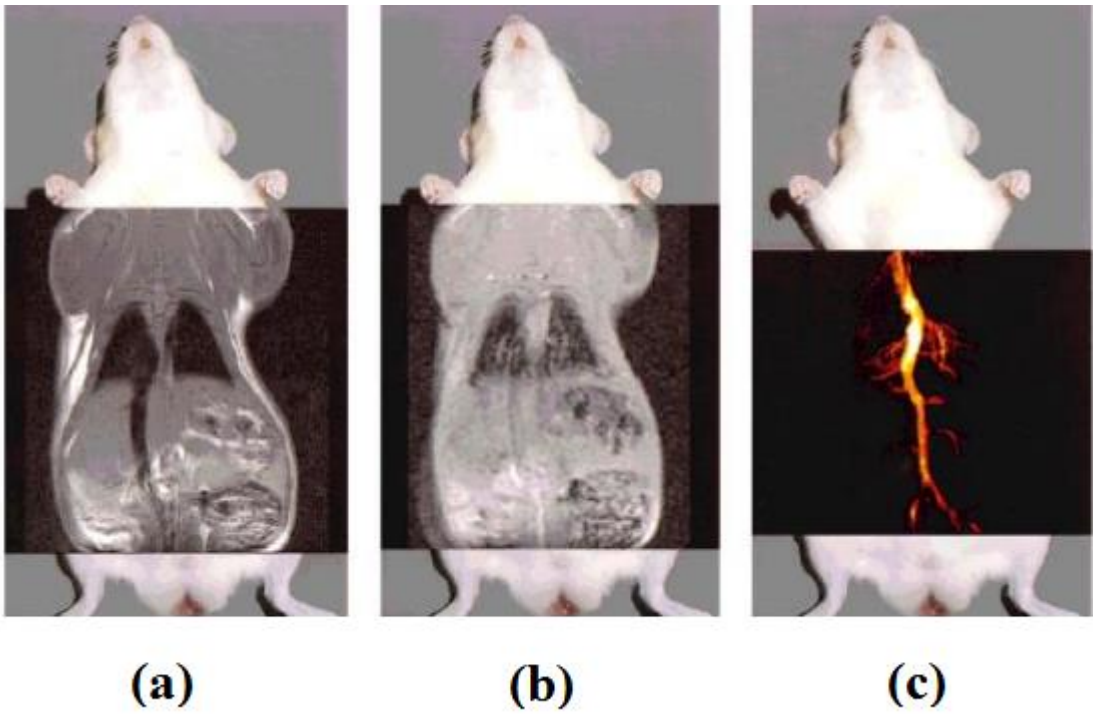

Figure 15: MRI images of a rat (generated at 2.4 T). (a) Conventional ^{1}H image with a scan time of 5.40 min, (b) ^{1}H image with a scan time of one second, (c) ^{13}C single shot image generated in one second. All images are superimposed onto a photograph of a rat to demonstrate the field of view. Images taken from Golman *et al.*, 2001[59]

Figure 15 demonstrates that hyperpolarised ^{13}C can yield detailed structural blood vessel information after only one second, whereas conventional proton imaging is unable to show anywhere near this level of detail after a much longer scan. The level of polarisation

was estimated at only 0.3%, which although small is clearly sufficient in the absence of a ^{13}C background signal *in vivo*.

The chief problem with PHIP is the requirement for relatively prefunctionalised substrates with unsaturated moieties incorporated and frequently ^{13}C labels also. This severely limits the scope of viable compounds and presents synthetic challenges to create suitable unsaturated precursors, particularly biologically-compatible examples.

1.3.2 Signal Amplification By Reversible Exchange (SABRE)

A more recent and promising form of PHIP is known as Signal Amplification By Reversible Exchange (SABRE), with the first results published in 2009.[1,2,60] It allows interaction of the *para*-hydrogen molecule and the target substrate without permanently binding the two together, instead temporarily binding through a transition metal catalyst intermediary. The temporary binding still allows great increases in NMR signal intensity but allows for a much wider scope of substrates to be investigated.[47,49,61-63]

When *para*-hydrogen binds to the aforementioned transition metal complex, it is broken in two to form a two hydride ligands. Concurrently, the substrate also binds to the metal complex. During the time that both the *para*-hydrogen-derived hydrides and the substrate are bound, long-range scalar coupling across the transition metal centre facilitates polarisation transfer from the hydride ligands to the substrate ligands. The binding of hydrogen and substrate is reversible, leading to dissociation of the hydrides to form ordinary molecular hydrogen and dissociation of the now-hyperpolarised substrate into solution. 'Fresh' *para*-hydrogen and substrate molecules can then bind to the now-vacant catalyst binding sites and the process repeats to gradually build-up a population of hyperpolarised substrate free in solution. A simplified schematic representation of the SABRE method is shown in Figure 16.

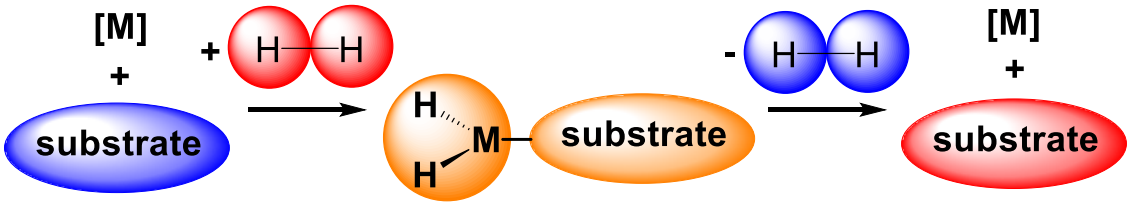

Figure 16: Schematic representation of the magnetisation transfer process in SABRE. [M] represents the transition metal complex with other ligands, blue represents non-hyperpolarised species, red represents hyperpolarised species and orange represents species exchanging polarisation. Image adapted from Adams *et al.*, 2009[1]

The transition metal template employed is iridium with an electron donating group attached, typically either a phosphine or carbene-based ligand. It is converted from a stable precatalyst to an 18-electron octahedral active form *in situ* upon the addition of hydrogen. There are two hydride ligands, three substrate ligands and the phosphine/carbene ligand. Figure 17 demonstrates production of this active catalyst complex with pyridine as the substrate and IrCl(COD)(IMes), an effective SABRE precatalyst reported by the Duckett group and others and the basis of all catalysts used in this project.[62-64] First, the substrate coordinates to the transition metal precatalyst (**I→II**). Hydrogen is added to give the active catalyst **III**. For reference, the addition of *para*-hydrogen to **III** to give intermediate **IV** is a more explicit description of the process previously described.

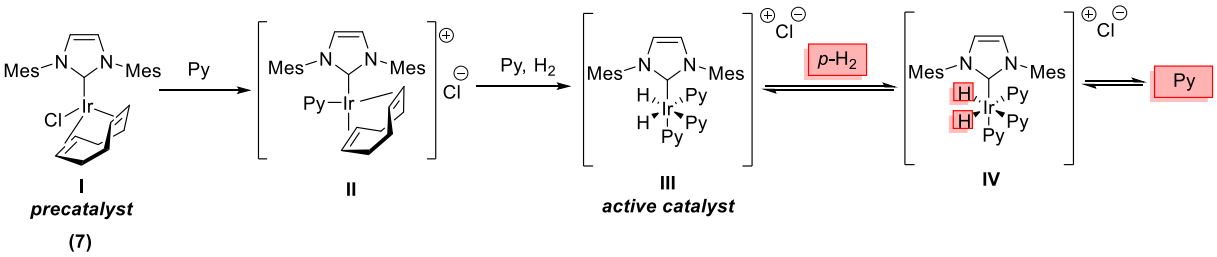

Figure 17: SABRE precatalyst acitvation and subsequent hyperpolarisation of substrate. 'Py' refers to pyridine, a common SABRE substrate. Those species highlighted in red are hyperpolarised

Pyridine has commonly been employed as the substrate molecule, exhibiting ideal 'soft' binding to the iridium centre. Cowley *et al.* observed a 6000-fold signal enhancement of pyridine using the IrCl(COD)(IMes) precatalyst after optimisation of conditions (Figure 18).[64]

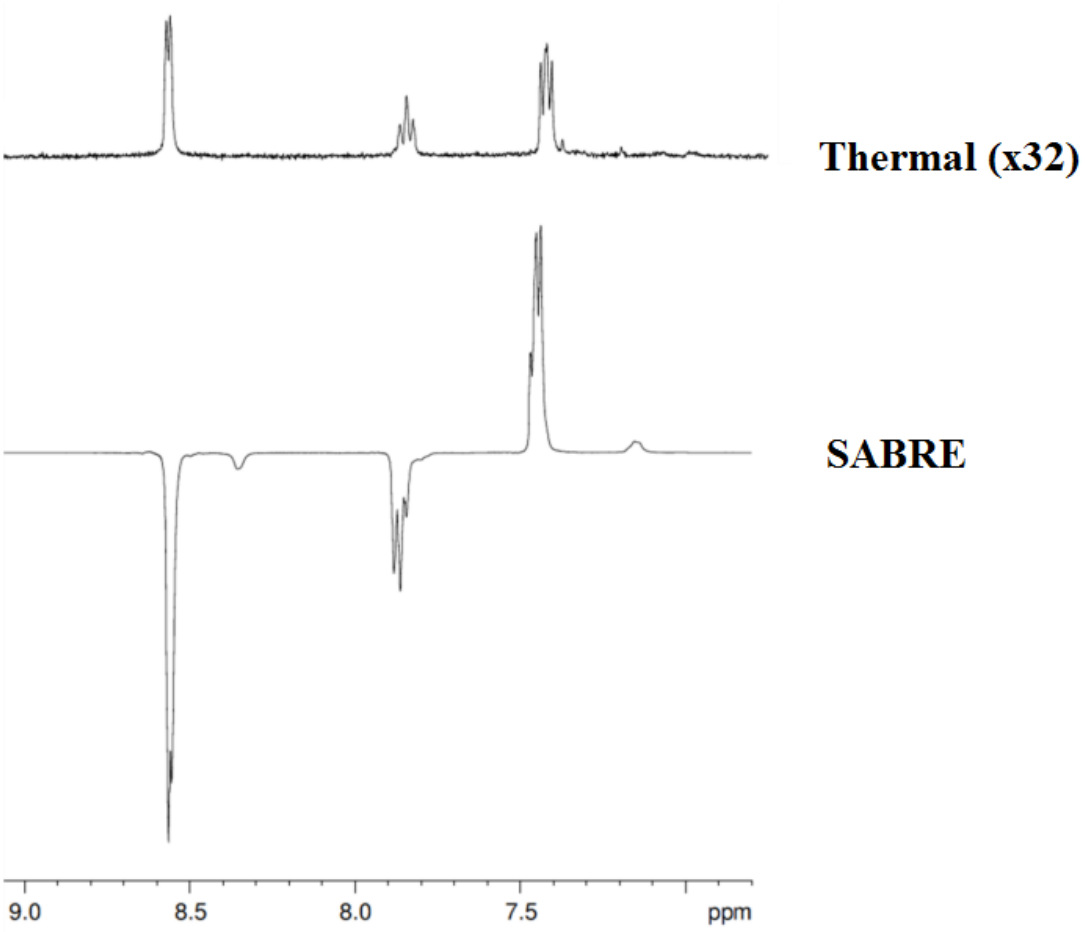

Figure 18: ^{1}H NMR spectra of pyridine, 7 – 9 ppm region shown only. The top trace is conventional ^{1}H NMR (*i.e.* thermally polarised) but magnified 32 times. The lower trace is for SABRE-enhanced pyridine. Adapted from Cowley *et al.*, 2011[64]

The pyridine signals in the enhance NMR spectrum were observed as in-phase multiplets (unlike that seen with PHIP), although a 180 ° phase difference was exhibited between some resonances. The phase difference was found by Cowley *et al.* to be dependent on the magnetic field where the hyperpolarisation takes place.

SABRE has proven successful with a wide variety of substrates including pyridine, nicotinamide, methyl nicotinate, pyradizine, quinolone, quinoxaline, dibenzothiophene and nicotine.[1,65,66]

The great advantage of SABRE over classical PHIP is that a hydrogenation of an unsaturated bond is not required. Therefore, the substrates need not be as heavily prefunctionalised and so substrate scope is much wider. The scope of SABRE is chiefly limited to substrates which possess ideal binding to the SABRE catalysts, typically soft nucleophiles such as those with a pyridine moiety. Another significant advantage is that

the reversible mechanism means *para*-hydrogen is the only reactant consumed. Consequently, substrate molecules can be repeatedly polarised within an experiment with a sufficient *para*-hydrogen reservoir *in situ* and the entire method is repeatable on a single sample solution if the *para*-hydrogen can be replenished.

In recent years, much effort has been expended on prolonging the SABRE response before it decays back to thermal equilibrium. A long hyperpolarised lifetime would be critical for imaging applications, as it takes time for an agent to be injected into a patient and reach the diagnostic site of interest and there is little purpose in doing so if the signal has significantly decayed in the process.

A well-documented route to improve the lifetime and efficacy of hyperpolarisation methods is the partial and selective deuteration of the substrate, first reported by Allouche-Arnon *et al.* and applied to DNP.[67] Deuteration reduces the effect of scalar coupling as a relaxation pathway for the ^{1}H hyperpolarised signal – deuterium and proton nuclei have different nuclear spins and so cannot couple to each other.[68] When applied by Rayner *et al.* to SABRE, significant gains in both magnetic lifetime (measured by T_1 relaxation time) and signal enhancement were obtained. For example, methyl 4,6-nicotinate-d_3 exhibited up to four-fold increases in hyperpolarised signal and up to five-fold increases in magnetic lifetimes when compared to the non-deuterated methyl nicotinate (Figure 19).[63-65] Similar improvements were achieved with labelling of nicotinamide, isoniazid and others.[69,70] This route will be investigated and discussed further in Chapter 3.

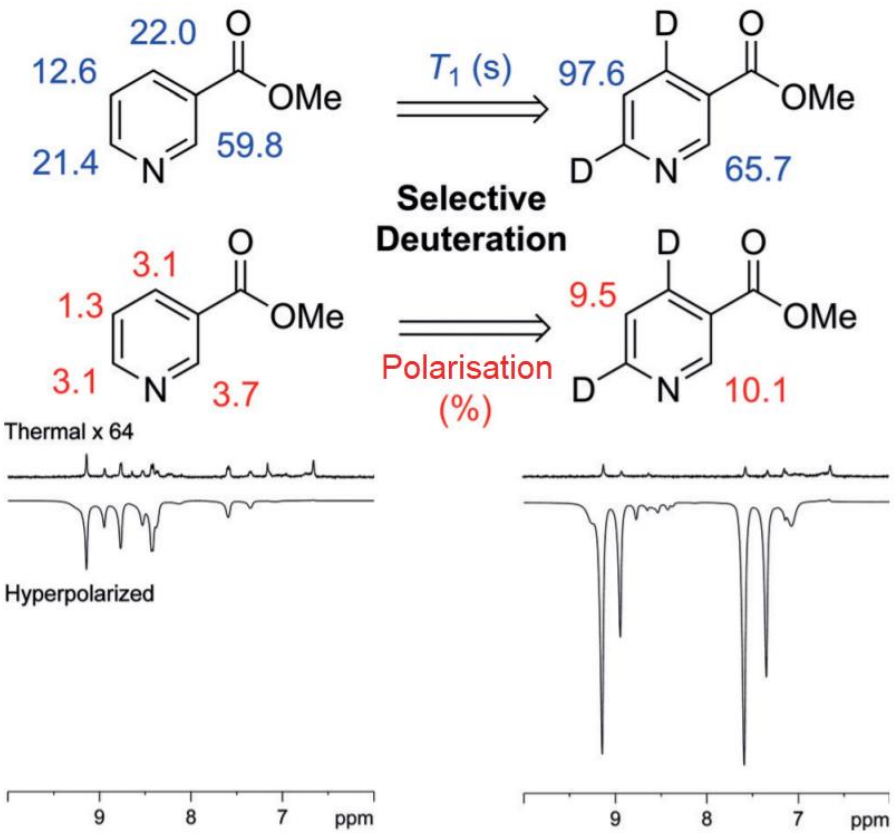

Figure 19: Methyl nicotinate and isotopologues methyl 4,6-nicotinate-d2 comparisons of T_1 relaxation times and polarisation by SABRE. ^{1}H NMR thermal (top) is expanded 64 times compared to the hyperpolarised spectrum (bottom). Image adapted from Rayner *et al.*, 2018[66]

A more recent development to improve SABRE magnetic lifetimes is the creation of a *pseudo*-singlet state in the substrate. As described previously, the hydrogen nuclei in *para*-hydrogen itself exist in a singlet state, *i.e.* non-magnetic spin isomers of a coupled spin pair. This prevents external dipolar coupling from affecting the molecule. It is possible to temporarily create an approximation of a singlet state from two similar, mutually-coupled but magnetically inequivalent protons in substrate molecules, first reported by Levitt *et al.*[71,72] A symmetrical singlet state can be imposed by application of a sequence of composite pulses specific to the coupling and chemical shift difference between the protons. It is maintained by a 'spin lock' and the signal can be observed by application of a final 90˚ RF pulse at specific time (Figure 20).[73,74]

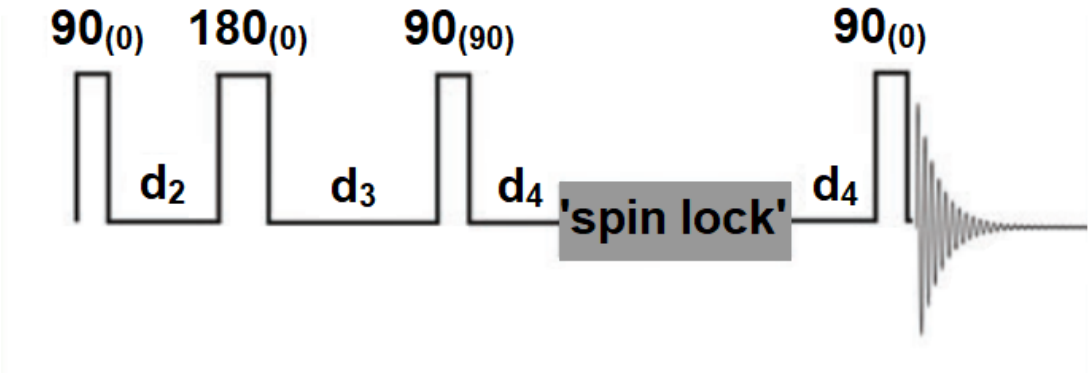

$$d_2 = \frac{1}{4J} \quad d_3 = \frac{1}{4J} + \frac{1}{2\Delta\nu} \quad d_4 = \frac{1}{4\Delta\nu}$$

Figure 20: pulse sequence used to create, maintain and observe singlet states. *J* is the scalar coupling constant and *Δν* is chemical shift difference between the two protons, both in Hz. Note notation for RF composite pulses – $90_{(90)}$ and $90_{(0)}$ denote RF pulses of 90° *duration* but 90° and 0° *phase*, respectively. Adapted from Roy *et al.*, 2016[73]

SABRE can be applied in conjunction with such a state, where a substrate is hyperpolarised immediately before imposing the singlet state. Successful storage of hyperpolarisation was observed in the strongly-coupled pair of protons in 2-aminothiazole[75] and in nicotinamide and pyrazinamide derivatives selectively-deuterated to isolate coupled proton pairs.[73] Hyperpolarised *pseudo*-singlet states of several minutes have been reported for pyradizine derivatives, with observable signal still detected fifteen minutes after storage in one example (Figure 21).[76]

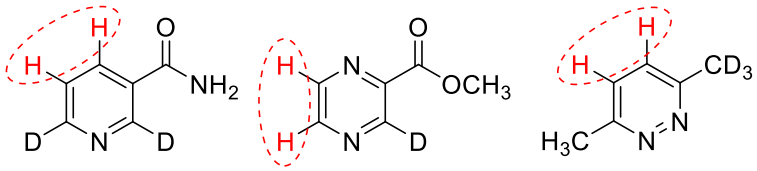

Figure 21: examples of molecules successfully hyperpolarised with SABRE and subsequently converted to a pseudo-singlet state. Pairs of similar, mutually-coupled but inequivalent protons are highlighted in red – selective deuteration is used to isolate the pairs except in the case of the pyradizine derivative (right) where it is used to break the symmetry of the molecule

1.4 Project outline

The primary aim of this thesis was to develop a family of (−)-nicotine derivatives as potent SABRE substrates with a view unlocking their future biological applications in

areas such as MRI. Focus has been on synthesis of small isotopically-labelled, biologically-appropriate organic molecules with long magnetic lifetimes (T_1 relaxation times) which were then hyperpolarised with *para*-hydrogen in SABRE. To this effect, several deuterium-labelled derivatives of (−)-nicotine **1** have been prepared and tested. As SABRE enhancements are affected by numerous variables, such as the field for *para*-hydrogen binding and the kinetics of molecule exchange, a key focus of this report is on the optimisation of these complex variables to give superior performance. A second key effort was made to better characterise the SABRE process through assessment and quantification of the critical exchange of substrate molecules.

(−)-Nicotine **1** and isotopologue derivatives were selected for these studies, as it is known that the iridium hyperpolarisation catalysts used in SABRE bind readily to pyridyl moieties.[6] **1** also has a significant degree of biological compatibility in humans, albeit in very small quantities as a potent psychostimulant. It is also known to cross the blood-brain barrier with ease,[77] making it of particular interest in imaging applications of the brain. (−)-Nicotine **1** has been very widely cited for the last century as highly toxic with a human oral LD_{50} of 0.5-1.0 mg/kg (corresponding to 40-60 mg ingested for an adult), although recent scrutiny of past experiments and notable case study exceptions (summarised in a review by Mayer[78]) suggest the lethal dose is around 500 mg or higher. Therefore, small amounts of **1** and its isotopologue derivatives should be theoretically safe to use.

2: Synthesis of isotopically-labelled nicotines

2.1 Synthetic strategy and design

The focus of this project is the synthesis and evaluation of (−)-nicotine **1**, its derivatives and its isotopologues. In order to achieve the goal of improved NMR/MRI detectability of (−)-nicotine **1** and its derivatives, synthetic strategy is first required to prepare a range of ^{2}H-labelled isotopologues of (−)-nicotine **1**.

The general synthetic plan will be to regioselectively introduce chlorine substituents into the pyridine ring of (−)-nicotine **1**, followed by hydrogenolysis with deuterium gas and a metal catalyst to give the deuterium-labelled compounds (Scheme 1). Work by Comins *et al.* on regioselective pyridine and nicotine lithiations formed the basis for the planned routes.[79-82] The targeted isotopically-labelled nicotine analogues were selected based on their expedient synthesis *via* these established literature procedures, but also to provide a variety of structures to probe the somewhat poorly-understood mechanism of hyperpolarisation transfer about the pyridine ring. The methods employed here use different organolithium bases to introduce the chlorine substituents at different positions on the ring, which variously use sterics, coordination to nitrogen(s) and/or directed *ortho* metalation (DoM) effects to achieve the observed regioselectivity.[83-85]

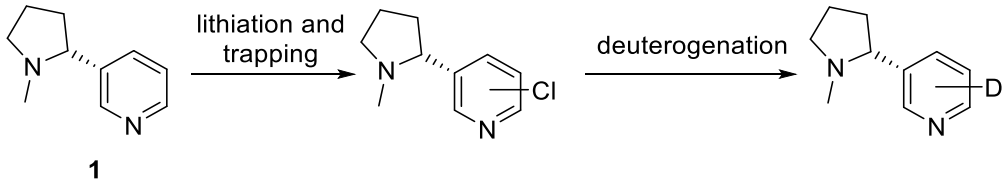

1

Scheme 1: general synthetic route to deuteronicotines

The starting point of this work was the preparation of the different regioisomers of mono- and dichloronicotines using a range of procedures which are available from the literature. An overview of the synthetic approaches is shown in Scheme 2. A literature route for the regioselective chlorination of (−)-nicotine **1** to give 6-chloronicotine **2** is known, with 2-chloronicotine **3** as a minor product.[79] Hydrogenolysis of **2** would give 6-nicotine-d_1 **4**. Additionally, treatment of 6-chloronicotine **2** with a variety of organolithium bases has been reported to give regioisomers 5,6-dichloronicotine **5**, 4,6-dichloronicotine **6** and 2,6-

dichloronicotine **7**.[80] Subsequent deuterogenolyses of these dichloronicotines would give 5,6-nicotine-d_2 **8**, 4,6-nicotine-d_2 **9** and 2,6-nicotine-d_2 **10**, respectively.

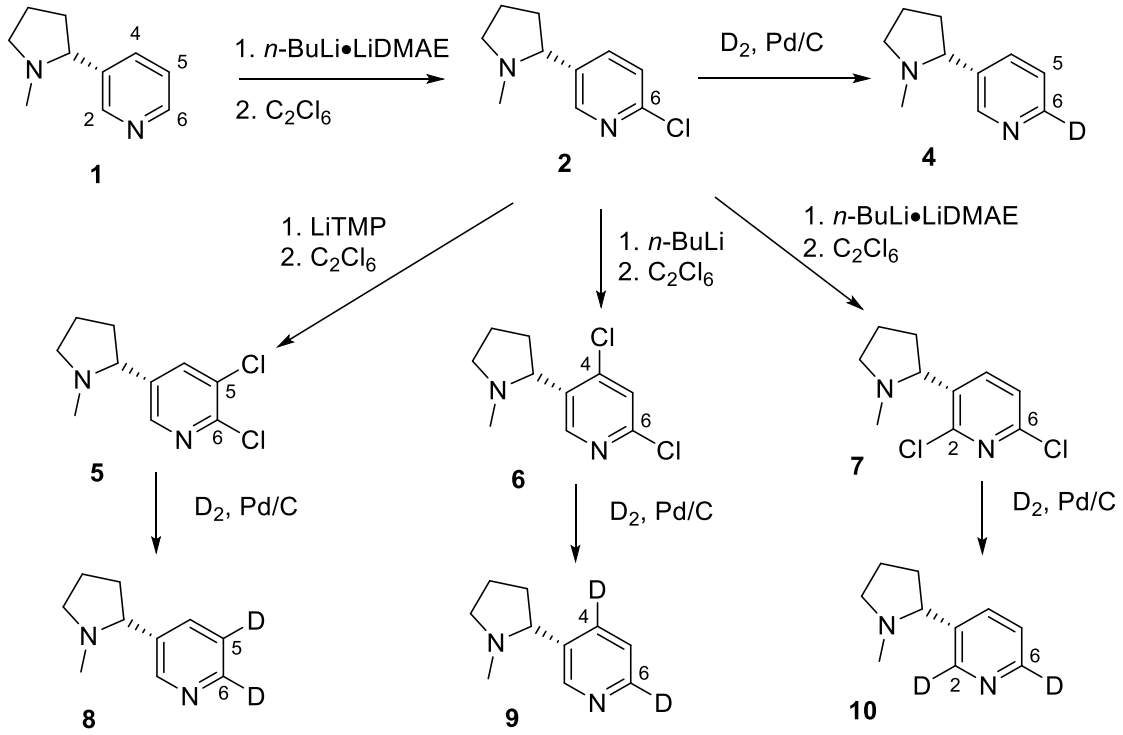

Scheme 2: full synthetic route to nicotine isotopologues

2.2 Synthesis of halonicotines

To start with, a chlorine substituent was introduced in the 6-pyridyl position of (−)-nicotine **1**, as it would be a precursor to 6-deuteronicotine **4** and it was planned that it would act as an *ortho*-directing group for further lithiations at the 5-pyridyl position. Regioselective lithiation was achieved using *n*-BuLi·LiDMAE, a 'superbase' complex of *n*-butyllithium and lithiated 2-dimethylaminoethanol (DMAE), *via* a protocol previously reported by Comins.[79] Using Comins' procedure on a 1 mmol initial scale, 3.0 eq. of DMAE in *n*-hexane was treated with 5.4 eq. of *n*-BuLi at 0 °C for 30 min to produce 3.0 eq. of LiDMAE *in situ* with 2.4 eq. *n*-BuLi left over. The *n*-BuLi/LiDMAE mixture was then used to lithiate (−)-nicotine **1** at −20 °C for 1 h. Subsequent trapping with a solution of 4 eq. of hexachloroethane in *n*-hexane at −78 ºC for 1 h gave 6-chloronicotine **2** in moderate yield (51%), along with a small quantity of 2-chloronicotine **3** (6%) and a 40:60 mixture of **2** and **3** (5%) (Scheme 3). The regioisomers were primarily identified by their pyridyl proton splitting patterns in their ^{1}H NMR spectrum, with **2** exhibiting its most downfield peak (i.e. adjacent to the pyridyl nitrogen) as a doublet (J = 2.0 Hz) and **3**

instead exhibiting a peak of near-identical chemical shift but doublet of doublets splitting (J = 4.5, 2 Hz) (Figure 22).

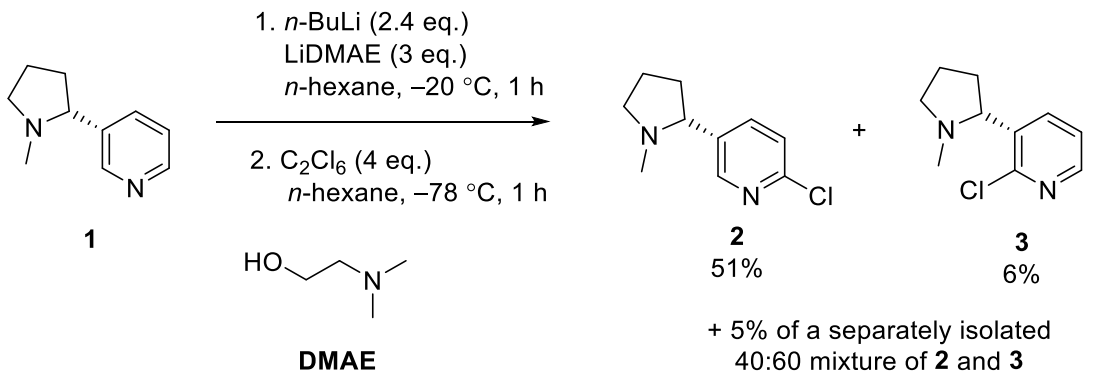

Scheme 3: reagents and conditions to produce 6-chloronicotine *2* and 2-chloronicotine *3*

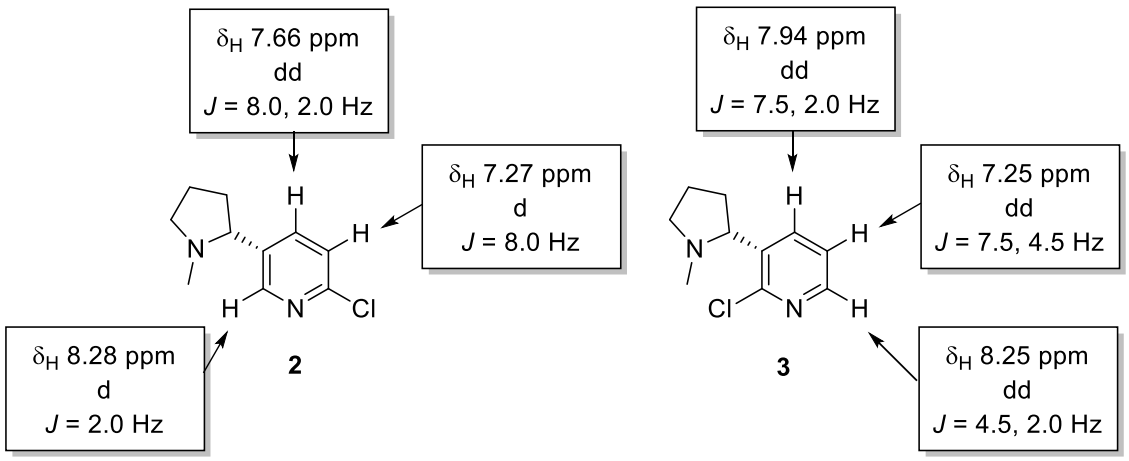

Figure 22: Chemical shifts and splitting patterns in the ^{1}H NMR spectra for 6-chloronicotine *2* and 2-chloronicotine *3*

To explain the regioselectivity, the *n*-BuLi·LiDMAE complex is believed to coordinate to the pyridyl nitrogen, abstracting an adjacent proton. Steric clashing between the complex and the pyrrolidine ring hinders formation of the 2-lithiated intermediate **11** (Figure 23). Instead, preferential lithiation takes place α to nitrogen but away from the pyrrolidine ring, giving the 6-lithiated intermediate **12** as the major regioisomer.[79] *n*-Hexane was used as the solvent, as a non-coordinating and apolar solvent was reported by Gros[86-88] to be essential to the integrity of the superbase-nicotine aggregate. Common coordinating solvents such as THF or diethyl ether would break up this aggregate and likely lead to reduced regioselectivity.

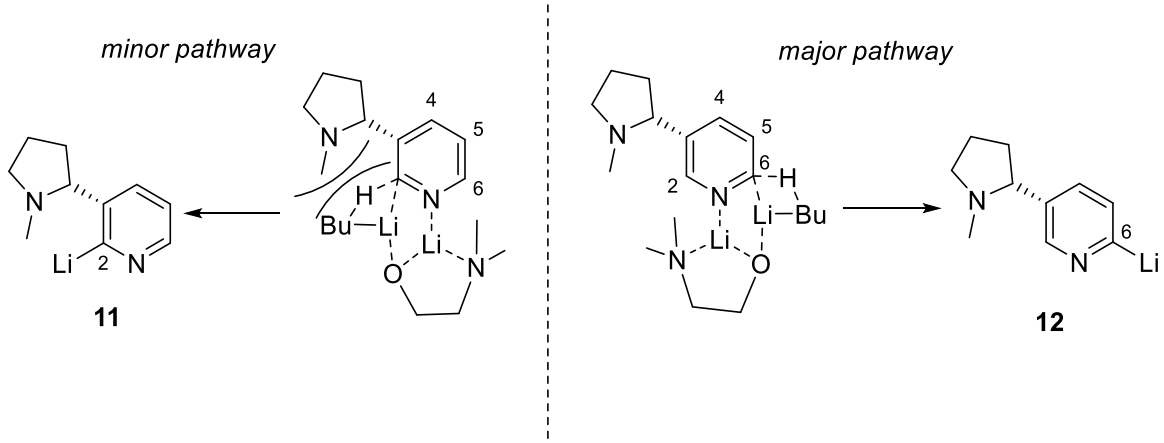

Figure 23: major and minor pathways for lithiation adjacent to nitrogen in (−)-nicotine *1*

Separation of regioisomers 6-chloronicotine **2** and 2-chloronicotine **3** proved problematic, as despite reasonable separation indicated by TLC (R_F 0.26 for **3** *vs* 0.14 for **2** in EtOAc), their elution in flash column chromatography led to a large proportion of overlapped fractions. Numerous variations in conditions to separate the two regioisomers, including the use of reverse phase column chromatography, preparatory HPLC and alumina in place of silica gel, reduced the overlapped fractions to an extent, but ultimately mixed fractions of **2** and **3** were always obtained. The mixture varied in its ratio from column to column, but was always between 70:30 and 40:60 of **2** and **3**. The mixed material did, however, find use later on (see Scheme 13) and so was not wasted.

Scale up of the synthesis to 3 mmol of (−)-nicotine **1** also proved challenging. Use of otherwise identical lithiation and trapping conditions in *n*-hexane to those described above gave a significantly poorer yield of the desired 6-chloronicotine **2** (20%) and large quantities of recovered starting material (−)-nicotine **1** (44%) (Scheme 4). There was evidence of trace quantities of 2-chloronicotine **3** in the ^{1}H NMR spectrum of the crude product, but it was not isolated after column chromatography.

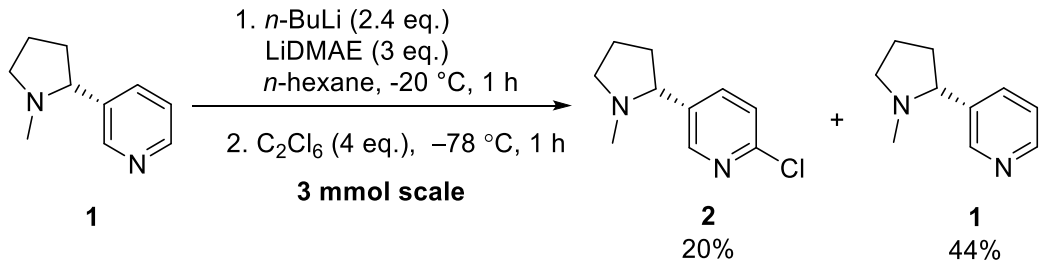

Scheme 4: failed reagents and conditions to produce pure 6-chloronicotine *2*

It became apparent that with the larger quantities of reagents involved, the hexachloroethane electrophile was poorly soluble in *n*-hexane, even at room temperature. Therefore, the hexachlorethane was likely completely insoluble in the sub-zero reaction mixture, crashing out of solution upon addition. With minimal electrophile in solution, most of the unreacted lithiated intermediate would be converted back to (−)-nicotine **1** upon quenching. Merely increasing the volume of *n*-hexane to alleviate the poor electrophile solubility would have required an impractically large quantity. Therefore, the effect of dissolving the electrophile in a co-solvent with similar properties to *n*-hexane was investigated. Treatment of 6 mmol of (−)-nicotine **1** with 5.4 eq. of *n*-BuLi and 3.0 eq. DMAE in *n*-hexane with subsequent trapping with a solution of 4 eq. of hexachloroethane in toluene gave full conversion and a much improved yield of 6-chloronicotine **2** (51%). In addition, 2-chloronicotine **3** (5%) and a 70:30 mixture of **2** and **3** (26%) were also isolated. The overall yield of trapped products was 81% (Scheme 5).

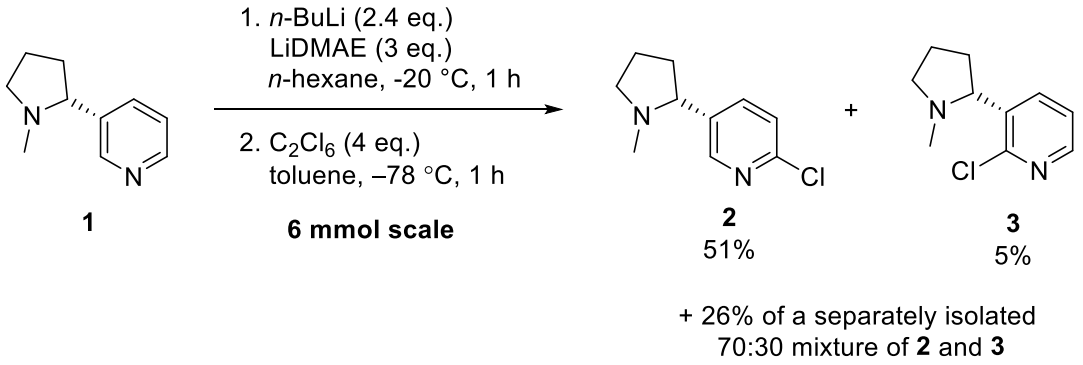

Scheme 5: superior reagents and conditions to produce 6-chloronicotine *2* and 2-chloronicotine *3*

Multiple repetitions up to 20 mmol scale gave similar results, with 6-chloronicotine **2** always the major product by far. Overall yields of both regioisomers were consistently in the 70-75% range. In one instance, 46 mmol of (−)-nicotine **1** was treated under these conditions (the largest quantity that can be treated with 5.4 eq. of *n*-BuLi and a full 100 mL bottle of 2.5 M *n*-BuLi solution in hexane) to produce 6-chloronicotine **2** (43%), a small quantity of 2-chloronicotine **3** (1%) and a 35:65 mixture of **2** and **3** (21%) (Scheme 6). However, this result necessitated two extremely large flash column separations taking considerable time and using in excess of ten litres of solvent. It was therefore deemed impractical to regularly synthesise these compounds on such a large scale.

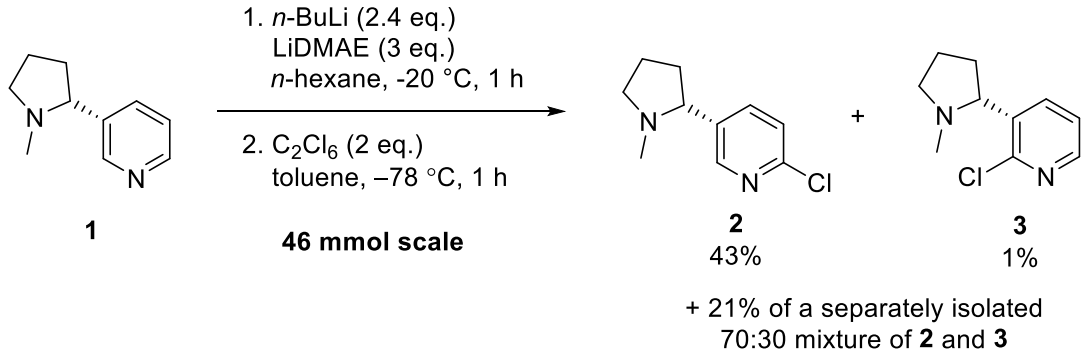

Scheme 6: large-scale preparation of 6-chloronicotine *2* and 2-chloronicotine *3*

The relative quantities of reagents (*n*-BuLi, DMAE, C_2Cl_6) to produce 6-chloronicotine **2** and 2-chloronicotine **3** were derived directly from the work by Comins[79,81] and remained unchanged thus far because the synthesis demonstrably worked. However, such a large excess of *n*-BuLi·LiDMAE and electrophile represented a practical concern as they are relatively expensive and wasteful, particularly with large-scale preparations. To overcome this, the effect of reducing these excesses was investigated. Initially, the quantity of hexachlorethane electrophile was reduced from four to two equivalents with no significant changes in yields of products observed (<5% reduction of all regioisomers) (Scheme 7).

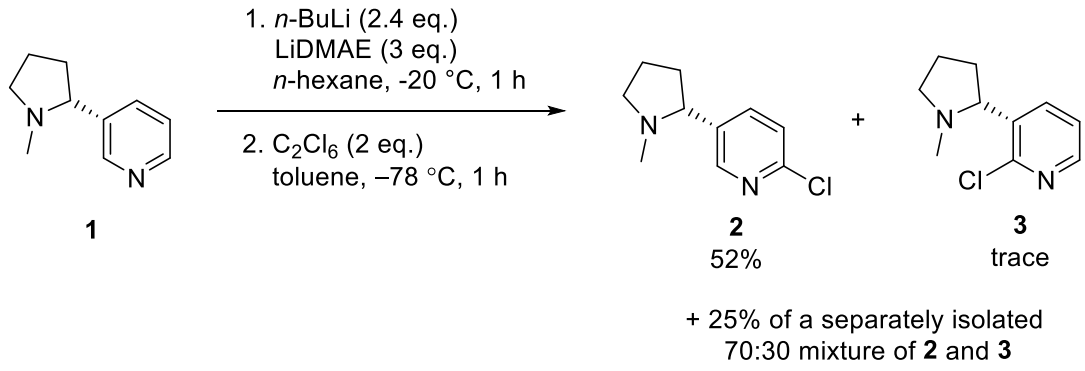

Scheme 7: reagents and conditions to produce 6-chloronicotine *2* and 2-chloronicotine *3* with reduced electrophile quantity

The initial success was then expanded to also reduce the quantity of *n*-BuLi·LiDMAE from three 'equivalents' (*i.e.* 5.4 eq. *n*-BuLi and 3 eq. DMAE) to two (*i.e.* 3.6 eq. *n*-BuLi and 2 eq. DMAE), again yielding similar results to previous conditions (Scheme 8).

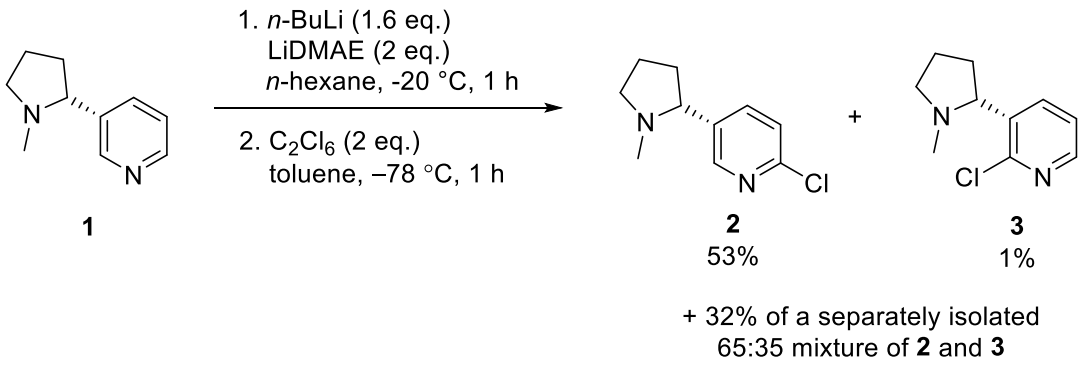

Scheme 8: reagents and conditions to produce 6-chloronicotine *2* and 2-chloronicotine *3* with reduced reagent excesses

With 6-chloronicotine ***2*** in hand, 5,6-dichloronicotine **5** was synthesised by a directed *ortho* lithiation.[80,85,89] Following a different Comins procedure, 6-chloronicotine **2** was treated with 1.1 eq. of LiTMP (formed *in situ* from *n*-BuLi (1.1 eq.) and tetramethylpiperidine (TMP, 1.1 eq.)) in THF. Subsequent trapping with a solution of hexachloroethane in THF gave 5,6-dichloronicotine **5** in 60% yield with no other detectable regiosiomers (Scheme 9). The observation of only two mutually-coupled aromatic signals (J = 2.5 Hz) in the ^{1}H NMR spectrum, corresponding to a slightly deshielded 4-pyridyl proton and a slightly shielded 2-pyridyl proton (Figure 24), was consistent with insertion of a chlorine at the 5-pyridyl position. The reaction was successfully scaled up to convert 5.44 mmol of **2** into **5** with only a slight reduction of yield to 53%.

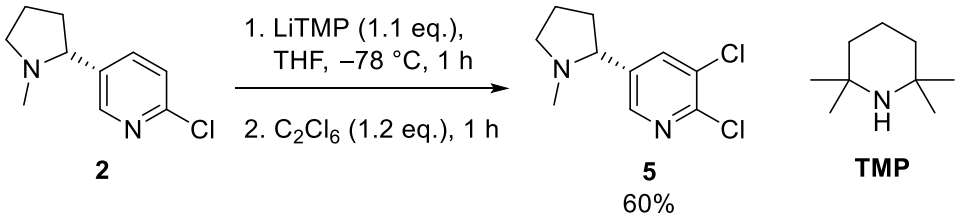

Scheme 9: reagents and conditions to produce 5,6-dichloronicotine *5*

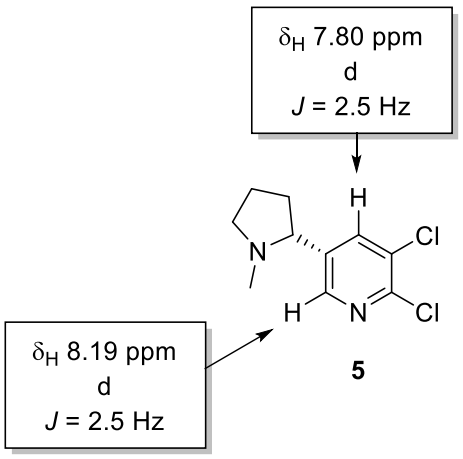

Figure 24: Chemical shifts and splitting patterns in the ^{1}H NMR spectrum for 5,6-dichloronicotine *5*

As chlorine substituents are only moderate *ortho*-directing groups,[83-85] it is believed that the steric bulk of the LiTMP base also contributes to the high regioselectivity observed. Steric clashing of the approaching base and the pyrrolidinyl *N*-methyl group prevents coordination to the pyrrolidine nitrogen and makes deprotonation at either the 2- or 4-position unfavourable. Instead, coordination to the 6-chloro substituent occurs to effect lithiation at the 5-position, exclusively giving the 5-lithio-6-chloronicotine intermediate **13** (Figure 25).

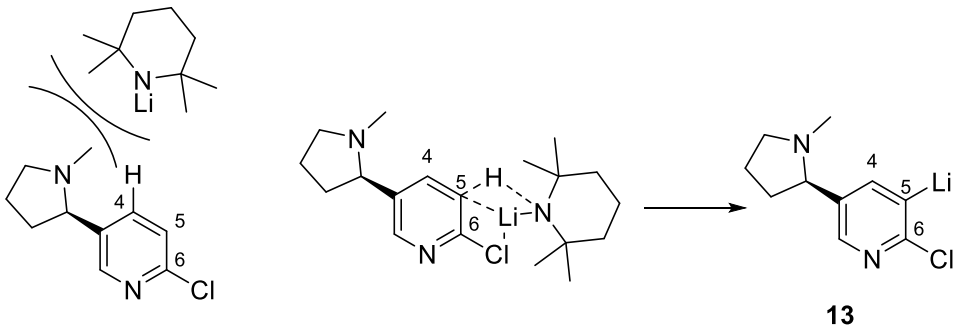

Figure 25: steric clashing between the bulky base and pyrrolidinyl ring combines with coordination to chlorine to effect DoM

Synthesis of regioisomeric 4,6-dichloronicotine **6** was then attempted using a different base, reported by Comins.[80,81] 4,6-dichloronicotine **6** was successfully produced by treating 6-chloronicotine **2** with 1.1 eq. *n*-BuLi in THF at −78 ºC. The lithiated intermediate was subsequently trapped with a solution of hexachloroethane in THF at −78 ºC, giving 4,6-dichloronicotine **6** in 76% yield (Scheme 10). Two singlet aromatic proton

peaks with chemical shift closely corresponding to the 2-pyridyl and 5-pyridyl protons in **2** indicated that the 4-pyridyl proton had been replaced by a chlorine substituent without any other changes to the pyridine ring (Figure 26). This result was noticeably superior to the 63% yield obtained and published by Comins *et al.* on a similar scale. The reaction was also successfully scaled up to convert 10.4 mmol of **2** into **6** in 75% yield.

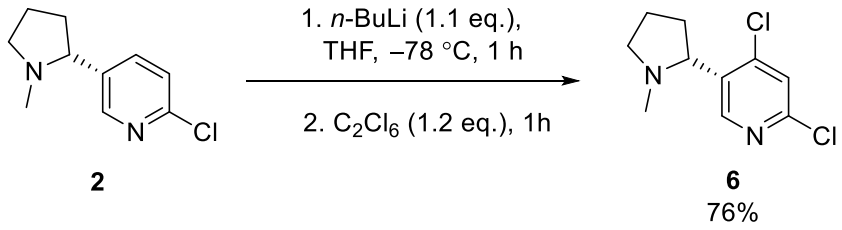

Scheme 10: reagents and conditions to produce 4,6-dichloronicotine *6*

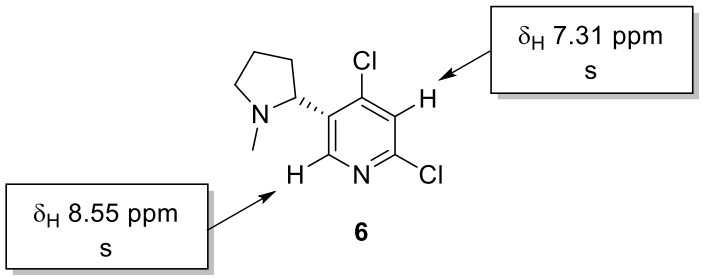

Figure 26: Chemical shifts and splitting patterns in the ^{1}H NMR spectrum for 4,6-dichloronicotine *6*

Due to issues encountered in the initial stages of the synthesis of 4,6-nicotine-d_2 **9** (as described in Chapter 2.3), two other 4,6-halonicotines **14** and **15** were produced as alternative deuteration precursors. They were synthesised from 6-chloronicotine **2** with the same Comins-derived conditions[79-81] using *n*-BuLi organolithium species but a different electrophile was employed to introduce 4-bromo and 4-iodo substituents (Scheme 11). It was hoped such substituents would be more easily and quickly exchanged for deuterium. Both products **14** and **15** were produced in moderate to poor yields, although the bromochloronicotine **14** showed itself to be so unstable that even after it was stored in a freezer under argon, it decomposed completely after two days. The problems with the synthesis of 4,6-nicotine-d_2 **9** were ultimately solved (as described in Chapter 2.3) and consequently, no further studies with analogues **14** and **15** were carried out.

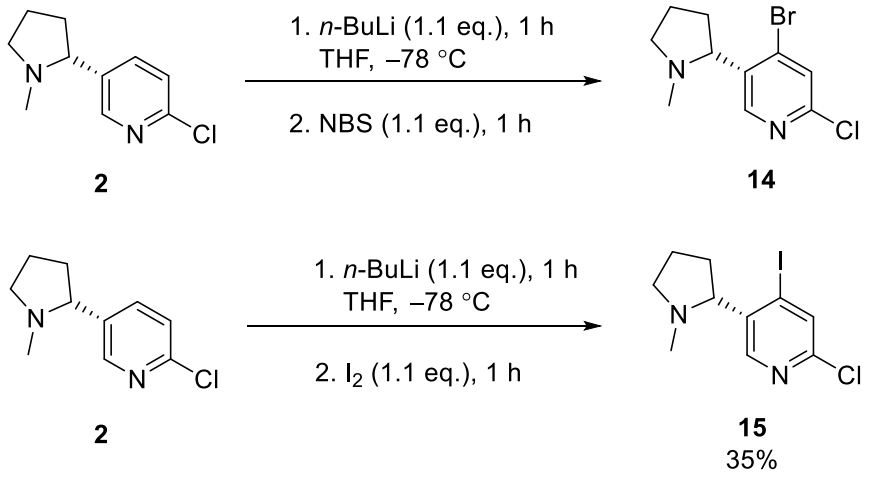

Scheme 11: reagents and conditions to produce 4-bromo-6-chloronicotine *14* and 4-iodo-6-chloronicotine *15*

In contrast to the regioselectivity to produce 5,6-dichloronicotine **5**, it is believed that the relatively small *n*-BuLi molecule coordinates to the pyrrolidine nitrogen, thus overcoming the moderate *ortho*-directing effect of the 6-chloro substituent in 6-chloronicotine **2** (Figure 27).[18,22] The pyrrolidine ring itself acts as a $CHNR_2$ *ortho*-directing group, with strong directing power resulting from strong coordination to the organolithium base. The relative strengths of the two *ortho*-directing effects is most apparent insofar as no production of **5** is observed at all.

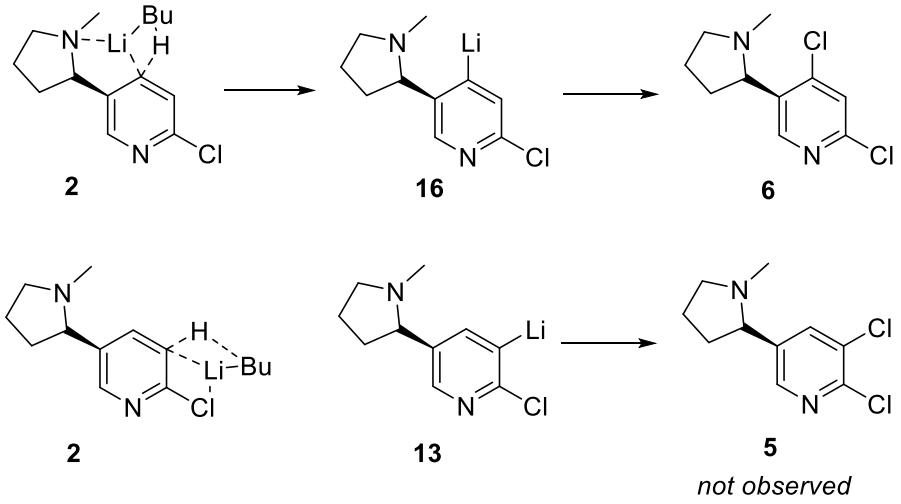

Figure 27: comparison of effects of $CHNR_2$ and Cl as *ortho*-directing functional groups

2,6-Dichloronicotine **7** was also prepared from 6-chloronicotine **2**.[18] Following the same Comins procedure[79,80] used to produce 6-chloronicotine **2**, further treatment of **2** with *n*-BuLi·LiDMAE (5.4 eq. *n*-BuLi and 3.0 eq. DMAE) in *n*-hexane at −20 ºC and trapping with a solution of hexachloroethane in toluene afforded 2,6-dichloronicotine **7** in

moderate yield (52%) (Scheme 12). The ^{1}H NMR spectrum contained mutually-coupled doublet signals (J = 8.0 Hz) with chemical shifts corresponding to the 4-pyridyl and 5-pyridyl protons in 6-chloronicotine **2** and this confirmed the regiochemistry (Figure 28). As conditions to produce 2,6-dichloronicotine **7** were essentially identical to those used previously for synthesis of **2**, an idea to use otherwise wasted material was formed.

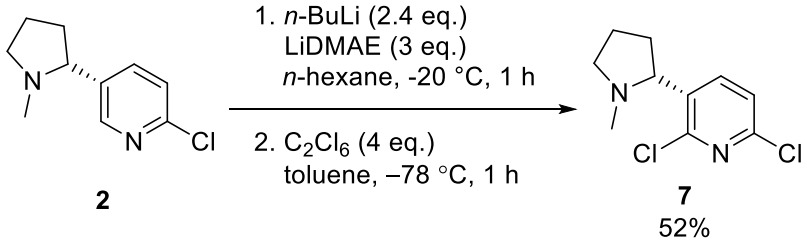

Scheme 12: reagents and conditions to produce 2,6-dichloronicotine *7*

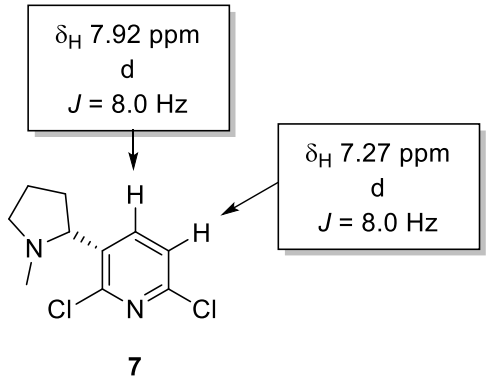

Figure 28: Chemical shifts and splitting patterns in the ^{1}H NMR spectrum for 2,6-dichloronicotine *7*

It was theorised that a mixture of regioisomeric 2-chloronicotine **3** and 6-chloronicotine **2** could be used as starting material for this reaction, with a chlorine substituent being incorporated at the unsubstituted α-position in each regioisomer to give 2,6-dichloronicotine **7**. This would give a use for the mixed material consistently produced by the incomplete separation of **2** and **3**, instead of it requiring further purification. A slight modification was made to the conditions originally used to produce 6-chloronicotine **2** and 2-choronicotine **3**- the entire reaction was carried out in toluene at −78 °C rather than a *n*-hexane/toluene mixture at warmer temperatures. Treatment of an 80:20 mixture of **2** and **3** with *n*-BuLi·LiDMAE (5.4 eq. *n*-BuLi and 3.0 eq. DMAE) in toluene and trapping with a solution of hexachloroethane provided 2,6-dichloronicotine **7** in excellent yield (83%) (Scheme 13).

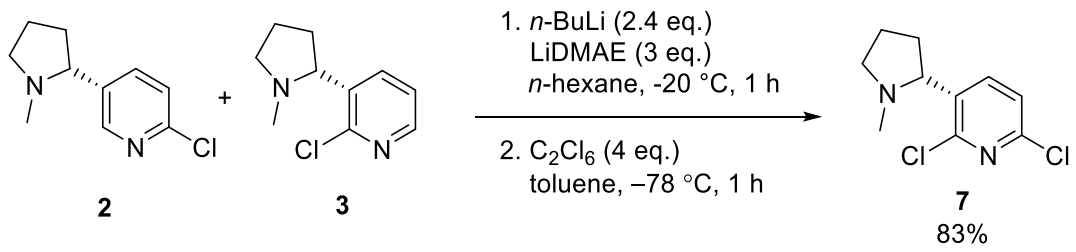

Scheme 13: reagents and conditions to produce 2,6-dichloronicotine *7* using chloronicotine mixture as starting material

It was theorised that a different isotopologue precursor, 2,4-dichloronicotine **17**, could be produced by treating 2-chloronicotine **3** with *n*-BuLi (Scheme 14), analogous to the conversion of 6-chloronicotine **2** into 4,6-dichloronicotine **6**. The chief problem with this strategy was that **3** was very difficult to isolate in quantity with the established synthetic methodology. It was only obtained as a minor by-product in the synthesis of 6-chloronicotine **2** or as a ~35:65 mixture of **2** and **3**.

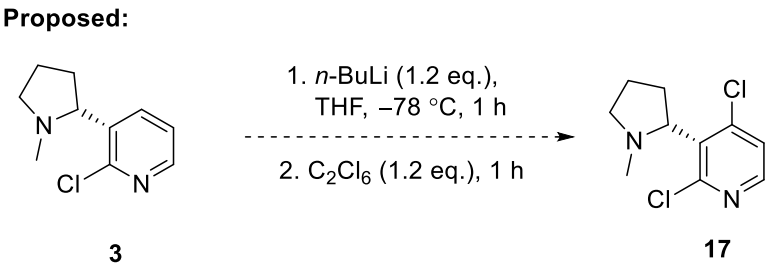

Scheme 14: proposed synthesis of 2,4-dichloronicotine *17*

It was therefore decided to use the 35:65 mixture of 6-chloronicotine **2** and 2-chloronicotine **3** as the starting material with a view to attempting separation of the two products that would be formed. Treatment of the **2**/**3** mixture with 1.1 eq. *n*-BuLi in THF at −78 ºC and subsequent trapping with hexachloroethane in THF appeared successful, with ^{1}H NMR spectroscopic analysis of the crude product showing clean conversion to a 35:65 mixture of 2,4-dichloronicotine **17** and 4,6-dichloronicotine **6** in 61% crude yield (Scheme 15). However, it was discovered that **17** and **6** have almost identical R_F values in a variety of conditions (e.g. R_F 0.57 vs. 0.55 in EtOAc). When separation by flash column chromatography was attempted, it proved impossible to successfully isolate each regioisomer from one another.

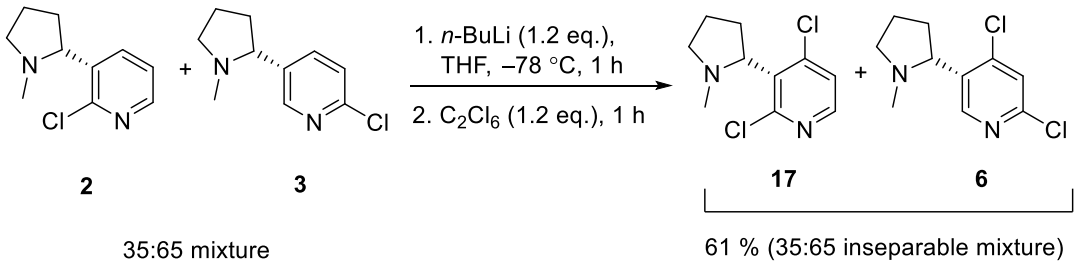

Scheme 15: reagents and conditions to produce 2,4-dichloronicotine *17* from chloronicotine mixture

Overall, the synthetic methods outlined in this section were successful in isolating five different halogenated derivatives of (−)-nicotine **1**. ^{1}H NMR spectroscopy characterisation was instrumental in confirming that the desired products had been successfully produced (full characterisation data are listed in Chapter 6). The compounds were produced with yields ranging from 52 to 83%, which were deemed sufficient for further functionalisation. Thus, routes to a range of mono- and dihalonicotines were successfully developed using organolithium chemistry.

2.3 Synthesis of deuteronicotines

The conversion of the chloronicotine precursors **2**, **5**, **6** and **7** into the desired deuterated analogues was then attempted. A common preparation in the Duckett group would be to treat a halogenated precursor with a palladium catalyst (*e.g.* Pd/C) and deuterium gas to effect the desired deuteration, derived from a preparation by Pavlik *et al*.[90] For this work, deuterium gas and palladium on activated carbon were combined to effect a catalytic reaction that was applicable to all substrates. Potassium carbonate was used as an additive to scavenge residual protons in the reagents and solvent and ensure complete deuteration (Figure 29).

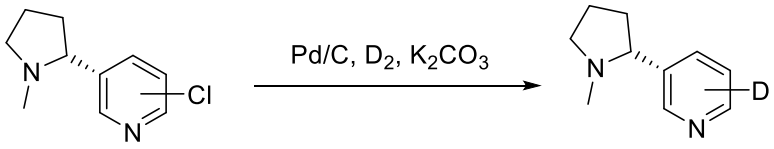

Figure 29: general method for production of deuteronicotines from halonicotines

This deuterodehalogenation synthetic route typically requires high pressures in order to be effective, requiring use of a Parr compact pressure reactor to maintain a large deuterium excess. In turn, a polar solvent with high hydrogen/deuterium solubility was needed, typically an alcohol or DMF.[91] Ethanol has superior hydrogen and deuterium

solubility to methanol[92] while remaining inexpensive, relatively safe, easy-to-use and readily available. The partially-deuterated ethan-(ol)-D (CH_3OD) was selected instead to eliminate potential H/D exchange with the ethanol hydroxyl proton, which would lead to undesired hydrodehalogenation. Lastly, because industry-supplied deuterated chemicals are never guaranteed as 100% deuterated, a base was incorporated to act as a hydrogen/proton scavenger and ensure only deuterium was incorporated into the products.

The overall reaction proceeds by a deuterodehalogenation catalytic cycle (Figure 30).[91,93] The cycle begins with oxidative addition of palladium into the carbon-chlorine bond(s) of the precursor material and subsequent coordination of deuterium gas onto the metal centre. One of the deuterons coordinates directly to the palladium and the other is incorporated into the nicotine structure in a rearrangement referred to as 'deprotonation'. Lastly, the remaining ligands on palladium are removed by reductive elimination to produce DCl and regenerate the Pd(0) catalyst.

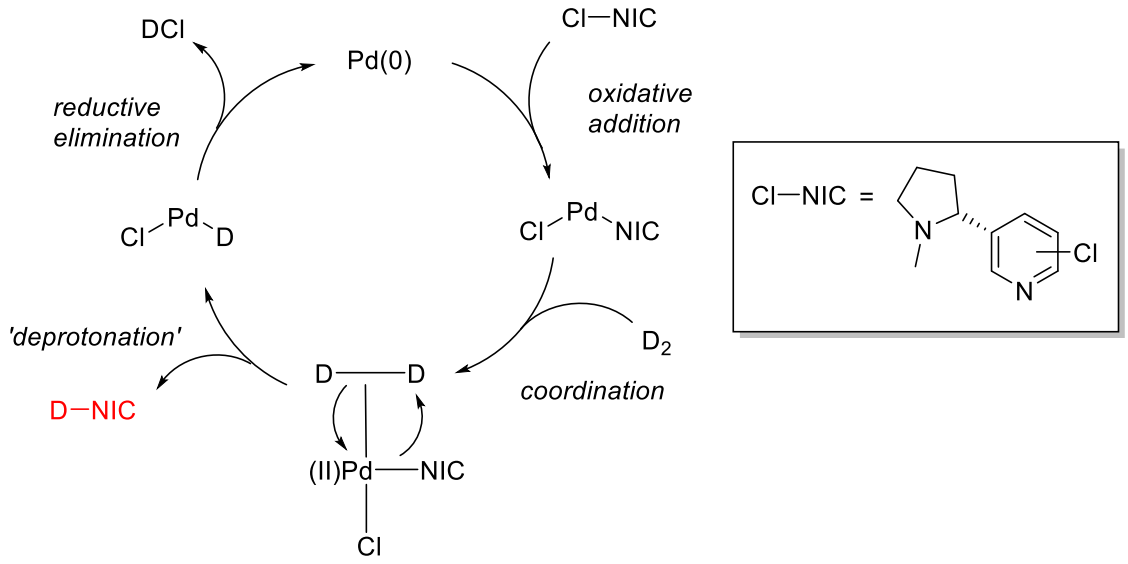

Figure 30: deuterodehalogenation catalytic cycle for conversion of halonicotines to the corresponding deuteronicotines

The scale of deuteronicotine production was not only limited by the availability of starting reagents, but also by the size of the available Parr reactors. There were two reactor types available, a smaller version appropriate for approximately 1-1.5 grams of precursor and a much larger version appropriate for 10 or more grams of starting material. The latter Parr reactor type was excessive for the quantities of precursor produced throughout the project and hence the smaller reactor was used exclusively. It was found that loading the

small reactor with more than ~2 grams of halonicotine led to substantially extended time required for full conversion to the corresponding deuteronicotine, as the volume of hydrogen in the reactor was fixed.

Initial conditions for the deuterodehalogenation of 6-chloronicotine **2** were 10% by weight loading of 5% Pd/C catalyst, 8 bar of deuterium and 2 equivalents of potassium carbonate base in ethan-(ol)-D stirring at room temperature for 18 h. Reaction progress was monitored by LC-MS experiments observing the starting material peak with *m/z* [M (^{35}Cl) + H] 197 disappearing and product peak with *m/z* [M + H] 164 appearing in its place. Purification by chromatography gave 6-nicotine-d_1 **4** in 50% yield (Scheme 17). In addition to mass spectrometry evidence, ^{1}H NMR spectroscopy showed three aromatic signals at 8.48, 7.65 and 7.21 ppm, corresponding to the 2-pyridyl, 4-pyridyl and 5-pyridyl signals respectively in (−)-nicotine **1**. A characteristic quaternary C-D 1:1:1 triplet at 148.2 ppm ($^1J_{CD}$ = 27.0 Hz) was also observed in the ^{13}C NMR spectrum.

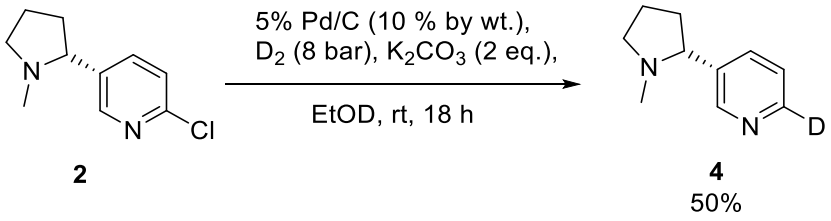

Scheme 16: reagents and conditions to produce 6-deuteronicotine *4*

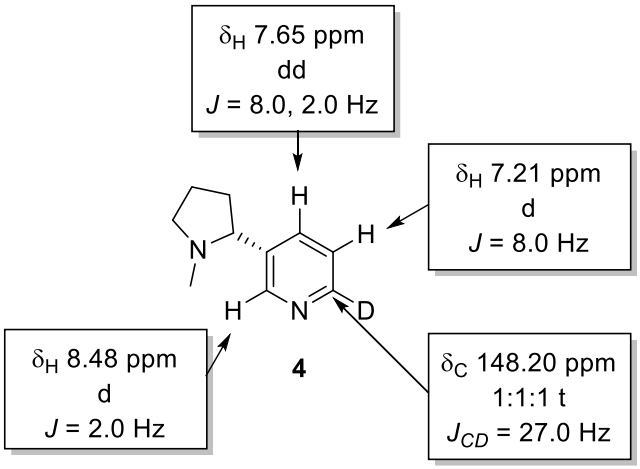

Figure 31: Chemical shifts and splitting patterns in the ^{1}H NMR spectrum for 6-deuteronicotine *4*

Deuterium-incorporation to give 5,6-nicotine-d_2 **8** was then successfully achieved. This involved the use of identical reagents and conditions as for 6-nicotine-d_1 **4** (10% by weight 5% Pd/C catalyst, 8 bar deuterium, K_2CO_3 (2 eq.) in ethan-(ol)-D) on 5,6-dichloronicotine **5**, although yields of 5,6-nicotine-d_2 **8** were moderate (46%). The reaction time with the original 10% catalyst loading was considerably longer than for 6-nicotine-d_1 **4**, taking over four days to run to completion. Such a long reaction time was deemed impractical, with subsequent reactions successfully run to completion in a few hours with the catalyst loading doubled to 20% by weight and no significant change in yield (Scheme 18). The expected pair of quaternary C-D 1:1:1 triplets were not resolved in the ^{13}C NMR spectrum, but the two singlets at 8.51 and 7.68 ppm in the ^{1}H NMR spectrum (corresponding to 2-pyridyl and 4-pyridyl protons) indicated success (Figure 32). Mass spectrometry analysis confirmed that full deuterodehalogenation had successfully occurred, with the starting material peak at *m/z* [M ($^{35}Cl_2$) + H] 231 being replaced first by two peaks for singly-deuterated intermediates at *m/z* [M (^{35}Cl) + H] 197 and then exclusively by the product peak at *m/z* [M + H] 165.

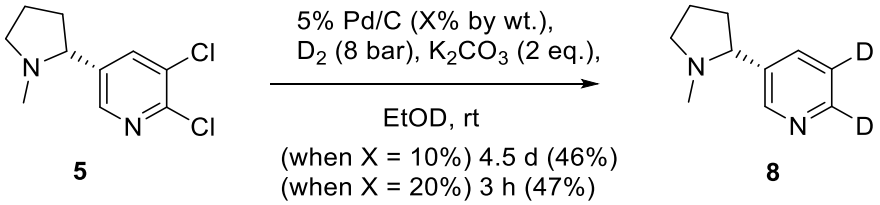

Scheme 17: reagents and conditions to produce 2,6-nicotine-d_2 8

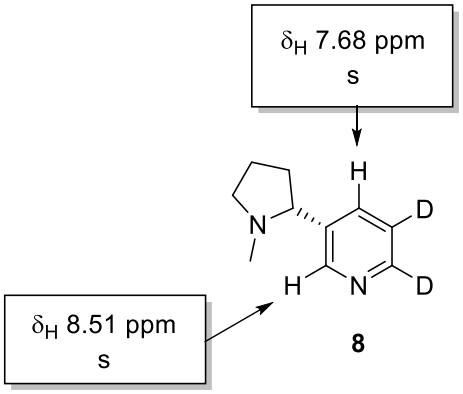

Figure 32: Chemical shifts and splitting patterns in the ^{1}H NMR spectrum for 5,6-nicotine-d_2 *8*

Next, deuterodehalogenation of 4,6-dichloronicotine **6** was explored. Treatment of dichloronicotine **6** using the original set of deuterogenolysis conditions (10% by weight

Pd/C catalyst, 8 bar of deuterium) proved slow and problematic, with partial conversion to 4,6-nicotine-d_2 **9** taking several days and formation of an unidentified by-product (*m/z* = 168) preventing isolation of **9**. After several failed attempts, 4,6-nicotine-d_2 **9** was successfully produced in moderate yield (43%) by doubling the catalyst loading to 20% by weight and drastically reducing the reaction time to only two hours. Careful monitoring of reaction progress by buffered LC-MS was needed to stop the reaction once full conversion to the desired product was achieved. In this way, over-reaction to the unidentified product was prevented (Scheme 19). The singlet aromatic ^{1}H NMR spectroscopy signals at 8.52 and 7.25 ppm (corresponding to 2-pyridyl and 5-pyridyl, respectively) confirmed successful deuteration at the 4-pyridyl and 6-pyridyl positions (Figure 33) and MS analysis confirmed full deuteration with the product peak appearing exclusively at *m/z* [M + H] 165. The two expected quaternary C-D 1:1:1 triplets were, however, not well-resolved in the ^{13}C NMR spectrum. To date, the by-product has not been identified as it could not be isolated for further analysis. However, it should be noted that this reaction was repeated successfully with the increased catalyst multiple times on scales up to 9 mmol of 4,6,-dichloronicotine **6** without the *m/z* 168 by-product being observed again at any stage.

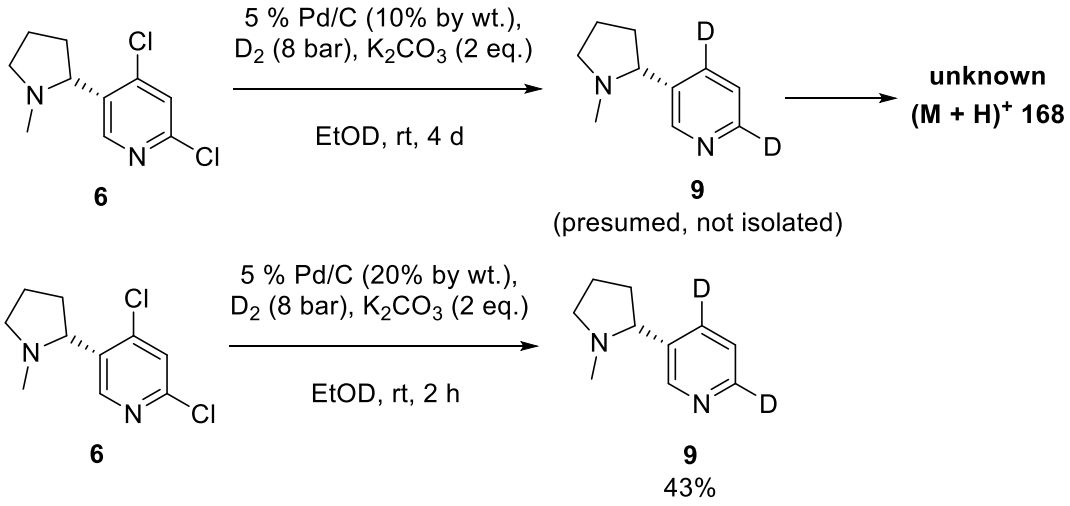

Scheme 18: reagents and conditions to produce 4,6-nicotine-d_2 9

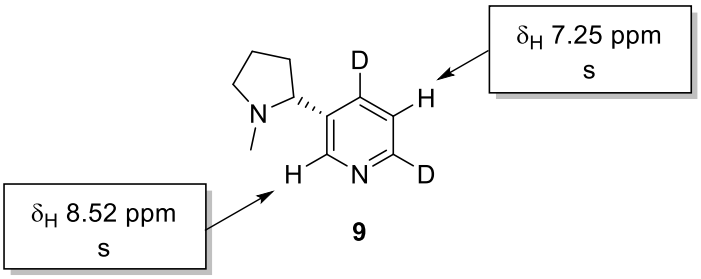

Figure 33: Chemical shifts and splitting patterns in the ^{1}H NMR spectrum for 4,6-nicotine-*d*$_2$ *9*

Conversion of 2,6-dichloronicotine **7** into its derivative 2,6-dideuteronicotine **10** was achieved using 20% by weight loading of Pd/C catalyst, 2 eq. of K_2CO_3 and 8 bar of deuterium in ethan-(ol)-D. Full conversion was slow in comparison to the three dideuteronicotines studied under these conditions, taking a full four hours. In addition, despite several repetitions, the yield was consistently poor (Scheme 20). Two quaternary C-D 1:1:1 triplets in the ^{13}C NMR spectrum at 149.1 ppm ($^{1}J_{CD}$ = 28.0 Hz) and 148.3 ppm ($^{1}J_{CD}$ = 27.0 Hz) indicated successful deuterogenolysis. Success was further demonstrated by MS analysis and a lone *m/z* [M + H] 165 product peak and singlet signals at 7.67 ppm and 7.23 ppm in the ^{1}H NMR spectrum, corresponding to the 4-pyridyl and 5-pyridyl protons, respectively (Figure 34).

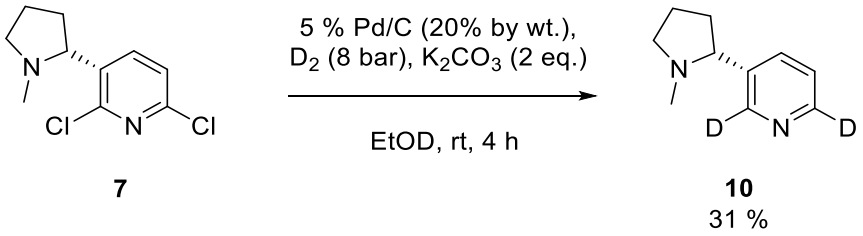

Scheme 19: reagents and conditions to produce 2,6-nicotine-*d*$_2$ 10

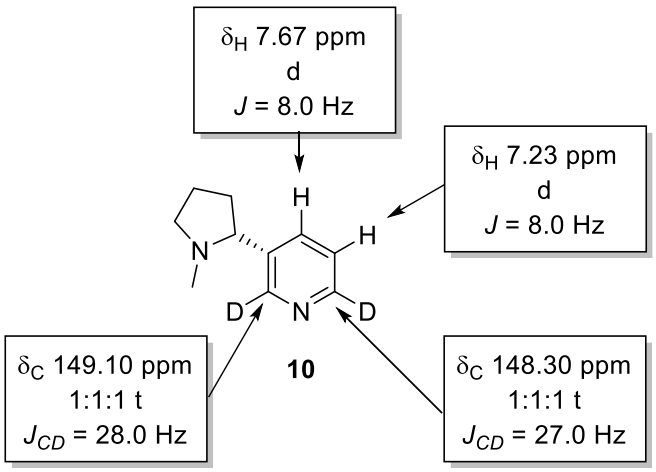

Figure 34: Chemical shifts and splitting patterns in the ^{1}H NMR spectrum for 2,6-nicotine-*d*$_2$ 10

In summary, a number of singly and doubly deuterated nicotine substrates were successfully prepared using catalytic deuterogenolysis reactions (Figure 35). With these substrates in hand, assessment of their hyperpolarisation properties could begin.

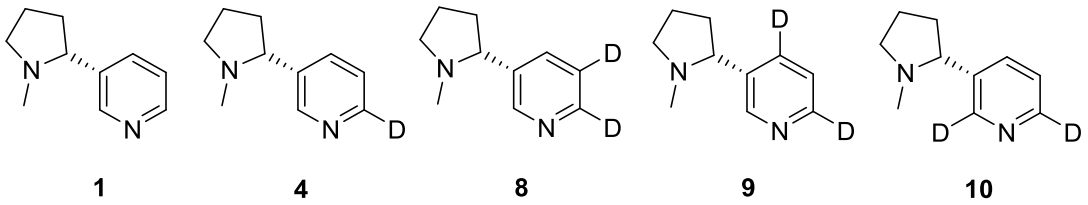

Figure 35: nicotine isotopologues produced in the project

3: NMR spectroscopic studies on nicotine isotopologues

(−)-Nicotine **1** and its isotopologues **4**, **8**, **9** and **10** were evaluated by NMR spectroscopy to determine their potential suitability as MRI contrast agent candidates. This assessment was primarily quantified by two parameters, namely the extent to which the proton NMR signals intensity could be improved through hyperpolarisation by SABRE and the lifetime of this magnetic enhancement, quantified by the T_1 relaxation times of protons in the molecule. Given that there are a multitude of interdependent factors (detailed throughout this chapter) that affect both the signal intensities and lifetimes of hyperpolarised systems[64], it would be grossly impractical to assess all of the hundreds of possible permutations in a reasonable timeframe. The project has therefore sought to streamline optimisation of SABRE by eliminating non-ideal combinations and conditions as soon as possible and in a sensible order.

3.1 SABRE substrate screen

3.1.1 Screen for enhancement

To achieve polarisation, samples were subject to a series of 'shake-and-drop' NMR experiments in order to determine their signal enhancement levels when hyperpolarised with SABRE. Samples of nicotine **1** and isotopologues **4**, **8**, **9** and **10** were prepared in methanol-d_4, along with the [Ir(IMes)(COD)Cl] SABRE precatalyst **18** in 5 mm Young's tap-fitted NMR tubes. The relative concentrations of the substrate and precatalyst were set to an intial 5-fold excess of substrate to ensure complete activation of the iridium precatalyst. After degassing each sample under vacuum, single-scan thermally-polarised ^{1}H NMR spectra were recorded as a baseline measure of the compounds' normal NMR signal intensity. The sample tubes were then charged with 4 bar (absolute) of *p*-H_2 and shaken vigorously by hand for ten seconds in a 65 G magnetic field to activate the polarisation transfer – said field was determined by theory and literature results for similarly-structured *N*-heterocycles to be the likely optimum (discussed in further detail in Chapter 3.5).[64] The field was assessed by using a gaussmeter to find a point in a spectrometer's stray field where the strength was 65 G and shaking the sample there. Immediately after shaking, the sample was placed in the spectrometer and another single-scan ^{1}H NMR spectrum was recorded. Further scans would be fruitless, as once encoded, the hyperpolarisation would at once start to return to thermal equilibrium and each

subsequent scan would therefore see a markedly weaker signal). Evaluation of the hyperpolarisation signal enhancement was achieved by direct comparison of integrals between the activated thermal and hyperpolarised single-scan spectra. Because of the inherently inconsistent nature of the shaking to activate (harder shaking gives better mixing of contents and effective *para*-hydrogen concentration, hence better signal), one-scan spectra were repeatedly recorded with fresh *p*-H_2 until at least three had the same measured signal enhancement per proton to within ± 50-fold. Reproducibility is an important criterion in learning from comparative measurements. The associated errors are estimated in Chapter 7.

The pyridyl proton signals of hyperpolarised unlabelled nicotine **1** had NMR peak integrals on average ~200 times larger than their non-hyperpolarised ('thermal') counterparts, proving the initial conditions were able to successfully facilitate SABRE of **1**. However, a ~200-fold signal enhancement per proton corresponds to less than 0.7% polarisation, indicating significant improvements might still be achieved with optimisation of conditions. Each pyridyl proton signal (those at 8.43, 8.37, 7.78 and 7.36 ppm) was noticeably increased in signal intensity – note that these peaks correspond to the species free in solution (the identity and characterisation of free and bound species peaks is explored in Chapter 4). There did not appear to be any significant enhancement for the protons in the pyrrolidine ring (signals between 3.5 and 1.5 ppm), suggesting that polarisation does not transfer significantly beyond the pyridine ring, as shown in Figure 36. Spectra of similar appearance to this were obtained for each of the isotopologues tested.

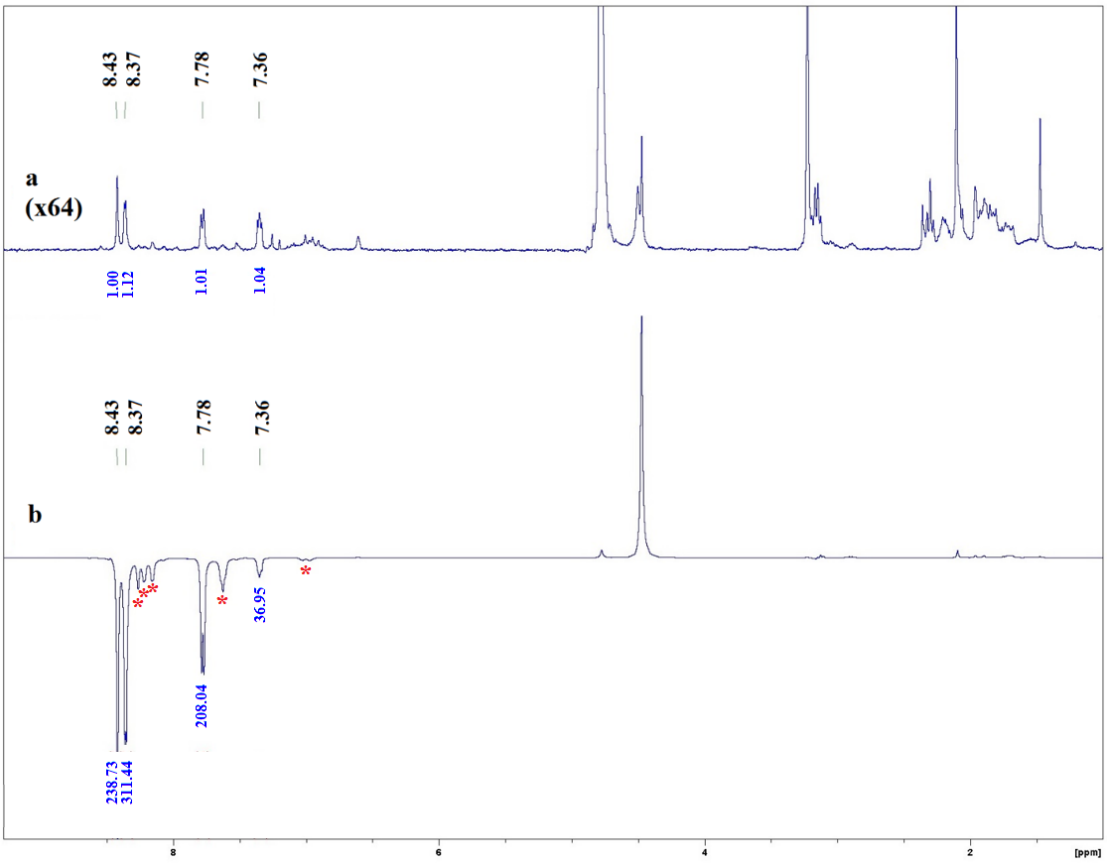

Figure 36: thermal (a) and hyperpolarised (b) ^{1}H NMR spectra of (−)-nicotine *1* in the presence of the active form of IMes precatalyst species *18*. Thermal spectrum (a) intensity scaled up by 64 times relative to the hyperpolarised spectrum (b). Peak integrals for species free in solution given in blue, red asterisks indicate peaks corresponding to species bound to the catalyst

The increase in signal intensity was not uniform for all resonances − those protons closest to the pyridine nitrogen (2-pyridyl and 6-pyridyl) showed significantly stronger enhancement (over 240x increase), in line with expectations that protons nearest the catalyst binding site (and therefore *para*-hydrogen) would be polarised most strongly. In comparison, the 4-pyridyl proton most distant from the catalyst binding site achieved the average enhancement (~200x), while for the 5-pyridyl proton it was noticeably poorer (~50x), despite being closer to the nitrogen than 4-pyridyl (Figure 37). The disposition of the varying degrees of enhancement indicated immediately that proximity to the *para*-hydrogen polarisation source was not the only important factor for good SABRE performance. Polarisation transfer within similar *N*-heterocycles reported in the literature yielded a similar pattern of enhancement, although the precise mechanism of intramolecular transfer remains poorly defined.[94]

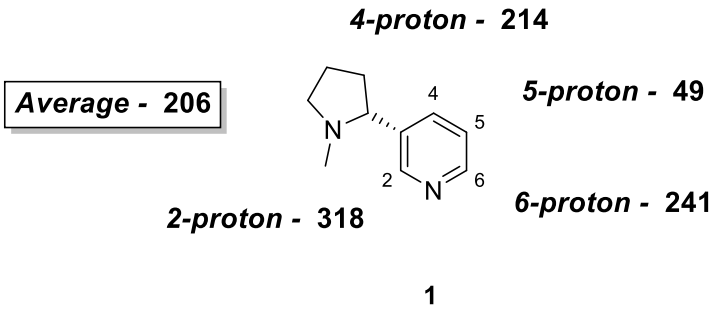

Figure 37: SABRE hyperpolarised signal enhancements per proton for (−)-nicotine *1* with IMes *18* precatalyst, relative to thermal signal

Singly-deuterated 6-nicotine-d_1 **4** showed slightly improved average signal enhancements relative to unlabelled (−)-nicotine **1** at ~275-fold per proton. The actual enhancement per proton was similarly non-uniform as for **1** – the 5-pyridyl proton again exhibited very poor performance (only a ~30x increase). However, the 2-pyridyl and 4-pyridyl protons displayed approximately 400x signal enhancements when hyperpolarised (Figure 38), corresponding to a substantial ~31% and ~75% increase, respectively, versus their equivalents in undeuterated (−)-nicotine **1**. Such increases could be attributed to polarisation from the limited *para*-hydrogen supply in the tube being diluted across only three protons in **4** versus four protons in **1**, but the still-poorly-enhanced 5-pyridyl proton once more alluded to other factors being relevant. Testing of other isotopologues would shed more light on these as-yet ill-defined factors.

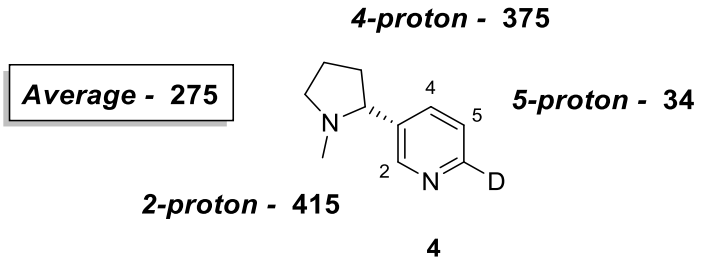

Figure 38: SABRE hyperpolarised signal enhancements per proton for 6-nicotine-d_1 *4* with IMes *18* precatalyst, relative to thermal signal

5,6-Nicotine-d_2 **8** showed decidedly poorer enhancement than the singly deuterated **4**, disrupting a potential correlation between the number of deuterium substituents incorporated and signal enhancement. Whilst the average signal intensity did increase compared to (−)-nicotine **1**, the individual signals in **8** were noticeably poorer (~40-45%)

than most of the resonances in **1** (Figure 39). The greatly-reduced magnitude of the 2-pyridyl proton enhancement (~26% worse than in the completely undeuterated (−)-nicotine **1**) despite this proton being directly next to the catalyst binding site demonstrated clearly that the deuterium substituents had a dramatic effect on transfer of polarisation about the molecule.

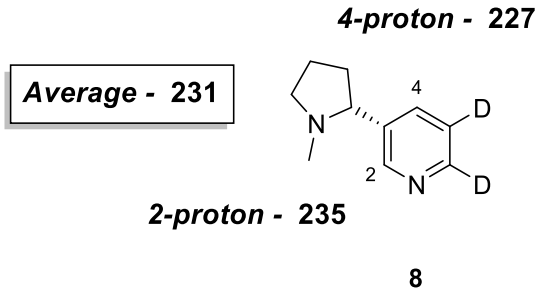

Figure 39: SABRE hyperpolarised signal enhancements per proton for 5,6-nicotine-d_2 *8* with IMes *18* precatalyst, relative to thermal signal

The best performing substrate in this series by far, 4,6-nicotine-d_2 **9** displayed greatly superior signal enhancement levels, both as an average (~750x) and as individual resonances – now, the 5-pyridyl proton showed over a 1000-fold increase in signal intensity when hyperpolarised (Figure 40). The 5-pyridyl proton's excellent enhancement came as a surprise in light of its isolation from the nitrogen binding site and the dismal performance of 5,6-nicotine-d_2 **8**. This further demonstrated the complexity of how the polarisation transfers proceeds within the pyridine ring and how substituents affect it. However, previous group work on 4,6-deuterio-labelled nicotinamide[24] resulted in a similar pattern of enhancement; a more weakly enhanced 2-pyridyl proton and a very strongly enhanced 5-pyridyl proton, suggesting there is a both a logical mechanism for these results and an as-yet unidentified relationship between two protons.

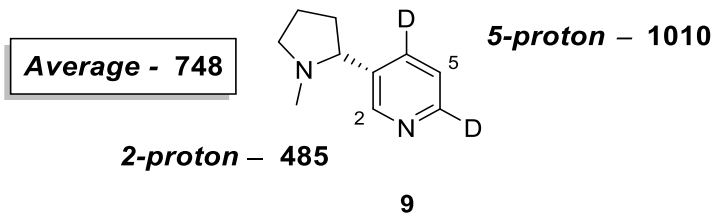

Figure 40: **SABRE hyperpolarised signal enhancements per proton for 4,6-nicotine-d_2 *9* with IMes *18* precatalyst, relative to thermal signal**

The signal enhancements exhibited by 2,6-nicotine-d_2 **10** were expected to be disappointing, as related compounds (pyridine, nicotinamide, etc.) with this deuteration pattern reported in literature had generally shown very poor signal enhancements.[95] Transfer of polarisation into pyridyl rings is believed to occur mainly through ^4J ^{1}H-^{1}H scalar coupling between the catalyst hydride(s) and pyridyl α-protons directly adjacent to the catalyst binding site.[94,96,97] The absence of both α-protons in a doubly-α-deuterated pyridyl system explains why such systems usually exhibit relatively poor enhancement – polarisation transfer would be forced along longer and less-efficient pathways.

Surprisingly, the SABRE performance of **10** was not as poor as expected (Figure 41), with an average signal enhancement almost identical to that of natural (−)-nicotine **1** at just over 200-fold signal enhancement per proton. However, such SABRE performance was inferior to every other nicotine isotopologue tested under these conditions. It was concluded that the positive aspects of deuterium incorporation (reduced dilution of polarisation and fewer relaxation pathways) were countered almost exactly by inhibition of polarisation transfer from its source by the α-deuterium substituents.

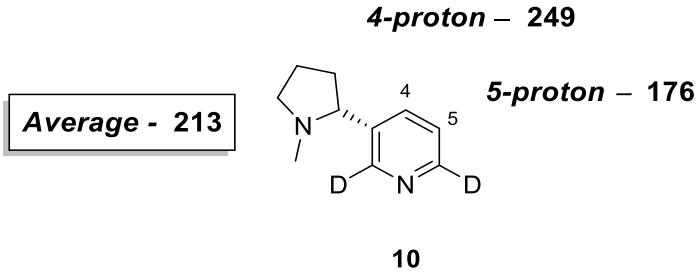

10

Figure 41: SABRE hyperpolarised signal enhancements per proton for 2,6-nicotine-d_2 *10* with IMes *18* precatalyst, relative to thermal signal

Therefore, no clear trend between deuteration levels and positions and the signal enhancement was observed - though for the most part the labelled nicotines showed stronger enhancement for individual proton resonances than the unlabelled nicotine **1**. However, it was deemed obvious that 4,6-nicotine-d_2 **9** was by far the best performing substrate for signal enhancement under the initial conditions.

3.1.2 Screen for T_1 magnetic lifetime

The effects of the deuterium labelling on the magnetic lifetimes of these isotopologues was the focus of the project. The slower/longer the relaxation process, the longer a molecule will retain its signal intensity and so the longer a hyperpolarised contrast agent molecule would remain useful for – important when said agent must be polarised before entering the patient and reach the area of diagnostic interest with sufficient signal remaining. Relaxation occurs through several different pathways such as dipole-dipole interactions, chemical shift anisotropy and tumbling[98], with a prominent route being *via* through-bond scalar coupling to other nuclei. Removing these through-bond couplings by replacing adjacent nuclei with examples which are not coupled to (i.e. non-I = ½ nuclei such as I = 1 deuterium in place of an I = ½ proton) was expected to slow down the speed at which a nucleus could relax.

The magnetic lifetimes of the isotopologues were quantified with measurement of the substrates' proton T_1 relaxation times. T_1 is a constant for each system otherwise known as the *spin-lattice relaxation time*, so called because the process radiates excess energy from the spins to surrounding nuclei, atoms and molecules (the 'lattice'). The T_1 relaxation time does not represent full relaxation of nuclear spins back to equilibrium with an external magnetic field, instead it is the time for longitudinal magnetization (M_z) to recover approximately 63% (specifically, 1-(1/e)) of its initial value (M_0) after movement into the observable *xy*-plane (M_{xy}). By extension, the T_1 therefore indicates the time elapsed when ~37% of an experiment's NMR signal would still be observable. The exponential decay of observable signal means complete recovery to equilibrium magnetisation is only complete at approximately 5(T_1).[99,100]

The *inversion-recovery* and *saturation-recovery* T_1 experiments were both employed throughout the project as measures of T_1 relaxation times. The pulse sequences (described fully in Chapter 6) and defining equations vary slightly between the two experiments. However, they both involve an initial RF pulse and a subsequent 90° RF pulse after an increasing delay to observe the recovery of M_z. The T_1 times derived from each are very similar, hence the two techniques have been used interchangeably throughout the project. Figure 42 shows the equation and recovery of longitudinal magnetisation for the saturation-recovery pulse sequence.

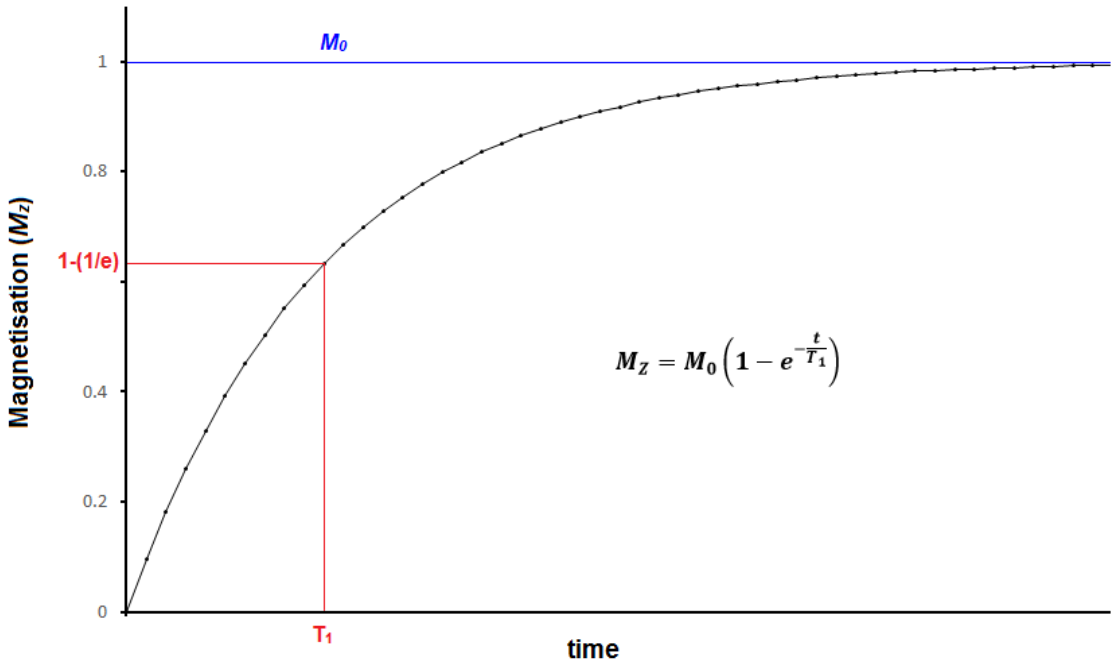

Figure 42: saturation-recovery of equilibrium magnetisation M_z/decay of observable signal by T_1 a.k.a spin-lattice relaxation. T_1 itself is a time constant for a given system and conditions, which affects the rate at which M_z is recovered.

By measuring the NMR signal intensity of each proton multiple times over a given period, a curve could be plotted from which the T_1 relaxation time of that proton could be derived. Such T_1 relaxation NMR experiments were performed on nicotine and deuteronicotine samples in methanol-d_4 of identical substrate concentration as for the initial enhancement studies. Addition of the IMes precatalyst **18** and hydrogen to simulate the conditions of a SABRE experiment is now known to increase the rate of proton relaxation[101], primarily via through-bond coupling between the substrate and catalyst as shown in Figure 43. Therefore, the substrate T_1 relaxation times were calculated both for samples with catalyst and hydrogen added (hereafter referred to as *activated* conditions) as well as without catalyst and under vacuum (hereafter referred to as *unactivated* conditions). The activated conditions were considered a reasonable approximation of a 'shake-and-drop' experiment. It should be noted that, as substrate and hydrogen ligands are constantly exchanging with the catalyst under experimental conditions, the activated conditions T_1 measurements represent a weighted average of the bound and free forms of the substrate.

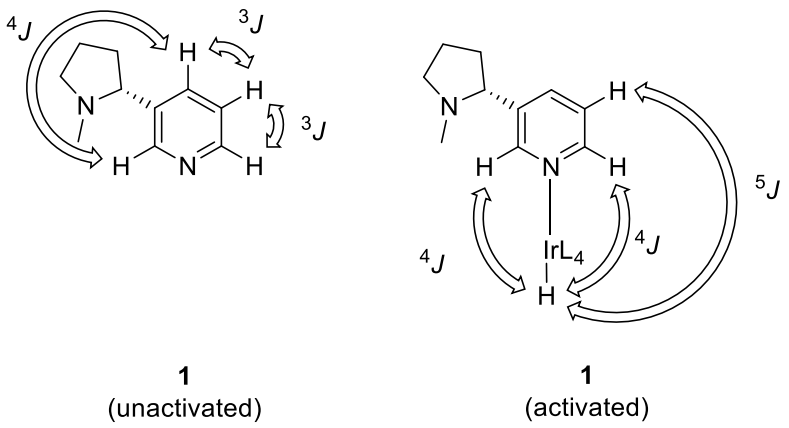

Figure 43: Major through-bond coupling relaxation pathways in (−)-nicotine *1* under both unactivated and activated conditions. Note that, for clarity, not all pathways are shown/duplicated. L are the other ligands present on the iridium centre

The protons in unmodified (−)-nicotine **1** were found to have short T_1 relaxation times, with all four resonances being between 8 and 12 seconds in the absence of catalyst. However, the same protons were found to have even shorter T_1 times under activated conditions, with no proton T_1 exceeding four seconds (Figure 44). The decrease was most apparent near the catalyst binding site, with the 2-proton and 6-proton exhibiting a 67 and 75% reduction in T_1 respectively in the presence of the catalyst. Such rapid relaxation indicated nicotine **1** would be an unsuitable candidate for medical imaging on magnetic lifetime grounds alone. The fast relaxation in combination with relatively poor signal enhancement highlights their mutual relationship – a rapidly-relaxing nucleus would bleed away large amounts of signal before it could be observed, hence a poor signal enhancement measured. In theory, much more rapid relaxation in the presence of the catalyst implies more efficient polarisation of the substrate, as polarisation and relaxation both occur via the same scalar coupling network. However, magnetic lifetime will be the key parameter for any imaging application as highly efficient polarisation is pointless if none of it remains by the time the agent reaches the diagnostic site of interest.

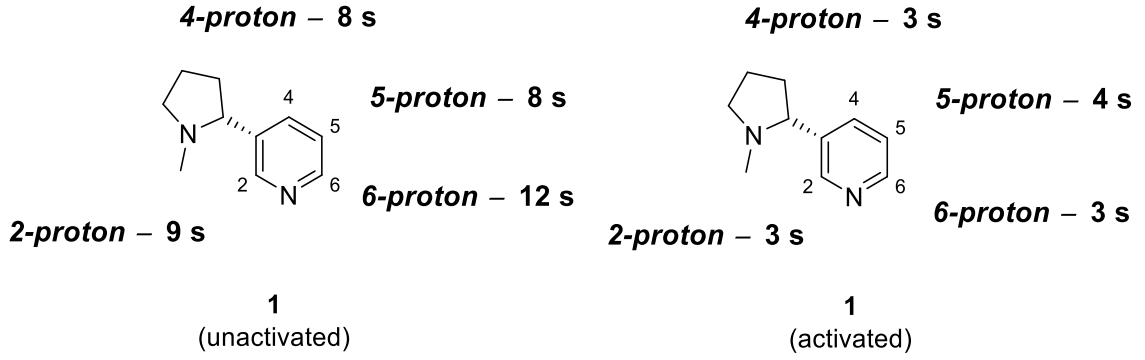

Figure 44: (−)**-nicotine** ***1 T₁*** **relaxation times, both under unactivated and activated conditions**

Addition of a single deuterium substituent in 6-nicotine-d_1 **4** resulted in different T_1 relaxation times for the remaining proton resonances. In the unactivated studies, the 4-pyridyl proton T_1 remained unchanged from the equivalent in (−)-nicotine **1** at 8 seconds, the 5-pyridyl proton T_1 increased by over sixty percent to 13 seconds and the 2-pyridyl proton T_1 shortened slightly to 6 seconds. More promisingly, under activated conditions, all three resonances were slower relaxing than their equivalents in unlabelled nicotine **1**, with the 5-pyridyl resonance having a T_1 twice as long in **4** as in **1**. The longest T_1 was still only eight seconds, but reinforced the hypothesis that further deuteration would likely lead to increased relaxation time (Figure 45).

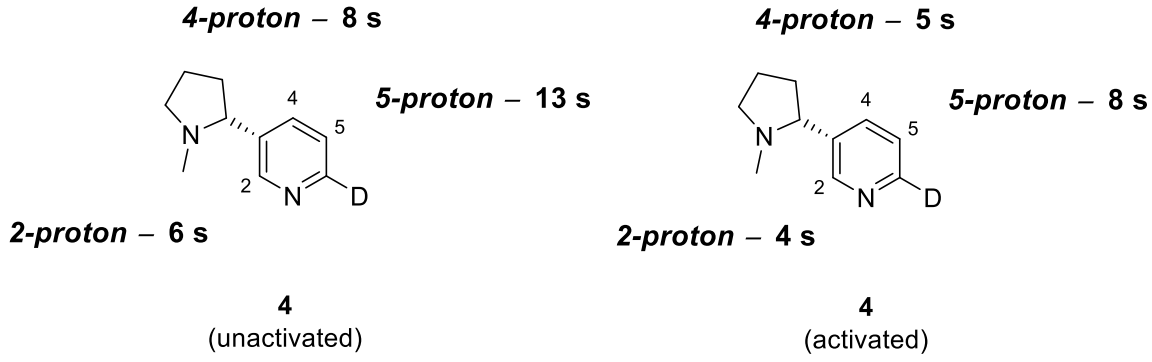

Figure 45: 6-nicotine-d_1 ***4 T₁*** **relaxation times under unactivated and activated conditions**

The signal enhancement studies on 5,6-deuteronicotine **8** initially appeared to be somewhat disappointing as their T_1 relaxation times under unactivated conditions were barely any better than those in singly-deuterated **4** (Figure 46). The 4-pyridyl proton was the slower relaxing of the two resonances at 14 seconds unactivated. However, under activated conditions the T_1 times decreased by a relatively small proportion (~22-37%)

compared to (−)-nicotine **1** (~50-75%) and 6-nicotine-d_1 **4** (~37-50%). Therefore, **8** exhibited the longest activated T_1 relaxation times yet observed at 11 seconds for the 4-pyridyl proton and 5 seconds for the 2-pyridyl proton. While this result represented a step in the right direction for increasing the T_1 times, these values were still too short to be of much use in practical application of SABRE.

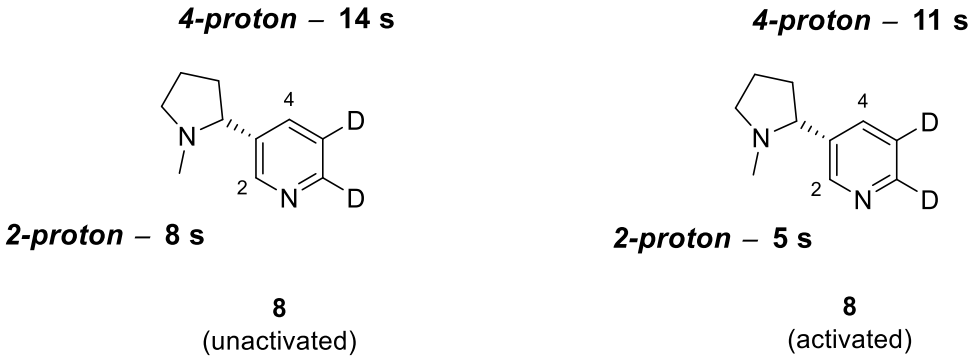

Figure 46: 5,6-nicotine-d_2 *8* T_1 relaxation times under unactivated and activated conditions

By isolating the 5-pyridyl proton in 4,6-nicotine-d_2 **9** and thereby removing through-bond coupling as a relaxation pathway, it was hoped a greatly increased T_1 relaxation time could be obtained. This hypothesis proved to be correct, with the unactivated conditions 5-pyridyl T_1 time measured at 31 seconds, more than double the next longest T_1 observed in any of the isotopologues (Figure 47). Furthermore, the activated conditions T_1 time for the 5-pyridyl proton was only slightly shorter at 27 seconds, which was nearly three times longer than the next best activated T_1 and by far the smallest reduction in T_1 between the unactivated and activated conditions observed for all substrates. It is likely that a direct ^5J interaction to the catalyst is the only through-bond coupling present, hence this relaxation pathway only exists in the brief time the substrate is bound to the catalyst and the impact on T_1 is small (only around ~13% reduction for the 5-pyridyl proton). In contrast, the 2-pyridyl proton signal relaxed much more quickly, in a matter of a few seconds regardless of conditions. It could be that the 4-deutero substituent boosts interaction of the 2-pyridyl proton with the nearest aliphatic proton on the pyrrolidine ring, which is likely to relax quickly and thereby reducing the T_1 of the 2-pyridyl proton. There is no observed coupling for the 2-pyridyl proton, suggesting interaction with the aliphatic proton is of 1 Hz or less. Tessari *et al.* have demonstrated that polarisation transfer via ^{4}J and ^{5}J coupling in SABRE is still possible despite typically small couplings of 1 Hz or less.[62] Despite poor 2-pyridyl proton relaxation, 4,6-nicotine-d_2 **9** was

determined to have the most promise for further optimisation and study with the largest signal enhancement and longest proton T_1 time of all substrates observed by far. The superior performance of **9** again reinforced the relationship between long relaxation and high signal enhancement.

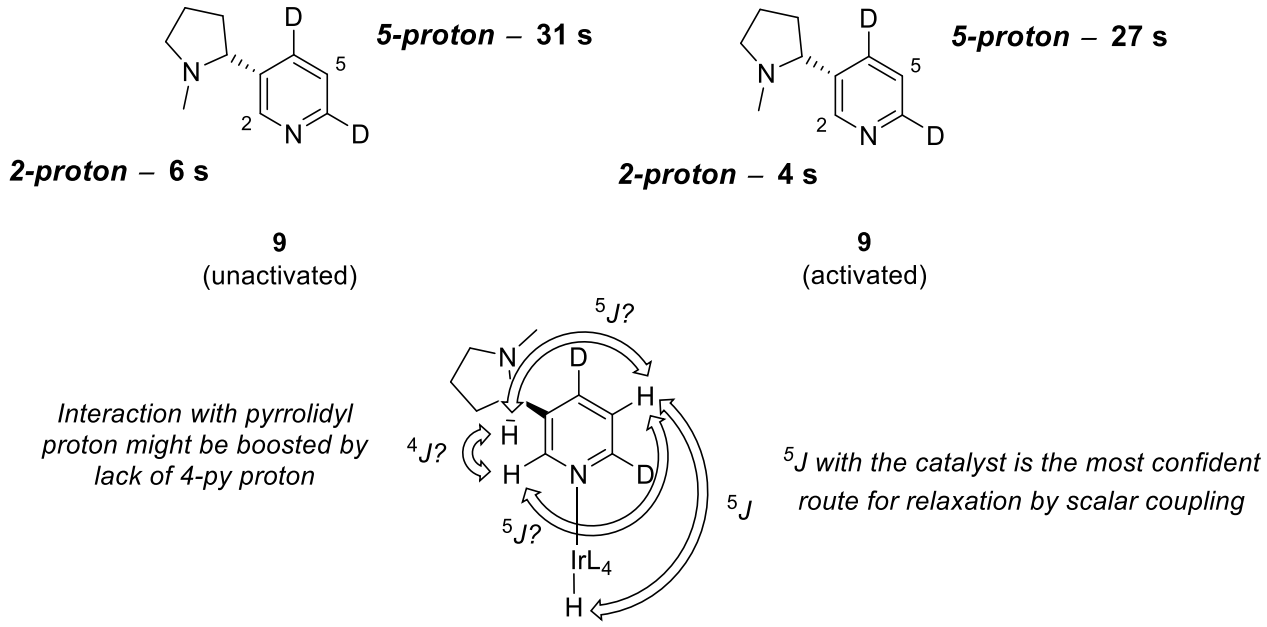

Figure 47: 4,6-nicotine-d_2 9 T_1 relaxation times under unactivated and activated conditions in methanol-d_4 and associated coupling mechanisms to explain T_1 performance

The relaxation performance of 2,6-nicotine-d_2 **10** was disappointing. The T_1 times under unactivated conditions were on par with several other isotopologues (at 9 and 15 seconds for the 4-pyridyl and 5-pyridyl proton, respectively), but still markedly inferior to the best performing substrate, 4,6-nicotine-d_2 **9**. Measurement of T_1 relaxation times under activated conditions revealed extremely fast relaxation of less than two seconds for either pyridyl proton (Figure 48). Such rapid relaxation strongly suggested that 2,6-nicotine-d_2 **10** would not be a suitable substrate for imaging application proton SABRE, even with optimisation. However, the rapid relaxation of the 4- and 5-pyridyl protons in the presence of catalyst reinforced the theory that a direct ^5J coupling (both for polarisation and relaxation) was an important factor.

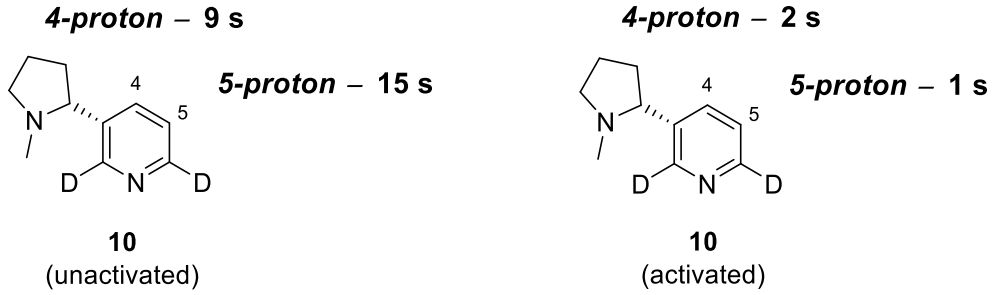

Figure 48: 2,6-nicotine-d_2 *10* T_1 relaxation times under unactivated and activated conditions in methanol-d_4

With a view towards improving the biological compatibility and relevance of these studies, T_1 magnetic lifetime experiments were performed in ethanol-d_6 in place of methanol-d_4. All other sample and experimental parameters were as for the methanol studies. Previous attempts by the group to use ethanol and ethanol/water mixtures gave much reduced activated T_1 relaxation times compared to otherwise identical experiments conducted in methanol, but it was decided to test the nicotine isotopologues regardless in the substantially less toxic ethanol. Only the best substrate from the methanol studies, 4,6-nicotine-d_2 **9**, was selected for this further testing.

It was found that 4,6-nicotine-d_2 **9** had superior T_1 relaxation times under unactivated conditions in ethanol compared to those in methanol, the 5-pyridyl signal lasting for 37 seconds. However, as observed in other compounds in ethanol in the group[102], the magnetic lifetime of all resonances dropped to only a few seconds upon activation with catalyst and hydrogen (Figure 49).

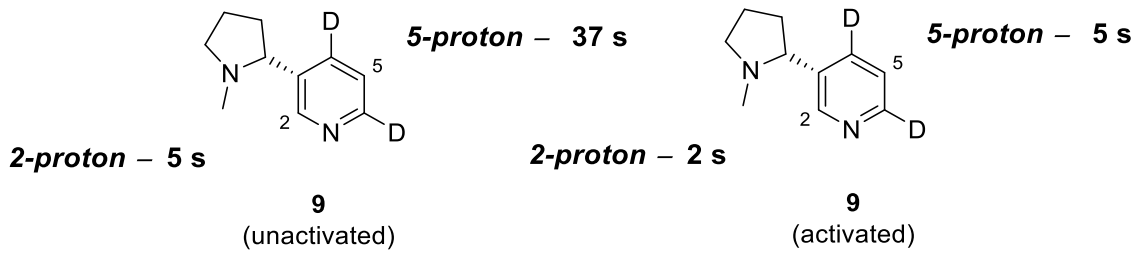

Figure 49: 4,6-nicotine-d_2 *9* T_1 relaxation times under unactivated and activated conditions in ethanol-d_6

The sharply reduced activated T_1 relaxation times in ethanol-d_6 prompted efforts to be focused elsewhere. However, rapid relaxation through the catalyst also implies rapid polarisation. Recent technique advances in biphasic SABRE to sequester the catalyst once polarisation is achieved (thereby slowing relaxation) indicate that further study with ethanol-d_6, water or potentially a mixture of both is warranted.[103]

In conclusion, the variety of (−)-nicotine isotopologues prepared in Chapter 2 were successfully hyperpolarised using SABRE and their proton T_1 relaxation times were shown to be altered significantly by the incorporation of deuterium substituents. High performance was apparently more dependent on the position/pattern of deuteration about the pyridyl ring than merely the number of deuterium substituents incorporated. Noticeable shortening of the T_1 times were observed for substrates in the presence of the SABRE (pre)catalyst and hydrogen compared to substrate free in solution, with the magnitude of this shortening varying significantly with deuteration pattern. 4,6-nicotine-d_2 **9** was identified as the most promising substrate, with greatly superior SABRE signal enhancement and T_1 relaxation times measured.

3.2 Only *Para*-hydrogen Spectroscopy (OPSY)

There was concern that polarisation in (−)-nicotine **1** and its isotopologues might be being 'leaked' through to the pyrrolidine ring protons, thereby reducing the detected signal enhancement of the pyridyl protons. A definite solution to this problem would be to selectively replace all the pyrrolidyl protons with deuterium, however, such a route would present a significant and time-consuming synthetic challenge. Instead, the potential for 'leaking' was investigated by Only *Para*-hydrogen Spectroscopy (OPSY). OPSY is an NMR method that can remove signals derived from nuclei with thermally equilibrated spin state populations whilst leaving signals derived from *para*-hydrogen intact, thereby identifying which nuclei are directly affected by SABRE.[61,104]

OPSY achieves distinction between thermal and hyperpolarised signals via pulsed field gradients (PFGs, an application of spatially-varied magnetic fields), also known as gradient pulses. PFGs interact differently with the distinct spin orders created in multi-pulse experiments – this principle is also used in more common NMR experiments such as HSQC, where ^{12}C isotopomer signals are removed and ^{13}C signals remain.

Figure 50 shows the experimental protocol.[61,104] The substrate is hyperpolarised in a 'shake-and-drop' procedure and subjected to a 90˚ RF pulse, which creates I_z (single spin order term) and $2I_zI_{2z}$ (two spin order term) magnetic states. A subsequent PFG of set intensity and duration defocusses both magnetic states – the extra spin order term in the *para*-hydrogen-derived nuclei mean that this defocussing occurs twice as quickly. After a brief delay (~1.5 μs), a second 90˚ RF pulse is applied, followed immediately by a gradient pulse of double intensity and opposite polarity to the first PFG.

Thermal nuclei = I_z **_Para_-hydrogen-derived nuclei = $2I_zI_{2z}$**

As the *para*-hydrogen derived signals defocuss twice as fast as the thermal signals, they are refocussed by the second, double-intensity gradient pulse into a visible signal. The thermal signals remain unfocussed and hence, unobserved. This sequence is known as a double-quantum (DQ) coherence selection and an OPSY experiment using such a sequence is called OPSY-*d*.

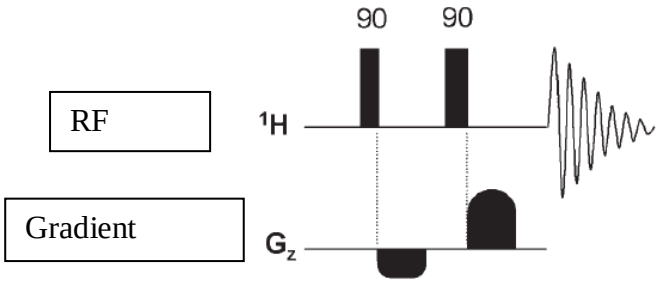

Figure 50: OPSY-*d* experimental protocol. The two rows represent the different pulse types employed, where RF/^{1}H is the standard radio-frequency pulse and G_z is a pulsed field gradient (PFG) in the *z*-axis. The orientation of the two gradient pulses are reversed from one another

There is a variant of OPSY called OPSY-*z* with a similar pulse sequence, known as zero-quantum (ZQ, sometimes also called single-quantum, SQ) coherence selection. The OPSY-*z* pulse sequence is identical to that in OPSY-*d* except that there is no second pulse gradient. The absence of a specific refocussing pulse gradient means this method is susceptible to some thermal signals remaining observable.

(−)-Nicotine **1** was subjected to both OPSY-*d* and OPSY-*z* experiments to probe if polarisation transferred into the pyrrolidine ring from the pyridine component. In both experiments, signals for several of the pyrrolidinyl protons (in the region 3.2 – 1.6 ppm)

were observed, indicating that polarisation in (−)-nicotine **1** does indeed 'leak' to protons on the pyrrolidine ring (Figure 51). Close comparison to the thermal ^{1}H NMR spectrum of (−)-nicotine **1** revealed the signals corresponding to H_g (2.30 ppm) and *N*-methyl protons H_i (2.16 ppm) were not observed in the OPSY experiments, hence these protons were unaffected by hyperpolarisation (Figure 52). Although over half of the protons in the pyrrolidyl ring received some hyperpolarisation, the intensity of their signals was vastly reduced compared to the pyridyl proton signals, barely visible above the baseline. It was therefore concluded that polarisation transfer between the rings was relatively inefficient and the impact of the 'leak' for **1** was at most marginal. It should be emphasised that these spectra give antiphase peaks and are typically recorded in magnitude mode, hence the distortions in line shape observed.

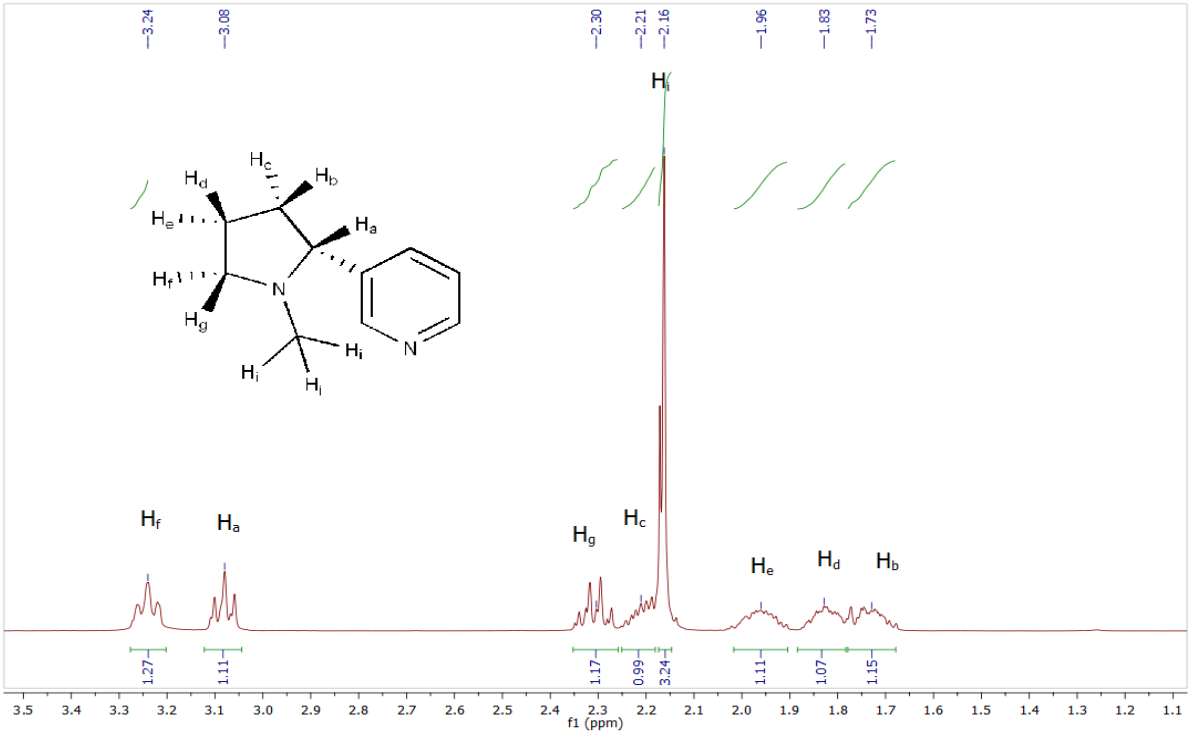

Figure 51: Thermal ^{1}H NMR spectrum of (−)-nicotine *1* for direct comparison to OPSY spectra, focused on the pyrrolidyl proton signals at ~1.5-3.5 ppm

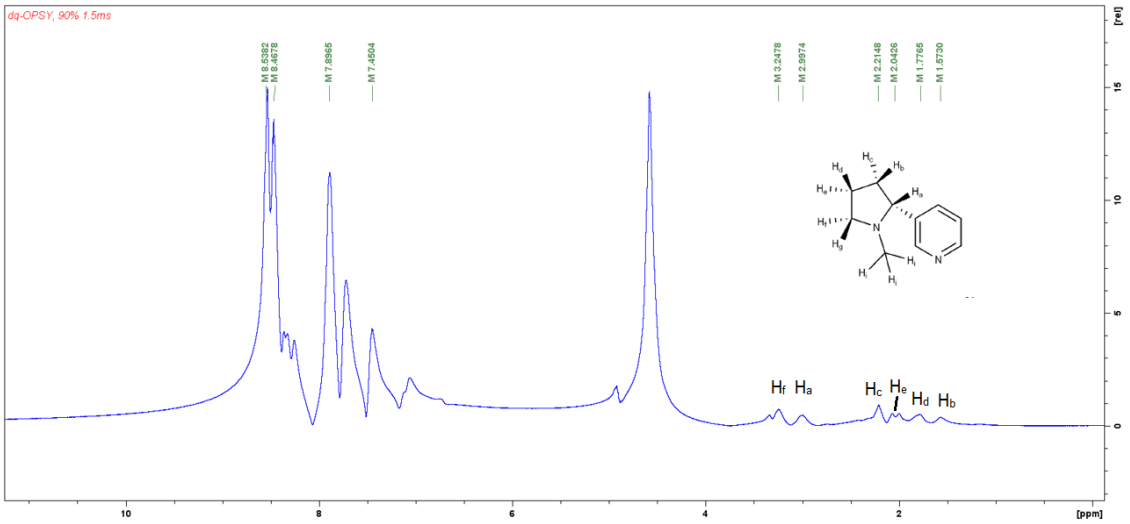

Figure 52: OPSY-*d* of (−)-nicotine *1*. Peaks for some of the pyrrolidyl protons (H_a – H_f) were still observed although their magnitude was far less than that of the pyridyl protons at 7.5-8.5 ppm

3.3 Optimisation overview

Optimising SABRE catalysis is essential for imaging applications. This is in order to give maximum signal for the minimum amount of contrast agent - beneficial for both avoiding metabolic side-effects in the patient and unnecessary costs. Unfortunately, this is not as simple as it may sound.

The performance of the SABRE technique is affected by a number of relatively well-known variables.[50,64,105]

1. **Kinetics** - the rates of exchange of hydrogen and substrate molecules on the catalyst and their relaxation
2. **Magnetic field** – efficient polarisation transfer and the corresponding field (PTF)
3. **Mixing** – the addition of components, their adequate mixing and interaction

Several of these factors are interdependent on one another and are summarised in Figure 53.

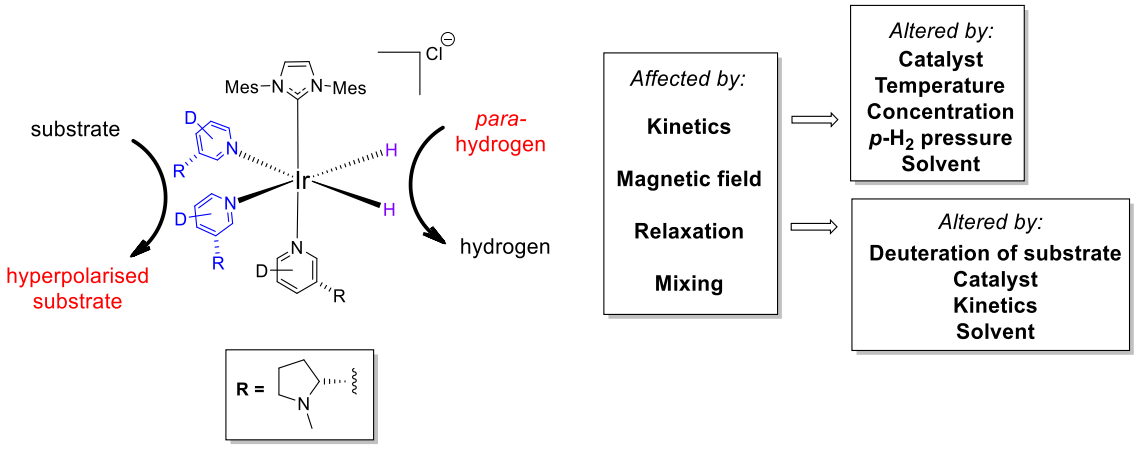

Figure 53: summary of the factors affecting SABRE

The exchange of molecules on the iridium centre are reversible processes and so depend themselves on the ratio of catalyst to substrate, the temperature of the experiment and the pressure of hydrogen. Less well-known variables that have become apparent during this work and corroborated by others are the coupling/relaxation properties of the catalyst and substrate, their interdependencies and the effects they have on the above variables. Solvent can dramatically affect relaxation, exchange of molecules and the solubility of hydrogen – different solvents have not been investigated in detail because of this multitude of potential impacts.

The initial substrate screening in Chapter 3.1 focused on testing a variety of nicotine isotopologues under a fixed set of conditions, evaluated by their signal enhancements and T_1 relaxation times. Such studies reflected efforts to optimise the aforementioned coupling/relaxation properties by identifying the pattern of labelling that gave the best performance. The samples used involved standard solutions of 5 mM solution of IrCl(COD)(IMes) precatalyst **18** with 5 equivalents of the substrate in methanol-d_4. All 'shake-and-drop' SABRE experiments were performed at room temperature with 4 bar of *para*-hydrogen, shaking for 10 seconds in a 65 G polarisation transfer field adjacent to the spectrometer. T_1 experiments always used 4 bar of hydrogen and methanol-d_4 as the solvent (except a small number that used ethanol-d_6 instead).

4,6-nicotine-d_2 **9** was by far the best-performing substrate tested under these original conditions for both signal enhancement and T_1 relaxation times. Hereafter, a series of experiments with varied conditions were run to optimise the performance of **9** further, with similar experiments performed on natural (−)-nicotine **1** for comparison.

3.4 Kinetics optimisation

SABRE kinetics – primarily the exchange of molecules onto and from the catalyst – is one of the key factors in producing optimum signal enhancement. The scheme of SABRE depicted from **III** onwards in Chapter 1.3.2 is a gross simplification - the likely exchange mechanism is a series of equilibria shown in Figure 54.[106] The first step is dissociation of a bound substrate molecule (**A→B**), followed by binding of a 'fresh' molecule of *para*-hydrogen (**B→C**). Subsequent dissociation of the 'old' hydrogen molecule (**C→D**) and binding of a new substrate molecule from solution (**D→E**) complete the process. As a series of equilibria, these kinetic processes are affected by the relative abundances, environment and energy of the species involved, such as variations in concentration or temperature.

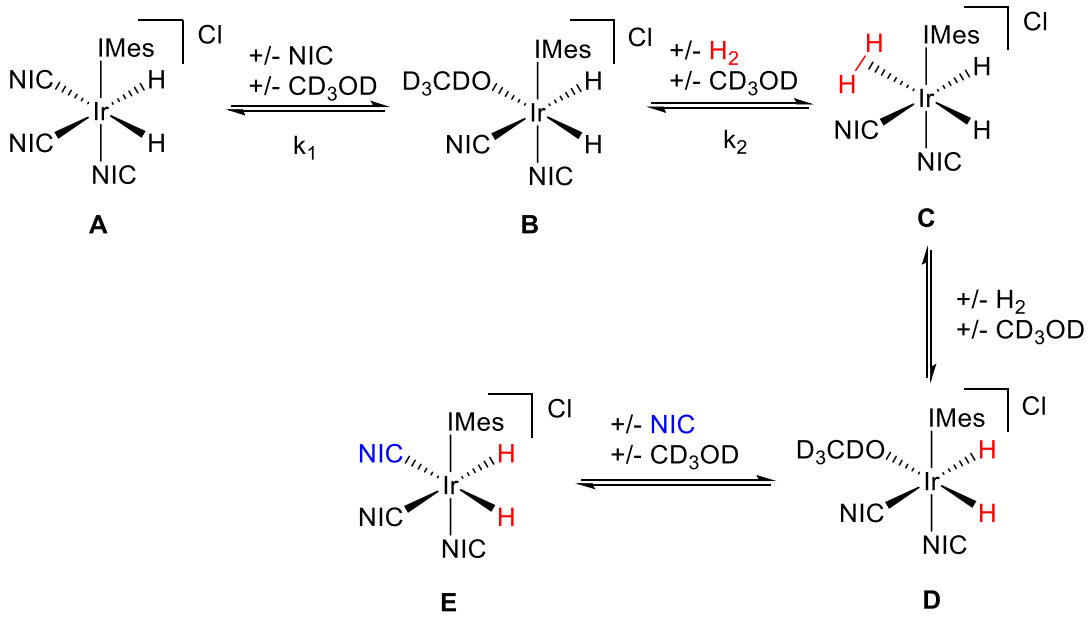

Figure 54: substrate and hydrogen exchange mechanism for $[Ir(H)_2(IMes)(NIC)_3]$ Cl (A) in methanol-d_4. A is the active form of the IMes precatalyst *18*, 'NIC' represents the nicotine substrate molecules bound via their pyridyl nitrogen.

Increased overall exchange of substrate and *para*-hydrogen theoretically means more substrate molecules can be polarised in a given time, referred to as increased *catalyst turnover*. However, this also means that substrate and *para*-hydrogen molecules will spend less time bound to the catalyst and able to transfer polarisation between them, known as reduced *catalyst lifetime*.[105,107]

3.4.1 Alternative SABRE catalysts

A family of SABRE precatalysts have been developed by the Duckett group that are similar to IrCl(COD)(IMes) **18**, differing in their *N*-heterocyclic carbene component by sterics and electronics. Some give a different exchange rate of hydrogen/substrate molecules, some have decreased coupling interactions between catalyst and substrate and some have been designed to do both (Figure 55).

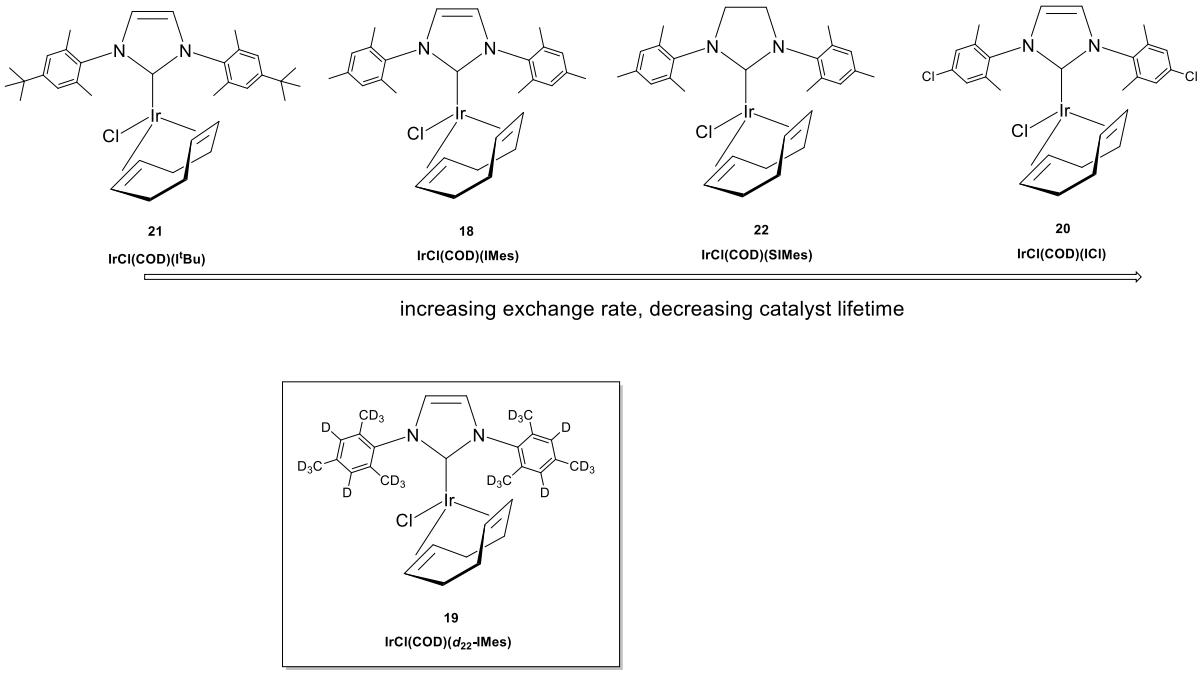

Figure 55: alternative SABRE catalysts in order of increasing typical exchange rates

Because exchange rates will vary between substrates, the catalyst must be tailored to the substrate in question for optimal performance. d_{22}-IMes **19** was the first alternative precatalyst investigated, a deuterated analogue of IMes **18** that has shown excellent signal enhancement and T_1 relaxation performance for other Duckett group members.[65] Preliminary evaluation of the fast-exchanging IMes-derivative ICl **21** and slow-exchanging IMes-derivative I^{t}Bu **20** precatalysts was undertaken.

A series of 'shake-and-drop' experiments were performed on 4,6-nicotine-d_2 **9** with fixed concentrations of precatalysts **19**, **20** or **21** at 5 mM in methanol-d_4 with 25 mM of substrate at 298 K (Figure 56).

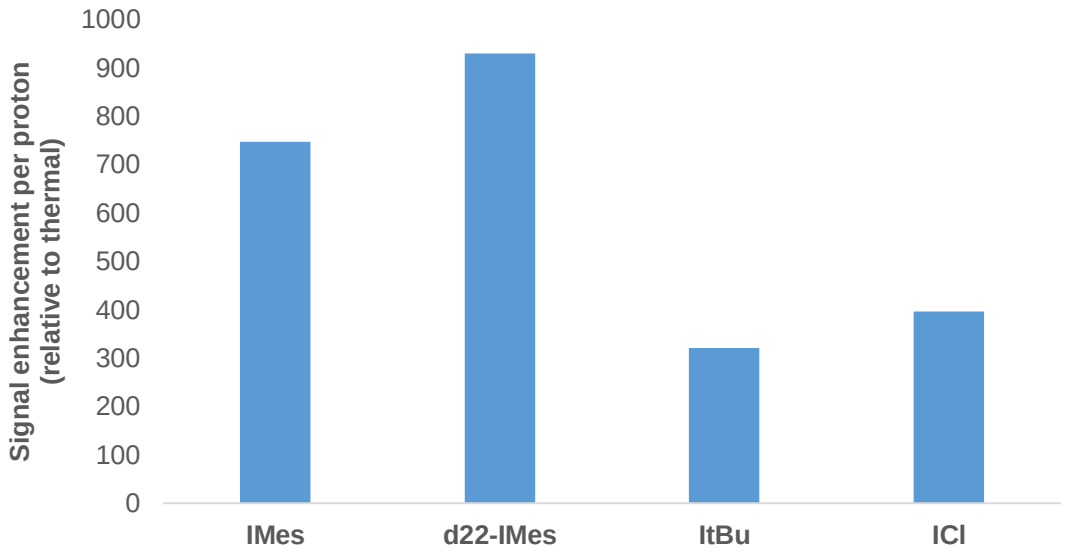

Figure 56: **signal enhancement vs. precatalyst for 'shake-and-drop' experiments on 4,6-nicotine-*d*$_2$ *9*. Conditions and quantities are the standard 5 mM precatalyst, 25 mM substrate in methanol-*d*$_4$ with 4 bar *p*-H$_2$ shaken in a ~65 G stray field for ten seconds**

It was observed that d_{22}-IMes **19** offered noticeably (~25%) improved signal enhancement compared to the undeuterated IMes **18** for the same conditions, at over 900-fold increase compared the thermal signal. Such a large increase was rationalised using similar logic to that applied in Chapter 3.1 – the deuteration of the catalyst carbene should reduce the number of relaxation pathways available through the catalyst, hence slowing the negative impact of relaxation on overall signal enhancement. The slightly increased steric bulk of the carbene relative to IMes **18** was also considered to potentially affect the SABRE process and was later investigated (see Chapter 4).

In contrast, both I^{t}Bu **20** and ICl **21** gave noticeably poor performance compared to their IMes based equivalents, with neither precatalyst giving better than 400-fold signal enhancement. It was surmised that neither of these catalysts have ideal exchange rates at room temperature. Further study with varying temperatures would be needed to optimise their performance, but in the interests of time, it was decided to proceed with the excellent performance of d_{22}-IMes **19**.

3.4.2 Variable-temperature SABRE studies

In a typical complex, exchange of both hydrogen and substrate molecules increases with temperature. The balancing of catalyst turnover and catalyst lifetime combine to give an

optimum temperature for maximum signal enhancement for a given system. Another factor is hydrogen solubility – this is known to decrease in methanol with increasing temperature.[92,108]

The slower exchange rates of nicotines relative to established high-performance SABRE substrates such as methyl nicotinate and pyridine suggested that slow exchange was limiting signal enhancement.[64,109,110] A series of 'shake-and-drop' experiments were performed on (−)-nicotine **1** and 4,6-nicotine-d_2 **9** with increasing temperature to probe this theory (Figure 57). For safety reasons, temperatures above 313 K were not investigated – the NMR tubes currently employed are not rated beyond ~5 bar pressure. Stronger NMR tubes were available, but thicker walls and consequent reduction in tube volume were found to impede SABRE significantly, presumably through inferior mixing properties, reduction in *para*-hydrogen volume or a combination of the two.

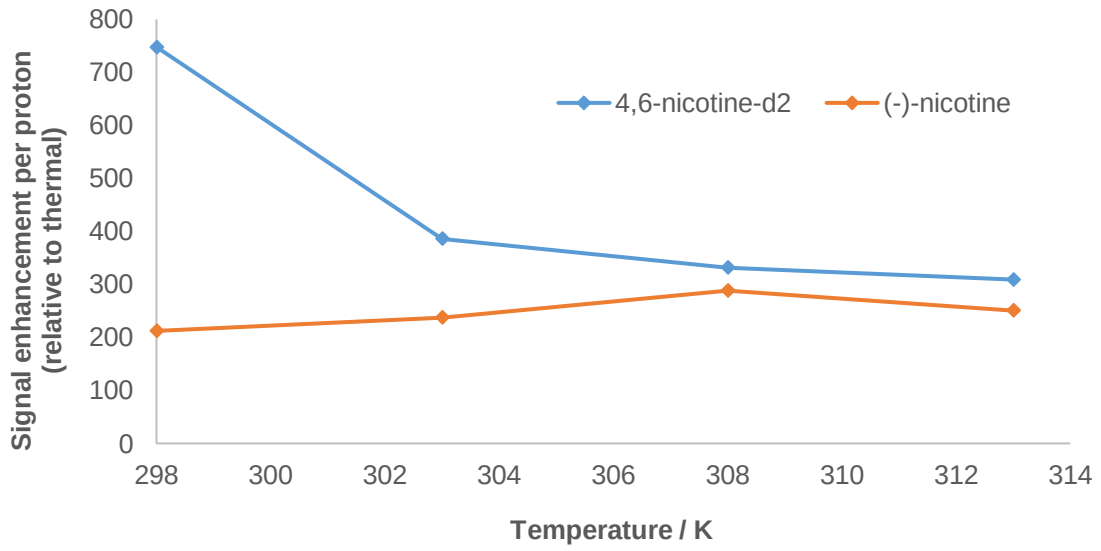

Figure 57: signal enhancement vs. temperature for (−)-nicotine *1* and 4,6-nicotine-d_2 *9*. Samples were the 'standard' concentration of 5 mM IMes precatalyst *18* with 5 equivalents of substrates in methanol-d_4, hyperpolarised in a 'shake-and-drop' protocol with 4 bar para-hydrogen (absolute) a ten second shake in a 65 G field

It was observed that the signal enhancement increased notably with temperature for (−)-nicotine **1**, giving credence to the theory that slow exchange had been a limiting factor thus far. The maximum signal enhancement of ~290-fold per proton was obtained at 308 K – this represents a 36% increase in signal enhancement compared to at 298 K with otherwise identical conditions. The signal enhancement started to fall above 308 K,

suggesting that the exchange rates had become too rapid for efficient polarisation. The decreasing solubility of hydrogen was likely also contributing to this decline in signal enhancement.

However, initial hopes that noticeable increases in SABRE performance could be easily achieved with a simple small increase in temperature were tempered by results for 4,6-nicotine-d_2 **9**. As demonstrated in Chapter 3.1, **9** exhibited vastly superior signal enhancements (~250%) at 298 K compared to the undeuterated **1**, but this superiority was rapidly eroded with even small increases in temperature. Indeed, at 308 K, 4,6-nicotine-d_2 **9** only exhibited a 15% superiority in signal enhancements relative to undeuterated nicotine. Such a sharp decrease strongly suggested other factors being affected by the temperature increases.

As relaxation in SABRE is known to also be affected by the kinetics of exchange, the T_1 relaxation times of (−)-nicotine **1** and 4,6-nicotine-d_2 **9** were measured with varying temperatures and otherwise identical conditions. Figure 58 shows the results for 4,6-nicotine-d_2 **9**.

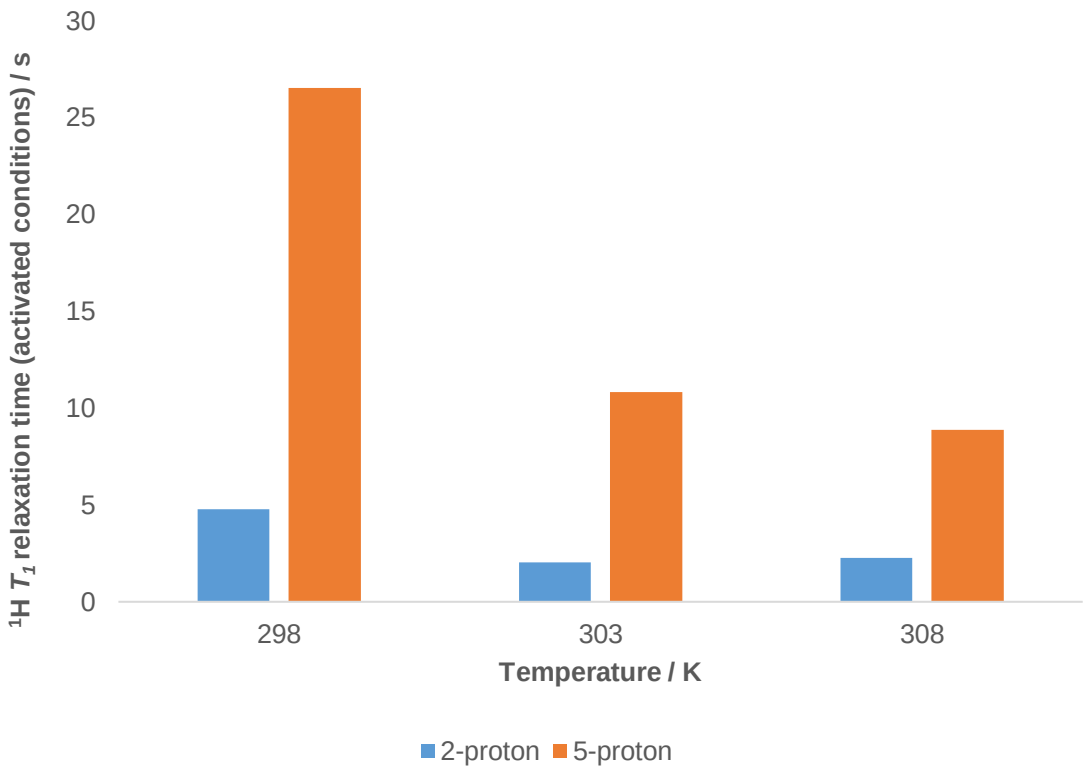

Figure 58: activated conditions proton T_1 relaxation time vs. temperature for 4,6-nicotine-d_2 *9* using precatalyst IMes *18*. Samples were the 'standard' concentration of 5 mM IMes precatalyst *18* with 5 equivalents of substrate in methanol-d_4 activated with 4 bar (absolute) hydrogen

It was observed that increases in temperature resulted in a dramatic shortening of the substrates' T_1 relaxation times - for example the T_1 of 4,6-nicotine-d_2 **9** under the conditions tested fell by approximately 60% with only a 5 K increase in temperature. Such a decrease fits with the markedly reduced enhancements observed in Figure 57, where increased exchange of substrate and hydrogen with increased temperature was leading to faster relaxation (via through bond coupling *etc.*) and hence inferior SABRE performance. Therefore, it was concluded that room temperature (298 K) was the optimal temperature for further studies.

3.4.3 Concentration of substrate vs. concentration of catalyst

There are two aspects to how abundance of catalyst, substrate and the ratio between them affect the exchange process and/or SABRE as a whole. The first aspect is related to catalyst turnover. Theoretically, a low substrate abundance relative to catalyst (i.e. a high catalyst loading) would mean substrate molecules could experience multiple, mutually-reinforcing polarisations in a given time, whereas increased substrate abundance would mean more molecules available to be polarised, although each molecule would be less likely to be repeatedly polarised.

The second aspect relates to the competition between exchange of substrate and exchange of *para*-hydrogen. For example, the rate of change of intermediate **B** in Figure 54 is dependent on concentration of both substrate, affecting rate of conversion back to **A** ($-k_1$), and hydrogen, affecting rate of conversion to **C** (k_2). The result is that increased substrate concentration will inevitably inhibit the exchange of *para*-hydrogen and therefore have a limiting effect on the NMR signal enhancement. Increased pressure of *para*-hydrogen should ameliorate the negative effects of increased substrate concentration on SABRE performance and this is discussed later in Chapter 3.4.4. Finding a 'sweet-spot' between these cases is paramount and every substrate is likely to be different.

Given a *tris*-pyridyl catalyst-substrate complex (**A** in Figure 54), three bound substrate molecules will be on the activated catalyst. Such a complex imposes a practical lower

limit of four equivalents of substrate per catalyst molecule to ensure sufficient substrate free in solution and ready to bind upon bound substrate dissociation (Figure 54, **A→E**). In order to find a 'sweet spot' for sample concentration, a series of 'shake-and-drop' experiments were performed on (−)-nicotine **1** and 4,6-nicotine-d_2 **9** with fixed concentration of IMes precatalyst **18** and increasing substrate equivalents. The results were quantified by the signal enhancements (as in previous studies), by activated-conditions ^{1}H T_1 relaxation times and also by the signal-to-noise ratio (SNR) for each concentration. SNR is, as the name describes, a measure of the absolute signal obtained from a sample compared to the background noise of the instrument and setup. Noise for a given setup is relatively constant, therefore SNR is an important parameter in assessing performance of a substrate.

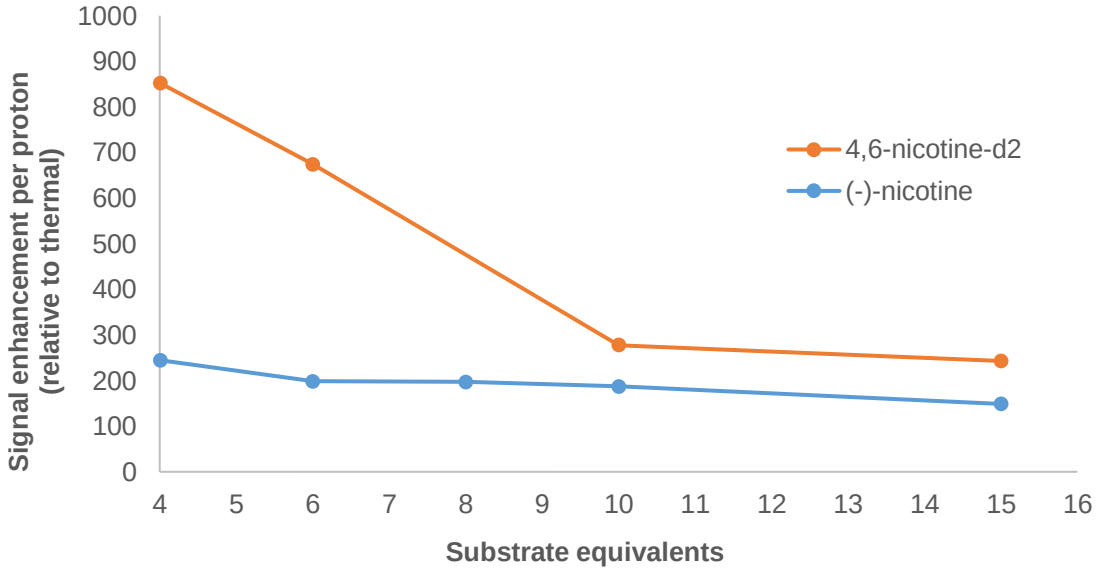

Figure 59: signal enhancement vs. substrate concentration @ 298 K for (−)-nicotine *1* and 4,6-nicotine-d_2 *9* using precatalyst IMes *18*. 'Substrate equivalents' refers to the concentration of substrate relative to the precatalyst. Samples were the 'standard' concentration of 5 mM IMes precatalyst *18* in methanol-d_4, hyperpolarised in a 'shake-and-drop' protocol with 4 bar para-hydrogen (absolute) a ten second shake in a ~65 G stray field at 298 K

It was observed that the signal enhancement was best at a low substrate concentration, decreasing as substrate abundance increased. However, the initially superior signal enhancement performance of 4,6-nicotine-d_2 **9** tails off with increasing substrate concentration far more quickly than (−)-nicotine **1**, so much so that **9** has the same signal enhancement per proton at fifteen equivalents of substrate that **1** had at five. This can be further rationalised by the differing T_1 relaxation networks found in each substrate/catalyst combination, essentially a reverse of the polarisation pathways described later in Chapter 3.5 and depicted in Figure 60.

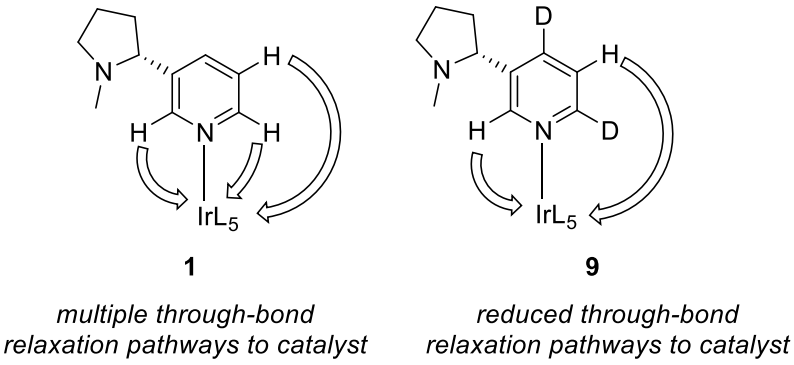

Figure 60: potential through-bond couplings from substrate to catalyst as relaxation pathways for (−)-nicotine *1* and 4,6-nicotine-d_2 *9*

Another factor to consider is the limited supply of *para*-hydrogen in the sample tube. The sharp decrease in 4,6-nicotine-d_2 **9** performance with increasing substrate concentration can be explained by *para*-hydrogen becoming limiting. The effect is less pronounced for the less efficiently-polarised (−)-nicotine **1**.

These theories can be backed up empirically by measurement of ^{1}H T_1 times across a range of concentrations under the same conditions, the results of which are displayed in Figures 61 and 62.

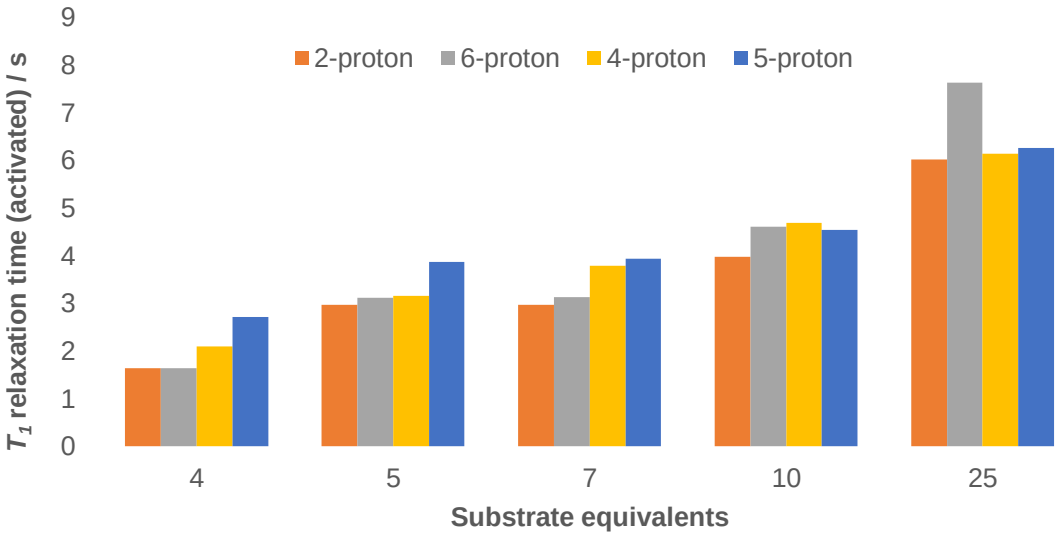

Figure 61: activated conditions proton T_1 relaxation time vs. substrate concentration @ 298 K for (−)-nicotine *1* using precatalyst IMes *18*. 'Substrate equivalents' refers to the concentration of substrate relative to the precatalyst. Samples were the 'standard' concentration of 5 mM IMes precatalyst *18* in methanol-d_4 activated with 4 bar (absolute) hydrogen at 298 K

The T_1 relaxation times of (−)-nicotine **1** did indeed increase with increasing substrate concentration, reinforcing the theory that interactions with the catalyst are the dominant relaxation pathway for that substrate. Despite longest T_1 time of only eight seconds, such an increasing trend suggested promise for imaging applications, where experiments are typically run with relatively high substrate equivalents. Sequestration of the catalyst after polarisation would likely improve this T_1 further.

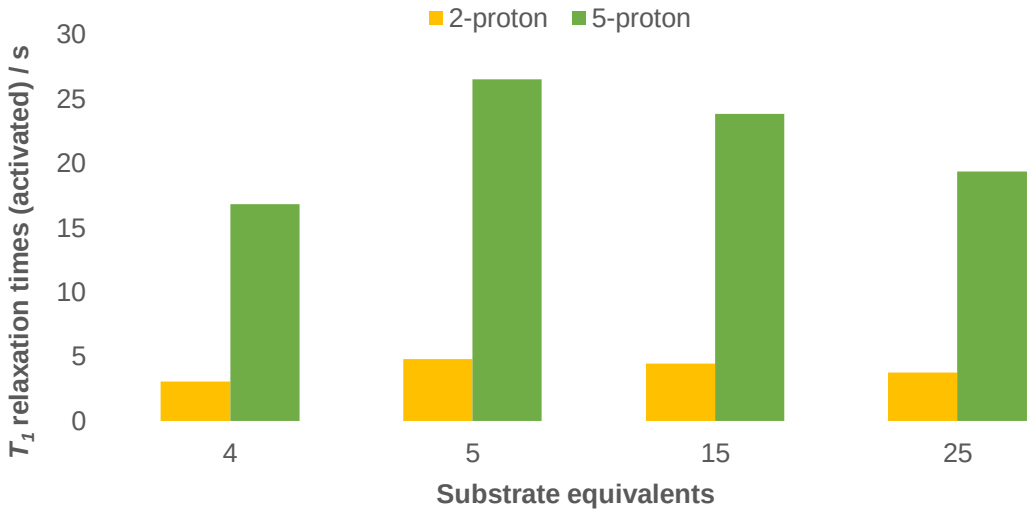

Figure 62: activated conditions proton T_1 relaxation time vs. substrate concentration @ 298 K for 4,6-nicotine-d_2 *9* using precatalyst IMes *18*. 'Substrate equivalents' refers to the concentration of substrate relative to the precatalyst. Samples were the 'standard' concentration of 5 mM IMes precatalyst *18* in methanol-d_4 activated with 4 bar (absolute) hydrogen at 298 K

T_1 relaxation times for 4,6-nicotine-d_2 **9** were noticeably shortened at four equivalents of substrate, where approximately three-quarters of all substrate molecules are bound at any given time and therefore can relax extensively through the catalyst regardless of relaxation pathways. However, the markedly *reduced* enhancement at five equivalents despite the significantly improved T_1 relaxation times reinforces the notion that *para*-hydrogen is limiting for 4,6-nicotine-d_2 **9**.

The SINO function in Bruker TopSpin was used to compare signal intensity to background noise to give the SNR (Figure 63).

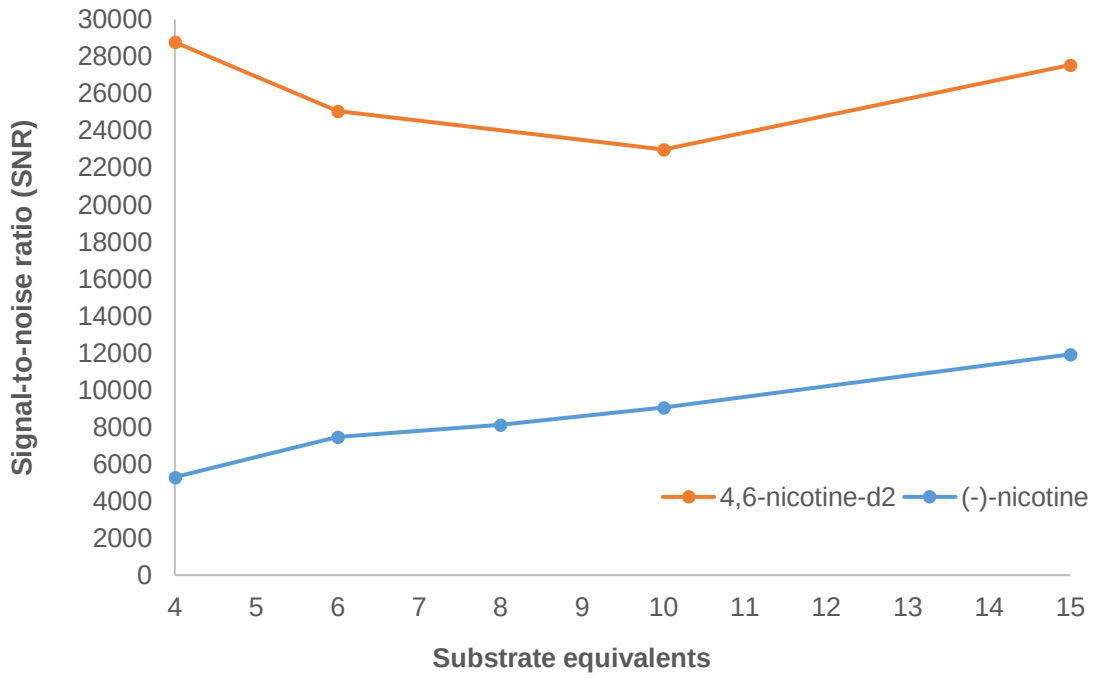

Figure 63: signal-to-noise ratio vs. substrate concentration @ 298 K for (−)-nicotine *1* and 4,6-nicotine-d_2 *9* using precatalyst *18*. 'Substrate equivalents' refers to the concentration of substrate relative to the precatalyst. Samples were the 'standard' concentration of 5 mM IMes precatalyst *18* in methanol-d_4, hyperpolarised in a 'shake-and-drop' protocol with 4 bar para-hydrogen (absolute) a ten second shake in a ~65 G stray field at 298 K

The signal-to-noise ratio for both substrates generally increases with in line with the quantity of substrate. This positive correlation fits with the theory that at higher substrate concentration, each individual molecule is polarised less (i.e. poor signal enhancement), but far more molecules are being polarised and a greater total signal results (increased SNR).

The SNR of 4,6-nicotine-d_2 **9** is far superior to that of (−)-nicotine **1** at all concentrations tested, although it shows a trend of initially decreasing SNR with increasing substrate before increasing again above ~ 10 equivalents. This is likely related to the initially sharply decreasing signal enhancement that **9** exhibits as described previously.

Overall, it was concluded that superior enhancements were obtained with very low substrate concentration, but the best absolute signal was obtained at higher substrate concentrations. Further tests at even higher substrate concentration would be ideal to further confirm this observation. Whichever of these factors is most important depends

on requirements, but absolute signal would be more desirable in a diagnostic imaging experiment such as MRI.

Owing to the superior performance of 4,6-nicotine-d_2 **9** and the theorised reduction in relaxation pathways, it was decided to repeat the studies of varying substrate concentration with d_{22}-IMes **19** (Figure 64).

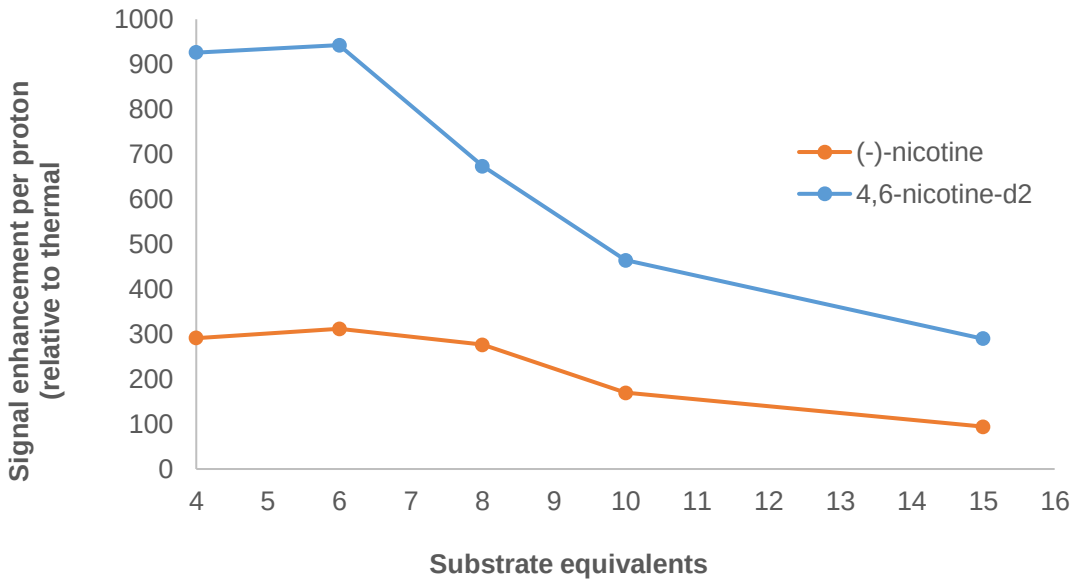

Figure 64*:* signal enhancement vs. substrate concentration @ 298 K for (−)-nicotine *1* and 4,6-nicotine-d_2 *9* using precatalyst d_{22}-IMes *19*. 'Substrate equivalents' refers to the concentration of substrate relative to the precatalyst. Samples were the 'standard' concentration of 5 mM d_{22}-IMes precatalyst *19* in methanol-d_4, hyperpolarised in a 'shake-and-drop' protocol with 4 bar para-hydrogen (absolute) a ten second shake in a ~65 G stray field at 298 K

The use of d_{22}-IMes **19** as precatalyst afforded noticeably improved enhancement levels for all concentrations tested compared to the equivalent studies with IMes **18**. In addition, 4,6-nicotine-d_2 **9** displayed superior enhancements compared to (−)-nicotine **1** at all substrate concentrations tested with d_{22}-IMes **19**. Although this superiority is eroded somewhat between six and ten equivalents of substrate, the deuterated nicotine **9** has between 140 and 220% better signal enhancement than (−)-nicotine **1**, in contrast to the IMes **18** concentration studies where the two substrates' performance was nigh indistinguishable for fifteen equivalents of substrate.

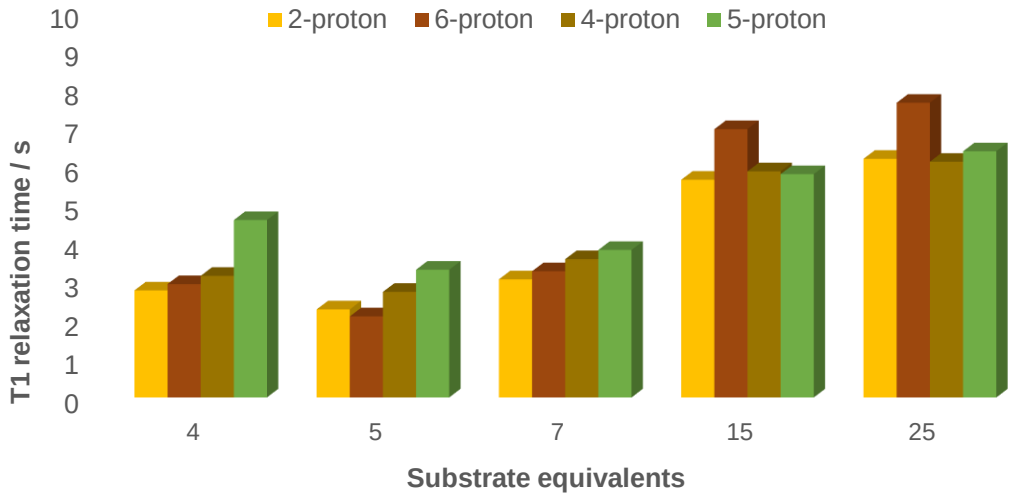

Figure 65: Activated conditions proton T_1 relaxation time vs. substrate concentration @ 298 K for (−)-nicotine *1* using precatalyst d_{22}-IMes *19*. 'Substrate equivalents' refers to the concentration of substrate relative to the precatalyst. Samples were the 'standard' concentration of 5 mM d_{22}-IMes precatalyst *19* in methanol-d_4 activated with 4 bar (absolute) hydrogen at 298 K

The trend of increasing T_1 relaxation time with increasing substrate concentration observed for (−)-nicotine **1** with IMes **18** is also observed for d_{22}-IMes **19**, with the T_1 times increasing from around two-three seconds at 4-5 equivalents of substrate to over seven seconds at fifteen equivalents and higher. The T_1 relaxation times observed were on average 67% improved upon their equivalents with IMes **18** at four equivalents, falling to on average 36% at fifteen equivalents (Figure 66). Deuteration on the catalyst clearly slows relaxation while bound, which in turn boosts the enhancement.

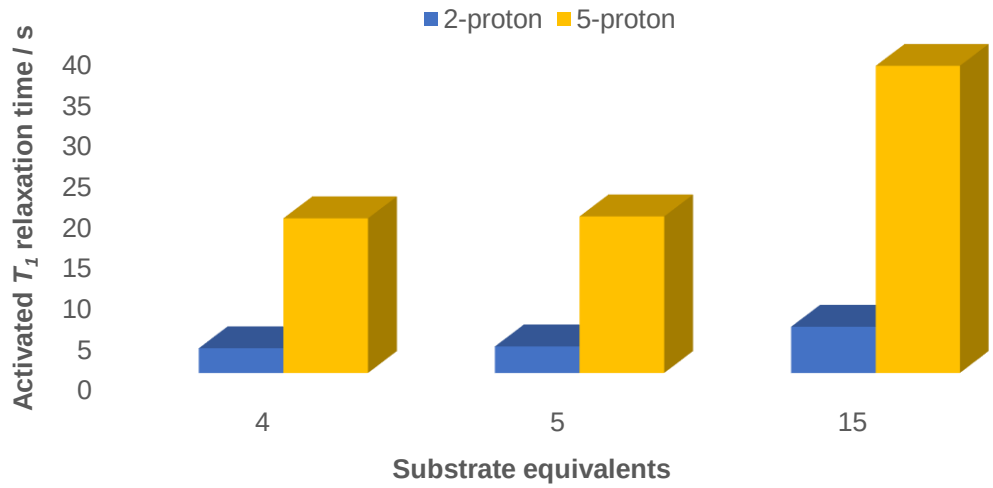

Figure 66: activated-conditions proton T_1 relaxation time vs. substrate concentration @ 298 K for 4,6-nicotine-d_2 *9* using precatalyst d_{22}-IMes *19*. 'Substrate equivalents' refers to the concentration of substrate relative to the precatalyst. Samples were the 'standard' concentration of 5 mM d_{22}-IMes precatalyst *19* in methanol-d_4 activated with 4 bar (absolute) hydrogen at 298 K

The effect on T_1 relaxation times is far clearer when 4,6-nicotine-d_2 **9** with d_{22}-IMes **19** at higher substrate concentrations is considered. For a 15-equivalent loading, the high-performing 5-proton activated conditions T_1 time is a full thirteen seconds longer than with IMes, a 52% increase. Therefore, a combination of a deuterated catalyst and deuterated substrate is ideal.

Signal-to-noise ratios observed with d_{22}-IMes **19** were also consistently superior at almost all concentrations to the corresponding studies with IMes **18** for both substrates tested. 4,6-nicotine-d_2 **9** reached an SNR of over 40,000 at higher substrate excesses with this precatalyst. At higher substrate excesses, the signal-to-noise ratio of **9** started to plateau. At even higher loadings, a fall in SNR was reported (Figure 67). This is due to the suppression of hydrogen exchange at higher substrate concentrations because of the competition for the same reaction intermediate. Furthermore, there will be an impact on the total amount of hydrogen present, which will lead to a further reduction in signal gain.

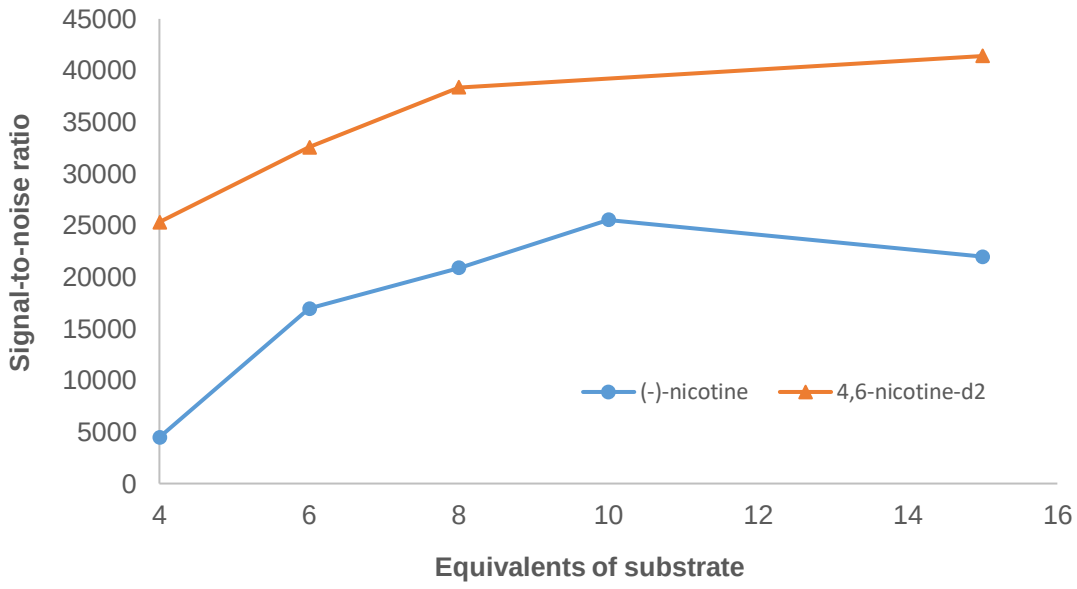

Figure 67: signal-to-noise ratio vs. substrate concentration @ 298 K for (−)-nicotine *1* and 4,6-nicotine-d_2 *9* using precatalyst d_{22}-IMes *19*. 'Substrate equivalents' refers to the concentration of substrate relative to the precatalyst. Samples were the 'standard' concentration of 5 mM IMes precatalyst *19* in methanol-d_4, hyperpolarised in a 'shake-and-drop' protocol with 4 bar para-hydrogen (absolute) a ten second shake in a ~65 G stray field at 298 K

The apparent discrepancy that exists between the results for 4,6-nicotine-d_2 **9** with the two precatalysts at 4 equivalents of substrate is due to the effects of line width. The SINO function used to calculate SNR compares signal intensity of peaks with the intensity of a

designated ‘noise region’. However, this does not take peak signal integration into account – hence broader signals will give lower calculated SNR than sharper peaks even if their integrations and therefore the actual ‘size’ of the two are similar (Figure 68). ‘Shake-and-drop’ experiments are run with the spectrometer deuterium lock turned off, which tends to give increasingly broad NMR spectrum peaks with repeated iterations. Therefore, a relatively large margin of error is inevitable in SNR data. Nonetheless, clear trends can still be observed.

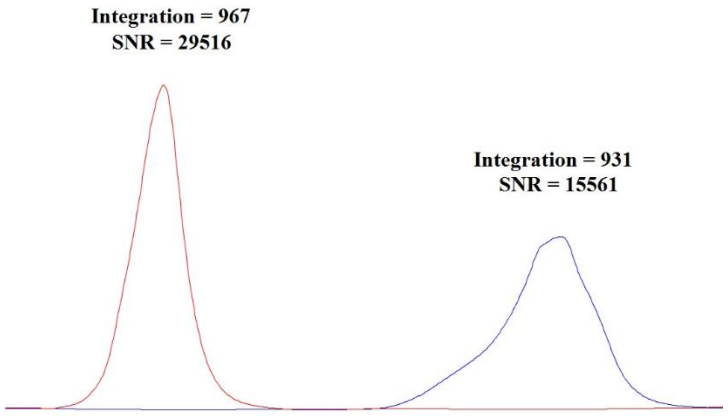

Figure 68: comparison of signal-to-noise ratio calculations using the SINO function for different iterations of the same ‘shake-and-drop’ experiment.

3.4.4 Variable-pressure SABRE studies

As alluded to in Chapter 3.3, the SABRE exchange process involves a series of equilibria that will be affected by the concentration of reactants (hydrogen, substrate, catalyst) present. Increasing the concentration of substrate competitively and negatively affects the addition of 'fresh' *para*-hydrogen onto the catalyst (**B→C** in Figure 69), thereby limiting the rate at which substrate can be hyperpolarised and reducing signal enhancement.

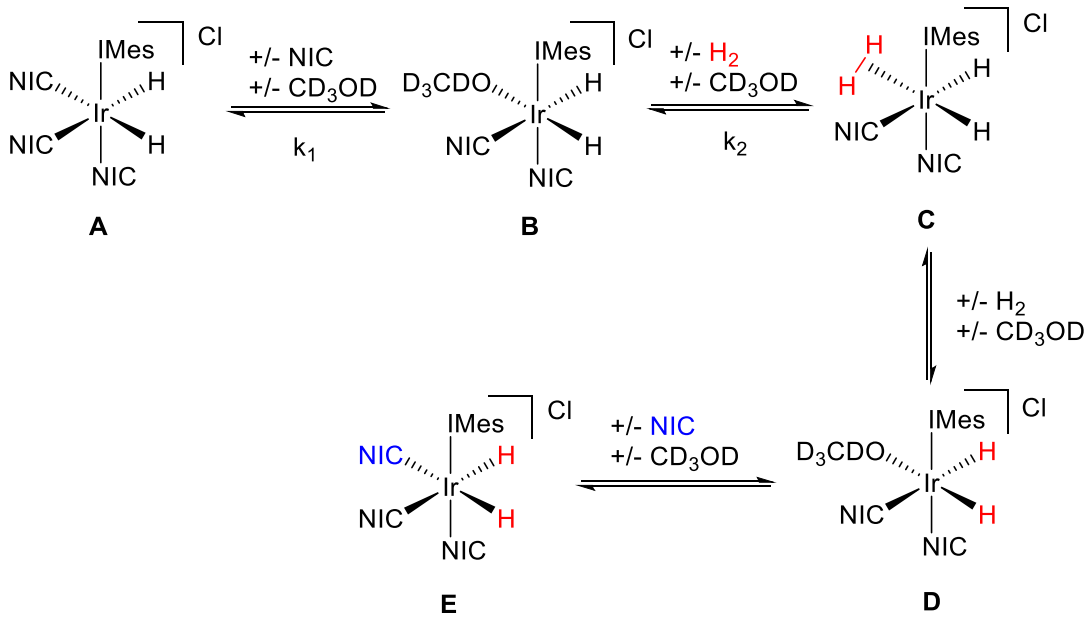

Figure 69 (repeat of Figure 54): substrate and hydrogen exchange mechanism for [Ir(H)$_2$(IMes)(NIC)$_3$] Cl (A) in methanol-*d*$_4$. A is the active form of the IMes precatalyst *18*, 'NIC' represents the nicotine substrate molecules bound via their pyridyl nitrogen

To probe amelioration of this effect, a series of 'shake-and-drop' experiments were run on (−)-nicotine **1** and 4,6-nicotine-*d*$_2$ **9** where the *para*-hydrogen pressure was increased from the 'standard' 4 bar absolute up to 6 bar absolute (Figure 70). Higher pressures were not investigated for similar reasons to high temperatures in Chapter 3.4.2 – the standard NMR tubes available are only rated to 5 bar pressure relative to the environment (i.e. ~6 bar absolute pressure).

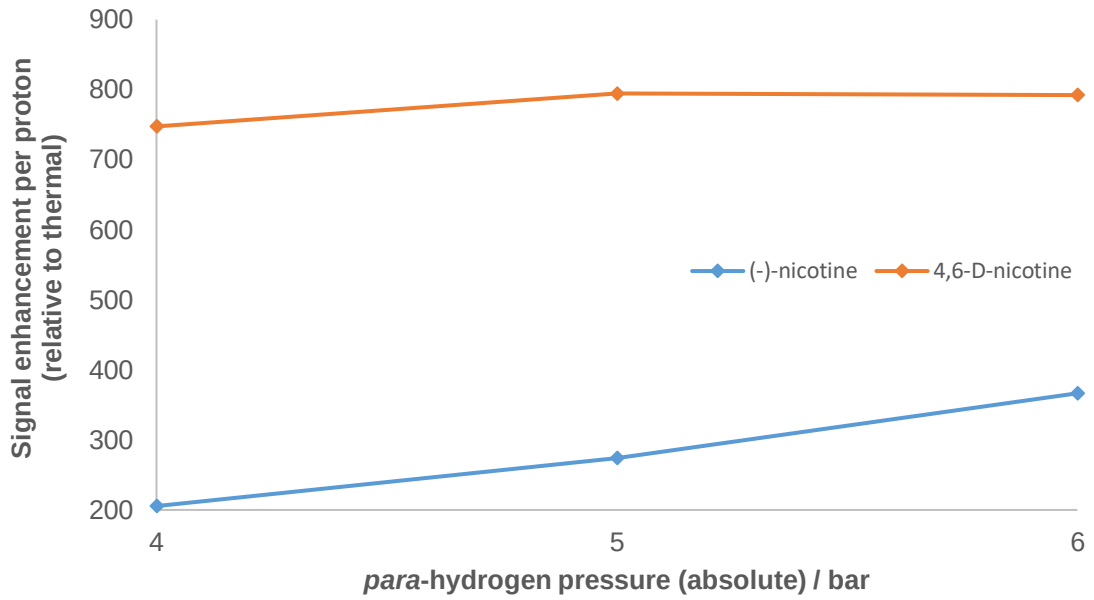

Figure 70: signal enhancement vs. para-hydrogen pressure for (−)-nicotine *1* and 4,6-nicotine-d_2 *9*. Samples were the 'standard' concentration of 5 mM IMes precatalyst *18* with 5 equivalents of substrates in methanol-d_4, hyperpolarised in a 'shake-and-drop' protocol with a ten second shake in a ~65 G stray field at 298 K

It was observed that the signal enhancement of (−)-nicotine **1** was substantially and disproportionately enhanced by increasing *para*-hydrogen pressure. The ~370-fold enhancement per proton observed for **1** at 6 bar *para*-hydrogen represented a 78% increase in enhancement for a 50% increase in hydrogen pressure. However, when the study was repeated with 4,6-nicotine-d_2 **9**, only a marginal increase of up to ~7% was observed with increased pressure. Given the typical margin of error for 'shake-and-drop' experiments of 2-3%, the 7% performance boost obtained for **9** is not statistically significant. Hence, we can conclude in one case relaxation is limiting, while in the second *para*-hydrogen is limiting. This observation matches expectations based on efficiency of transfer.

3.5 Polarisation transfer optimisation

3.5.1 Varied PTF

Polarisation transfer between the *para*-hydrogen (specifically the two derived hydrides on the iridium) and the substrate occurs via long-range ^4J scalar coupling to a proton, specifically one situated *ortho* to the Ir-N bond.[94,96,97] It had been previously shown that the magnitude of this ^4J coupling is not the key factor in obtaining good polarisation

transfer. Instead, ideal polarisation transfer is achieved when the chemical shift difference between the hydrides and the substrate nuclei – hereafter referred to as $\Delta\delta_{HH}$ – matches the ^{2}J coupling between said hydrides.[1] As chemical shift is dependent on magnetic field – the Zeeman effect – and scalar coupling is not, there will be an optimum field strength for optimum polarisation transfer.

Magnetic environments that are considered 'high field' are not appropriate for polarisation transfer, such as 94,000 G found inside a 400 MHz NMR spectrometer. At such a field, the $\Delta\delta_{HH}$ of ~30 ppm typical of substrates produced in this project is equivalent to ~12,000 Hz, vastly different to the 5-10 Hz estimate of the $^{2}J_{HH}$ coupling it needs to match to facilitate efficient transfer of polarisation.[19] $\Delta\delta_{HH}$ is reduced to ~8 Hz at only 65 G, which is why such a PTF has been used as a standard in the project thus far. All substrate/catalyst combinations are different, however, and it was speculated that there may be a PTF different to 65 G that gives superior SABRE performance for nicotine isotopologues. To confirm whether this was or was not the case, a series of experiments were run on (−)-nicotine **1** and 4,6-nicotine-d_2 **9** using the automated flow setup detailed in Chapter 6, with standard concentration samples (5 mM IMes precatalyst, 25 mM substrate in methanol-d_4). The results are shown in Figure 71 below.

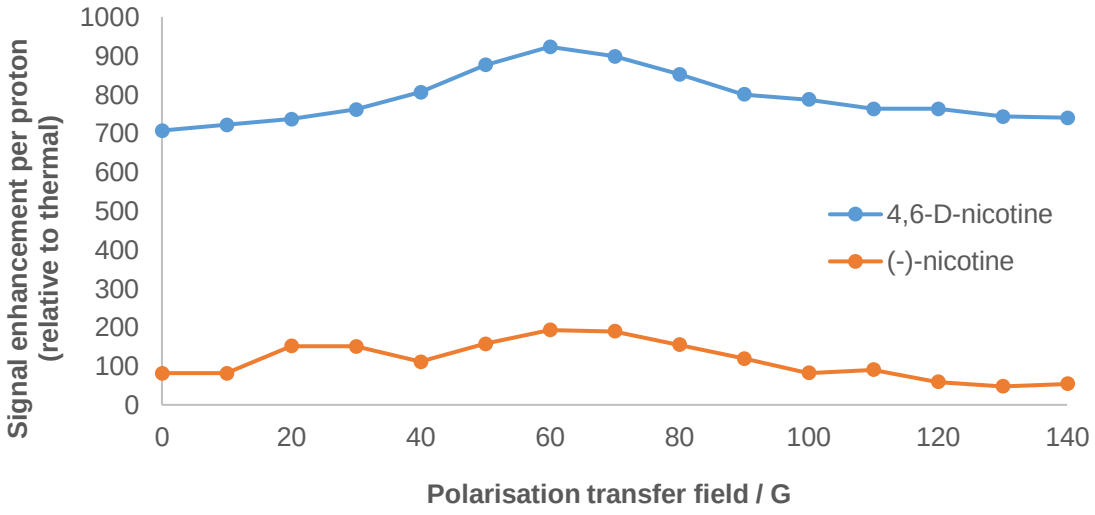

Figure 71: Signal enhancement vs. polarisation transfer field for (−)-nicotine *1* and 4,6-nicotine-d_2 *9* using the automated flow setup. Samples were the 'standard' concentration of 5 mM IMes precatalyst *18* and 25 mM substrate in methanol-d_4, hyperpolarised by bubbling with 4 bar para-hydrogen (absolute) for ten seconds at 298 K

It was observed that 60-70 G was the best field strength for polarisation transfer under these conditions for both substrates tested, consistent with expectations from theory and literature.[94,96,97] The maximum magnitude of the signal enhancement observed was different for both substrates compared to their 'shake-and-drop' equivalents. The peak enhancement for 4,6-nicotine-d_2 **9** was noticeably superior at ~930-fold enhancement per proton (versus ~750-fold for 'shake-and-drop') although the peak enhancement for (−)-nicotine **1** was marginally worse at ~190-fold enhancement per proton (versus ~205-fold for 'shake-and-drop'). The improvements observed for **9** were attributed to a more homogenous transfer field and more thorough and consistent mixing of the substrate, catalyst and hydrogen in the flow setup compared to that possible in a 'shake-and-drop' experiment. It was concluded that a lack of similar improvement for (−)-nicotine **1** with the flow setup was due to that substrate's short T_1 relaxation times suppressing any gains that might be made, as the transfer time into the spectrometer is longer than in a 'shake-and-drop' (see Chapter 6 for experimental methods).

Regarding the shape of the curves, whilst that of 4,6-nicotine-d_2 **9** showed a simple maximum at ~65 G, (−)-nicotine **1** had a more complicated relationship between PTF and enhancement. Three maxima are observed at ~25, ~65 and ~110 G. This observation can be rationalised with polarisation transfers to several protons on the pyridyl ring with different chemical shift, such as inequivalent *ortho* protons via ^4J couplings or *meta* protons via ^5J couplings, shown in Figure 72.[111] As established previously, the magnitude of these couplings does not affect polarisation transfer, hence it is the varying $\Delta\delta_{HH}$ that gives a different optimal PTF for each proton. The multiple maxima phenomenon was not seen for 4,6-nicotine-d_2 **9** as it only has a single *ortho* proton for ^4J coupling to the hydride. However, as ^5J transfer to the *meta* proton was firmly established as viable, it is believed this coupling is also maximised at ~65 G given the single maximum observed.

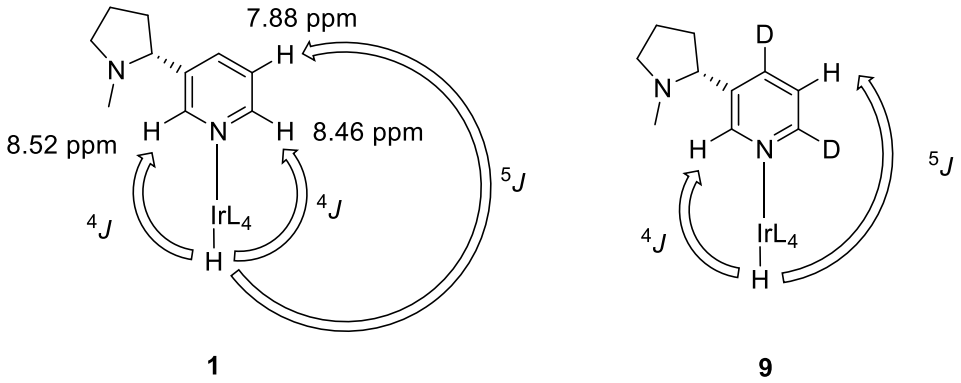

Figure 72: Different possible polarisation transfers from catalyst hydrides to (-)-nicotine *1* and 4,6-nicotine-d_2 *9*. 'IrL$_4$' represents the rest of an activated SABRE precatalyst of the IMes *18* form where the ligands 'L' are the other hydride, two other substrate molecules and the carbene.

3.5.2 Varied shake/bubble time

Hyperpolarisation of the substrate only occurs when unreacted *para*-hydrogen and substrate interact on and exchange with the iridium catalyst in the polarisation transfer field. The poor solubility of gaseous hydrogen in most applicable solvents means it requires vigorous physical mixing to maintain a supply of 'fresh' *para*-hydrogen and maintain the polarisation process.[92,108] Mixing was achieved by shaking the reactants in an NMR tube in the case of 'shake-and-drop' experiments and by bubbling *para*-hydrogen through the reaction vessel in the automated flow setup.

The hyperpolarisation process can continue indefinitely until all available *para*-hydrogen is used up and only hydrogen remains – this difficult to probe using a 'shake-and-drop' setup on account of the limited tube volume, however the automated flow setup has an effectively unlimited supply of *para*-hydrogen to bubble. Overarching these factors is the inevitable relaxation of hyperpolarised material, meaning there should be a practical maximum for shake/bubble time after which no appreciable further increase in polarisation can be achieved.

To this end, a series of SABRE experiments were run on (-)-nicotine **1** and 4,6-nicotine-d_2 **9** using the automated flow setup with standard concentration samples (5 mM IMes **18** precatalyst, 25 mM substrate in methanol-d_4) and identical parameters save for varied bubble time. The results are shown in Figure 73.

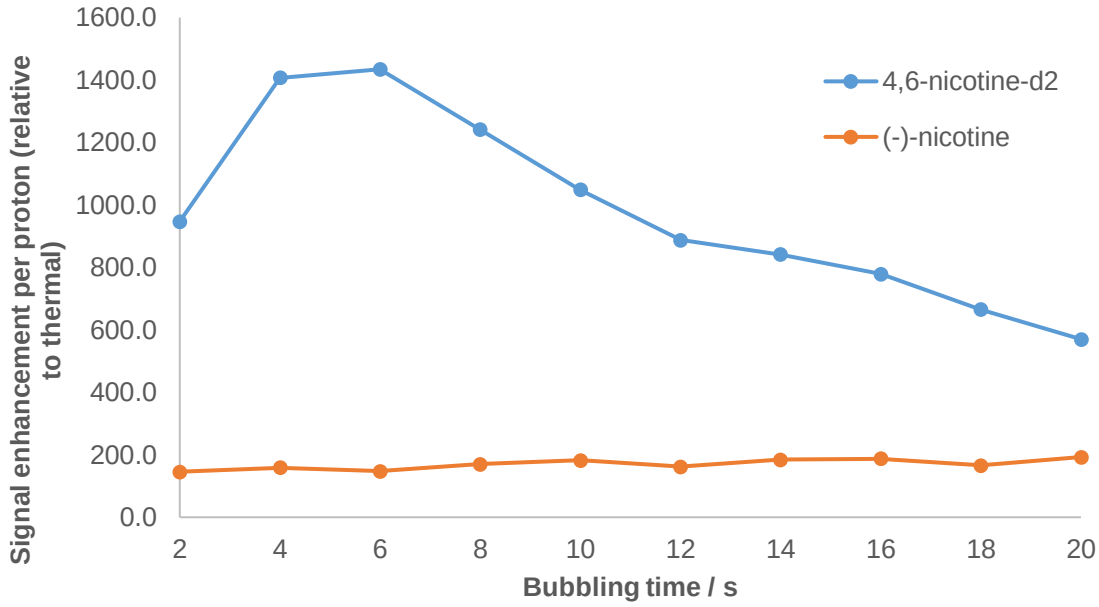

Figure 73: Signal enhancement vs. bubble time for (-)-nicotine *1* and 4,6-nicotine-d_2 *9* using the automated flow setup. Samples were the 'standard' concentration of 5 mM IMes precatalyst *18* and 25 mM substrate in methanol-d_4, hyperpolarised by bubbling with 4 bar para-hydrogen (absolute) in a 65 G field at 298 K

The overall relationship between bubble time and signal enhancement was not as clear as for the polarisation transfer field data. For (−)-nicotine **1**, the bubble/shake time results rapidly plateau within experimental error. In contrast, the results with 4,6-nicotine-d_2 **9** were superior at all bubbling times – there is an initial rapid rise in signal enhancement followed by a fall. **9** exhibited a far more definitive series of results, with a maximum signal enhancement per proton of ~1400x the thermal signal observed between just 4 and 6 seconds bubbling time. This peak enhancement was a huge ~35% increase over the previously employed 10 second bubble/shake time, suggesting relaxation of the signal at longer bubble/shake times was more important for overall performance than the benefits of repeated polarisations were. This clearly also reflects the idea that *para*-hydrogen is no longer limiting. At longer bubbling times, the falloff is known and suggests *para*-hydrogen has again become limiting.

3.6 Mixing optimisation

The efficient transfer of polarisation from *para*-hydrogen in gaseous form to an appropriate substrate in solution via a catalyst necessitates that all these elements may interact and exchange with each other freely. Therefore, thorough mixing of such components is crucial for high-performance in SABRE.

The standard 'shake-and-drop' experiments detailed thus far involved physically shaking a sealed Young's tap NMR tube in a specific part of an NMR spectrometer's stray magnetic field to mix the components and transfer polarisation between them. However, being forced to manually shake the tube meant consistent, thorough mixing was difficult and tiring to achieve, particularly with the constraint of needing to shake in the same place for a specific polarisation transfer field (PTF). The spectrometer stray field is by no means homogenous, with noticeable differences (20-30 G or higher) in field strength being observed by moving only a few centimetres in space. It was realised early in the project that it was very unlikely a shaken tube was experiencing the desired magnetic field throughout more than part of its shake. Results in Chapter 3.5.1 confirmed that varying PTF had a significant impact on SABRE performance, hence changes in field throughout the shake were highly undesirable. It was therefore concluded that a system with more vigorous shaking and a more consistent field strength would be needed for peak performance.

The automated flow setup used in Chapter 3.5 has a much more homogenous magnetic field than that surrounding a spectrometer, but the setup was deemed too slow and awkward to use as an everyday tool for assessing SABRE performance of a wide variety of samples and conditions. In particular, the setup has almost no capacity for varying temperatures or gas pressures. Instead, a new piece of technology was perfected in the closing stages of the project – the magnetic shaker assembly (Figure 74). The assembly consists of a secure but easily-accessible housing for an NMR tube and spectrometer spinner, so that the contents can be removed quickly. The tube housing is surrounded by a stack of ring-shaped permanent magnets arranged to give a near-homogenous field of a specific strength – a range of shakers with different magnet arrangements give different desired fields. The assembly is used in the same manner as a conventional 'shake and drop' – the tube is shaken in the housing for the desired time, then removed and immediately placed in a spectrometer for measurement. A homogenous field strength

inside the shaker means there is no restriction on where it can be shaken, therefore there is no restriction on how vigorous the shaking is either, thereby eliminating two serious flaws with the original protocol.

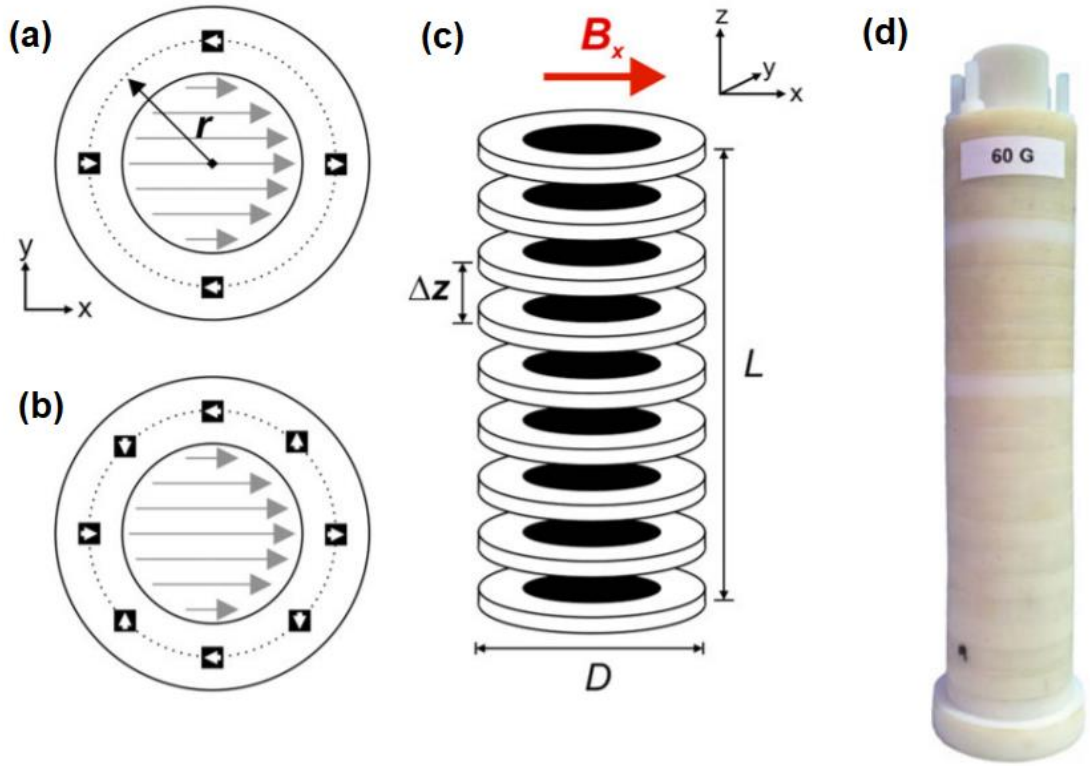

Figure 74: **Schematic and photographic representation of the SABRE magnetic shaker. Individual rings are composed of** (a) **4 or** (b) **8 solid-state magnets arranged at fixed distance *r* from the centre of the ring, oriented into a Halbach configuration to generate a homogeneous field along the *x*-axis in the centre.** (c) **shows rings combined with uniform spacing Δ*z* to form a cylinder of length *L* with an outer diameter of *D*, shown photographically in** (d)**. An NMR tube sitting in the centre of the cylinder will experience a net magnetic field B_x transverse to the long (*z*) axis of the cylinder. Adapted from Richardson *et al.*, 2018**[112]

A brief series of 'shake-and-drop' experiments were run on 4,6-nicotine-d_2 **9** to test the improved shaker setup (Figure 75).

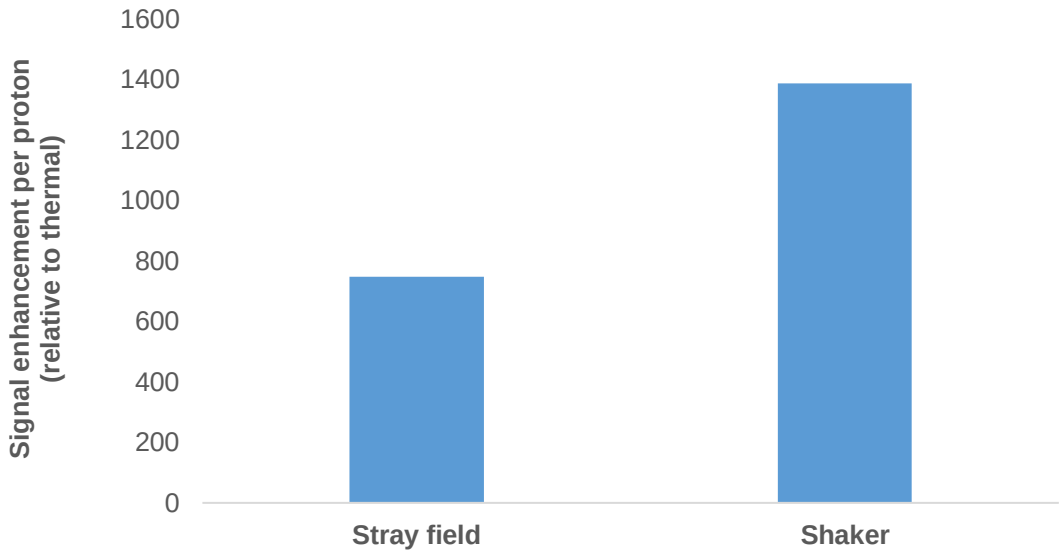

Figure 75: **signal enhancement obtained in stray magnetic field versus with the magnetic shaker @ 298 K for 4,6-nicotine-d_2 *9* using precatalyst IMes *18*. Samples were the 'standard' concentration of 5 mM IMes precatalyst *18* in methanol-d_4, hyperpolarised in a 'shake-and-drop' protocol with 4 bar para-hydrogen (absolute) and a ten second shake at 298 K in either ~65 G stray field or in a 60 G shaker**

It was immediately obvious that the magnetic shaker produced vastly superior results to the original stray field protocol – 85% superior signal enhancement was obtained per proton with otherwise identical conditions. The new shaker assembly also demonstrated much more reliable and consistent results, significantly reducing the time taken to obtain a full set of at least three highly similar results.

The arrival of the new magnetic shakers coincided with the variable *para*-hydrogen pressure studies detailed in Chapter 3.4.4. It was hypothesised that the marginal improvement with increasing pressure previously observed for 4,6-nicotine-d_2 **9** might be due to inefficient mixing wasting a greater available quantity of *para*-hydrogen. Therefore, another series of 'shake-and-drops' were performed on 4,6-nicotine-d_2 **9** with increasing *para*-hydrogen pressure but utilising the magnetic shaker assembly instead of the spectrometer stray field (Figure 76).

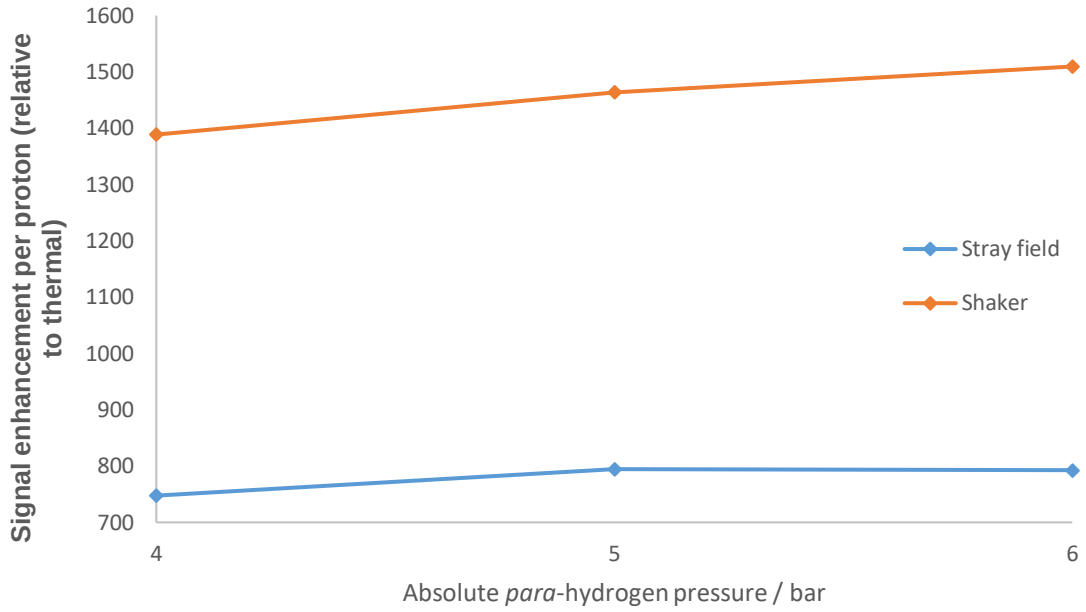

Figure 76: **signal enhancement vs. para-hydrogen pressure for 4,6-nicotine-d_2 *9* with differing experimental mixing/PTF protocol. Samples were the 'standard' concentration of 5 mM IMes precatalyst *18* with 5 equivalents of substrates in methanol-d_4, hyperpolarised in a 'shake-and-drop' protocol with a ten second shake in either a ~65 G stray field or a 60 G magnetic shaker assembly at 298 K**

The magnetic shaker still offered vastly better performance than shaking in the stray field for a given set of conditions (approximately double the signal intensity), but such gains in performance were overshadowed by the continued minimal impact of increased hydrogen pressure. There was a small and tangible increase in hyperpolarisation of 4,6-nicotine-d_2 **9** when increasing from 4 to 6 bar (absolute) of *para*-hydrogen, with signal enhancement boosted from ~1390-fold to ~1500-fold per proton. However, this increase represents only around a 9% increase in signal intensity for a 50% increase in hydrogen pressure (compared to ~7% observed with the same pressure increase shaken in the stray field). Therefore, the previously-theorised idea (see Chapter 3.4.4) that insufficient mixing was hampering increased-pressure SABRE performance gains of **9** was discounted.

3.7 'Doping' studies with fully-deuterated co-ligand

It was considered that polarisation from *para*-hydrogen would be diluted between the multiple bound substrate ligands on the catalyst, similar to polarisation being diluted between protons on each substrate molecules themselves (Chapter 3.1.1).[65] Extensive

catalyst redesign would be needed to eliminate multiple copies of the substrate on the iridium centre - it was theorised that a fully-deuterated co-ligand might achieve the same effect but much more quickly and easily. Such a co-ligand would bind competitively to the catalyst but without receiving polarisation, thereby reducing dilution of polarisation. This approach would effectively lower the substrate loading on the catalyst and more efficiently 'funnel' polarisation to the substrate (Figure 77) without the corresponding reduction in relaxation times previously observed with low substrate equivalents.

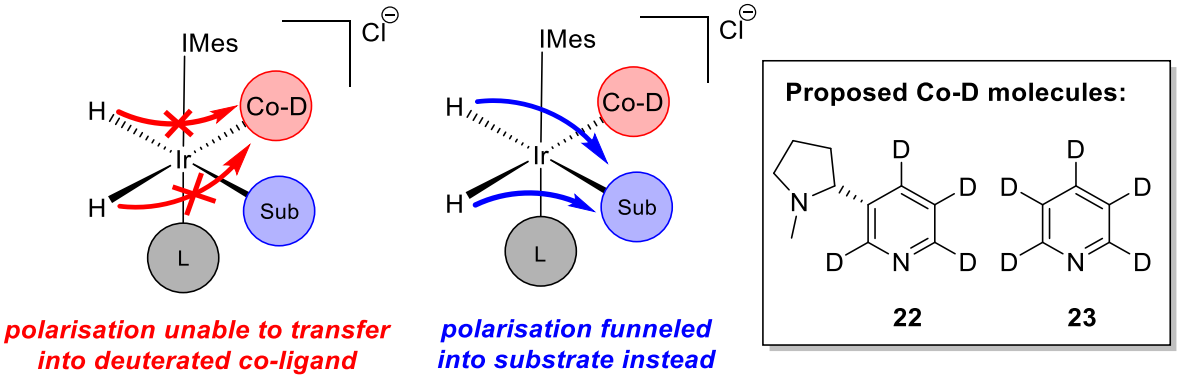

Figure 77: use of a fully-deuterated co-ligand (Co-D) in conjunction with the desired substrate (Sub) to reduce dilution of polarisation between multiple bound substrate molecules. Ligand L is either Co-D or Sub at any given time but is not considered relevant as the axial ligand receives minimal polarisation from *para*-hydrogen

The deuterated co-ligand would ideally be a more highly deuterated analogue of the desired substrate to minimise undesired kinetic changes to the system – such as displacement of the substrate by preferential binding of the co-ligand. 2,4,5,6-tetradeuteronicotine **22** was therefore selected as the desired co-ligand, although several attempts to synthesise it were unsuccessful. Given time constraints, it was decided to instead test the co-ligand approach with a sub-optimal but more readily-available alternative. Pyridine-d_5 **33** was selected given its similar structural and iridium-binding motifs to nicotines and easy acquisition as an NMR solvent. A series of 'shake-and-drops' were performed using nicotine **1** and 4,6-nicotine-d_2 **9** as substrates, IMes **18** and d_{22}-IMes **19** as precatalysts, pyridine-d_5 as co-ligand and the magnetic shaker assembly detailed in Chapter 3.6. In order to directly assess any benefit of using the co-ligand, the samples prepared had 2.5 equivalents of substrate and 2.5 equivalents of co-ligand to match the 5 equivalents of substrate used as standard in previous testing. A comparison of these results is shown in Figure 78.

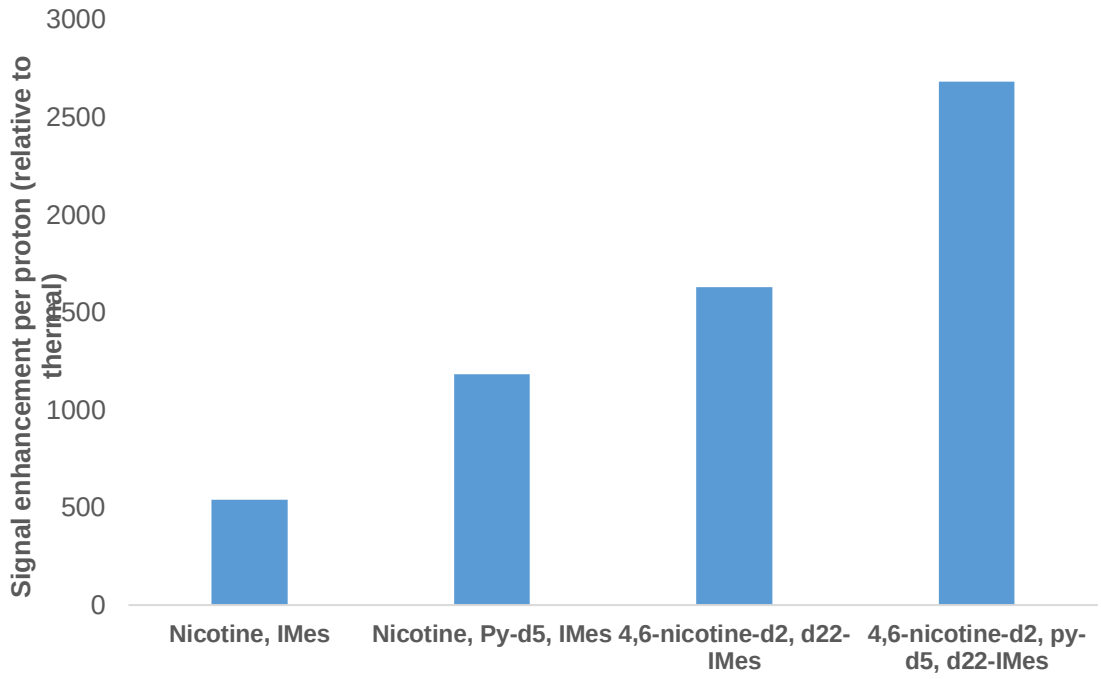

Figure 78: **signal enhancement for various substrate, catalyst and co-ligand combinations. Samples were the 'standard' concentration of 5 mM IMes precatalyst** X **with either 5 equivalents of substrate or 2.5 equivalents each of substrate and co-ligand. Samples were in methanol-d_4, hyperpolarised in a 'shake-and-drop' protocol with 4 bar (absolute) of *para*-hydrogen and a ten second shake in a 60 G magnetic shaker assembly at 298 K**

The samples with co-ligand pyridine-d_5 **23** exhibited consistently and substantially improved signal enhancements compared to those with just the substrate. The mixture of deuterated nicotine **9**, deuterated d_{22}-IMes **19** precatalyst and deuterated pyridine-d_5 **23** co-ligand combined to give a hitherto unprecedented signal enhancement of ~2700-fold per proton – equivalent to ~9% polarisation. Such a high level of hyperpolarisation is more than five times greater than using natural nicotine **1** alone with an undeuterated catalyst and serves to highlight explicitly the impact deuterium incorporations have to boost SABRE performance. To date, this is ~2700-fold enhancement is the single biggest polarisation achieved during the project.

However, as previously established, signal enhancements are not fully informative when assessing a system for MRI feasibility – the raw, bulk signal is more important, quantified by the signal-to-noise ratio (Figure 79).

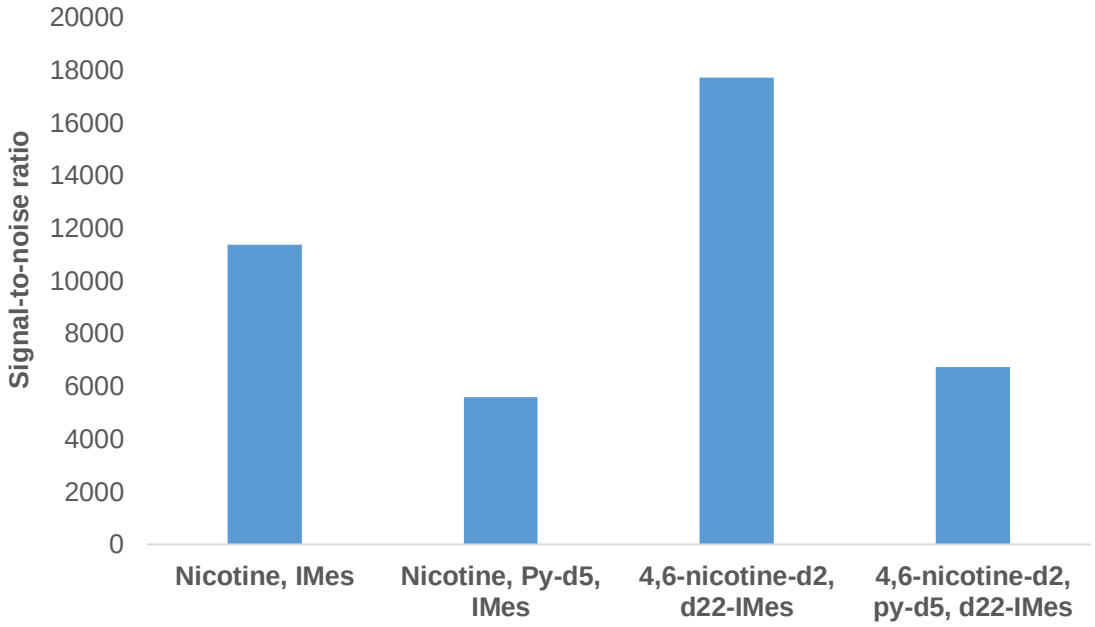

Figure 79: **signal-to-noise ratio for various substrate, catalyst and co-ligand combinations. Samples were the 'standard' concentration of 5 mM IMes precatalyst** X **with either 5 equivalents of substrate or 2.5 equivalents each of substrate and co-ligand. Samples were in methanol-d_4, hyperpolarised in a 'shake-and-drop' protocol with 4 bar (absolute) of *para*-hydrogen and a ten second shake in a 60 G magnetic shaker assembly at 298 K**

Unfortunately, it was observed that the signal-to-noise ratio in those samples with co-ligand was markedly inferior to their equivalents with substrate alone, indicating poor suitability for use in imaging applications. It was concluded that while each substrate molecule is substantially more efficiently polarised in the presence of the co-ligand, the reduced abundance of the substrate molecules ensures that the bulk signal observed is much smaller than in the absence of the co-ligand. It is also believed that using a more-rapidly exchanging molecule (pyridine-d_5 **23**) as the co-ligand may be adversely affecting the results, with the co-ligand effectively displacing the substrate from the catalyst and impeding the repeated polarisations desirable for strong bulk signal. Results in the literature show that polarisation levels up to 45% per proton are possible with use of a more highly-deuterated analogue of a substrate as co-ligand and some optimisation of relative quantities.[65] Therefore, it may yet be possible to improve on these mixed initial results for co-ligand use.

3.8 Imaging experiments

Given the overall project aim to develop and refine agents for eventual use in imaging applications, it was considered prudent to probe the performance and signal lifetime of the nicotine substrates produced in some imaging experiments – even before optimisation of SABRE was complete. Such probing was achieved through a series of RARE (*Rapid Acquisition with Relaxation Enhancement*)[113] and FISP (*Fast Imaging with Steady-State Free Precession*)[114] experiments undertaken by colleague Alexandra Olaru. Both RARE and FISP are variants of the *spin-echo* experiment (Figure 80).

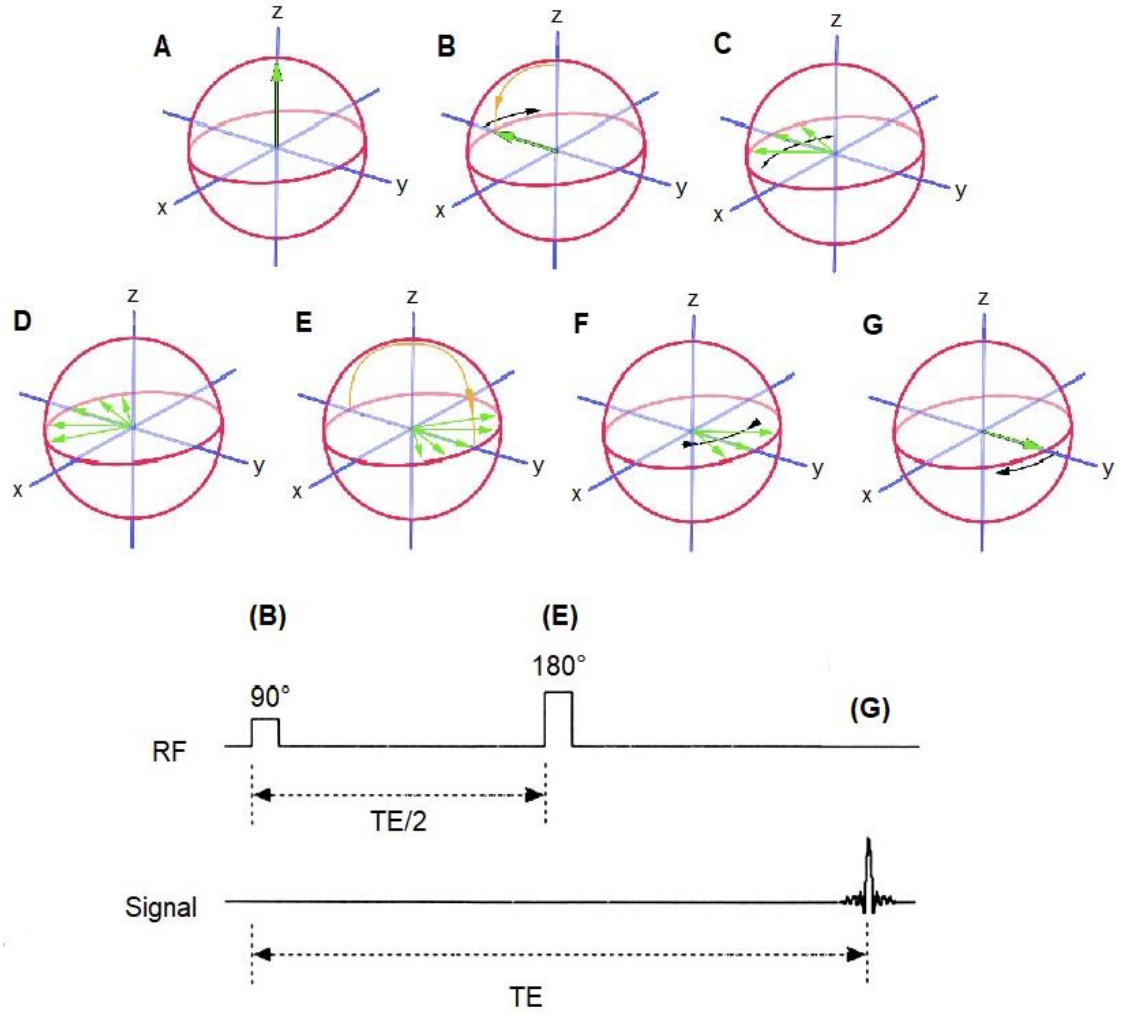

Figure 80: **the spin-echo experiment, the basis of most imaging techniques. Magnetisation in the *z*-axis (**A**) is transferred into the (observable) *xy*-plane by a 90° RF pulse (**B**). The spins start to defocus about the *xy*-plane due to local field inhomogeneities (**C, D**). A second RF pulse of 180° is applied (**E**), flipping the defocusing spins in the *xy*-plane so that they start to refocus (**F**). When the spins refocus, an 'echo' signal is produced at the *echo time* TE (**G**), where TE is *exactly* twice the time interval the 180° pulse was applied at. The simplified sequence described above ignores any quantum decoherence or imprecision in the RF pulses, which would realistically degrade the quality of the echo**

The ‘echo’ signal produced in a spin-echo experiment is converted into spatial information about nuclei in the sample with pulsed field gradients (PFGs, spatially-varied magnetic fields as previously mentioned in Chapter 3.2). These PFGs are described as either *phase-encoding* or *frequency-encoding*, in which the applied gradients affect the phase or frequency (respectively) of the precession of each nucleus differently depending on their position in space. These differences are detected by the quadrature coils of the instrument and recorded mathematically in a grid known as *k-space*. *k*-space is not an image itself, but a deconstructed mathematical representation of the nuclear spatial frequencies in the sample. Each row (k_y) in the grid is determined by the phase-encoding gradient(s) and is ‘filled’ (in k_x) by data points from the application of frequency-encoding gradients (Figure 81). The rows are ‘filled’ one-by-one by application of different gradients on subsequent echoes - once the *k*-space grid is filled entirely, it can be 2D Fourier-transformed to produce the actual image.[115,116]

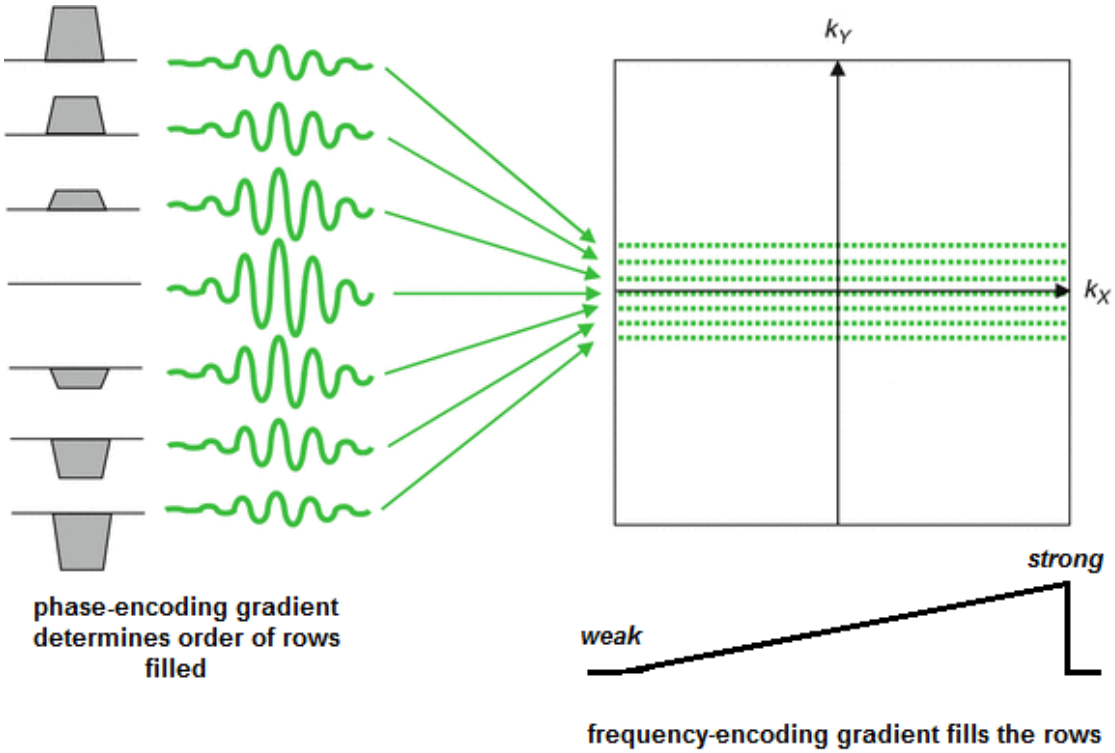

Figure 81: **the filling of *k*-space with data points using field gradients.[116] Once filled, *k*-space can be 2D Fourier-transformed to give the image**

Such a process could be analogised as light reflected off an object passing through a lens – all the light will be refracted but by different amounts dependent on where the light originated from and therefore where it hits the lens. The light after the lens does not show

an image of the object but contains information about its appearance (analogous to *k*-space). A second lens (analogous to the 2D Fourier-transform) converts this data back into a recognisable image of the object (Figure 82).[115]

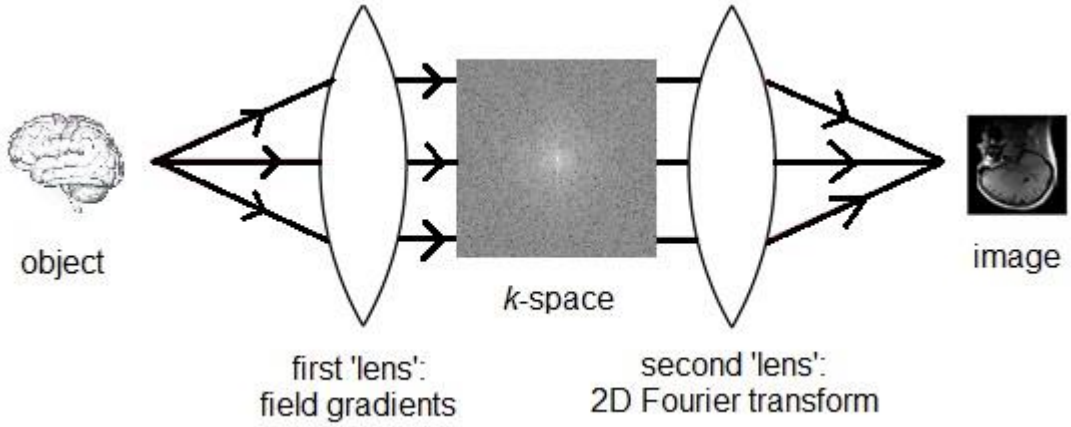

Figure 82: **lens analogy for the process of imaging from a spin-echo experiment. The lines represent echoes from the sample/object, which are turned into data points in *k*-space by the first 'lens' of field gradients, then converted back to an image by the second 'lens' of 2DFT to produce a 2D image of the object**

RARE is a technique focusing on providing high-intensity single-shot images of a compound, whereas FISP was instead focused on estimating the magnetic lifetime of the (hyperpolarised) signal in an imaging setting. Thus, RARE was considered somewhat analogous to measuring signal enhancements in conventional SABRE and FISP somewhat analogous to conventional measuring of T_1 times.

3.8.1 Rapid Acquistion with Relaxation Enhancement (RARE) studies

In imaging applications, the absolute signal produced by a sample is key and was assessed by a series of RARE experiments. RARE is also known as a *fast spin-echo* experiment and was pioneered by Hennig et al. in 1986.[113] It improves upon the conventional spin-echo by employing a train of 180° RF pulses to generate multiple echoes from a single 90° excitation pulse rather than just one (Figure 83). Each of these echoes has different phase-encoding gradients applied, thereby populating multiple rows of *k*-space within a single repetition time (TR, the time between excitations once relaxation to equilibrium is *nominally* complete). This echo train can be continued until the spins start to lose coherence by T_2 relaxation – *echo train length* (ETL) is typically between 4 and 32 echoes for routine imaging.[113,117]

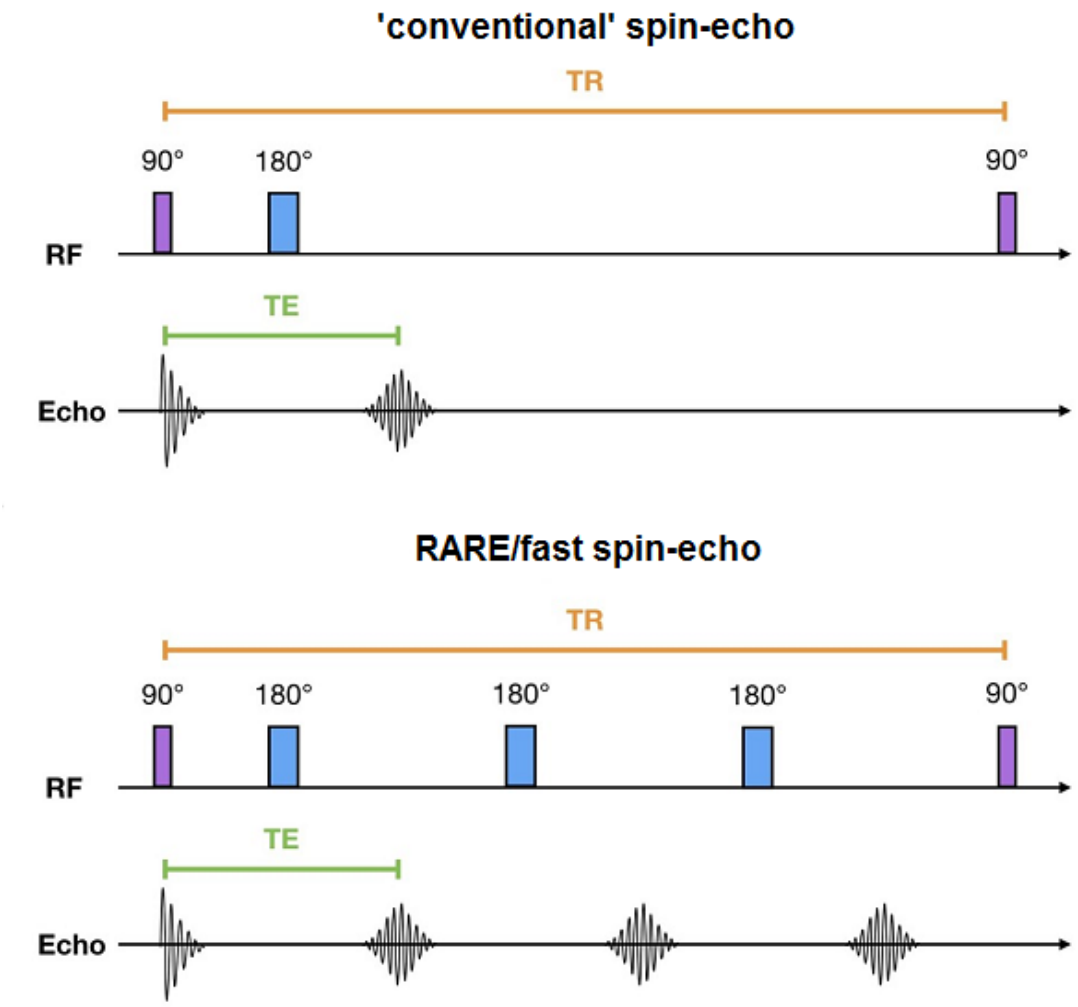

Figure 83: comparison of the RARE sequence to a conventional spin-echo. Multiple echoes can be recorded within the repetition time (TR) before relaxation is complete and another 90° excitation pulse is needed. Each echo is treated with different phase- and frequency-encoding field gradients to fill multiple lines of *k*-space within TR[117,118]

The greatest advantage of recording multiple echoes per excitation is that the overall imaging process is dramatically sped up. It is so much faster than a conventional spin-echo that extra time can be afforded recording more rows in *k*-space with extra phase-encoding gradients to improve image resolution, or signal-to-noise can be improved via a lengthened TR to ensure full recovery of longitudinal magnetisation before the next excitation. Shorter imaging times also reduce the incidence of magnetic susceptibility effects, in which repeated exposure to gradient fields starts to magnetise the sample over time and significantly distort the produced image.

A series of RARE experiments were combined with SABRE and the established 'shake-and-drop' methodology (albeit shaking in a stray magnetic field) to assess the potential

of (−)-nicotine **1** and 4,6-nicotine-d_2 **9** for use in an imaging context. The results of these experiments are shown in Figure 84 and Table 2.

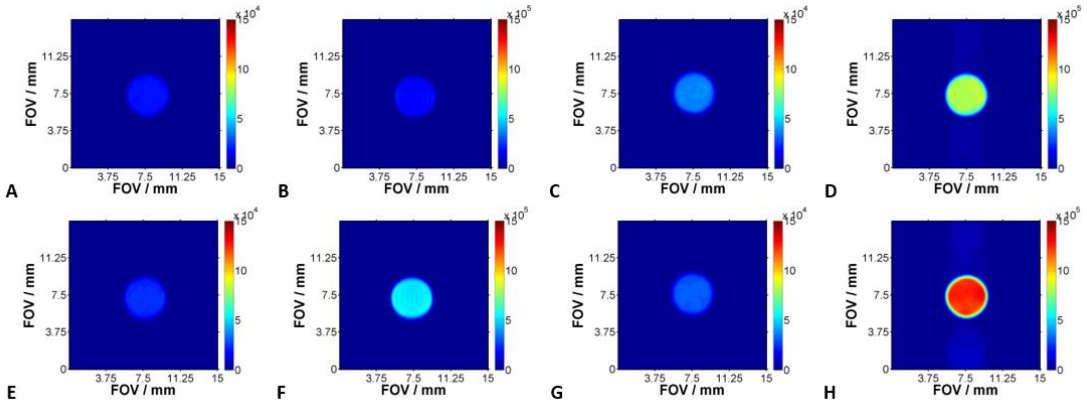

Figure 84: **One-shot 2D ^{1}H MRI RARE results of *A* (−)-nicotine *1* with IMes *18* precatalyst (thermal), *B* (−)-nicotine *1* with IMes *18* precatalyst (hyperpolarised), *C* (−)-nicotine *1* with d_{22}-IMes precatalyst *19* (thermal), *D* (−)-nicotine *1* with d_{22}-IMes precatalyst *19* (hyperpolarised), *E* 4,6-nicotine-d_2 *9* with IMes precatalyst *18* (thermal), *F* 4,6-nicotine-d_2 *9* with IMes precatalyst *18* (hyperpolarised), *G* 4,6-nicotine-d_2 *9* with d_{22}-IMes precatalyst *19* (thermal), and *H* 4,6-nicotine-d_2 *9* with d_{22}-IMes precatalyst *19* (hyperpolarised). Samples were 5 mM precatalyst *with 20 equivalents of substrate* in methanol-d_4, hyperpolarised in a 'shake-and-drop' protocol with a ten second shake in a ~65 G stray field at 298 K. The image acquisition parameters were: field of view (FOV) 1.5 x 1.5 cm^2, matrix 64 x 64, slice thickness 2 mm, TE/TE$_{eff}$/TR = 4/4/600 ms. Raw data were zero-filled up to 256 x 256 prior to the FFT and a sinebellsquared filter was applied to reduce the amount of white noise. The final resolution of the images obtained was 58 x 58 µm^2**

Substrate	Precatalyst	SNR (thermal)	SNR (hyperpolarised)	SNR gain (SNR_{hyp}/SNR_{th})
(−)-nicotine **1**	IMes **18**	46	423	9.2
(−)-nicotine **1**	d_{22}-IMes **19**	44	962	21.9
4,6-nicotine-d_2 **9**	IMes **18**	54	1138	21.1
4,6-nicotine-d_2 **9**	d_{22}-IMes **19**	41	1446	35.3

Table 2: **signal-to-noise ratios calculated for one-shot 2D ^{1}H MRI rare results**

It was observed that the combination of 4,6-nicotine-d_2 **9** and d_{22}-IMes **19** produced the most intense image by far, with a signal-to-noise ratio of nearly 1500. This result matched expectations given the established superiority of **9** and **19** in conventional SABRE studies. In contrast, the combination of non-deuterated (−)-nicotine **1** with non-deuterated IMes **18** produced an image barely one-quarter as intense.

3.8.2 Fast Imaging with Steady-state free Precession (FISP) studies

There are many variations of the classical spin-echo experiment. Several of these variations rely on the concept of *steady-state free precession* (SSFP), a phenomenon observed when the repetition time (TR) of a classical spin-echo experiment is reduced to significantly less than T_2 of the sample. Rapid repetition of the sequence means transverse magnetisation (M_{xy}) from the preceding excitation/echo is unable to fully relax to longitudinal magnetisation (M_z) before the next excitation pulse. When the next RF excitation is applied, this residual M_{xy} is flipped to M_z and vice-versa. Over several repetitions a constant/equilibrium M_{xy} (referred to as M'_{ss}) component develops (Figure 85). This equilibrium is manifested in the FID and echo signals merging after several repetitions (Figure 86).[114,119]

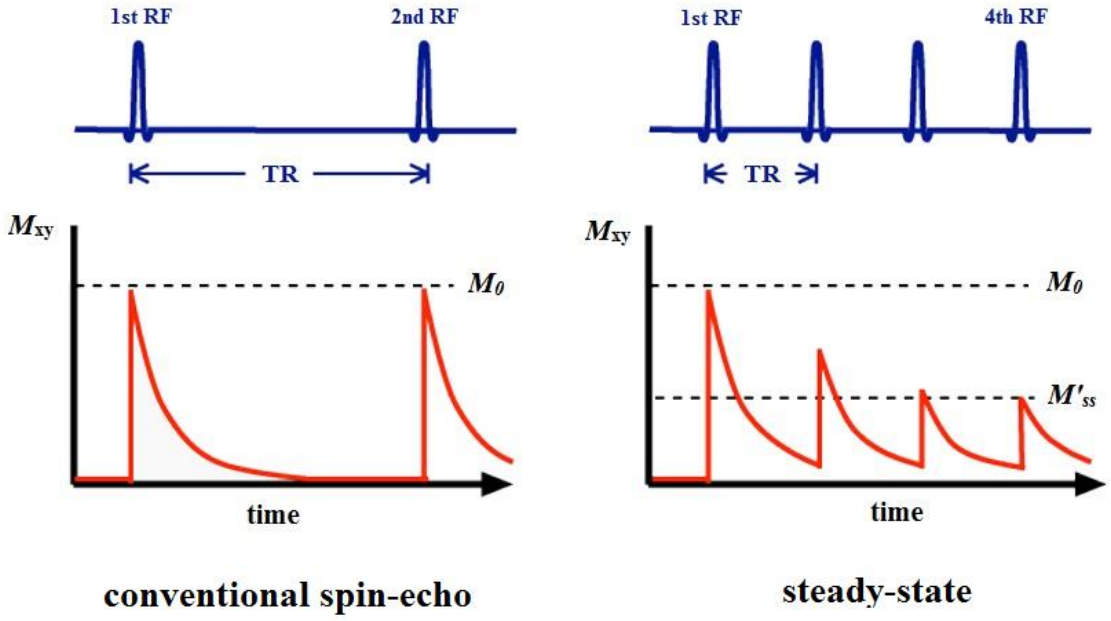

Figure 85: establishment of a magnetic steady-state (M'_{ss}), viewed in terms of magnetisation, from spin-echo experiments with short repetition times (TR<<T_2). M_0 is the maximum signal possible, where all spins are coherent and in the same plane at any given time

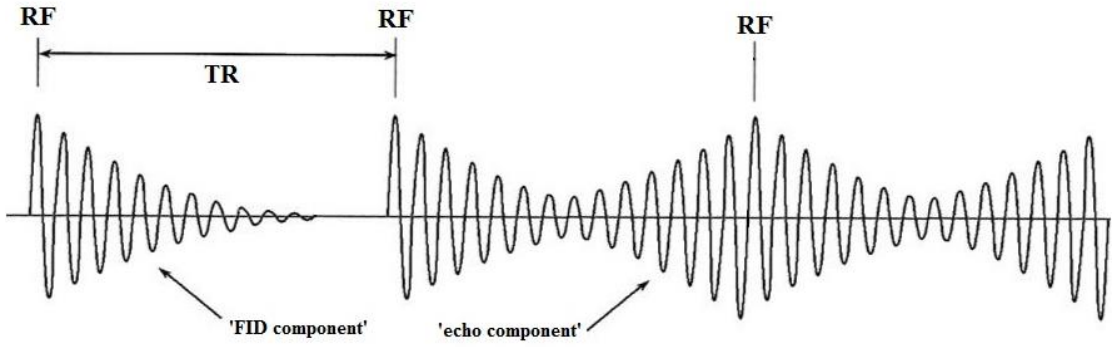

Figure 86: **establishment of magnetic steady-state, viewed in terms of signal, from spin-echo experiments with short repetition times (TR<<T_2). The FID signal from the second RF excitation overlaps with the echo from the first RF excitation – there is always some observable signal from then on**

The short TR of SSFP sequences means images can be acquired very quickly, sometimes even faster than in fast spin-echo sequences such as RARE. The degree of steady-state equilibrium increases with flip angle (*i.e.* the power of the RF excitation pulse from 0 to 90°) with a flip angle of 50-80° typically yielding the best steady-state signals.[114,117,120] A series of FISP experiments were performed on the same samples as in Chapter 3.8.1 with a mere 5° flip angle – although low flip angles give a poor SNR for the images, they allow TR to become extremely short. Therefore, decay of the hyperpolarised image could be observed multiple times over only a few seconds from polarisation. One such series is shown in Figure 87.

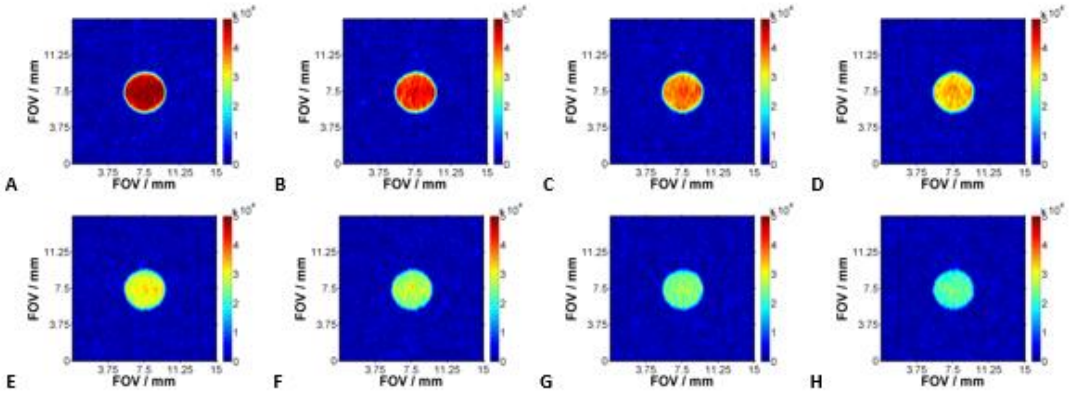

Figure 87: **One-shot 2D ^{1}H hyperpolarised MRI FISP results of 4,6-nicotine-d_2 *9* in conjunction with the d_{22}-IMes precatalyst *19* acquired after *A* 0.6 s, *B* 1.2 s, *C* 1.8 s, *D* 2.4 s, *E* 3.0 s, *F* 3.6 s, *G* 4.2 s and *H* 4.8 s from the polarisation transfer step. Time values calculated based on the intervals between each two consecutive scans and do not include the image acquisition times (~1 second). Image acquisition parameters were: field of view (FOV) 1.5 x 1.5 cm^2, matrix 64 x 64, slice thickness 5 mm, TE/TR/TR_{scan} = 2/4/600 ms. Raw data were zero-filled up to 256 x 256 prior to the FFT and a sinebellsquared filter was applied to reduce the amount of white noise. The final resolution of the images obtained was 58 x 58 µm^2**

Visual inspection of the images shows the expected decay of signal intensity. The amplitude of the signal for each sample series was plotted as a function of time after normalisation to their respective maximum initial values (Figure 88). Given that the initial maximum signal is markedly different for each series, direct comparisons between series is ill-advised.

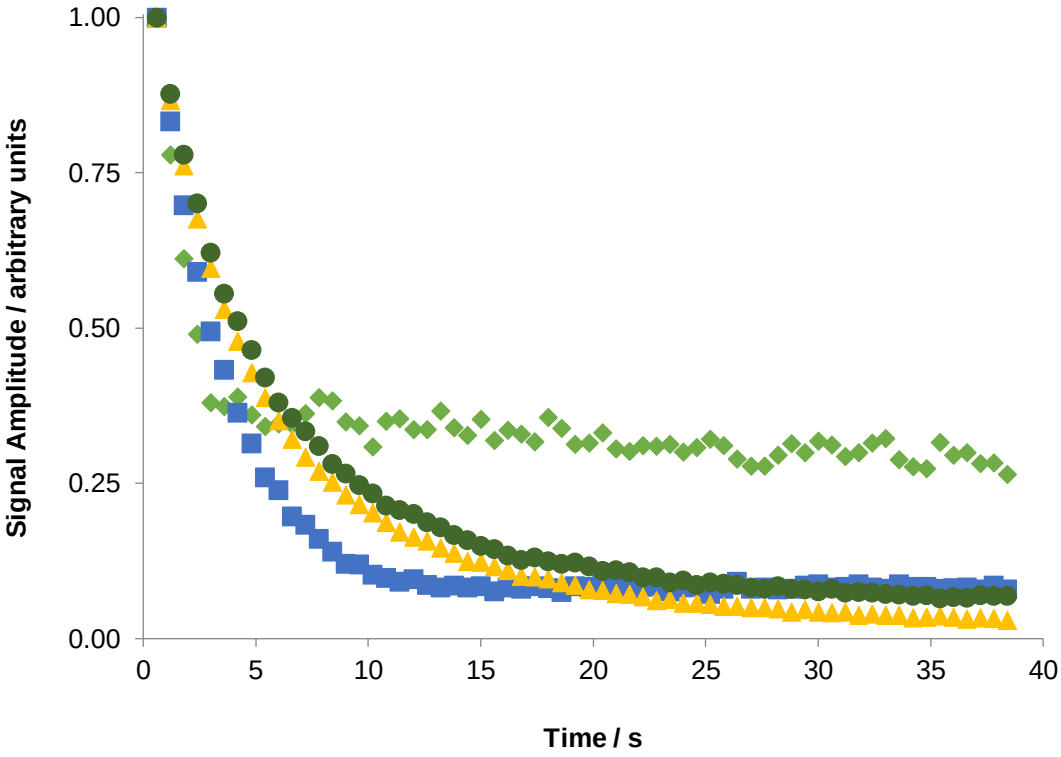

Figure 88: ^{1}H MRI signal decay expressed as a function of time as a fraction of the initial maximum signal, derived from low flip-angle FISP images of (−)-nicotine *1* with IMes *18* precatalyst (green diamonds), (−)-nicotine *1* with d_{22}-IMes precatalyst *19* (blue squares), 4,6-nicotine-d_2 *9* with IMes precatalyst *18* (yellow triangles) and 4,6-nicotine-d_2 *9* with d_{22}-IMes precatalyst *19* (dark green circles)

By visual inspection alone, it was observed that (−)-nicotine **1** in conjunction with the IMes **18** catalyst polarises quite weakly, with the maximum signal intensity being only ~70% higher than the value of the rapidly-reached signal at thermal equilibrium. Use of 4,6-nicotine-d_2 **9** or the deuterated catalyst d_{22}-IMes **19** significantly slowed the decay of this signal, with a combination of the two yielding the slowest decay of all. Such results fell in line with the trends established with earlier SABRE studies.

A quantitative assessment of the performance of each sample can be obtained by calculating the decay rate for each signal versus time dependence using the Equation 2.

$$y = M_0 \cos(\theta)^{t/3} e^{-t/T_1} + c$$

Equation 2: T_1 decay constant equation for MRI data – M_0 is the maximum initial magnetisation, θ is the flip angle, t is time and c is the intercept

Equation 2 was used in place of the standard T_1 decay calculation, as the latter only applies to measurements made using an inversion-recovery or saturation-recovery experiment and hence is not suitable for MRI data. Signal decay constants were calculated for each sample and the results, together with the associated errors, are presented in Table 3. These however cannot be taken as the true T_1 times of the substrate signals, as the FISP method uses many excitation pulses during the experiment and residual signal in the *xy*-plane after such an excitation pulse can cause further dephasing and hence a reduction in signal. Therefore, the calculated decay constants are strongly suspected to be much smaller than the true T_1 relaxation times of (−)-nicotine **1** and 4,6-nicotine-d_2 **9** under these conditions.[121]

Ligand	Catalyst precursor	T_{1eff} / s	Error (±/ s)	R^2
(−)-nicotine **1**	IMes **18**	1.355	0.175	0.945
(−)-nicotine **1**	d_{22}-IMes **19**	3.014	0.054	0.999
4,6-nicotine-d_2 **9**	IMes **18**	5.279	0.194	0.996
4,6-nicotine-d_2 **9**	d_{22}-IMes **19**	5.332	0.177	0.997

Table 3: effective T_1 relaxation times calculated

3.9 Conclusions

Study and optimisation of SABRE performance and magnetic lifetime for nicotine isotopologues **1**, **4**, **8**, **9** and **10** has revealed significant complexity to the technique not previously fully recognised. Our evolving understanding has permitted a maximum polarisation of ~8.38 % and maximum activated T_1 relaxation time of over 30 seconds compared to initial results of just ~0.64 % polarisation and ~ 8 seconds for the longest T_1. The best performing substrate and conditions have been demonstrated as successful in preliminary imaging tests. It should be noted that there is still significant scope for further optimisation and better results may yet be possible. Refinement of the co-ligand protocol and new developments in biocompatible solvents and catalyst removal techniques should allow even greater performance to be achieved from this family of compounds.

4: SABRE exchange kinetics and modelling

Chapter 3 demonstrated that the performance and longevity of the SABRE response is dramatically affected by the exchange rate of molecules between the iridium catalyst centre and the surrounding solution. The exchange processes are affected by concentration, temperature and catalyst, hence it was considered prudent to quantify the exchange rates for a range of conditions and thereby better focus further optimisation efforts.

4.1 The nicotine-iridium complex and Exchange Spectroscopy (EXSY)

4.1.1 Complex characterisation

The active form of the substrate-catalyst complex for the nicotine isotopologues was initially assumed to have six ligands around iridium as is the case with pyridine.[64] Three of those ligands bear pyridyl moieties, therefore this structure is hereafter referred to as a *tris*-pyridyl complex. Such an arrangement would typically have two equivalent equatorial pyridyl ligands (in this case, nicotine and derivatives bound through their pyridyl nitrogens) *trans* to equivalent hydrides, a distinct, inequivalent axial pyridyl ligand *trans* to the carbene ligand and a single hydride environment (Figure 90). However, two inequivalent, mutually-coupled and equal-intensity hydrides were consistently observed (Figure 89) in the nicotine-derived substrates, indicating there must be a different ligand arrangement.

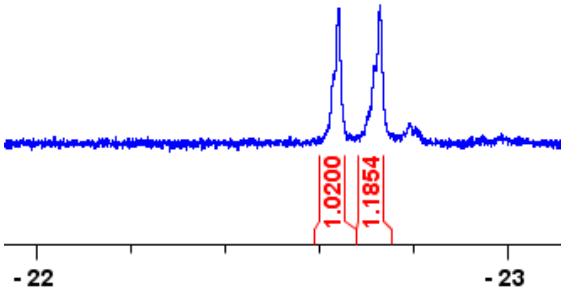

Figure 89: **^{1}H NMR spectrum showing two distinct hydride signals when (−)-nicotine *1* and IMes precatalyst *18* react in methanol-d_4 at 298 K with 4 bar of hydrogen.**

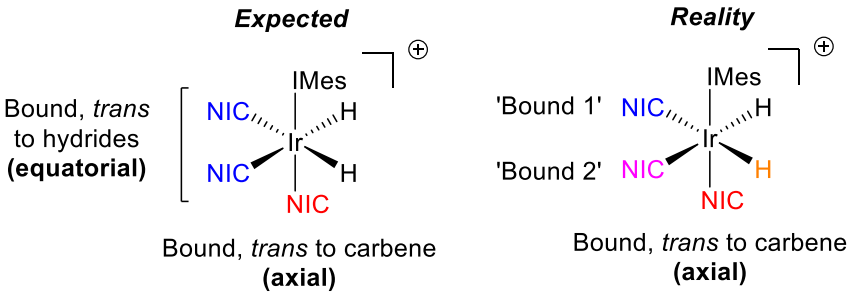

Figure 90: the arrangement of substrate (NIC) molecules around the iridium centre in a typical SABRE catalyst. Colours correspond to a single magnetic environment

It was also observed that there were consistently a multitude of new, distinct peaks produced when a nicotine substrate-precatalyst complex was converted to the active form by addition of hydrogen. These new peaks were considered too numerous to support a simple *tris*-pyridyl arrangement of substrate ligands, too numerous to be a complex containing a chloride or solvent ligand and too homogenous in their position and integration to be some sort of contaminant. COSY and NOESY NMR experiments revealed four distinct sets each of four pyridyl proton environments, all between 6.9 and 8.6 ppm (Figures 91 and 92). These peaks correspond to three distinct pyridyl environments on the iridium centre and a fourth free in solution, consistent with an overall complex structure of a *tris*-pyridyl type, but with all ligands distinct from one another. The specific cause for this phenomenon was concluded as the bulky and chiral nature of the (−)-nicotine **1**-based substrate ligands – by definition multiple chiral species binding to an achiral centre must be inequivalent, as there is no plane of symmetry in the resulting complex.

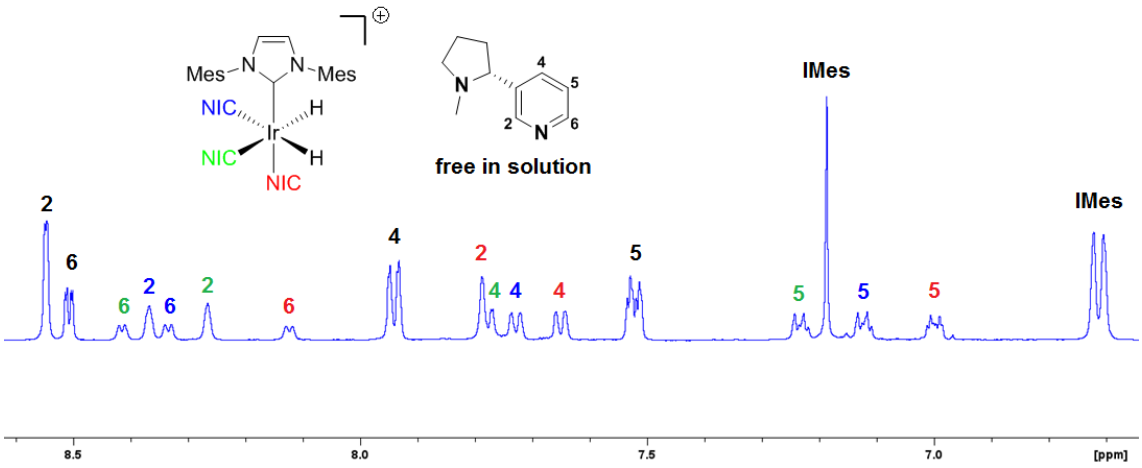

Figure 91: assignment of (−)-nicotine *1* ^{1}H NMR peaks at 243 K to specific resonances in specific binding sites on the IMes *18* iridium centre, assigned using COSY and NOESY experiments. The number above the peak corresponds to the pyridyl proton it is associated with, the colour indicates the ligand the proton is in

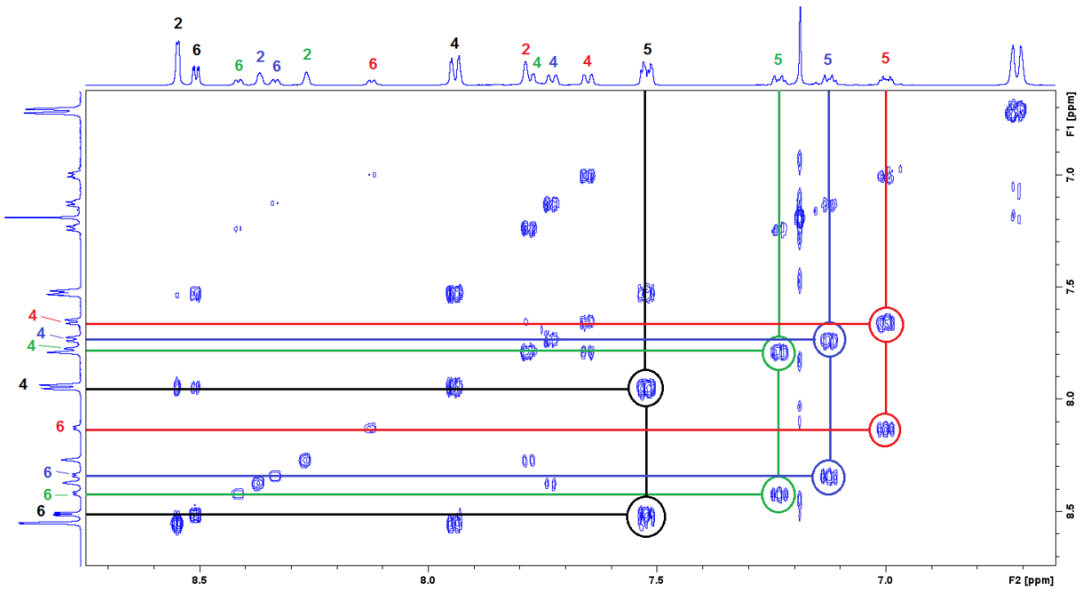

Figure 92: COSY of (−)-nicotine *1* with IMes *18* at 243 K with colour labels matching Figure 91. Correlations between four distinct 5-pyridyl protons to their corresponding 4-pyridyl and 6-pyridyl environments are highlighted, helping confirm there are four different nicotine environments on and around the iridium centre. COSY details: DS =16, NS = 4, TD/size of FID = 2048/64

The axial nicotine ligand has significantly different chemical shifts to those *trans* to the hydrides, hence it is not strongly polarised in a SABRE experiment (as mentioned previously in Chapter 2). In addition, similarly-positioned have previously exhibited very slow exchange processes owing to increased strength of the nitrogen-iridium bond.[105] For these reasons, the specific behaviour of the axial nicotine ligand was not investigated.

4.1.2 Exchange Spectroscopy (EXSY)

Having established that there were two equatorial ligand environments for the bound species which could exchange, their rates of exchange were quantified by Exchange Rate Spectroscopy (EXSY).[122] In many other experiments, when a signal is excited, detection usually follows immediately. In EXSY, a single resonance is selectively excited and a short delay (referred to as mixing time, τ_{mix}) elapses before measurement. During this mixing time, the nuclei associated with the signal can move to a different site in the sample. In other words, a reaction has taken place or an exchange process has occurred. By varying the delay (τ_{mix}) in a series of experiments, the evolving abundance of excited nuclei at each site can be observed and the rate of exchange between them can be determined. This was achieved using the *selnogp* pulse sequence, in which selective excitation is achieved through the use of a shaped 180° RF pulse and the resulting magnetisation is refocused into observable signal by a series of 90° and 180° RF pulses (Figure 93).[123-125]

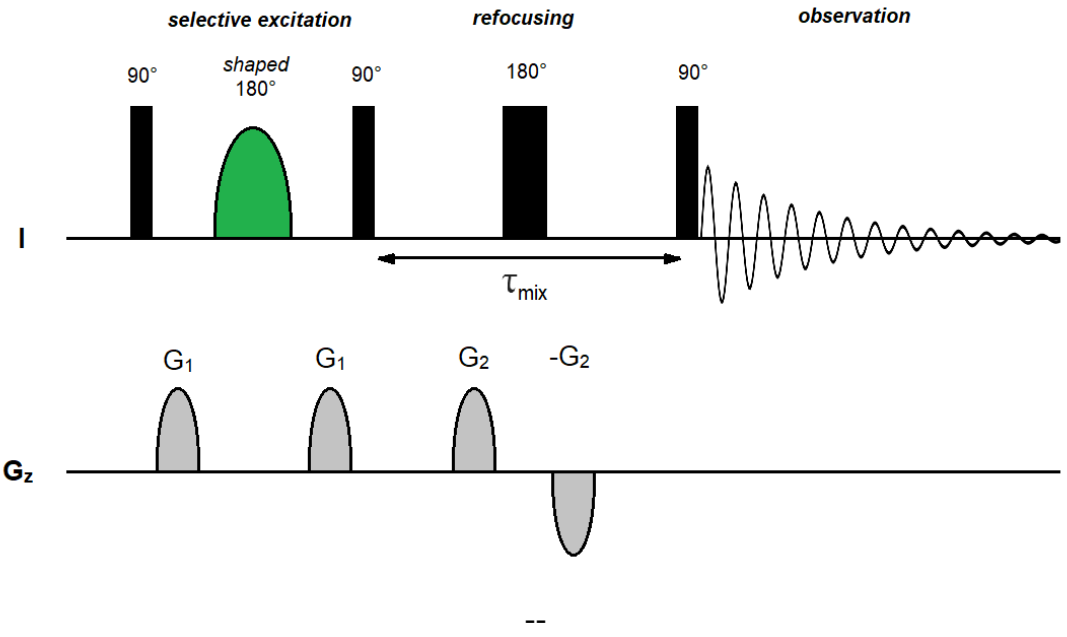

Figure 93: The *selnogp* pulse sequence. I refers to operations on the RF coils, whereas G_z are operations to create pulsed field gradients (PFGs) in the z-axis. The 'shaped' RF pulse has its frequency offset to excite a specific resonance. τ_{mix} is the mixing time.[123]

The initial work focused on determining observed rate constants for dissociation of substrate from the catalyst. Such rate constants were derived from fitting simulated data for abundance of the excited species against the real peak integration data via non-linear

least-squares analysis. The simulated data was constructed from an initial kinetic model, hereafter referred to as **Model 1**, that considered two equatorial ligands (Bound 1 and Bound 2 in Figure 90) exchanging with ligands free in solution and with each other, with any intermediates ignored. It was considered from the onset that the exchanges rates of the two inequivalent ligands should be treated and calculated independently (although it was presumed that any differences due to the inequivalence would be minor). Therefore, data from excitation of both equatorial ligands was simultaneously fitted to the model data when deriving observed rate constants (Figure 94). As an example, the exchange of H_5 in (−)-nicotine **1** from the Bound 1 position to the Bound 2 position and free-in-solution is shown in Figure 94 in both real and simulated data – the observed rate constants k_{AB}, kAC, kBA, kBC, kCA and kCB were altered until a satisfactory fit to the real data was obtained. The points (Free, Bound1, Bound2) represent the real, recorded data whereas the lines (Free (sim), Bound1 (sim), Bound2 (sim)) represent the corresponding simulated data – the abundance of excited ligands at the initial site decreases with time as they exchange into the Bound 2 site and to free in solution, approaching equilibrium by the end of observation at 0.5 seconds.

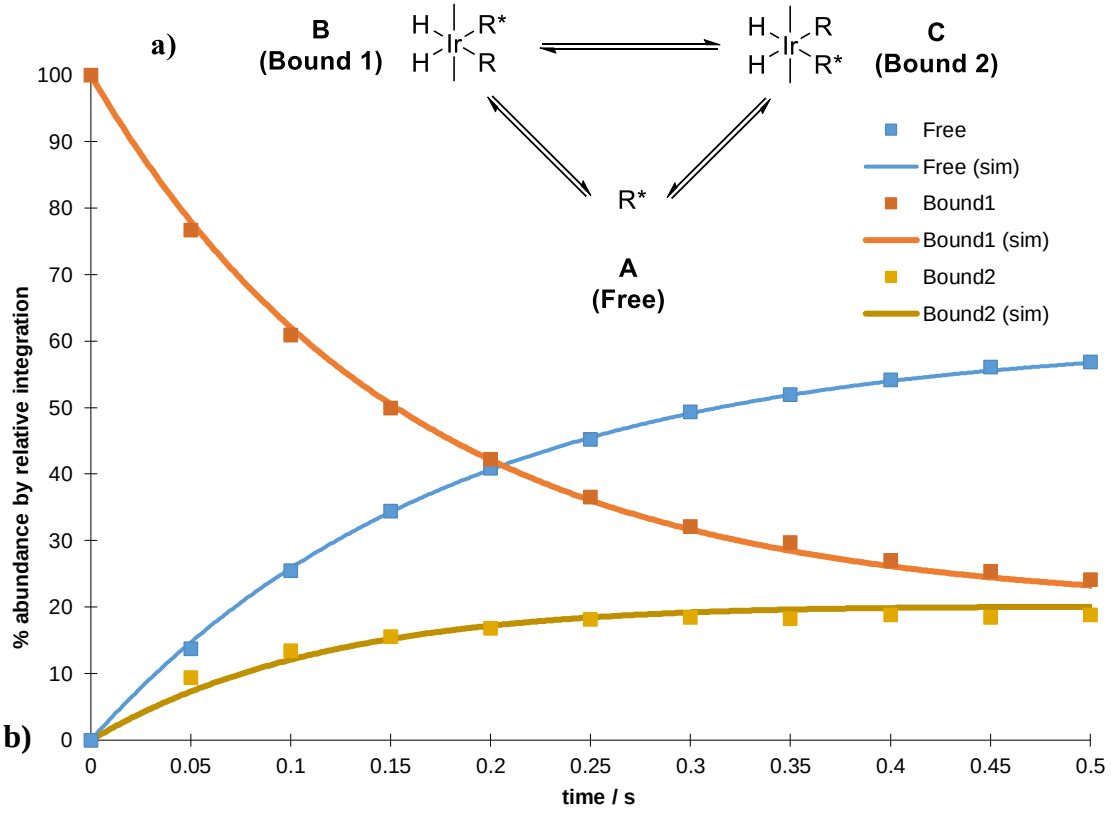

Figure 94: a) Model 1, the initial kinetic model b) raw real and simulated data for observed exchange of (−)-nicotine *1* molecules with precatalyst IMes *18* using Model 1, following selective excitation of the 'Bound 1' resonance at 298 K. Samples were 5 mM precatalyst in methanol-d_4 with five equivalents of substrate, activated with 4 bar of hydrogen.

A selection of observed rate constants for each substrate/precatalyst combination at 298 K is displayed for comparison below in Figure 95. The rate constants all increase greatly with temperature - full results for all temperatures are listed in Chapter 7. Very poor fits were observed for many of the entries, with minimum sum-of-least-squares well in excess of 100 frequently observed. Minimum sum-of-least-squares should not be used in direct quantitative comparison with one another, but large values still indicate a poor fit to reinforce the visually obvious.

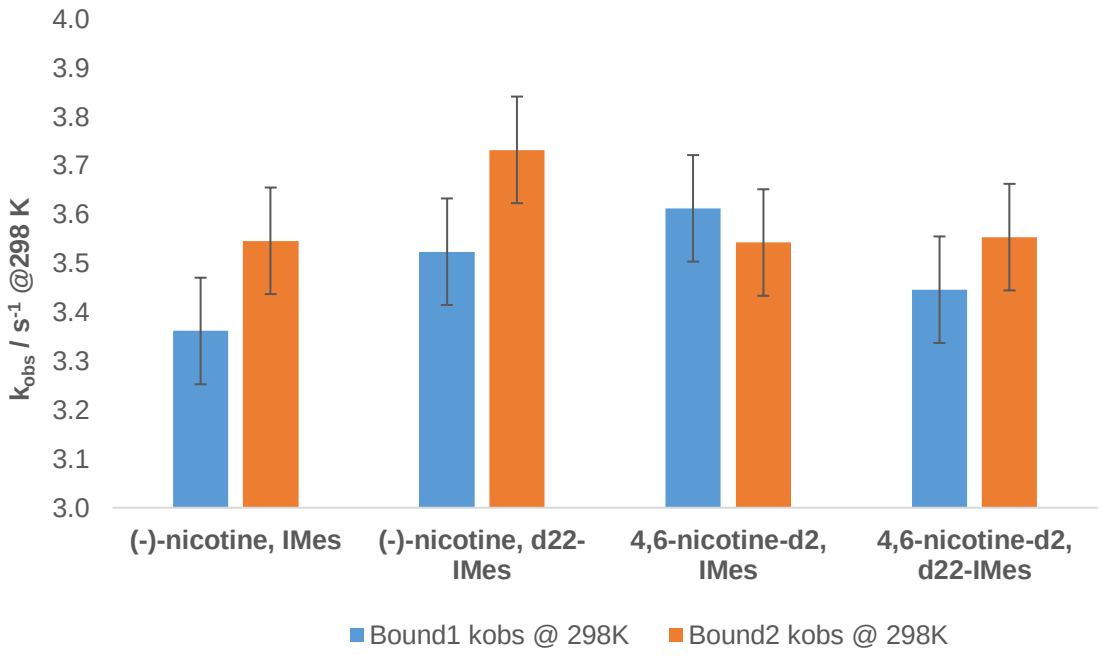

Figure 95: observed rate constants for dissociation of substrate molecules at 298 K using Model 1. Samples were 5 mM precatalyst in methanol-d_4 with five equivalents of the substrate, activated with 4 bar of hydrogen. Error bars shown are the standard deviation of all results (n=8).

All combinations of precatalyst (IMes **18** and d_{22}-IMes **19**) and nicotine substrate ((−)-nicotine **1** and 4,6-nicotine-d_2 **9**) were determined to have dissociation rate constants between 3.3 and 3.8 s^{-1} at 298 K, with an average of 3.56 ± 0.16 s^{-1}. This indicates far slower exchange processes than other substrates previously tested for SABRE in the group and that are known to hyperpolarise well, such as methyl nicotinate (~10 s^{-1} with IMes **18** at 298 K) and pyridine (~21 s^{-1} with IMes **18** at 298 K).[102]

The noticeable differences by visual inspection and lack of an obvious trend between substrate and/or precatalyst deuteration and the observed rate constants suggested that Model 1 was flawed. Deuterium incorporation was expected to have a minimal effect on

the kinetics of SABRE, as no C-H bonds are broken during the exchange process and hence there should only small secondary kinetic isotope effects observed from deuterium substituents. Another potential cause for the deviation was T_1 relaxation time variation for each of the bound equatorial ligands. The rate constants in EXSY are derived from the relevant abundances of each of the bound and free ligands as measured by NMR integration. However, these integrals will be affected by relaxation of all the species involved, which do not necessarily occur at the same rate. If an equatorial ligand had a shorter T_1 than the free material, then its signal intensity would diminish more rapidly during the EXSY observation than that of the free material. Hence, the rate constants would be overestimated.

It was also observed that the rate constants for Bound 1 and Bound 2 in each combination were very similar. However, in other cases (particularly between substrates) the difference is large enough to suggest statistical relevance and imply more complex interactions are taking place. It should be noted that standard deviation is a simplified assessment of the data, but hints at a wider problem as half of the eight entries were more than one standard deviation from the mean. As with variations between substrate/catalyst combinations, flaws in Model 1 and/or a lack of consideration of relaxation were suspected for the deviations. It should be emphasised that this was unexpected as such a model has been used widely. A more concrete and quantitative test of the variations between substrate/catalyst entries, such as analysis of variance (ANOVA), is questionable as there are insufficient data to produce a meaningful and reliable answer. Repeat experiments would be necessary to quantify the significance of such differences.

Increasing the temperature of the experiments from 298 to just 303 K appeared to almost double the rate of substrate dissociation for all combinations of substrate and precatalyst tested. These observations empirically demonstrated the strong temperature dependence of the exchange processes in accordance with theory.[64,105]

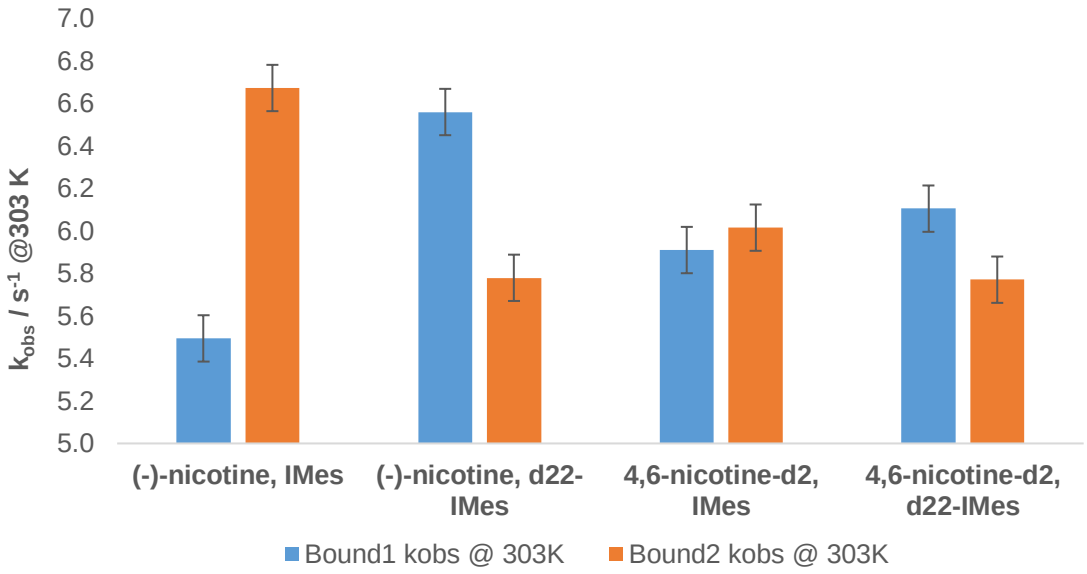

Figure 96: observed rate constants for dissociation of substrate molecules at 303 K using Model 1. Samples were 5 mM precatalyst in methanol-*d*$_4$ with five equivalents of the substrate, activated with 4 bar of hydrogen

The measuring of rate constants over a range of temperatures allowed construction of Eyring plots to determine the enthalpy and entropy of activation for the processes. A rearrangement of the Eyring equation (Equation 3) showed that a plot ln(*k*/T) versus 1/T would give a straight line with gradient equal to $-\Delta H^{\ddagger}/R$ and intercept of $\ln(k_B/h) + \Delta S^{\ddagger}/R$.

$$k = \frac{k_B T}{h} e^{-\frac{\Delta G^{\ddagger}}{RT}} \equiv \ln\left(\frac{k}{T}\right) = -\frac{\Delta H^{\ddagger}}{RT} + \ln\left(\frac{k_B}{h}\right) + \frac{\Delta S^{\ddagger}}{R}$$

Equation 3: the Eyring equation and its rearrangement to derive enthalpy and entropy of activation. k_B is Boltzmann's constant, h is Planck's constant and R is the universal gas constant

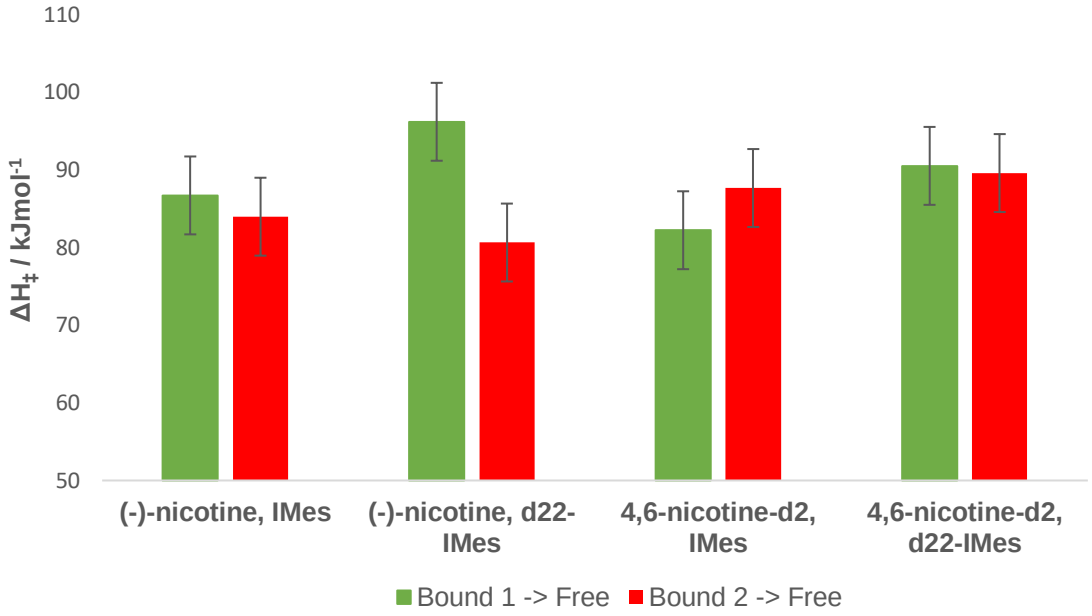

Figure 97: Enthalpies of activation for the dissociation of bound substrate molecules from iridium using data from Model 1. Error bars are the standard deviation of the mean (n=8)

It was observed that every substrate/precatalyst combination gave roughly similar calculated enthalpies of activation, with an average of 87.19 ± 5.02 kJ mol^{-1}. However, deviations were observed that were significant enough to cause concern at the viability of Model 1 – four out of eight combinations were more than one standard deviation from the mean. The same nitrogen-iridium bond is being broken in each case and so only secondary isotope effects from incorporated deuterium should have any impact on the strength of this bond. These secondary isotope effects are typically quite small, hence there should be near uniformity in the enthalpies of dissociation with an accurate model.

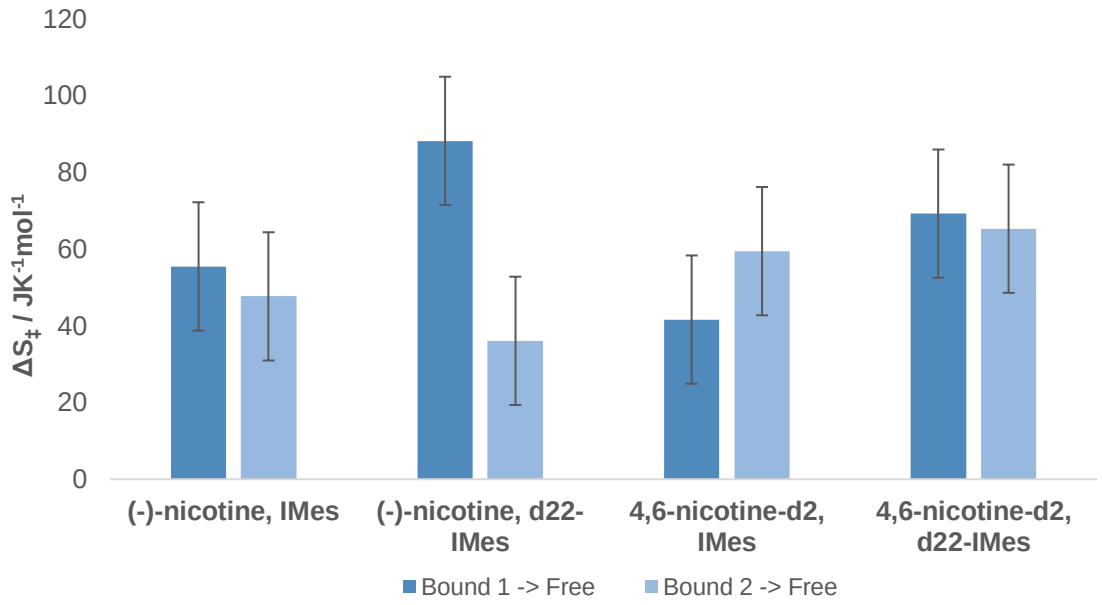

Figure 98: Entropies of activation for the dissociation of bound substrate molecules from iridium using Model 1

Entropy of activation relates to the energy of the dissociation transition state. No obvious correlation was observed between deuteration of the catalyst and/or deuteration of the substrate and this parameter. However, when the calculated activation enthalpies and entropies of ligand dissociation were combined to calculate the Gibbs free energy of dissociation, strong uniformity was observed as expected by theory (Figure 99) at an average of 69.82 ± 0.13 kJ mol^{-1}. All entries are within one standard deviation of the mean, except for two entries which are within 1.5 standard deviations of the mean.

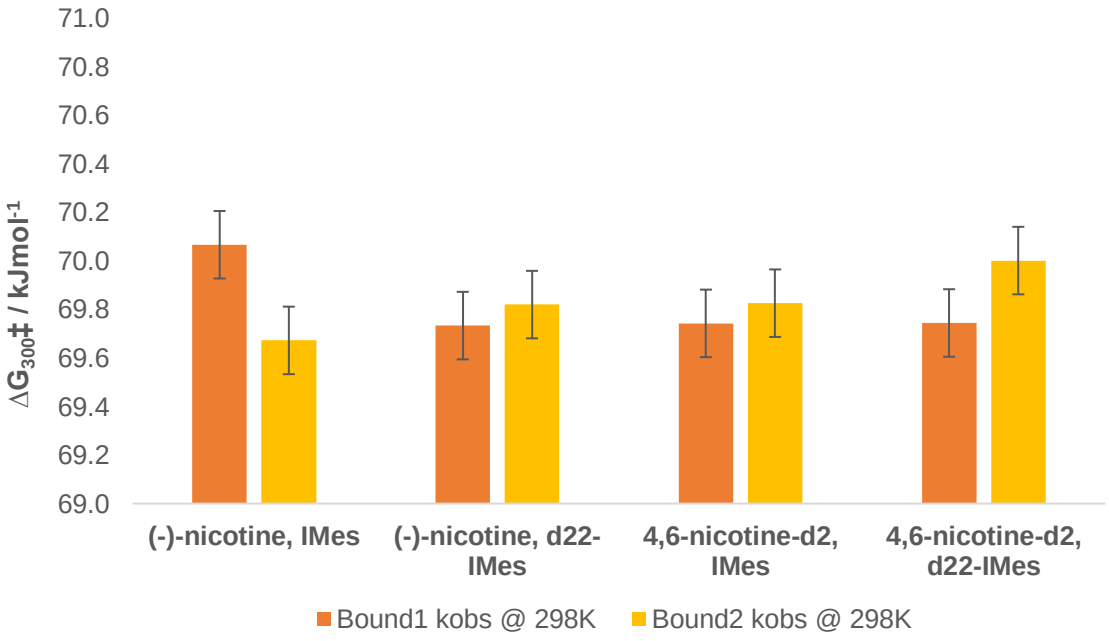

Figure 99: Gibbs free energies of activation for the dissociation of bound substrate molecules from iridium using Model 1

It was concluded overall that there were just too many unexplained and seemingly inconsistent deviations for Model 1 to be considered an accurate or reliable model of the SABRE exchange processes for (−)-nicotine isotopologues. Despite the relatively homogenous calculated free energies of activation being in line with theoretical expectations, it was decided a more thorough and considered model was required.

4.2 Kinetic model improvements

4.2.1 Models 2 and 3

Model 1 was based on well-established existing model for ligand exchange in SABRE substrate-catalyst complexes with two equivalent equatorial ligand environments.[105] It was not designed to take account of the increased complexity of two distinct equatorial environments that can both be individually excited/observed in EXSY and exchange ligands between one another. Hence, several distinct intermediates and increased number of species must also play a role, all of which are ignored by Model 1. Secondly, as outlined, the effects of relaxation on the kinetic data obtained are not incorporated into Model 1. Relaxation rates of bound and free ligands are known (see Chapter 3.1.2) to be different.

To overcome the first of these limitations, a new model (Figure 100) was proposed that would consider as many species as possible, even those that cannot be observed directly. This model will hereafter be referred to as Model 2. It was considered prudent to tackle each of these substantial flaws sequentially rather than all at once, hence inclusion of the effects of relaxation will be discussed primarily in Chapter 4.2.2.

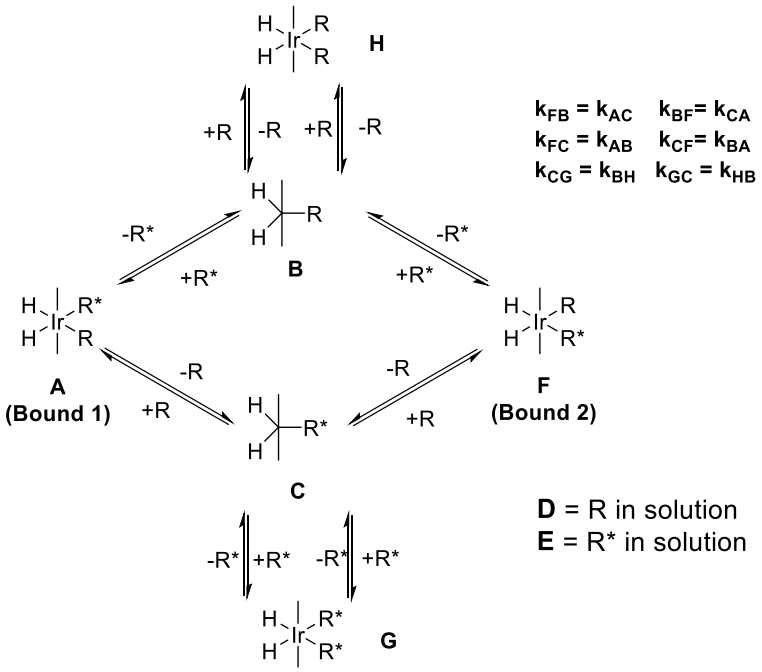

Figure 100: Model 2 – a kinetic model of the SABRE substrate exchange process for nicotines that considers intermediates and other species. Only those species marked with * have excited ligands and are therefore able to be directly observed by NMR

As EXSY revolves around selectively exciting specific resonances/ligands, only those species that contain excited ligands can be observed. Species **A** and **F** are analogous to 'Bound 1' and 'Bound 2' in the original model. Species **H** is derived from replacement of the excited ligand in either **A** or **F** with an unexcited ligand present in solution – the resulting lack of excited ligands means **H** is unobservable. **G** is an important species that cannot be directly observed, as NMR signals for each of its excited ligands will overlap completely with the excited ligand in **A** and in **F**. This means that signals observed ostensibly for **A** or **F** are instead representative of **A** + **G**/2 and **F** + **G**/2, respectively, and must be taken into account in the model. Species **B** and **C** are the (presumed) trigonal bipyrimidal intermediates, whereas **D** and **E** represent substrate ligands free in solution, unexcited and excited respectively.

In order to further improve on Model 1, a series of constraints were placed upon Model 2 to ensure that the rate constants produced were sensible. Initially, the only constraints were that all chemically-identical processes must have equal rates, *e.g.* dissociation of a ligand from the iridium centre from a specific binding site must occur at the same rate same regardless of whether that ligand has been NMR-excited or not.

Lastly, the real and simulated abundance of each of the species was expressed as a percentage of the whole, measured by NMR integration. The initial results of applying the new model and its constraints to existing data can be seen in Figures 6 and 7 below.

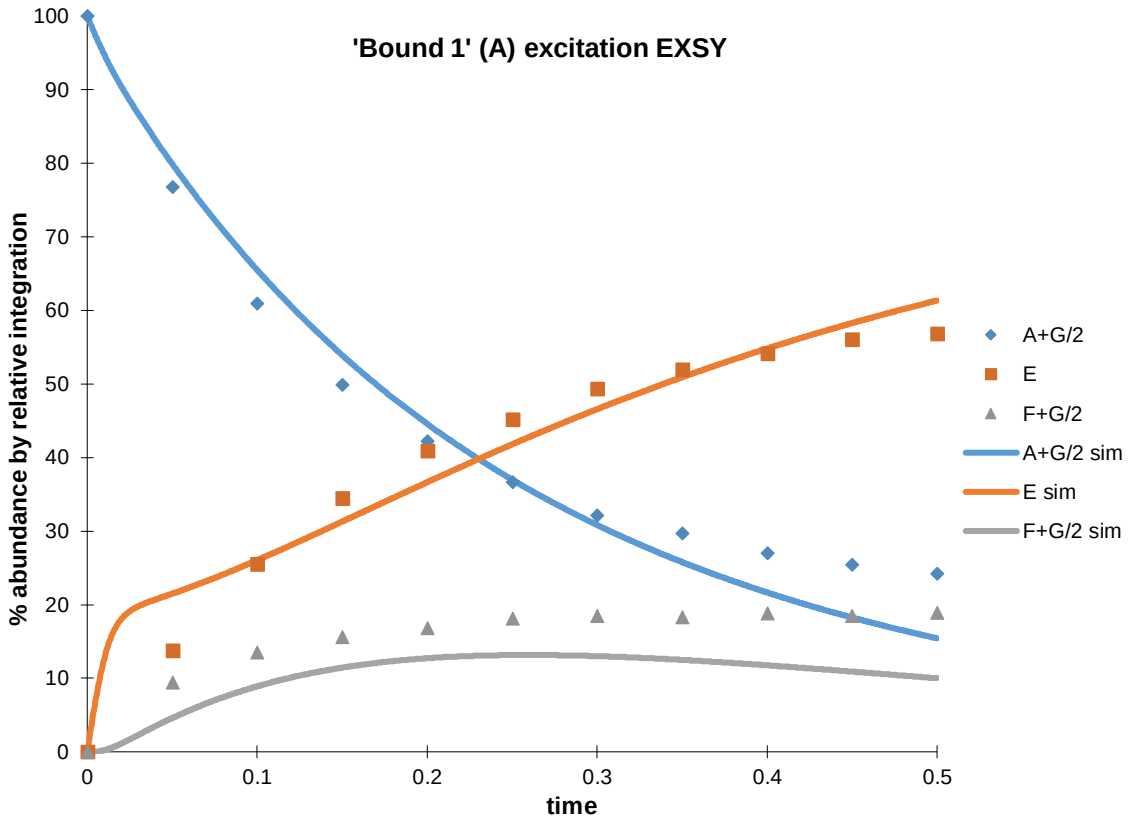

Figure 101: raw real and simulated data for observed exchange of (−)-nicotine *1* molecules with precatalyst IMes *18* using Model 2, following selective excitation of Bound 1 (species A) resonance at 298 K. Samples were 5 mM precatalyst in methanol-d_4 with five equivalents of substrate, activated with 4 bar of hydrogen.

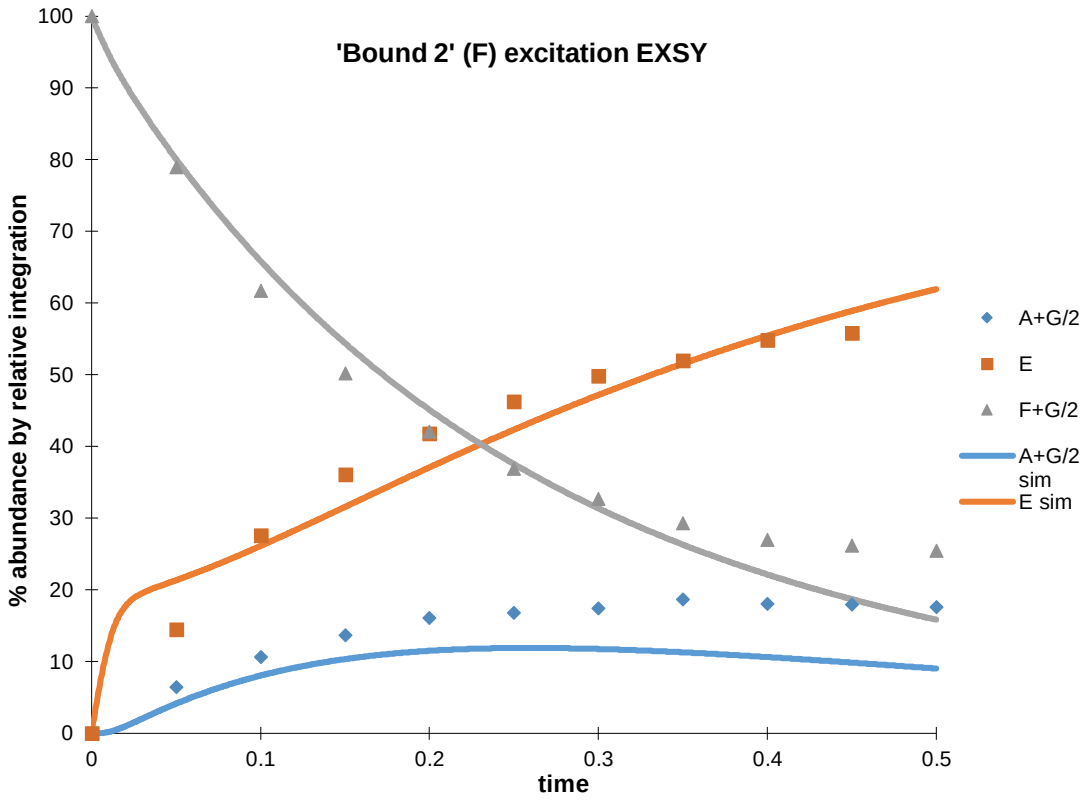

Figure 102: **raw real and simulated data for observed exchange of (−)-nicotine *1* molecules with precatalyst IMes *18* using Model 2, following selective excitation of Bound 1 (species** F**) resonance at 298 K. Samples were 5 mM precatalyst in methanol-d_4 with five equivalents of substrate, activated with 4 bar of hydrogen**

Visual inspection of the plots was sufficient to determine Model 2 was producing a very poor fit, especially with the initial fit of free excited ligand **E** and the exchange between species **A** and **F** at higher mixing times. In addition, the rate constants produced by this model were also obviously nonsensical – this is shown in Table 4. It should be noted for comparison that the rate constants k_{AB} and k_{AC} in this model are equivalent to the dissociation rate constants from 'Bound 1' and 'Bound 2' in Model 1, respectively.

-20.674	**2.826**	**2.749**	0	15.099	0	0	0	**A**
1.921	-27.375	0	0	0	2.065	0	23.391	**B**
2.065	0	-27.375	0	0	1.921	23.391	0	**C**
8.244	0	0	-9.262	0	1.019	0	0	**D**
10.978	0	0	0	-21.959	10.979	0.002	0	**E**
0	2.749	2.826	0	14.670	-20.244	0	0	**F**
0	0	0	0	21.274	0	-21.274	0	**G**
0	0	0	0	0	0	0	0	**H**
A	**B**	**C**	**D**	**E**	**F**	**G**	**H**	

Table 4: **(observed) rate constants generated by Model 2 for (−)-nicotine *1* molecules with precatalyst IMes *18* at 298 K. k_{XY} = XY (i.e. k_{AB} is row A, column B). Only rates marked in green are actual rates, those in grey correspond to processes that do not exist. Rates marked in bold are equivalent to the 'Bound 1' and 'Bound 2' dissociations in Model 1.**

The calculated rate constants for dissociation from the Bound 1 (k_{AB}) and Bound 2 (k_{AC}) sites broadly matched their equivalents derived from Model 1 at ~ 3 s^{-1}. However, the rates of production of intermediates **B** and **C** did not equal their rates of consumption, a theoretical impossibility. Furthermore, many rates were set to zero by the data solver in an attempt to fit the simulated EXSY data to the real data. For example, the dissociation of species **A** to form equal amounts of intermediate **C** and unexcited free ligand **D** cannot have two different rates and yet Model 2 calculated k_{AC} and k_{AD} as 2.749 s^{-1} and 0 s^{-1}, respectively. It was obvious from these results that Model 2 was possibly even more flawed than Model 1 was and would require serious changes and refinements.

A major flaw in Model 2 was made apparent when all the rate constants were deliberately set to 2.5 s^{-1} to 'reset' the model for further improvement and fitting. It was observed that the fit by visual inspection was more reasonable and that the least-squares error (i.e. the deviation of the fitted data from the real data) for species **D** (unexcited ligand free in solution) and species **H** (complex with two unexcited equatorial ligands) made up more than 99% of the entire sum of least squares error for all species (Table 5, Figure 103). While it was accepted that the rate constants could not actually all be 2.5 s^{-1}, it was still concluded from the errors generated that species **D** and (to a lesser extent) **H** must be severely affecting the results as the solver attempted to reduce them to zero. Bias introduced by modelling of **D** and **H** was understandable, as they are the only two non-

intermediate species in the model that cannot be directly observed by NMR and therefore have no real data as backup or correction to the simulated data.

B	C	D	E	H	A+G/2	F+G/2	sum	time (s)
-	-	-	-	-	-	-	-	**0**
0.048	0.040	96.067	0.043	0.116	0.052	0.089	96.455	**0.05**
0.063	0.037	87.259	0.140	0.588	0.221	0.075	88.383	**0.1**
0.073	0.032	80.191	0.189	1.265	0.353	0.034	82.136	**0.15**
0.082	0.027	74.686	0.177	2.011	0.379	0.010	77.372	**0.2**
0.090	0.024	70.377	0.146	2.745	0.326	0.003	73.711	**0.25**
0.096	0.022	66.980	0.103	3.421	0.325	0.001	70.948	**0.3**
0.102	0.020	64.284	0.080	4.020	0.235	0.007	68.747	**0.35**
0.107	0.018	62.128	0.044	4.536	0.222	0.015	67.070	**0.4**
0.111	0.017	60.391	0.018	4.972	0.197	0.035	65.740	**0.45**
0.114	0.016	58.979	0.003	5.335	0.174	0.042	64.664	**0.5**
						Total:	**755.226**	

Table 5: **EXSY fitting least squares errors using Model 2 for (−)-nicotine *1* molecules with precatalyst IMes *18* at 298 K with all rate constants artificially set to 2.5 s^{-1}. The columns highlighted in green are the errors for species D and H and the sum of errors for all species – D and H make up more than 99% of the total error at each time interval and in total**

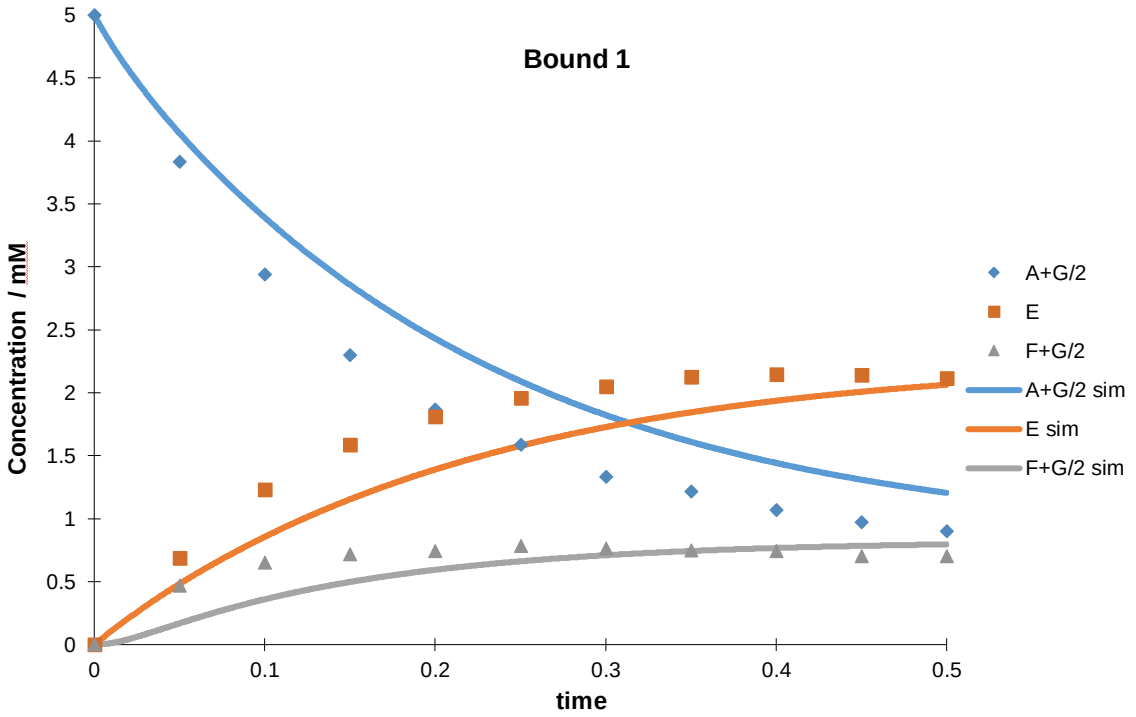

Figure 103: raw real and simulated data for observed exchange of (−)-nicotine *1* molecules with precatalyst IMes *18* using Model 2, following selective excitation of Bound 1 (species F) resonance at 298 K. Samples were 5 mM precatalyst in methanol-d_4 with five equivalents of substrate, activated with 4 bar of hydrogen

Model 2 was incrementally improved with the following changes:

- Unobservable species **D** and **H** were removed from consideration in the fitting process instead of attempting to use assumptions with no factual backup
- The percentage relative abundance of species by NMR integration was changed to an actual concentration as half of the species (**B**, **C**, **D** and **H**) present cannot be observed by NMR
- Further constraints were added to ensure negative or zero rate constants were forbidden, dissociative processes (*e.g.* **A** → **C** + **D**) *must* have the same rate for formation of each product (*i.e.* $k_{AC} = k_{AD}$) and the rate of production of intermediates **B** and **C** must equal the rates at which they are consumed
- A series of EXSY experiments exciting ligand free in solution (**E**) for each substrate/catalyst combination to provide a greater proportion of real data – these data are now simultaneously fit in an expanded model
- The inclusion of data points from free ligand (**E**) excitation means there are now nine sets of data being used to fit eight (**A**-**H**) variables whereas before there were only six sets of data. Eberhardt *et al.* show that at least *N-1* experiments are needed to robustly determine causal relationships between *N* variables – this condition is now satisfied by the extra data[126]

These cumulative improvements to the model, hereafter referred to as **Model 3**, are shown in Figures 104-106.

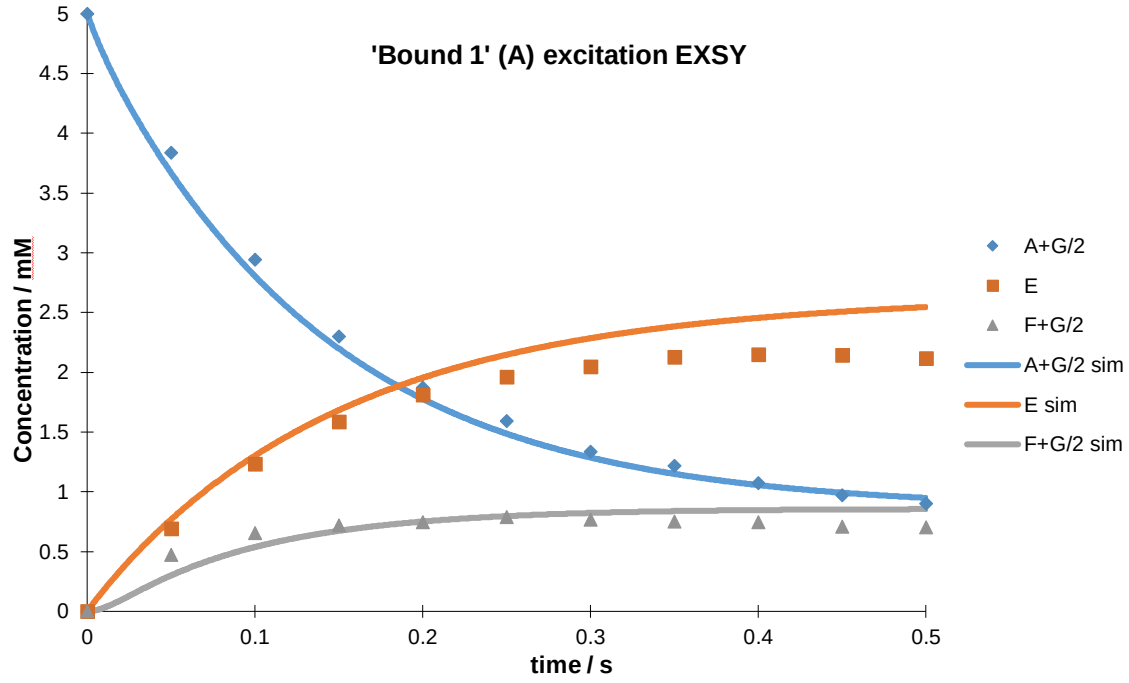

Figure 104: **raw real and simulated data for observed exchange of (−)-nicotine *1* molecules with precatalyst IMes *18* using Model 3, following selective excitation of Bound 1 (species** A**) resonance at 298 K. Samples were 5 mM precatalyst in methanol-d_4 with five equivalents of substrate, activated with 4 bar of hydrogen**

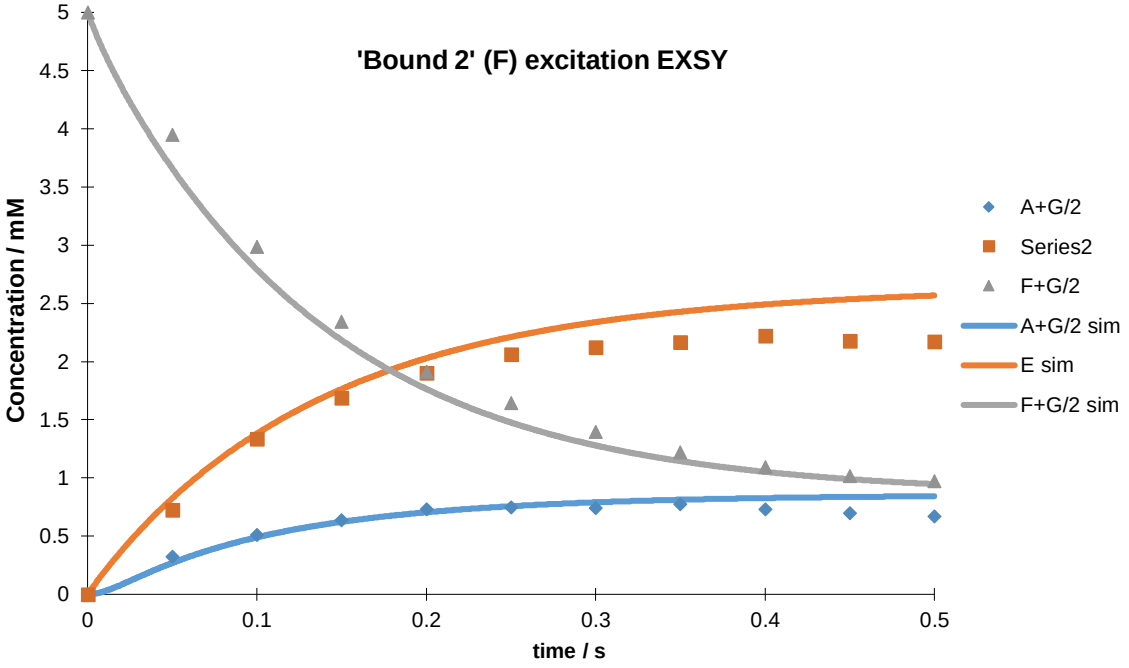

Figure 105: **raw real and simulated data for observed exchange of (−)-nicotine *1* molecules with precatalyst IMes *18* using Model 3, following selective excitation of Bound 1 (species** F**) resonance at 298 K. Samples were 5 mM precatalyst in methanol-d_4 with five equivalents of substrate, activated with 4 bar of hydrogen**

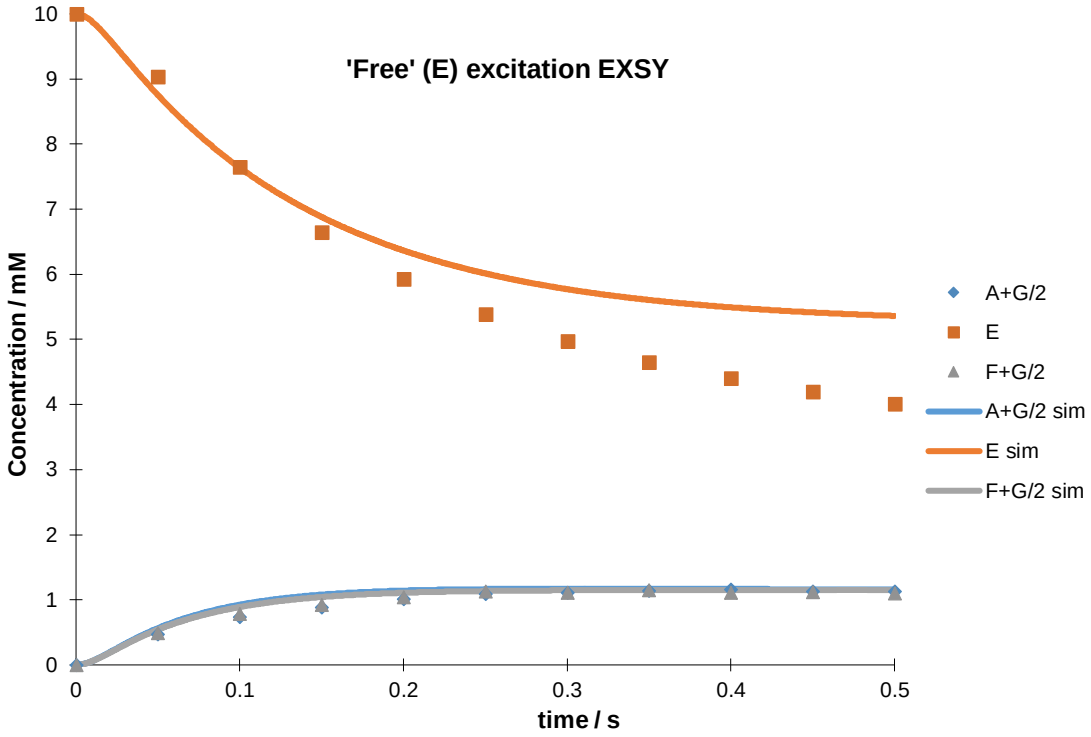

Figure 106: **raw real and simulated data for observed exchange of (−)-nicotine *1* molecules with precatalyst IMes *18* using Model 2, following selective excitation of ligand 'free' in solution (species** E**) resonance at 298 K. Samples were 5 mM precatalyst in methanol-d_4 with five equivalents of substrate, activated with 4 bar of hydrogen.**

It was observed that although the fit for Model 3 was much improved compared to Model 2, there was significant deviation between the real data and simulated data at higher time intervals. The deviation was particularly acute in excitation of ligand free in solution (Figure 106), where the observed concentration of excited free ligand dropped off far more quickly than predicted. This discrepancy was again attributed to relaxation of the NMR signal not yet being considered in the model. Model 3 was subsequently applied to a range of catalyst-substrate combinations across a range of temperatures (Figure 107).

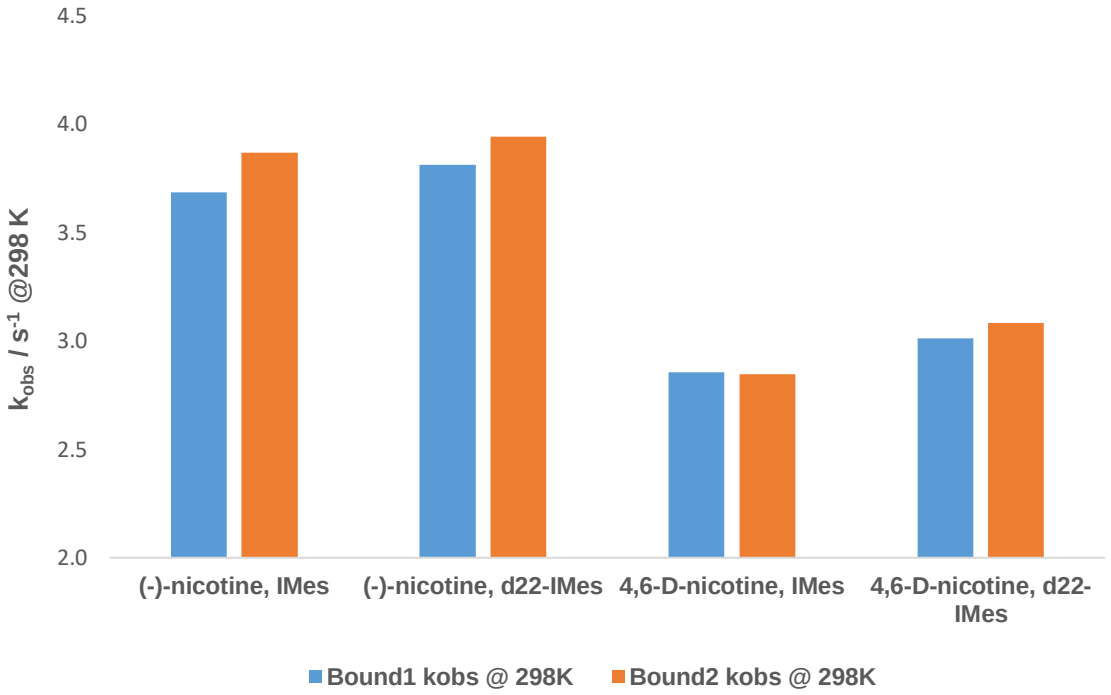

Figure 107: observed rate constants for dissociation of substrate molecules at 298 K using Model 3. Samples were 5 mM precatalyst in methanol-d_4 with five equivalents of the substrate, activated with 4 bar of hydrogen

The observed rates of dissociation of each bound form in a catalyst-substrate combination are much more homogenous than those obtained originally using Model 1 (see Figure 4). Furthermore, while Model 1 had no obvious correlation between rates and deuteration of catalyst and/or substrate, the results from Model 3 were more promising. There appeared to be a relationship between deuteration of the substrate and rate of dissociation, with both entries for 4,6-nicotine-d_2 **9** calculated as dissociating ~0.8 s^{-1} slower than their equivalents with (−)-nicotine **1**. This contrasted with the previous theory that deuterated substrates should not differ much from their undeuterated counterparts – as secondary kinetic isotope effects on molecules this size should be relatively small. However, it was yet again suspected that unaccounted relaxation differences were the culprit for the varied dissociation rates, as it was already well-established (Chapter 3) that 4,6-nicotine-d_2 **9** relaxes much more slowly than (−)-nicotine **1**. Relatively rapid relaxation of the signal for (−)-nicotine **1** would artificially inflate the rate at which substrate was dissociating compared to any similar effect on 4,6-nicotine-d_2 **9**, consistent with Model 3 observations above.

4.2.2 Model 4

Errors and fits observed with Models 2 and 3 showed it was paramount to properly account for relaxation effects when trying to model SABRE exchange. The solution proposed was relatively simple - a relaxation term was added to the end of calculations of simulated concentration of each species (Equation 4). This term approximated relaxation by removing a small amount of signal/apparent concentration (proportional to the relaxation time T_1) with each entry in the simulated series to help match the *observed* reduction of signal in the real data. Therefore, the data solver was not creating errors trying to fit two essentially different datasets as if they represented the same process.

$$\dots - \left(\frac{1}{T_1}\right)[X]_{prev}(\Delta t)$$

Equation 4: simulated relaxation term for kinetic modelling. $[X]_{prev}$ refers to the concentration of 'species X' in the previous iteration and Δt is the time elapsed since that previous iteration

As T_1 relaxation times are known to change dramatically between substrate free in solution and substrate bound to the catalyst, the value of T_1 used in Equation 4 was changed between the free and bound values as appropriate for the species it was applied to. It was also acknowledged that the values of T_1 used may not be entirely representative of the true T_1 times, for example, the T_1 values used for 'bound' ligand were actually the T_1 values of the ligand free in solution but in the presence of the activated catalyst (*i.e.* activated conditions as described in Chapter 3.1.2). This is a weighted average of the bound and free ligand T_1 values and is used because the rapid exchange of molecules at ambient temperatures makes measuring the 'true' bound ligand T_1 impractical. Therefore, the T_1 values inputted were constrained by a sensible range and allowed to be varied by the model to ensure a good fit.

It was also realised that rigidly defining the initial concentrations of the various species was likely causing bias in the fit. Every *measured* data point in each series varied by some margin of error (due to inherent experimental error, *etc.*) and so it was considered prudent to treat the starting point with some flexibility to compensate. Therefore, the initial concentration of each species was defined as a (limited) range about the theoretical value.

The cumulative improvements featured in Model 4 were applied to the EXSY spectra various combinations of precatalyst, substrate and temperature. As a sample, the results for 4,6-nicotine-d_2 **9** with IMes **18** at 298 K are shown below in Figures 108-110. Full results are listed in Chapter 7. Visually, the fits were much improved, with minimum sum-of-least-squares in single figures.

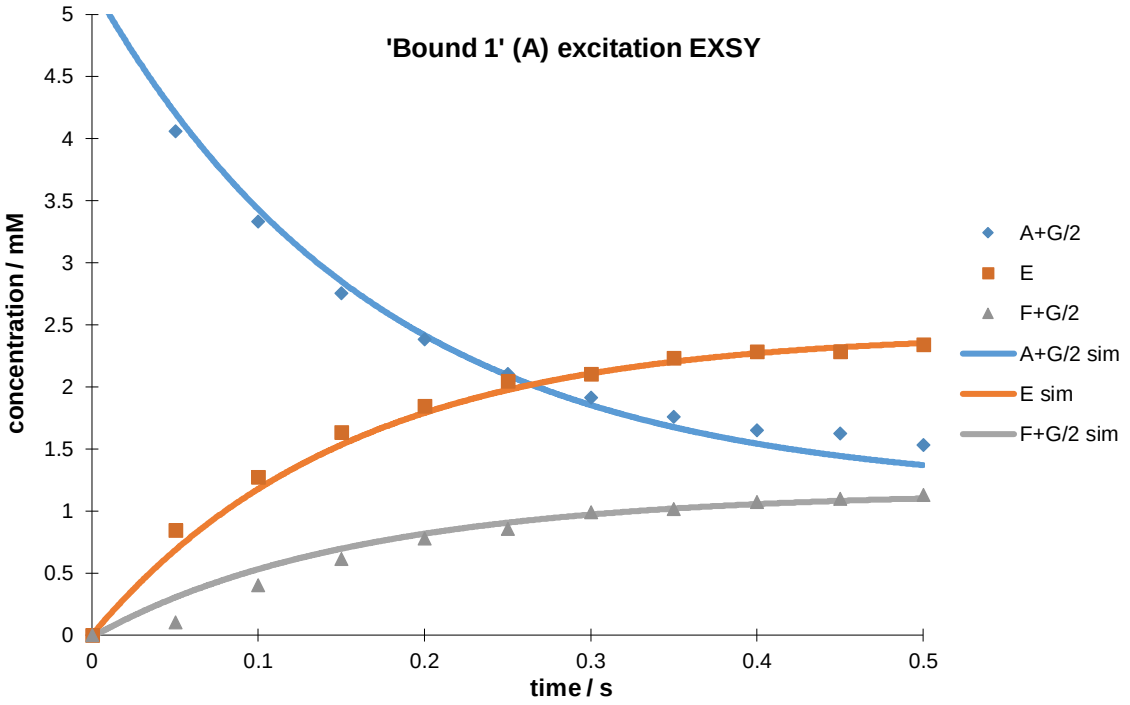

Figure 108: **raw real and simulated data for observed exchange of 4,6-nicotine-d_2 *9* molecules with precatalyst IMes *18* using Model 4, following selective excitation of Bound 1 (species** A**) resonance at 298 K. Samples were 5 mM precatalyst in methanol-d_4 with five equivalents of substrate, activated with 4 bar of hydrogen**

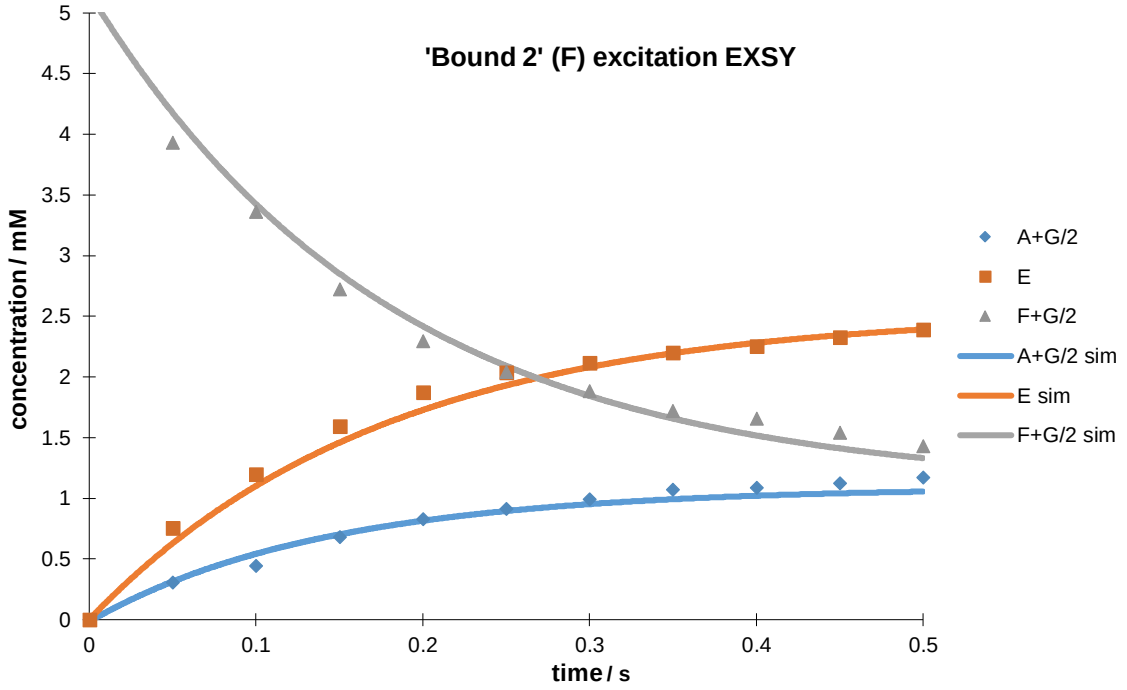

Figure 109: **raw real and simulated data for observed exchange of 4,6-nicotine-d_2 *9* molecules with precatalyst IMes *18* using Model 4, following selective excitation of Bound 2 (species F) resonance at 298 K. Samples were 5 mM precatalyst in methanol-d_4 with five equivalents of substrate, activated with 4 bar of hydrogen**

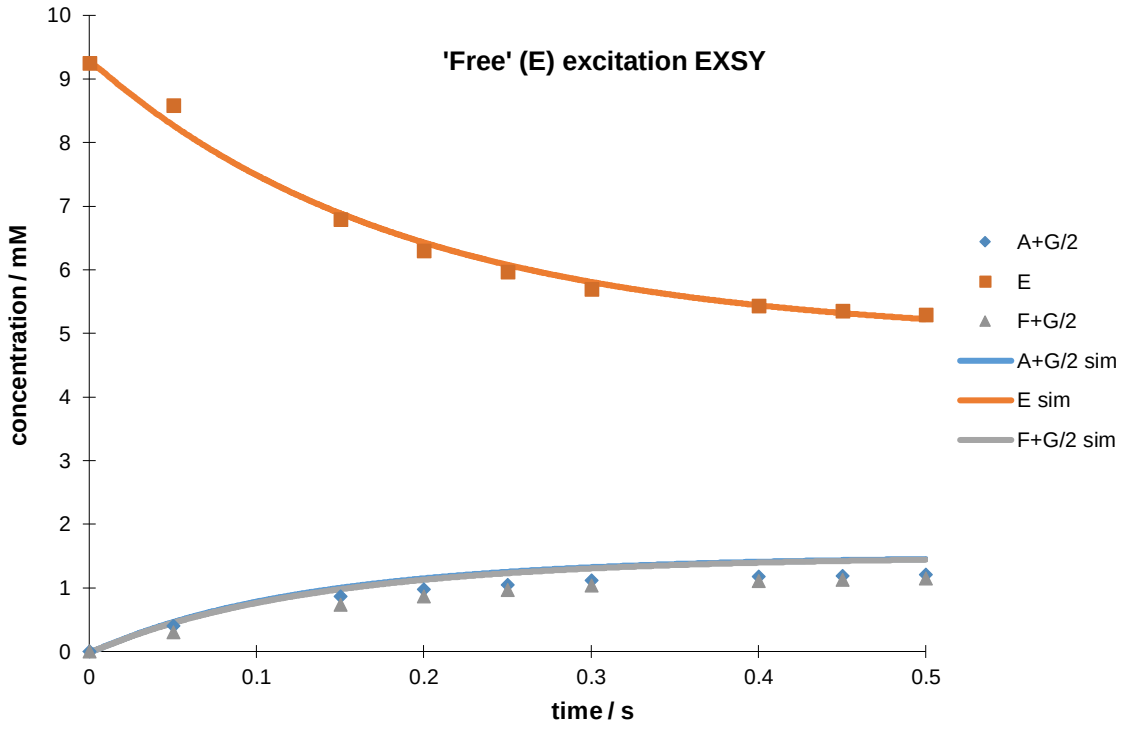

Figure 110: **raw real and simulated data for observed exchange of 4,6-nicotine-d_2 *9* molecules with precatalyst IMes *18* using Model 4, following selective excitation of ligand 'free' in solution (species E) resonance at 298 K. Samples were 5 mM precatalyst in methanol-d_4 with five equivalents of substrate, activated with 4 bar of hydrogen**

The results obtained using Model 4 indicated a significant improvement over previous models, with sum-of-least-squares values no greater than 5 indicating an excellent fit. In addition, the rate constants derived from this fit generally appear to be sensible (Table 6). The rate of dissociation of ligands from species **A** and **F** into their constituent species is consistently around 3 s^{-1} and the consumption of intermediates **B**, **C**, **D** and **E** are all approximately the same as each other.

-11.712	**3.058**	**2.798**	2.798	3.058	0	0	0	**A**
23.950	-50.273	0	0	0	23.249	0	3.075	**B**
23.249	0	-50.273	0	0	23.950	3.075	0	**C**
23.249	0	0	-50.273	0	23.950	0	3.075	**D**
23.950	0	0	0	-50.273	23.249	3.075	0	**E**
0	2.798	3.058	3.058	2.798	-11.712	0	0	**F**
0	0	44.417	0	44.417	0	-88.835	0	**G**
0	44.417	0	44.417	0	0	0	-88.835	**H**
A	**B**	**C**	**D**	**E**	**F**	**G**	**H**	

Table 6: **(observed) rate constants generated by Model 4 for 4,6-nicotine-*d*$_2$ *9* and IMes *18* at 298 K. k_{XY} = XY (i.e. k_{AB} is row A, column B). Only rates marked in green are actual rates, those in grey correspond to processes that do not exist. Rates marked in bold are equivalent to the 'Bound 1' and 'Bound 2' dissociations in Model 1**

Model 4 was subsequently applied to all combinations of substrate and precatalyst across a range of temperatures (Figure 111). The calculated dissociative rate constants appeared relatively homogenous as expected with theoretical predictions, at an average of 3.08 ± 0.07 s^{-1} for all combinations. Deviation between the bound forms and between substrate/precatalyst combinations was minimal, with all entries bar one within a single standard deviation of the mean. It should be noted that although the exchange rates appear more uniform in Model 4, the more important distinction is that the average dissociation rate is a full 15% lower than it was for the equivalent data analysed by Model 1. Given how crucial optimum exchange rates are for SABRE efficiency, this is a significant discovery.

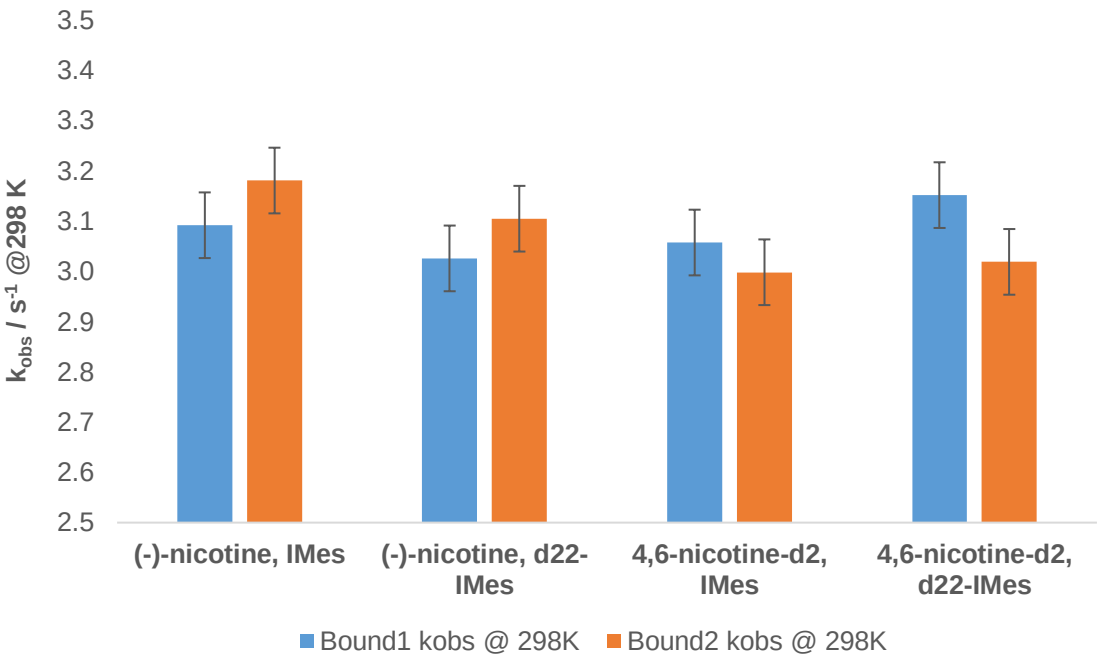

Figure 111: observed rate constants for dissociation of substrate molecules at 298 K using Model 4. Samples were 5 mM precatalyst in methanol-d4 with five equivalents of the substrate, activated with 4 bar of hydrogen. Error bars are the standard deviation of all results (n=8)

Once more, the measuring of rate constants over a range of temperatures using Equation 3 allowed construction of Eyring plots to determine the enthalpy (Figure 112) and entropy (Figure 113) of activation for dissociation of ligands for each combination of substrate and precatalyst.

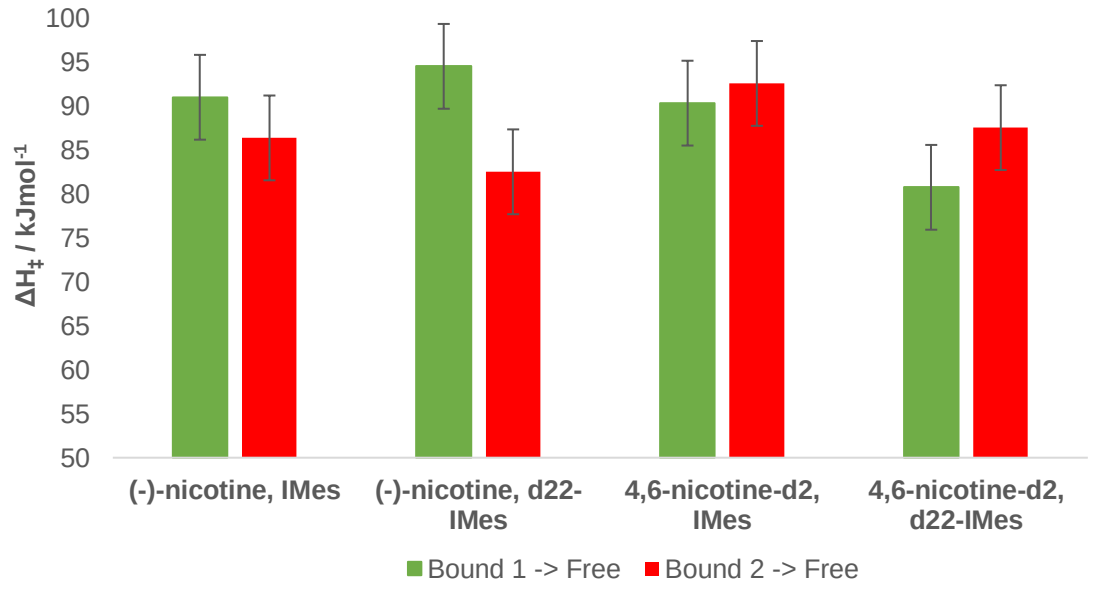

Figure 112: enthalpies of activation for ligand dissociation for a range of substrate/precatalyst combinations using Model 4. Error bars are the standard deviation of all results (n=8)

It was observed that every substrate/precatalyst combination gave very similar enthalpies of activation, at an average of 88.2 ± 4.8 kJ mol^{-1}. Some variations were still observed but less than those in the original Model 1 – five out of eight entries are within one standard deviation of the mean and all are within 1.5 standard deviations of the mean. The same nitrogen-iridium bond is being broken in each case – it can be concluded from the similarity in enthalpy that secondary isotope effects from incorporated deuterium have little effect on the strength of this bond.

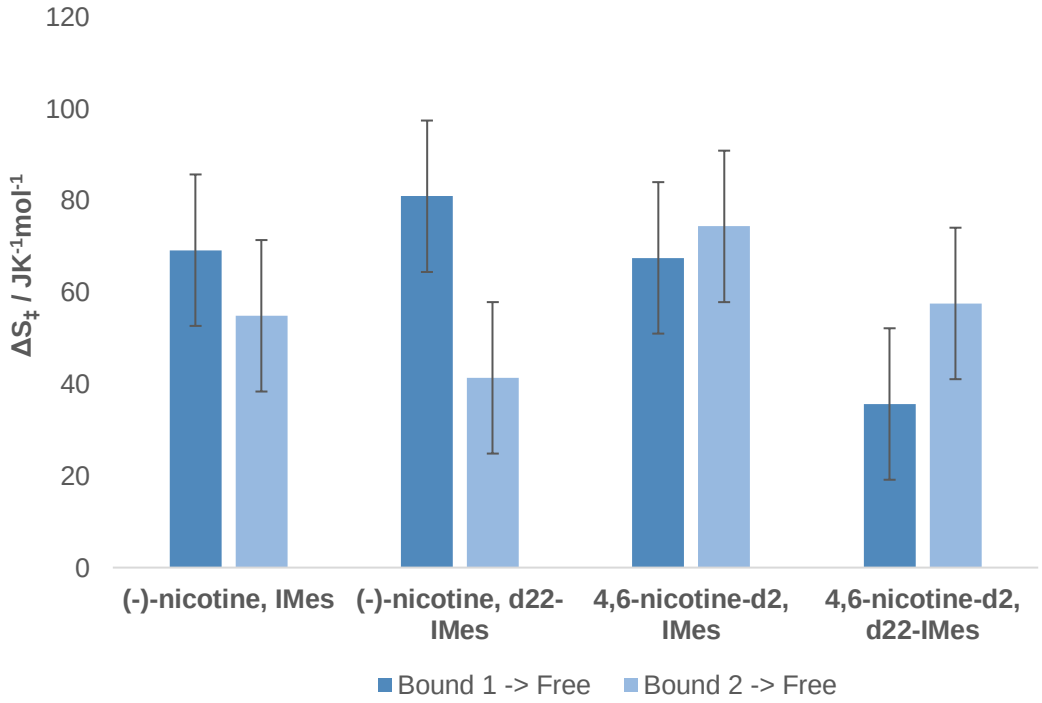

Figure 113: **entropies of activation for ligand dissociation for a range of substrate/precatalyst combinations. Error bars are the standard deviation of all results (n=8)**

Entropy of activation relates to the energy of the dissociation transition state. No obvious correlation was observed between deuteration of the catalyst and/or deuteration of the substrate and this parameter. Given the relative homogeneity of exchange rates at a given temperature and the enthalpies of activation, it can be concluded that variations in entropy of activation are not a key determining factor for the exchange processes.

As with Model 1, the activation enthalpies and entropies of dissociation were used to calculate the Gibbs free energies of dissociation for Model 4.

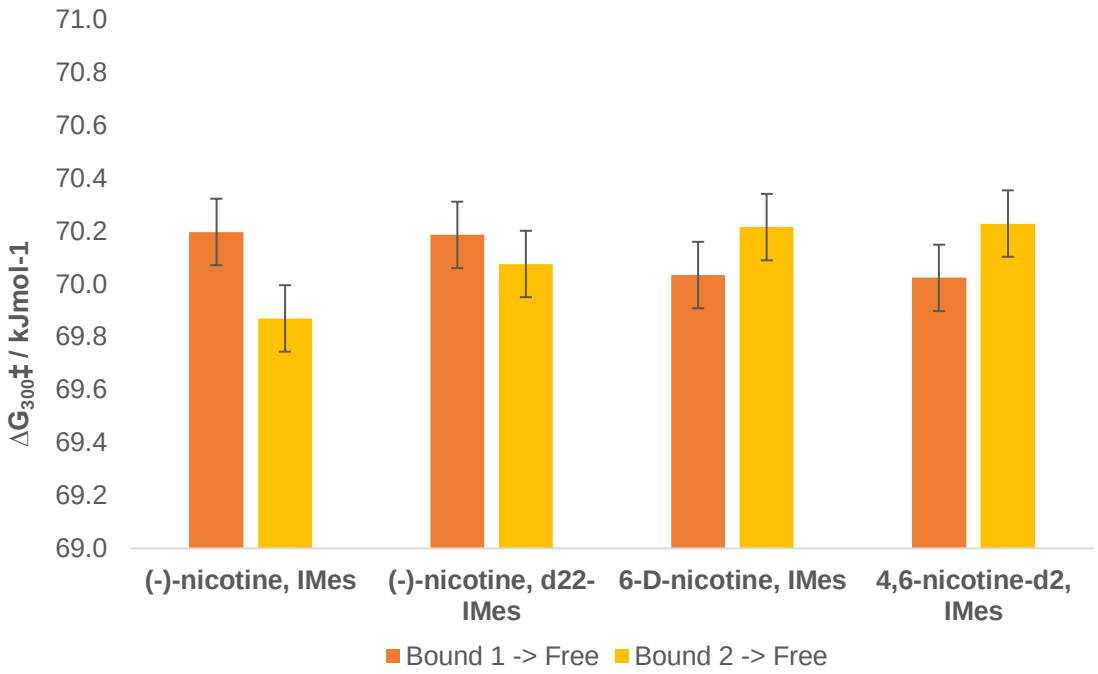

Figure 114: Gibbs free energies of activation for the dissociation of bound substrate molecules from iridium using Model 4

Strong uniformity in the results was observed, with an average of 70.10 ± 0.13 kJ mol^{-1} for every combination of catalyst and substrate tested. Only one entry lay outside one standard deviation of the mean giving good confidence in the reliability of the result.

4.3 Summary/Conclusions

Chirality is not a parameter considered previously in the analysis of SABRE. Once the unusual property of chemically-distinct ligands on the catalyst was noticed, it became apparent that reliably calculating exchange rates of chiral ligands was significantly more complex and many parameters were being ignored. The use of the existing simple model gave somewhat varied results with no obvious correlation – these variations were difficult to rationalise with the confident theory that deuterium-labelling makes minimal changes to the masses of the substrate and catalyst and secondary kinetic/remote isotope effects are typically small.

More thorough assessment considering intermediate and unobservable species led to Model 3, where a significantly lower, yet consistent dissociation rate was calculated for entries with deuterated substrate ligands versus their non-deuterated equivalents. This confirmed suspicions that relaxation of the signal, as-yet unmodelled, was artificially

boosting the calculated exchange rates of more rapidly-relaxing ligands (*i.e.* non-deuterated nicotine ligands) and artificially reducing the calculated rates for more slowly-relaxing ligands (*i.e.* deuterated nicotines). It is fortunate that the calculated exchange rates for nicotines are relatively slow, as other well-documented systems likely exchange too rapidly for the effects of relaxation on EXSY to be readily noticed.

Model 4 incorporated a term to help account for differing relaxation rates of various species. It calculated plausible observed rate constants for defined species *and* intermediates with reduced deviation observed in dissociation rate, activation enthalpies and free energies for varyingly deuterated substrates and precatalysts. The quality of fit was also noticeably improved upon all previous models. While it may appear by some measures that Model 4 is only a marginal improvement upon Model 1 for this system, it is important to recognise that Model 4 assesses considerably more variables and incorporates over 50% more raw data through the inclusion of free ligand excitation EXSY and relaxation data. Hence, the results produced can be more confidently expressed as accurate.

The key result for Model 4 is a significantly lower calculated average dissociation rate at 3.079 s^{-1} at 298 K versus 3.562 s^{-1} calculated using Model 1, a full 16% reduction. Similar reductions between 8 and 19% were observed for Model 4 versus Model 1 at the other temperatures tested (for full data, see the appendix in Chapter 7). As Model 1 is essentially the model by which the majority of literature SABRE exchange data has been calculated, it could be concluded that existing literature will have significantly overestimated exchange rates.

5: Future work

As a complex and multidisciplinary project, there is a wide scope for future work. Firstly, there is the potential for testing new nicotine-based SABRE substrates. Such substrates could have alternative deuteration patterns on the pyridine ring not covered by the Comins-derived methodology used thus far. Alternatively, deuteration of the pyrrolidine ring may yield improved results by reducing the small quantiy of hyperpolarisation 'leakage' into that ring observed by OPSY. Thirdly, isotopic labelling and SABRE studies could be readily extended to similar/related compounds such as isonicotine and nornicotine.

Continuation of SABRE studies on the nicotine isotopologues in this project is another option for further study. Optimisation of solvent was only briefly covered in the project, selection and refinement with a more biocompatible solvent would greatly lead in progressing the initial imaging studies undertaken so far into full *in vivo* MRI. Alternatively, SABRE-RELAY offers another promising route to testing nicotine isotopologues for *in vivo* use.

Lastly, the results from Model 4 suggest existing literature exchange rates are likely overestimates. Therefore, applying Model 4 to another chiral SABRE system to allow further refinement, or adapting the model to assess the more common achiral substrates should prove insightful. Chiral amines, particularly amino acids, are of great interest as potential SABRE substrates and initial efforts could focus there.

6: Experimental

6.1 Standard/general methods

All non-aqueous reactions were carried out under oxygen free Ar using flame-dried glassware. THF was freshly distilled from benzophenone, diethyl ether was freshly distilled over sodium. Alkyllithiums were titrated against *N*-benzylbenzamide before use.[37] (-)-Nicotine **1**, *n*-hexane and methanol were each distilled over CaH_2 before use. Brine refers to a saturated solution. Water is distilled water.

Flash column chromatography was carried out using Fluka Chemie GmbH silica (220-440 mesh). Thin layer chromatography was carried out using commercially available Merck F254 aluminium backed silica plates. Proton (400 MHz) and carbon (100.6 MHz) NMR spectra were recorded on a JEOL ECX-400 or Bruker Avance III instrument using 5mm inverse gradient probes and internal deuterium locks. For samples recorded in $CHCl_3$, chemical shifts are quoted in parts per million relative to $CHCl_3$ (δH 7.25) and $CDCl_3$ (δ_C 77.0, central line of triplet). Carbon NMR spectra were recorded with broad band proton decoupling and assigned using DEPT experiments. Coupling constants (*J*) are quoted in Hertz. Infrared spectra were recorded on a Perkin Elmer Spectrum Two FT-IR spectrometer with UATR attachment. Electrospray high and low resonance mass spectra were recorded at room temperature on a Bruker Daltronics microTOF spectrometer. Buffered LC-MS experiments were conducted at room temperature on a Thermo Scientific Dionex UltiMate 3000 with a 2.7 µm x 4.6 mm x 50 mm reversed-phase column, 0.6 mL min^{-1} flow rate and an 8 min continuous gradient from 10 mM ammonium $formate_{(aq)}$ to acetonitrile, connected to a Bruker amaZon SL ion trap spectrometer.

4 Bar of hydrogen/*para*-hydrogen refers to the absolute pressure in the sample vessel. The gauge pressure displayed on an MKS Baratron® capacitance manometer indicates pressure relative to ambient atmospheric conditions. 3 Bar on these gauges therefore correspond to approximately 4 bar of absolute pressure.

6.2 Specialised approaches

Preparation of *para*-hydrogen

Para-hydrogen was produced by cooling hydrogen gas to 25 K over iron (III) oxide in a *para*-hydrogen generator supplied by Bruker. 99% *para*-hydrogen produced in this manner was used throughout the project.

Standard sample preparation and activation (Method 1)

A specified substrate, a precatalyst and solvent were placed in an NMR tube fitted with a Young's tap. The standard concentrations of reagents was 25 mM substrate, 5 mM catalyst in 0.6 mL methanol-d_4 unless otherwise stated. This concentration was chosen because it leads to an active catalyst of form $[Ir(H)_2(NHC)(substrate)_3]Cl$ and a 2-fold excess of substrate in solution.

The sample was degassed under vacuum at −78 ºC, the warmed to rt, charged with 4 bar of hydrogen gas and shaken vigorously for ~10 s. This process allows catalyst activation to occur. Catalyst activation was viewed by following appearance of peaks in the hydride region (~22-23 ppm) of a thermal ^{1}H NMR spectrum. Complete activation had occurred when these peaks no longer increased in size.

Achieving SABRE (shake-and-drops in stray field) (Method 2)

A sample was prepared according to Method 1. The NMR tube was recharged with 4 bar of *para*-hydrogen and shaken vigorously in an up-down motion by hand for 10 s in the stray magnetic field of an NMR spectrometer at 65 G (unless otherwise stated), then immediately placed in the spectrometer for measurement with a one-scan ^{1}H NMR experiment.

The NMR tube was removed from the spectrometer and vented of remaining *para*-hydrogen before being recharged. The process was repeated to allow for error in the individual experiments.

Achieving SABRE (shake-and-drops with magnetic shaker) (Method 3)

A sample was prepared according to Method 1. The NMR tube was recharged with 4 bar of *para*-hydrogen, placed in the magnetic shaker assembly and sealed. The assembly was shaken vigorously in an up-down motion by hand for 10 s after which the NMR tube was removed and immediately placed in the spectrometer for measurement with a one-scan ^{1}H NMR experiment.

The NMR tube was removed from the spectrometer and vented of remaining *para*-hydrogen before being recharged. The process was repeated to allow for error in the individual experiments.

Calculation of signal enhancement

The ^{1}H NMR signal enhancement was calculated by direct comparison of integrals in the spectrum of a hyperpolarised sample to those in a reference spectrum of the same sample when completely relaxed and polarised thermally. Experimentally, the reference and hyperpolarised spectra were collected using the same NMR spectrometer with identical acquisition parameters (in particular the receiver gain). The raw integrals were compared using Equation 5, where E is the enhancement, S_{hyp} is the signal of the hyperpolarised sample measured by integral and S_{therm} is the signal of the thermally polarised sample measured by integral:

$$E = \frac{S_{hyp}}{S_{therm}}$$

Equation 5: equation for calculation of signal enhancement

Flow methodology (Method 4)

In a different approach, hyperpolarisation was achieved through use of an automated polariser setup. The volume of the cell was increased relative to that of an NMR tube, hence the new standard volume was 3 mL of solvent with the same standard 25 mM substrate and 5 mM precatalyst concentrations as for Method 1.

The full 3 mL sample was injected into the mixing chamber. Hydrogen at 4 bar was bubbled through the sample for activation, which was then shuttled via a transfer line into

the 125 µL cell of a *p*-H_2-modified Bruker TXI inverse gradient flow probe in the NMR spectrometer. A thermal ^1H spectrum was recorded for reference signal intensity as in Method 2.

After return of the sample to the mixing chamber, hyperpolarisation was achieved by *para*-hydrogen bubbling at 4 bar in a polarisation transfer field generated by the chamber's coil. Standard bubbling time was 10 seconds with 65 G transfer field unless otherwise specified. This mimicks the shaking action performed in Method 2. Subsequent, immediate shuttling to the spectrometer occured, followed by recording of a one-scan ^1H NMR spectrum.

The benefits of this approach are that the field and bubbling time can both be rigorously controlled. Potential problems are solvent evaporation with repeated shuttling and a ~5 s delay between polarisation and measurement. This compares to ~2s delay for the shake-and-drops.

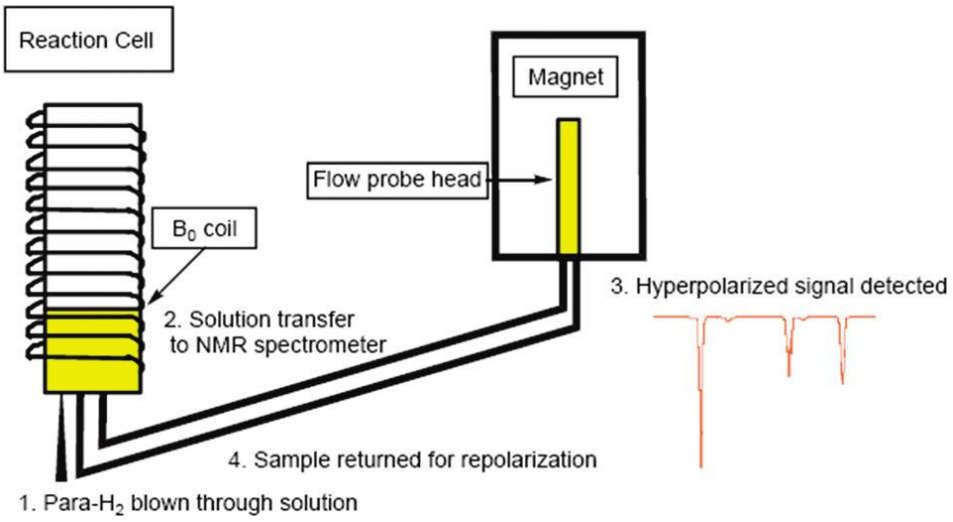

Figure 115: Depiction of automated flow setup for SABRE

^{1}H T_1 relaxation time measurement via inversion-recovery (Method 5)

A sample was prepared according to Method 1. The NMR tube was recharged with 4 bar of hydrogen and shaken vigorously in an up-down motion by hand. Catalyst activation was determined by thermal ^{1}H NMR.

Derivation of the substrate's ^{1}H T_1 relaxation times was achieved through the inversion-recovery pulse sequence depicted in Figure 116. An initial 180° pulse flips longitudinal magnetisation M_z into the –z axis. A subsequent 90° pulse after time delay τ moves magnetisation into the observable xy plane, where it is observed over time *t*. As the magnitude of magnetisation in –z gradually decreases with time, delay τ between the two pulses will give decreased observable signal intensity. Multiple iterations with variation of τ allows the decay/relaxation of the NMR signal to be observed and quantified.

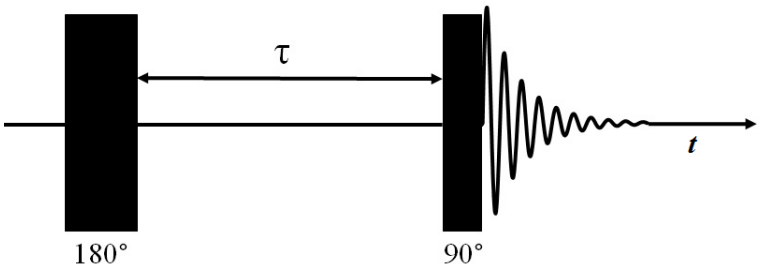

Figure 116: inversion-recovery pulse sequence to derive T_1 relaxation times

^{1}H T_1 relaxation time measurement via saturation-recovery (Method 6)

A sample was prepared according to Method 1. The NMR tube was recharged with 4 bar of hydrogen and shaken vigorously in an up-down motion by hand. Catalyst activation was determined by thermal ^{1}H NMR. Derivation of the substrate's ^{1}H T_1 relaxation times was achieved through the saturation recovery pulse sequence depicted in Figure 117. A train of rapidly-repeated 90˚ RF pulses (sometimes called a 'pulse comb') completely dephases longitudinal magnetisation M_z. M_z recovers over time delay τ and a subsequent 90° pulse moves recovered magnetisation into the observable *xy*-plane, where it is observed over time *t*. As the recovery of magnetisation in the *z*-axis gradually increases with time, increased delay τ between the two pulses will give increased observable signal intensity. Multiple iterations with variation of τ allows the decay/relaxation of the NMR signal to be observed and quantified.

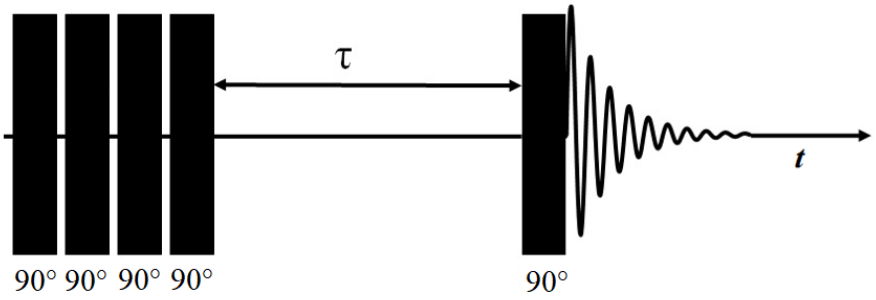

Figure 117: saturation-recovery pulse sequence to derive T_1 relaxation times. Note that the 'pulse comb' of repeated 90° pulses does not necessarily contain four pulses, this is merely a simplification

Exchange Spectroscopy (EXSY) (Method 7)

A sample was prepared according to Method 1. The NMR tube was recharged with 4 bar of hydrogen and shaken vigorously in an up-down motion by hand. Catalyst activation was determined by thermal ^{1}H NMR. When a signal is excited, detection usually follows immediately. If a signal is selectively excited and a short period elapses before measuring, then the nuclei associated with the signal can move to a different site in the molecule. In other words, a reaction has taken place or an exchange process has occurred. By varying the delay, the rate of this change can be determined.

This was achieved using the *selnogp* pulse sequence (described in Chapter 4.1.2). *selnogp* selectively excites a specific proton resonance in each catalyst form of the substrate in a series of experiments with varying mixing time. Observed rate constants for dissociation of substrate from the catalyst were determined via non-linear least-squares analysis of the results against simulated data. Repetitions of the process at different temperatures allowed construction of an Eyring plot to determine the activation entropy and enthalpy of this process.

Error calculation

Errors given throughout this project are the *standard error* (*i.e.* standard deviation of the mean) unless otherwise specified. Standard errors are calculated according to Equation 6 below.

$$S.E = \frac{\sigma}{\sqrt{n}}$$

Equation 6: equation for standard error (S.E.), where σ is the standard deviation and *n* is the number of entries in the data series

6.3 Synthetic results

(*R*)-6-Chloro-5-(1-methylpyrrolidin-2-yl)pyridine *2* (6-chloronicotine) and (*R*)-2-chloro-5-(1-methylpyrrolidin-2-yl)pyridine *3* (2-chloronicotine)

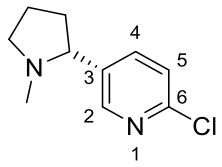

2

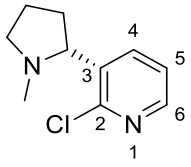

3

n-Butyllithium (13.00 mL of a 2.5 M solution in hexanes, 32.4 mmol, 5.4 eq.) was added dropwise to a stirred solution of 2-(dimethylamino)ethanol (0.90 mL, 18.0 mmol, 3.0 eq.) in *n*-hexane (10 mL) at 0 °C under Ar. The resulting solution was stirred at 0 °C for 30 min and then cooled to −20 °C. Then, (−)-nicotine **1** (0.95 mL, 6.0 mmol, 1.0 eq.) was added dropwise. The resulting solution was stirred at −20 °C for 1 h and then cooled to −78 °C. A solution of hexachloroethane (5.68 g, 24.0 mmol, 4.0 eq.) in toluene (15 mL) was added and the solution was stirred at −78 °C for 1 h. Saturated $NaHCO_{3(aq)}$ (20 mL) was added and the two layers were separated. The aqueous layer was extracted with CH_2Cl_2 (3 × 20 mL). The combined organic layers were dried ($MgSO_4$) and evaporated under reduced pressure to give the crude product. Purification by flash column chromatography on silica with EtOAc as eluent gave an 80:20 mixture (by ^{1}H NMR spectroscopy) of 2-chloronicotine **3** and 6-chloronicotine **2** (309 mg, 26%) as a pale yellow oil, R_F (EtOAc) 0.26; ^{1}H NMR (400 MHz, $CDCl_3$) diagnostic peaks for 2-chloronicotine **3**: 8.25 (dd, *J* = 4.5, 2.0 Hz, 1H, 6-py), 7.94 (dd, *J* = 7.5, 2.0 Hz, 1H, 4-py) and 6-chloronicotine **2** (592 mg, 51%) as a pale yellow oil, R_F (EtOAc) 0.14; $[\alpha]_D^{20}$ −121

(*c* 1.0 in CH_2Cl_2) (lit.,[38] –154 (c. 1.0 in MeCN)); IR (ATR): 2965, 2779, 1552, 1448, 1357, 1215, 1108, 880 cm^{-1}; ^1H NMR (400 MHz, $CDCl_3$): δ 8.28 (d, *J* = 2.0 Hz, 1H, 2-py), 7.66 (dd, *J* = 8.0, 2.0 Hz, 1H, 4-py), 7.27 (d, *J* = 8.0 Hz, 1H, 5-py), 3.21 (ddd, *J* = 9.5, 8.0, 2.0 Hz, 1H, NCH), 3.07 (dd, *J* = 8.5, 8.5 Hz, 1H, NCH), 2.29 (ddd, *J* = 9.5, 8.5, 8.5 Hz, 1H, NCH), 2.23-2.15 (m, 1H, CH), 2.14 (s, 3H, NMe), 1.98-1.88 (m, 1H, CH), 1.85-1.76 (m, 1H, CH), 1.71-1.60 (m, 1H, CH); ^{13}C NMR (100.6 MHz): δ 150.1 (C, 6-py), 149.2 (CH, 2-py), 138.0 (C, 3-py), 137.8 (CH, 4-py), 124.3 (CH, 5-py), 64.9 (NCH), 56.8 (NCH_2), 40.6 (NMe), 33.4 (CH_2), 22.8 (CH_2); MS (ESI) *m/z* 199 [(M (^{37}Cl) + H)$^+$, 31], 197 [(M (^{35}Cl) + H)$^+$, 100] ; HRMS *m/z* calculated for $C_{10}H_{13}{}^{35}ClN_2$ (M + H)$^+$ 197.0840, found 197.0846 (−1.9 ppm error). Spectroscopic data consistent with those reported in the literature.[38]

Lab book number: WHD/1/11/1

n-Butyllithium (3.80 mL of a 1.43 M solution in hexanes, 5.4 mmol, 5.4 eq.) was added dropwise to a stirred solution of 2-(dimethylamino)ethanol (0.30 mL, 3.0 mmol, 3.0 eq.) in *n*-hexane (2 mL) at 0 °C under Ar. The resulting solution was stirred at 0 °C for 30 min and then cooled to −20 °C. Then, (−)-nicotine **1** (0.16 mL, 1.0 mmol, 1.0 eq.) was added dropwise. The resulting solution was stirred at −20 °C for 1 h and then cooled to −78 °C. A solution of hexachloroethane (946 mg, 4.0 mmol, 4.0 eq.) in *n*-hexane (3 mL) was added and the solution was stirred at −78 °C for 1 h. Saturated $NaHCO_{3(aq)}$ (5 mL) was added and the two layers were separated. The aqueous layer was extracted with CH_2Cl_2 (3 × 10 mL). The combined organic layers were dried ($MgSO_4$) and evaporated under reduced pressure to give the crude product. Purification by flash column chromatography on silica with EtOAc as eluent gave 2-chloronicotine **3** as a pale yellow oil (12 mg, 6%), 6-chloronicotine **2** as a pale yellow oil (101 mg, 51%) and a 40:60 mixture (by ^1H NMR spectroscopy) of 2-chloronicotine **3** and 6-chloronicotine **2** as a yellow oil (10 mg, 5%).

Lab book number: WHD/1/1/1

n-Butyllithium (11.30 mL of a 1.43 M solution in hexanes, 16.2 mmol, 5.4 eq.) was added dropwise to a stirred solution of 2-(dimethylamino)ethanol (0.80 mL, 9.0 mmol, 3.0 eq.) in *n*-hexane (5 mL) at 0 °C under Ar. The resulting solution was stirred at 0 °C for 30 min and then cooled to −20 °C. Then, (−)-nicotine **1** (0.48 mL, 3.0 mmol, 1.0 eq.) was added dropwise. The resulting solution was stirred at −20 °C for 1 h and then cooled to −78 °C.

A solution of hexachloroethane (2.84 g, 12.0 mmol, 4.0 eq.) in *n*-hexane (10 mL) was added and the solution was stirred at −78 °C for 1 h. Saturated $NaHCO_{3(aq)}$ (10 mL) was added and the two layers were separated. The aqueous layer was extracted with CH_2Cl_2 (3 × 10 mL). The combined organic layers were dried ($MgSO_4$) and evaporated under reduced pressure to give the crude product. Purification by flash column chromatography on silica with EtOAc as eluent gave 6-chloronicotine **2** as a pale yellow oil (117 mg, 20%) and recovered (−)-nicotine **1** (216 mg, 44%). ^{1}H NMR spectrum of the crude product indicated trace quantities of 2-chloronicotine **3**, but this was not isolated.

Lab book number: WHD/1/5/1

(*R*)-5,6-Dichloro-5-(1-methylpyrrolidin-2-yl)pyridine *5* (5,6-dichloronicotine)

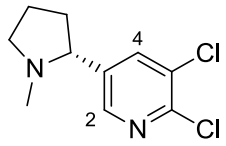

n-Butyllithium (0.50 mL of a 2.5 M solution in hexanes, 1.1 mmol, 1.1 eq.) was added dropwise to a stirred solution of 2,2,6,6-tetramethylpiperidine (0.20 mL, 1.1 mmol, 1.1 eq.) in THF (2 mL) at −78 °C under Ar. The resulting solution was stirred at −78 °C for 1 h. Then, a solution of 6-chloronicotine **2** (200 mg, 1.0 mmol, 1.0 eq.) in THF (1 mL) was added dropwise and the resulting solution was stirred at −78 °C for 1 h. A solution of hexachloroethane (290 mg, 1.2 mmol, 1.2 eq.) in THF (1 mL) was added and the solution was stirred at −78 °C for 1 h. Saturated $NaHCO_{3\,(aq)}$ (2 mL) was added and the two layers were separated. The aqueous layer was extracted with CH_2Cl_2 (2 × 10 mL). The combined organic layers were dried ($MgSO_4$) and evaporated under reduced pressure to give the crude product. Purification by flash column chromatography on silica with EtOAc as eluent gave 5,6-dichloronicotine **5** (136 mg, 59%) as a dark yellow oil, R_F (EtOAc) 0.55; $[\alpha]_D^{20}$ −138 (*c* 1.0 in CH_2Cl_2)(lit.,[18] $[\alpha]_D^{24}$ – 134 (*c* 0.55 in CH_2Cl_2)); IR (ATR): 2968, 2781, 1547, 1420, 1392, 1329, 1149, 1042 cm^{-1}; ^{1}H NMR (400 MHz, $CDCl_3$): δ 8.19 (d, *J* = 2.5 Hz, 1H, 2-py), 7.80 (d, *J* = 2.5 Hz, 1H, 4-py), 3.22 (ddd, *J* = 9.0, 7.0, 2.0 Hz, 1H, NCH), 3.10 (dd, *J* = 8.5, 8.5 Hz, 1H, NCH), 2.31 (ddd, *J* = 9.5, 9.0, 9.0 Hz, 1H, NCH), 2.24-2.18 (m, 1H, CH), 2.16 (s, 3H, NMe), 1.99-1.88 (m, 1H, CH), 1.86-1.76 (m, 1H, CH), 1.70-1.59 (m, 1H, CH) ; ^{13}C NMR (100.6 MHz): δ 147.7 (C, 6-py), 146.8 (CH, 2-py), 140.4 (C, 5-py), 137.9 (CH, 4-py), 130.8 (C, 3-py), 67.5 (NCH),

57.1 (NCH_2), 40.6 (NMe), 35.8 (CH_2), 22.8 (CH_2); MS (ESI) *m/z* 233 [(M ($^{35}Cl^{37}Cl$) + H)$^+$, 64], 231 [(M ($^{35}Cl_2$) + H)$^+$, 100]; HRMS *m/z* calculated for $C_{10}H_{12}{}^{35}Cl_2N_2$ (M + H)$^+$ 231.0450, found 231.0458 (−2.8 ppm error). Spectroscopic data consistent with those reported in the literature.[18]

Lab book number: WHD/1/9/4

(*R*)-4,6-Dichloro-5-(1-methylpyrrolidin-2-yl)pyridine *6* (4,6-dichloronicotine)

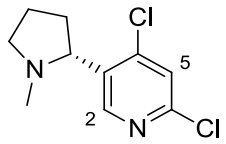

n-Butyllithium (0.88 mL of a 2.5 M solution in hexanes, 2.2 mmol, 1.1 eq.) was added dropwise to a stirred solution of 6-chloronicotine **2** (394 mg, 2.0 mmol, 1.0 eq.) in THF (3 mL) at −78 °C under Ar. The resulting solution was stirred at −78 °C for 1 h. A solution of hexachloroethane (520 mg, 2.2 mmol, 1.1 eq.) in THF (2 mL) was added and the solution was stirred at −78 °C for 1 h. Saturated $NaHCO_{3\,(aq)}$ (10 mL) was added and the two layers were separated. The aqueous layer was extracted with CH_2Cl_2 (3 × 10 mL). The combined organic layers were dried ($MgSO_4$) and evaporated under reduced pressure to give the crude product. Purification by flash column chromatography on silica with EtOAc as eluent gave 4,6-dichloronicotine **6** (349 mg, 76%) as a colourless oil, R_F (EtOAc) 0.57; $[\alpha]_D^{20}$ − 141 (*c* 1.0 in CH_2Cl_2)(lit.,[18] $[\alpha]_D^{27}$ – 182 (*c* 0.55 in CH_2Cl_2)); IR (ATR): 2955, 2778, 1556, 1450, 1357, 1215, 1108, 876 cm^{-1}; ^{1}H NMR (400 MHz, $CDCl_3$): δ 8.55 (s, 1H, 2-py), 7.31 (s, 1H, 5-py), 3.54 (dd, *J* = 8.0, 8.0 Hz, 1H, NCH), 3.23 (ddd, *J* = 9.5, 7.5, 2.0 Hz, 1H, NCH), 2.45-2.30 (m, 2H, NCH + CH), 2.23 (s, 3H, NMe), 1.94-1.76 (m, 2H, CH), 1.58-1.47 (m, 1H, CH); ^{13}C NMR (100.6 MHz): δ 149.7 (CH, 2-py), 149.6 (C, 6-py), 145.1 (C, 4-py), 136.2 (C, 3-py), 124.0 (CH, 5-py), 64.9 (NCH), 56.8 (NCH_2), 40.6 (NMe), 33.4 (CH_2), 22.8 (CH_2); MS (ESI) *m/z* 233 [(M ($^{35}Cl^{37}Cl$) + H)$^+$, 65], 231 [(M ($^{35}Cl_2$) + H)$^+$, 100]; HRMS *m/z* calculated for $C_{10}H_{12}{}^{35}Cl_2N_2$ (M + H)$^+$ 231.0450, found 231.0458 (−2.9 ppm error). Spectroscopic data consistent with those reported in the literature.[18]

Lab book number: WHD/1/21/3

(*R*)-2,6-Dichloro-5-(1-methylpyrrolidin-2-yl)pyridine *7* (2,6-dichloronicotine)

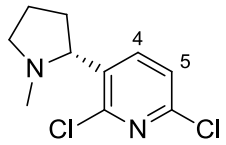

n-Butyllithium (3.20 mL of a 2.2 M solution in hexanes, 7.10 mmol, 5.4 eq.) was added dropwise to a stirred solution of 2-(dimethylamino)-ethanol (0.38 mL, 3.74 mmol, 3.0 eq.) in *n*-hexane (5 mL) at 0 °C under Ar. The resulting solution was stirred at 0 °C for 30 min and then cooled to −20 °C. Then, a solution of 6-chloronicotine **2** (245 mg, 1.25 mmol, 1.0 eq.) in *n*-hexane (1 mL) was added dropwise. The resulting solution was stirred at −20 °C for 1 h and then cooled to −78 °C. A solution of hexachloroethane (1.28 g, 5.39 mmol, 4.3 eq.) in toluene (5 mL) was added and the solution was stirred at −78 °C for 1 h. Saturated $NaHCO_{3(aq)}$ (5 mL) was added and the two layers were separated. The aqueous layer was extracted with CH_2Cl_2 (2 × 10 mL). The combined organic layers were dried ($MgSO_4$) and evaporated under reduced pressure to give the crude product. Purification by flash column chromatography on silica with EtOAc as eluent gave 2,6-chloronicotine **7** (148 mg, 51%) as a mid-yellow oil, R_F (EtOAc) 0.38; $[\alpha]_D^{20}$ −156 (*c* 1.0 in CH_2Cl_2) (lit.,[18] $[\alpha]_D^{26}$ – 191 (*c* 2.45 in CH_2Cl_2)); IR (ATR): 2936, 1547, 1452, 1424, 1322, 1138, 831, 781 cm^{-1}; ^1H NMR (400 MHz, $CDCl_3$): δ 7.92 (d, *J* = 8.0 Hz, 1H, 4-py), 7.27 (d, *J* = 8.0 Hz, 1H, 5-py), 3.51 (dd, *J* = 8.0, 8.0 Hz, 1H, NCH), 3.21 (ddd, *J* = 9.5, 7.5, 2.5 Hz, 1H, NCH), 2.45-2.32 (m, 2H, NCH + CH), 2.20 (s, 3H, NMe), 1.90-1.77 (m, 2H, CH), 1.54-1.42 (m, 1H, CH); ^{13}C NMR (100.6 MHz): δ 149.4 (C, 6-py), 148.0 (C, 2-py), 139.4 (C, 3-py), 137.4 (CH, 4-py), 123.5 (CH, 5-py), 65.8 (NCH), 56.8 (NCH_2), 40.6 (NMe), 33.4 (CH), 22.9 (CH); MS (ESI) *m/z* 233 [(M ($^{35}Cl^{37}Cl$) + H)$^+$, 64], 231 [(M ($^{35}Cl_2$) + H)$^+$, 100]; HRMS *m/z* calculated for $C_{10}H_{12}{}^{35}Cl_2N_2$ (M + H)$^+$ 231.0450, found 231.0458 (−3.4 ppm error). Spectroscopic data consistent with those reported in the literature.[18]

Lab book number: WHD/1/28/10

n-Butyllithium (4.39 mL of a 2.5 M solution in hexanes, 10.98 mmol, 5.4 eq.) was added dropwise to a stirred solution of 2-(dimethylamino)-ethanol (0.61 mL, 6.09 mmol, 3.0 eq.) in toluene (10 mL) at 0 °C under Ar. The resulting solution was stirred at 0 °C for 30

min and then cooled to −20 °C. Then, a solution of an 80:20 mixture of chloronicotines **2** and **3** (400 mg, 2.03 mmol, 1.0 eq.) in toluene (2 mL) was added dropwise. The resulting solution was stirred at −20 °C for 1 h and then cooled to −78 °C. A solution of hexachloroethane (1.44 g, 6.09 mmol, 3.0 eq.) in toluene (10 mL) was added and the solution was stirred at −78 °C for 1 h. Saturated $NaHCO_{3(aq)}$ (10 mL) was added and the two layers were separated. The aqueous layer was extracted with CH_2Cl_2 (2 × 10 mL). The combined organic layers were dried ($MgSO_4$) and evaporated under reduced pressure to give the crude product. Purification by flash column chromatography on silica with EtOAc as eluent gave 2,6-chloronicotine **7** (388 mg, 83%) as a mid-yellow oil.

Lab book number: WHD/1/85/10

(*R*)-4-Bromo-6-chloro-5-(1-methylpyrrolidin-2-yl)pyridine *14* (4-bromo-6-chloronicotine)

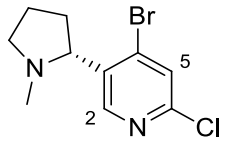

n-Butyllithium (0.45 mL of a 2.5 M solution in hexanes, 1.1 mmol, 1.1 eq.) was added dropwise to a stirred solution of 6-chloronicotine **2** (235 mg, 1.20 mmol, 1.0 eq.) in THF (2 mL) at −78 °C under Ar. The resulting solution was stirred at −78 °C for 1 h. A solution of *N*-bromosuccinimide (235 mg, 1.32 mmol, 1.1 eq.) in THF (1 mL) was added and the solution was stirred at −78 °C for 1 h. Saturated $NaHCO_{3(aq)}$ (10 mL) was added and the two layers were separated. The aqueous layer was extracted with CH_2Cl_2 (3 × 10 mL). The combined organic layers were dried ($MgSO_4$) and evaporated under reduced pressure to give the crude product (116 mg) as a brown oil, which contained a 60:40 mixture of 4-bromo-6-chloronicotine **14** and 6-chloronicotine **2** (by ^{1}H NMR spectroscopy), R_F (EtOAc) 0.52; ^{1}H NMR (400 MHz, $CDCl_3$) diagnostic peaks for 4-bromo-6-chloronicotine **14**: δ 8.51 (s, 1H, 2-py), 7.50 (s, 1H, 5-py). After storing in a freezer at −20 °C for 48 h, the product turned pink and had decomposed as shown by ^{1}H NMR spectroscopy and TLC.

Lab book number: WHD/1/18/8

(*R*)-4-Iodo-6-chloro-5-(1-methylpyrrolidin-2-yl)pyridine *15* (4-iodo-6-chloronicotine)

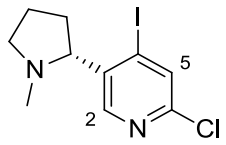

n-Butyllithium (0.45 mL of a 2.5 M solution in hexanes, 1.1 mmol, 1.1 eq.) was added dropwise to a stirred solution of 6-chloronicotine **2** (201 mg, 1.0 mmol, 1.0 eq.) in THF (2 mL) at −78 °C under Ar. The resulting solution was stirred at −78 °C for 1 h. A solution of iodine (279 mg, 1.1 mmol, 1.1 eq.) in THF (1 mL) was added and the solution was stirred at −78 °C for 1 h. Saturated $NaHCO_{3(aq)}$ (5 mL) was added and the two layers were separated. The aqueous layer was extracted with CH_2Cl_2 (3 × 10 mL). The combined organic layers were washed with 10% $Na_2S_2O_{3(aq)}$ (10 mL), dried ($MgSO_4$) and evaporated under reduced pressure to give the crude product. Purification by flash column chromatography on silica with EtOAc as eluent gave 4-iodo-6-chloronicotine **15** (113 mg, 35%) as a white solid, mp 97-99 °C (lit.,[18] 100-101 °C); R_F (EtOAc) 0.50; $[\alpha]_D^{20}$ −150 (*c* 1.0 in CH_2Cl_2) (lit.,[18] $[\alpha]_D^{27}$ −141 (*c* 3.45 in CH_2Cl_2); IR (ATR): 2936, 2804, 2759, 1552, 1530, 1437, 1360, 1215, 1110, 857 cm^{-1}; ^1H NMR (400 MHz, $CDCl_3$): δ 8.38 (s, 1H, 2-py), 7.75 (s, 1H, 5-py), 3.35 (dd, *J* = 8.0, 8.0 Hz, 1H, NCH), 3.25 (ddd, *J* = 9.5, 7.5, 2.0 Hz, 1H, NCH), 2.45-2.30 (m, 2H, NCH + CH), 2.22 (s, 3H, NMe), 1.94-1.76 (m, 2H, CH), 1.53-1.40 (m, 1H, CH); ^{13}C NMR (100.6 MHz): δ 149.6 (C, 6-py), 149.0 (CH, 2-py), 140.8 (C, 3-py), 133.7 (CH, 5-py), 112.3 (C, 4-py), 71.6 (NCH), 56.9 (NCH_2), 40.6 (NMe), 33.8 (CH_2), 22.8 (CH_2); MS (ESI) *m/z* 323 [(M (^{35}Cl) + H)$^+$, 100]; HRMS *m/z* calculated for $C_{10}H_{12}I^{35}ClN_2$ (M + H)$^+$ 322.9806, found 322.9802 (+1.2 ppm error). Spectroscopic data consistent with those in the literature.[18]

Lab book number: WHD/1/22/9

(*R*)-6-Deutero-5-(1-methylpyrrolidin-2-yl)pyridine *4* (6-nicotine-d_1)

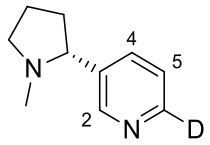

6-Chloronicotine **2** (222 mg, 1.13 mmol, 1.0 eq.), 5% palladium on activated charcoal (22 mg, 10% by weight, 10.3 μmol Pd), potassium carbonate (312 mg, 2.26 mmol, 2.0 eq.) and CH_3CH_2OD (10 mL) were place6d in a Parr reactor vessel. The Parr reactor was then sealed, purged with nitrogen and pressurised with deuterium gas to 8 bar. The reactor contents were stirred at room temperature for 18 h, when analysis by buffered LC-MS indicated that conversion to the product was complete. The Parr reactor was vented of remaining deuterium and the solids were removed by filtration through Celite. The filtrate was evaporated under reduced pressure to give the crude product. Purification by flash column chromatography on silica with 90:10 CH_2Cl_2-MeOH as eluent gave 6-nicotine-d_1 **4** (88 mg, 48%) as a very pale yellow oil, R_F (90:10 CH_2Cl_2:MeOH) 0.16; $[\alpha]_D^{20}$ −124 (*c* 1.0 in CH_2Cl_2); IR (ATR): 2941, 2773 (C-D), 1567, 1459, 1395, 1330, 1205, 1043, 1021, 896, 863 cm^{-1}; ^1H NMR (400 MHz, $CDCl_3$): δ 8.48 (br s, 1H, 2-py), 7.65 (dd, *J* = 8.0, 2.0 Hz, 1H, 4-py), 7.21 (d, *J* = 8.0 Hz, 1H, 5-py), 3.20 (ddd, *J* = 9.0, 7.5, 2.0 Hz, 1H, NCH), 3.04 (dd, *J* = 8.5, 8.5 Hz, 1H, NCH), 2.25 (ddd, *J* = 9.0, 9.0, 8.5 Hz, 1H, NCH), 2.21-2.13 (m, 1H, CH), 2.12 (s, 3H, NMe), 1.99-1.86 (m, 1H, CH), 1.86-1.74 (m, 1H, CH), 1.73-1.64 (m, 1H, CH); ^{13}C NMR (100.6 MHz): δ 149.5 (CH, 2-py), 148.2 (CD, 1:1:1 triplet, *J* = 27.0 Hz, 6-py), 138.6 (C, 3-py), 134.8 (CH, 4-py), 123.4 (CH, 5-py), 68.8 (NCH), 56.9 (NCH_2), 40.3 (NMe), 35.1 (CH_2), 22.5 (CH_2); MS (ESI) *m/z* 164 [(M + H)$^+$, 100]; HRMS *m/z* calculated for $C_{10}H_{13}DN_2$ (M + H)$^+$ 164.1293, found 164.1290 (+2.2 ppm error).

Lab book number: WHD/1/13/5

(*R*)-5,6-Dideutero-5-(1-methylpyrrolidin-2-yl)pyridine *8* (5,6-nicotine-d_2)

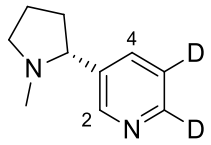

5,6-Dichloronicotine **5** (330 mg, 1.43 mmol, 1.0 eq.), 5% palladium on activated charcoal (33 mg, 10% by weight, 15.5 μmol Pd), potassium carbonate (395 mg, 2.86 mmol, 2.0 eq.) and CH_3CH_2OD (10 mL) were placed in a Parr reactor vessel. The Parr reactor was then sealed, purged with nitrogen and pressurised with deuterium gas to 8 bar. The reactor contents were stirred at room temperature for 24 h, when analysis by buffered LC-MS indicated conversion to the product was ca. 50 % complete. The reactor was repressurised with deuterium to 8 bar and stirred for another 72 h, when analysis by buffered LC-MS indicated conversion to product was complete. The Parr reactor was vented of remaining deuterium and the solids were removed by filtration through Celite. The filtrate was evaporated under reduced pressure to give the crude product. Purification by flash column chromatography on silica with 90:10 EtOAc-MeOH as eluent gave 5,6-nicotine-d_2 **8** (101 mg, 43%) as a pale yellow oil, R_F (EtOAc) 0.12; $[\alpha]_D^{20}$ −119 (*c* 1.0 in CH_2Cl_2); IR (ATR): 2955, 2515 (C-D), 1659, 1559, 1394, 1196, 928 cm^{-1}; ^1H NMR (400 MHz, $CDCl_3$): δ 8.51 (s, 1H, 2-py), 7.68 (s, 1H, 4-py), 3.23 (ddd, *J* = 9.5, 8.5, 1.5 Hz, 1H, NCH), 3.06 (dd, *J* = 8.0, 8.0 Hz, 1H, NCH), 2.25 (ddd, *J* = 9.5, 9.0, 9.0 Hz, 1H, NCH), 2.24-2.16 (m, 1H, CH), 2.15 (s, 3H, NMe), 1.99-1.89 (m, 1H, CH), 1.86-1.77 (m, 1H, CH), 1.74-1.64 (m, 1H, CH); ^{13}C NMR (100.6 MHz): δ 149.5 (CH, 2-py), 138.7 (C, 3-py), 134.7 (CH, 4-py), 68.9 (NCH), 57.0 (NCH_2), 40.4 (NMe), 35.1 (CH_2), 22.6 (CH_2) (2 x C-D resonances not resolved); MS (ESI) *m/z* 165 [$(M + H)^+$, 100]; HRMS *m/z* calculated for $C_{10}H_{12}D_2N_2$ $(M + H)^+$ 165.1355, found 165.1361.0846 (−3.2 ppm error).

Lab book number: WHD/1/17/7

(*R*)-4,6-Dideutero-5-(1-methylpyrrolidin-2-yl)pyridine *9* (4,6-nicotine-d_2)

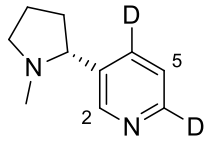

4,6-Dichloronicotine **6** (231 mg, 1.0 mmol, 1.0 eq.), 5% palladium on activated charcoal (46 mg, 20% by weight, 21.6 μmol Pd), potassium carbonate (274 mg, 2.0 mmol, 2.0 eq.) and CH_3CH_2OD (10 mL) were placed in a Parr reactor vessel. The Parr reactor was then sealed, purged with nitrogen and pressurised with deuterium gas to 8 bar. The reactor contents were stirred at room temperature for 2 h, when analysis by buffered LC-MS indicated conversion to the product was complete. The Parr reactor was vented of remaining deuterium and the reactor contents were filtered through Celite and evaporated under reduced pressure to give the crude product. Purification by flash column chromatography on silica with EtOAc as eluent gave 4,6-nicotine-d_2 **9** (75 mg, 45%) as a very pale yellow oil, R_F (EtOAc) 0.11; $[\alpha]_D^{20}$ −124 (*c* 1.0 in CH_2Cl_2); IR (ATR): 2945, 2777 (C-D), 1552, 1455, 1310, 1216, 1041, 901. 603 cm^{-1}; ^1H NMR (400 MHz, $CDCl_3$): δ 8.52 (s, 1H, 2-py), 7.25 (s, 1H, 5-py), 3.24 (ddd, *J* = 9.5, 8.5, 1.5 Hz, 1H, NCH), 3.09 (dd, *J* = 8.5, 8.5 Hz, 1H, NCH), 2.30 (ddd, *J* = 9.5, 9.0, 9.0 Hz, 1H, NCH), 2.25-2.17 (m, 1H, CH), 2.15 (s, 3H, NMe), 2.01-1.90 (m, 1H, CH), 1.87-1.78 (m, 1H, CH), 1.77-1.67 (m, 1H, CH); ^{13}C NMR (100.6 MHz): δ 149.4 (CH, 2-py), 138.5 (C, 3-py), 123.4 (CH, 5-py), 68.9 (NCH), 60.0 (NCH_2), 40.3 (NMe), 35.1 (CH_2), 22.5 (CH_2), 2x C-D resonances not resolved; MS (ESI) *m/z* 165 [$(M + H)^+$, 100]; HRMS *m/z* calculated for $C_{10}H_{12}D_2N_2$ $(M + H)^+$ 165.1355, found 165.1364 (−4.7 ppm error).

Lab book number: WHD/1/27/6

(*R*)-2,6-Dideutero-5-(1-methylpyrrolidin-2-yl)pyridine *10* (2,6-nicotine-d_2)

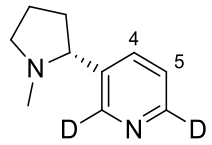

2,6-Dichloronicotine **7** (139 mg, 0.6 mmol, 1.0 eq.), 5% palladium on activated charcoal (28 mg, 20% by weight, 13.2 μmol Pd), potassium carbonate (166 mg, 2.0 mmol, 2.0 eq.) and CH_3CH_2OD (10 mL) were placed in a Parr reactor vessel. The Parr reactor was then sealed, purged with nitrogen and pressurised with deuterium gas to 8 bar. The reactor contents were stirred at room temperature for 2 h, when analysis by buffered LC-MS indicated conversion to the product was complete. The Parr reactor was vented of remaining deuterium and the solids were removed by filtration through Celite. The filtrate was evaporated under reduced pressure to give the crude product. Purification by flash column chromatography on silica with EtOAc as eluent gave 2,6-dideuteronicotine **10** (31 mg, 31%) as a very pale yellow oil, R_F (EtOAc) 0.10; $[\alpha]_D^{20}$ −127 (*c* 1.0 in CH_2Cl_2); IR (ATR): 2923, 1979, 1264, 1034, 734 cm^{-1}; ^1H NMR (400 MHz, $CDCl_3$): δ 7.67 (d, *J* = 8.0 Hz 1H, 4-py), 7.23 (d, *J* = 8.0 Hz, 1H, 5-py), 3.22 (ddd, *J* = 9.5, 7.5, 2.0 Hz, 1H, NCH), 3.06 (dd, *J* = 8.5, 8.5 Hz, 1H, NCH), 2.28 (ddd, *J* = 9.5, 9.0, 9.0 Hz, 1H, NCH), 2.22-2.16 (m, 1H, CH), 2.14 (s, 3H, NMe), 2.01-1.88 (m, 1H, CH), 1.85-1.76 (m, 1H, CH), 1.74-1.65 (m, 1H, CH); ^{13}C NMR (100.6 MHz): δ 149.1 (CD, 1:1:1 triplet, *J* = 28.0 Hz, 2-py), 148.3 (CD, 1:1:1 triplet, *J* = 27.0 Hz, 6-py) , 138.5 (C, 3-py), 134.8 (CH, 4-py), 123.4 (CH, 5-py), 68.8 (NCH), 57.0 (NCH_2), 40.3 (NMe), 35.1 (CH_2), 22.5 (CH_2); MS (ESI) *m/z* 165 [$(M + H)^+$, 100]; HRMS *m/z* calculated for $C_{10}H_{12}D_2N_2$ $(M + H)^+$ 165.1350, found 165.1355 (+3.1 ppm error).

Lab book number: WHD/1/29/11

6.4 SABRE and other NMR results

6.4.1 Varied substrate concentration – enhancements

Samples were prepared according to Method 1, although with varying concentration of the substrate. 'Equivalents' refers to substrate equivalents, where one equivalent is 5 mM concentration, the same as the standard precatalyst concentration. Therefore, four equivalents of substrate is 20 mM, etc. 'SNR' is signal-to-noise ratio. Polarisation was achieved via Method 2, *i.e.* with samples shaken in a stray field of 65 G.

(−)-nicotine 1, IMes 18

Lab book/raw file reference: WHD/A/1/1, WHD/A/7/7

Equivalents	Signal enhancement (relative to thermal)										SNR
	2-proton		6-proton		4-proton		5-proton		Avg. per proton		
4	303	(±14)	337	(±21)	320	(±10)	42	(±17)	251	(±15)	5296
5	237	(±9)	320	(±5)	215	(±11)	50	(±31)	206	(±14)	15254
6	237	(±18)	256	(±20)	233	(±18)	70	(±5)	199	(±15)	12176
8	228	(±12)	254	(±12)	218	(±11)	87	(±18)	197	(±13)	8289
10	217	(±2)	237	(±3)	200	(±4)	95	(±5)	187	(±3)	9339
15	166	(±12)	178	(±11)	147	(±11)	66	(±7)	139	(±10)	12278

4,6-nicotine-d_2 9, IMes 18

Lab book/raw file reference: WHD/A/1/1, WHD/A/9/9

Equivalents	Signal enhancement (relative to thermal)						SNR
	2-proton		5-proton		Avg. per proton		
4	759	(±9)	947	(±11)	853	(±10)	24371
5	485	(±17)	1010	(±14)	748	(±16)	24892
6	639	(±17)	711	(±14)	675	(±16)	26300
10	261	(±14)	297	(±19)	279	(±17)	25413
15	204	(±9)	231	(±11)	217	(±10)	26773

(−)-nicotine 1, d_{22}-IMes 19

Lab book/raw file reference: WHD/A/12/12

Equivalents	Signal enhancement (relative to thermal)										SNR
	2-proton		6-proton		4-proton		5-proton		Avg. per proton		
4	363	(±1)	427	(±8)	362	(±9)	14	(±7)	291	(±6)	4509
6	447	(±7)	441	(±11)	337	(±13)	24	(±0)	312	(±8)	16936
8	325	(±4)	373	(±6)	268	(±1)	46	(±13)	253	(±6)	24614
10	225	(±10)	225	(±7)	246	(±4)	48	(±5)	186	(±6)	24788
15	149	(±3)	119	(±3)	85	(±2)	25	(±6)	94	(±4)	22302

4,6-nicotine-d_2 9, d_{22}-IMes 19

Lab book/raw file reference: WHD/A/10/10

Equivalents	Signal enhancement (relative to thermal)						SNR
	2-proton		5-proton		Avg. per proton		
4	761	(±35)	1092	(±30)	926	(±32)	25528
6	793	(±43)	1088	(±27)	940	(±35)	32961
8	616	(±36)	731	(±2)	673	(±19)	38318
10	430	(±6)	485	(±13)	457	(±10)	35125
15	275	(±7)	304	(±9)	290	(±8)	40826

6.4.2 Varied substrate concentration studies – T_1

Samples were prepared according to Method 1, although with varying concentration of the substrate. ‘Equivalents’ refers to substrate equivalents, where one equivalent is 5 mM concentration, the same as the standard precatalyst concentration. Therefore, four equivalents of substrate is 20 mM, etc. T_1 relaxation times in this series were recorded using Method 5 (inversion-recovery).

(−)-nicotine 1, IMes 18

Lab book/raw file reference: WHD/A/8/8

Equivalents	T_1 relaxation time (activated conditions) / s			
	2-proton	6-proton	4-proton	5-proton
4	1.63	1.63	2.09	2.71
5	2.97	3.11	3.15	3.87
7	2.96	3.13	3.79	3.94
15	3.98	4.60	4.69	4.54
25	6.02	7.63	6.13	6.25

4,6-nicotine-d_2 9, Imes 18

Lab book/raw file reference: WHD/A/8/8

Equivalents	T_1 relaxation time (activated conditions) / s	
	2-proton	5-proton
4	3.05	16.84
5	4.79	26.50
15	4.46	23.80
25	3.78	19.35

(−)-nicotine 1, d_{22}-Imes 19

Lab book/raw file reference: WHD/A/11/11

Equivalents	T_1 relaxation time (activated conditions) / s			
	2-proton	6-proton	4-proton	5-proton
4	2.76	2.92	3.14	4.58
5	2.27	2.09	2.72	3.30
15	5.63	6.94	5.85	5.77

4,6-nicotine-d_2 9, d_{22}-IMes 19

Lab book/raw file reference: WHD/A/11/11

Substrate equivalents	T_1 relaxation time (activated conditions)/ s	
	2-proton	5-proton
4	3.02	18.93
5	3.24	19.17
15	5.65	37.63

6.4.2 Variable temperature SABRE – enhancements

Samples were prepared according to Method 1. Results were obtained using Method 2.

(−)-nicotine 1, IMes 18

Lab book/raw file reference: WHD/A/18/18.

	Signal enhancements (relative to activated thermal)									
Temperature / K	2-proton		6-proton		4-proton		5-proton		Avg. per proton	
298	237	±9	320	±5	215	±11	50	±31	212	±14
303	332	±24	315	±49	297	±15	6	±2	259	±3
308	525	±18	221	±4	399	±5	8	±1	295	±4
313	384	±23	275	±16	331	±11	13	±1	264	±4

4,6-nicotine-d_2 9, IMes 18

Lab book/raw file reference: WHD/A/18/18

	Signal enhancements (relative to activated thermal)					
Temperature / K	2-proton		5-proton		Avg. per proton	
298	485	±17	1010	±14	748	±16
303	317	±13	273	±9	295	±11
308	273	±4	391	±8	332	±6
313	260	±7	358	±6	309	±7

6.4.3 Variable pressure SABRE

Samples were prepared according to Method 1. Results were obtained using Method 2 or Method 3 as specified. Lab book/raw file reference: WHD/A/23/23

(−)-nicotine 1, IMes 18, shaken in stray field

Absolute *p*-H_2 pressure / bar	Signal enhancements (relative to activated thermal)									
	2-proton		6-proton		4-proton		5-proton		Avg. per proton	
4	237	±9	320	±5	215	±11	50	±31	212	±14
5	304	±2	406	±7	363	±8	24	±4	274	±5
6	556	±20	450	±8	440	±11	21	±4	366	±11

4,6-nicotine-d_2 9, IMes 18, shaken in stray field

Absolute *p*-H_2 pressure / bar	Signal enhancements (relative to activated thermal)					
	2-proton		5-proton		Avg. per proton	
4	485	±17	1010	±14	748	±16
5	657	±28	933	±25	795	±27
6	556	±20	21	±4	288	±12

4,6-nicotine-d_2 9, IMes 18, shaken with 60 G magnetic shaker

Absolute *p*-H_2 pressure / bar	Signal enhancements (relative to activated thermal)					
	2-proton		5-proton		Avg. per proton	
4	1064	±23	1713	±26	1389	±24
5	1145	±28	1782	±36	1464	±32
6	1212	±19	1807	±1	1510	±10

6.4.4 Flow experiments

Results were obtained using Method 3. Lab book/raw file reference: WHD/A/14/14

(−)-nicotine 1, with varying polarisation transfer field

	Signal enhancement (relative to thermal)				
PTF/G	**2-proton**	**6-proton**	**4-proton**	**5-proton**	**Avg. per proton**
0	42.8	72.6	72.3	138.0	81.4
10	57.6	85.2	78.2	103.7	81.2
20	125.0	180.6	168.0	131.1	151.2
30	147.2	200.1	182.8	73.8	151.0
40	124.4	154.5	146.7	19.1	111.2
50	193.9	197.5	190.3	46.3	157.0
60	216.3	224.2	226.7	103.7	192.7
70	206.7	218.7	222.9	107.8	189.0
80	166.0	175.2	187.5	89.1	154.4
90	123.1	120.8	141.6	92.4	119.5
100	80.1	74.7	85.0	89.3	82.3
110	94.9	86.5	86.0	93.7	90.3
120	68.1	72.8	68.6	27.8	59.3
130	58.1	65.4	60.9	5.5	47.5
140	55.2	68.7	64.8	28.2	54.2

(−)-nicotine 1 with varying bubbling time

	Signal enhancement (relative to thermal)				
Bubbling time / s	**2-proton**	**6-proton**	**4-proton**	**5-proton**	**Avg. per proton**
0	0.7	0.7	0.6	0.6	0.7
2	157.6	160.4	180.8	84.5	145.8
4	168.9	174.4	197.5	95.1	159.0
6	156.8	164.9	184.0	84.5	147.6
8	182.7	187.6	211.9	97.0	169.8
10	198.0	201.1	227.6	101.7	182.1
12	175.4	178.7	202.3	92.5	162.2
14	195.3	202.5	232.8	108.5	184.8
16	202.9	204.8	235.8	104.7	187.1
18	180.9	179.9	207.6	93.3	165.4
20	199.4	213.0	244.9	113.9	192.8

4,6-nicotine-d_2 9 with varying polarisation transfer field

PTF/G	Signal enhancement (relative to thermal)		
	2-proton	5-proton	Avg. per proton
0	977.3	436.7	707.0
10	763.1	680.8	721.9
20	756.1	717.5	736.8
30	654.9	867.8	761.3
40	629.4	981.6	805.5
50	659.9	1091.5	875.7
60	680.5	1165.1	922.8
70	659.8	1136.8	898.3
80	688.3	1015.6	852.0
90	662.4	937.8	800.1
100	630.5	942.5	786.5
110	696.3	829.0	762.7
120	676.4	849.2	762.8
130	656.3	830.3	743.3
140	592.0	887.3	739.6

4,6-nicotine-d_2 9 with varying bubbling time

Bubbling time / s	Signal enhancement		
	2-proton	5-proton	Avg. per proton
0	0	0	0.0
2	750.3	1143.3	946.8
4	1101.0	1712.9	1407.0
6	1059.7	1808.9	1434.3
8	931.0	1550.5	1240.7
10	806.5	1291.2	1048.8
12	668.6	1105.6	887.1
14	641.0	1041.0	841.0
16	599.6	957.5	778.5
18	530.2	800.6	665.4
20	445.2	694.9	570.1

6.4.5 Mixing studies results

(−)-nicotine 1, IMes 18 shaken in 60 G shaker assembly

Lab book/raw file reference: WHD/A/28/28

Signal enhancements (relative to activated thermal)										
2-proton		**6-proton**		**4-proton**		**5-proton**		**Avg. per proton**		**SNR**
637	±30	596	±54	642	±13	289	±18	541	±29	11382

6.5 EXSY results

Results were obtained using Method 5. Lab book/raw file reference: WHD/A/16/16. EXSY traces, Eyring plots and errors are included in Chapter 7.

(−)-nicotine 1, IMes 18

T / K	**k_{obs}/ s^{-1}**	
	Bound1->Free	**Bound2->Free**
288	0.797	1.040
293	1.460	1.666
298	3.092	3.181
303	5.303	6.465

	Bound 1 -> Free	**Bound 2 -> Free**
$\Delta H‡$ / kJmol^{-1}	90.947	86.330
$\Delta S‡$ / JK^{-1}mol^{-1}	69.169	54.870
$\Delta G_{300}‡$ / kJmol^{-1}	70.196	69.869

(−)-nicotine 1, d_{22}-IMes 19

T / K	k_{obs}/ s^{-1}	
	Bound1->Free	**Bound2->Free**
288	0.778	1.000
293	1.502	1.647
298	3.026	3.105
303	5.998	5.529

	Bound 1 -> Free	**Bound 2 -> Free**
ΔH‡ / kJmol-1	94.460	82.480
ΔS‡ / JK-1mol-1	80.917	41.351
ΔG_{300}‡ / kJmol-1	70.185	70.075

4,6-nicotine-d_2 9, IMes 18

T / K	k_{obs}/ s^{-1}	
	Bound1->Free	**Bound2->Free**
288	0.790	0.759
293	1.847	1.468
298	3.058	2.998
303	5.637	5.261

	Bound 1 -> Free	**Bound 2 -> Free**
ΔH‡ / kJmol-1	90.280	92.519
ΔS‡ / JK-1mol-1	67.490	74.349
ΔG_{300}‡ / kJmol-1	70.033	70.214

4,6-nicotine-d_2 9, d_{22}-IMes 19

T / K	kobs/ s-1	
	Bound1->Free	**Bound2->Free**
288	0.991	0.847
293	1.847	1.468
298	3.152	3.019
303	5.604	5.259

	Bound 1 -> Free	**Bound 2 -> Free**
$\Delta H‡$ / kJmol-1	80.716	87.497
$\Delta S‡$ / JK-1mol-1	35.647	57.563
$\Delta G_{300}‡$ / kJmol-1	70.022	70.228

7: Appendices

7.1 Model 1 EXSY plots and rate constant tables

7.1.1 Model 1 (−)-nicotine 1, IMes 18

288 K

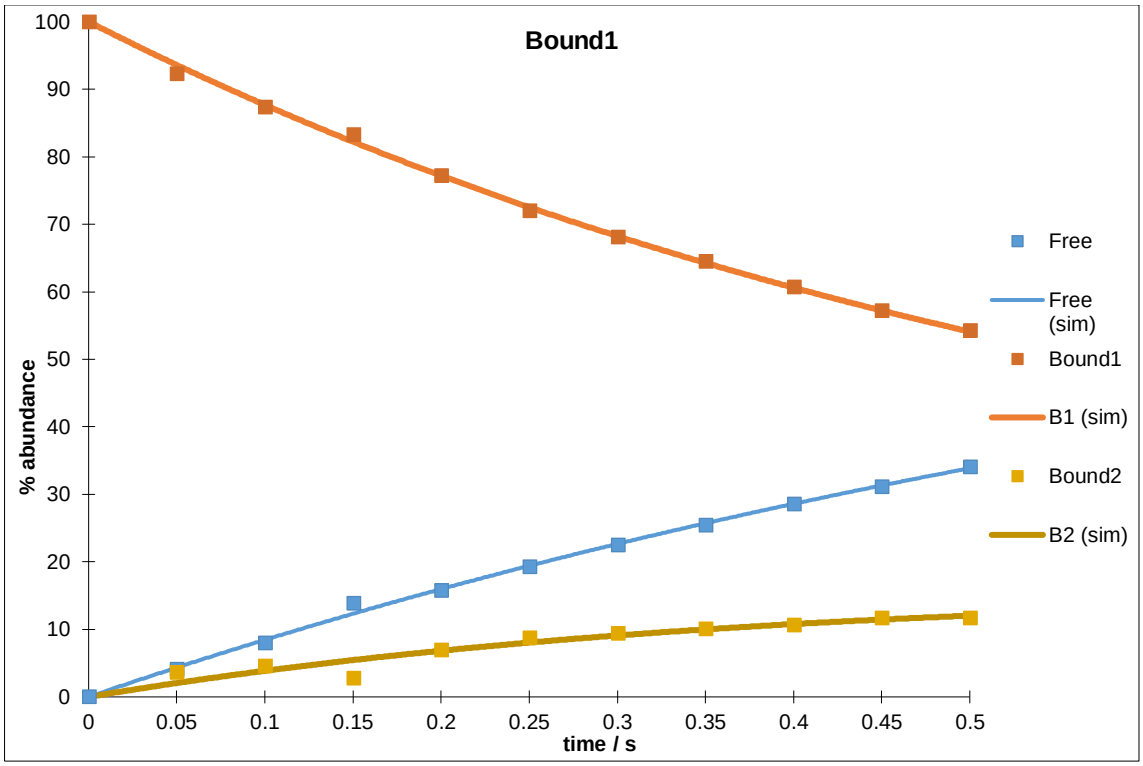

Figure 118: **'Bound 1' (A+G/2) excitation @ 288 K**

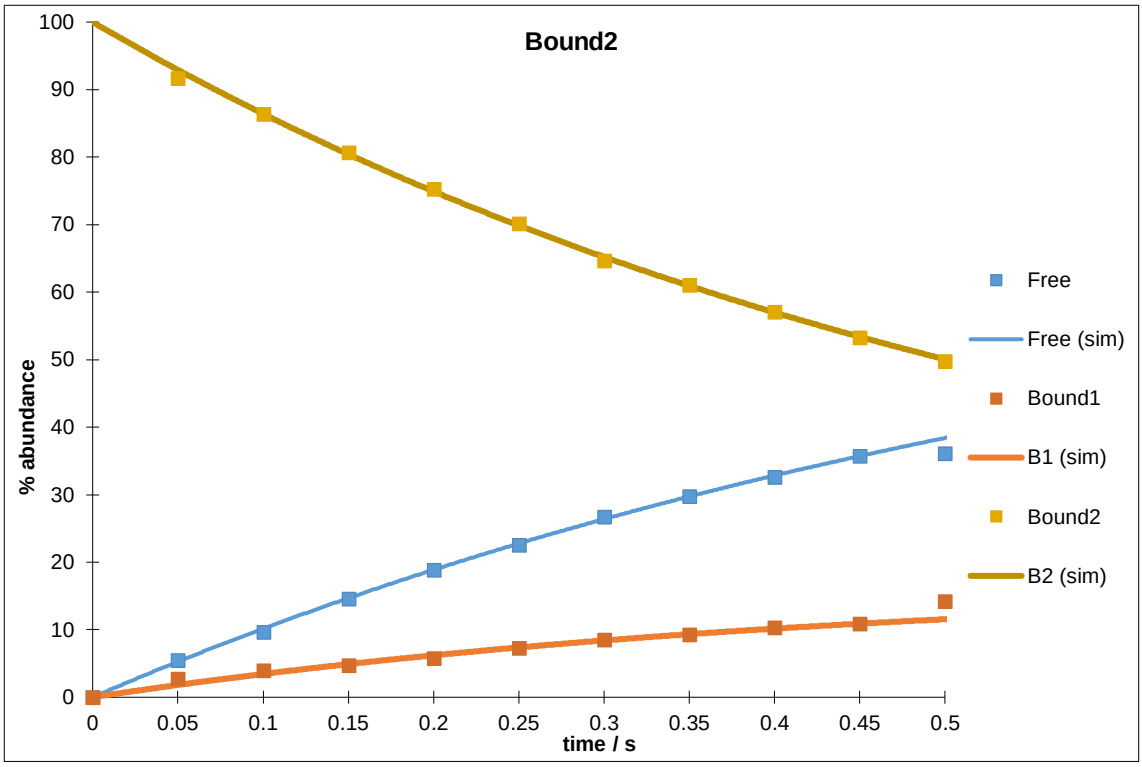

Figure 119: **'Bound 2' (F+G/2) excitation @ 288 K**

	Free	Bound1	Bound2
Free	-0.354	0.220	0.134
Bound1	0.894	-1.332	0.438
Bound2	1.093	0.383	-1.477

Table 7: **Model 1 observed rate constants for (−)-nicotine *1*, IMes *18* @ 288 K. Rate constants are read as k_{XY}, *i.e.* k_{AB} is row A, column B**

Excitation	Sum of least squares
Bound 1	16.857
Bound 2	3.932
Total	20.788

Table 8: sum of least squares for each plot

293 K

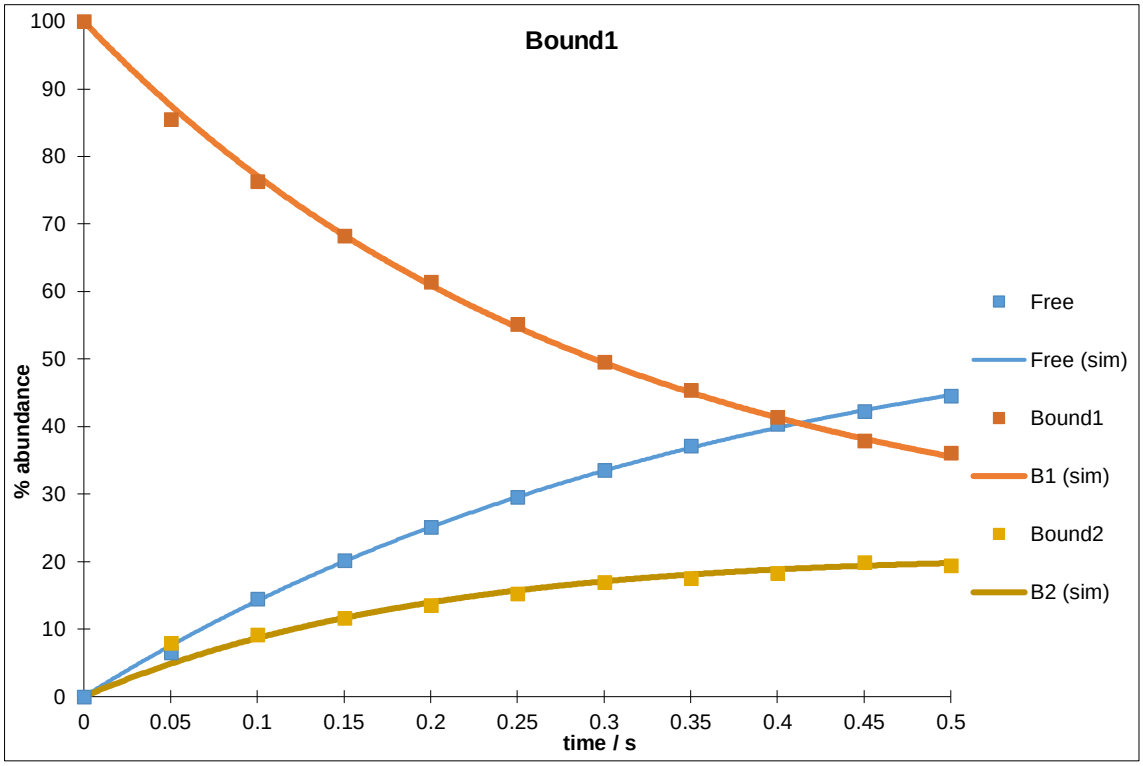

Figure 120: **'Bound 1' (A+G/2) excitation @ 293 K**

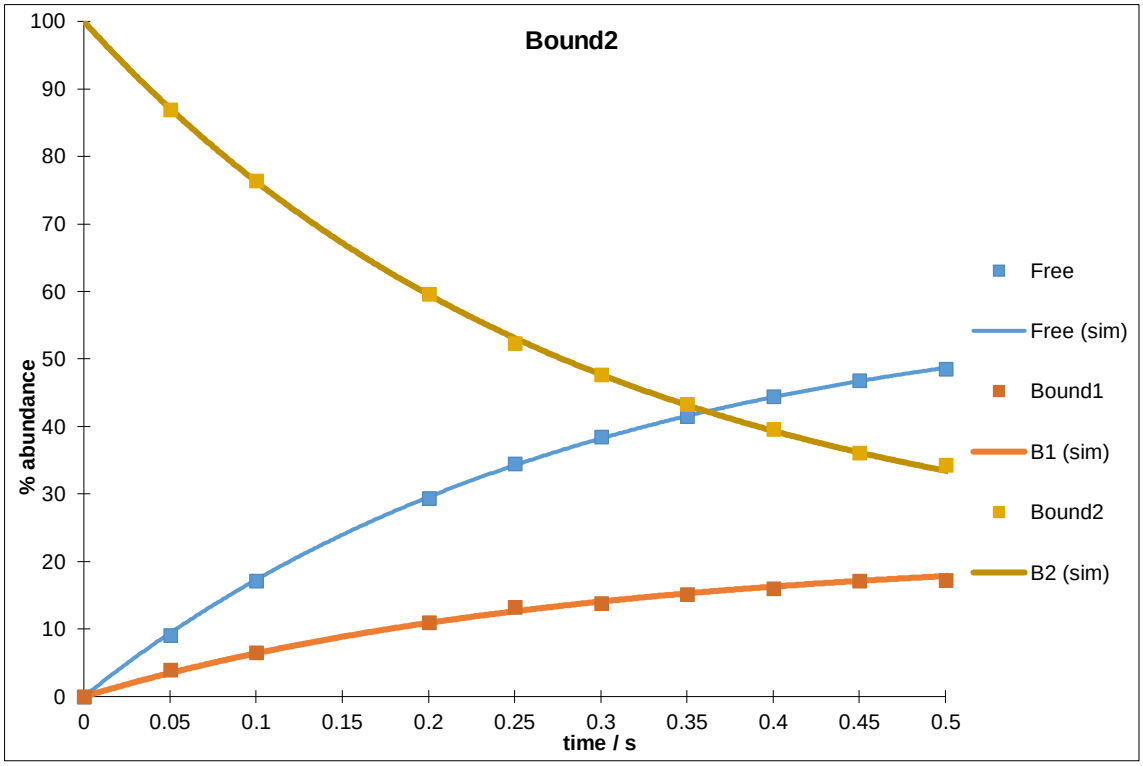

Figure 121: **'Bound 2' (F+G/2) excitation @ 293 K**

	Free	Bound1	Bound2
Free	-1.249	0.733	0.516
Bound1	1.608	-2.698	1.090
Bound2	2.044	0.760	-2.804

Table 9: Model 1 observed rate constants for (−)-nicotine *1*, IMes *18* @ 293 K. Rate constants are read as k_{XY}, *i.e.* k_{AB} is row A, column B

Excitation	Sum of least squares
Bound 1	17.735
Bound 2	2.756
Total	20.490

Table 10: sum of least squares for each plot

298 K

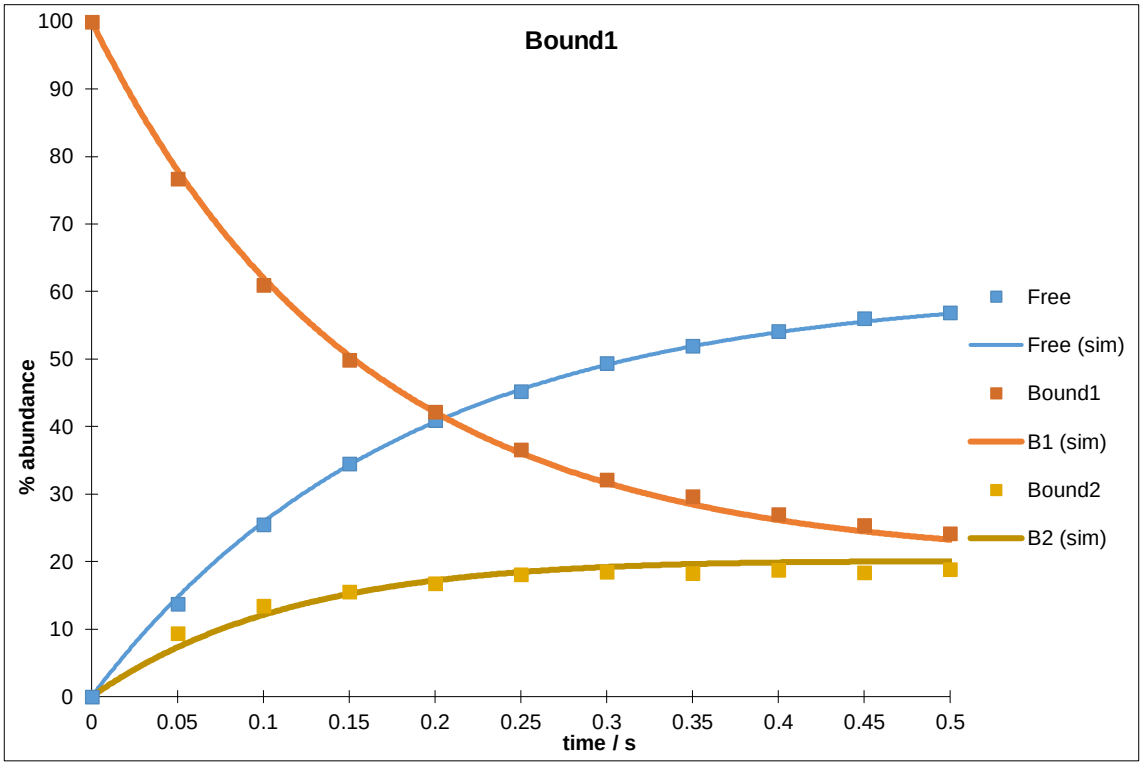

Figure 122: 'Bound 1' (A+G/2) excitation @ 298 K

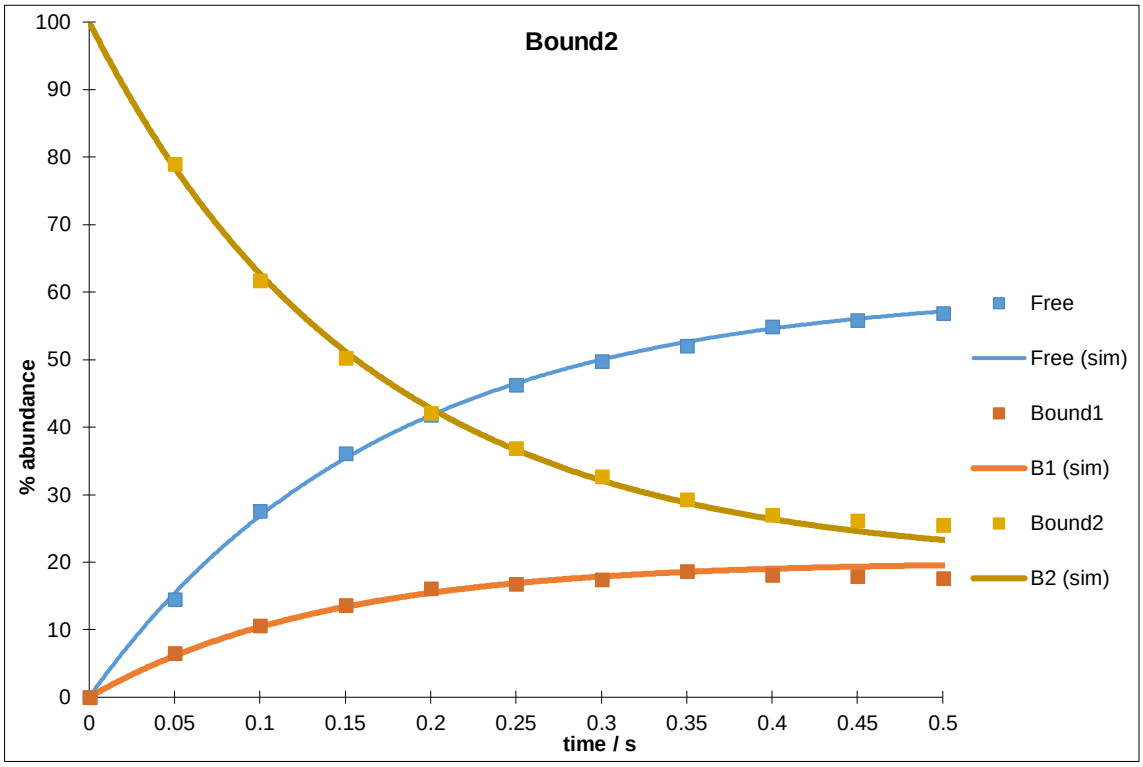

Figure 123: **'Bound 2' (A+G/2) excitation @ 298 K**

	Free	Bound1	Bound2
Free	-2.270	1.228	1.043
Bound1	3.362	-5.136	1.775
Bound2	3.546	1.455	-5.001

Table 11: **Model 1 observed rate constants for (−)-nicotine *1*, IMes *18* @ 298 K. Rate constants are read as k_{XY}, *i.e.* k_{AB} is row A, column B**

Excitation	Sum of least squares
Bound 1	21.405
Bound 2	19.876
Total	41.281

Table 12: sum of least squares for each plot

303 K

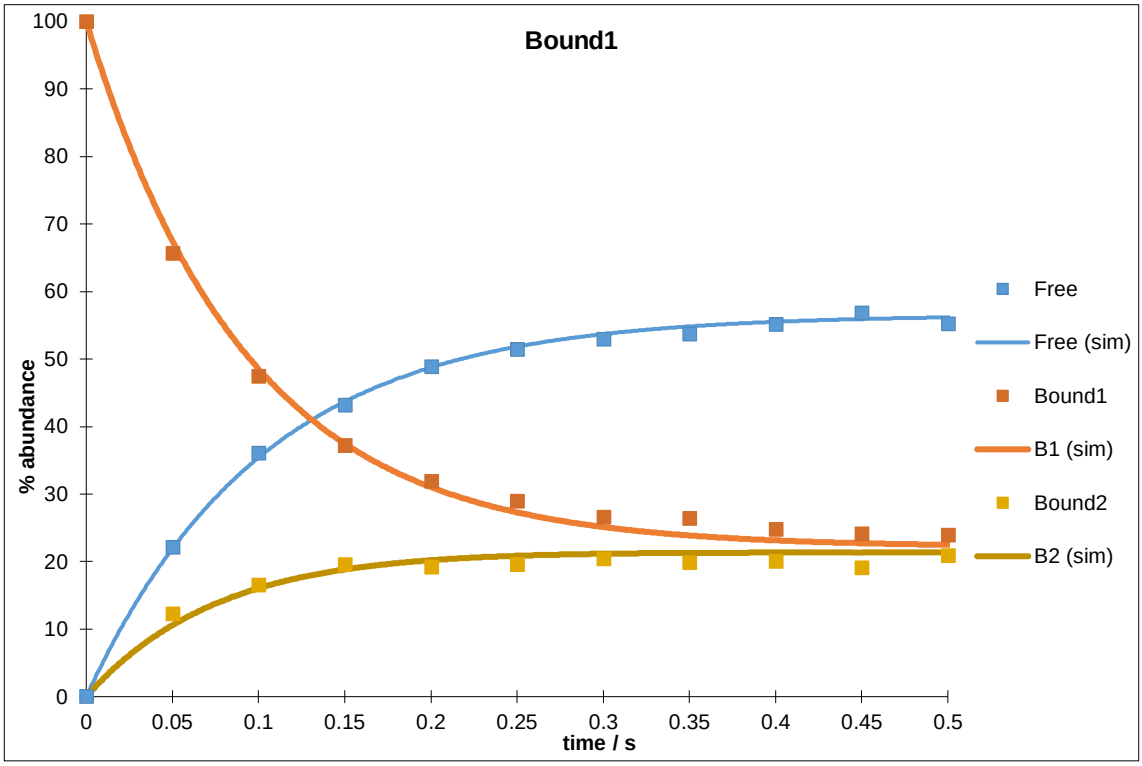

Figure 124: **'Bound 1' (A+G/2) excitation @ 303 K**

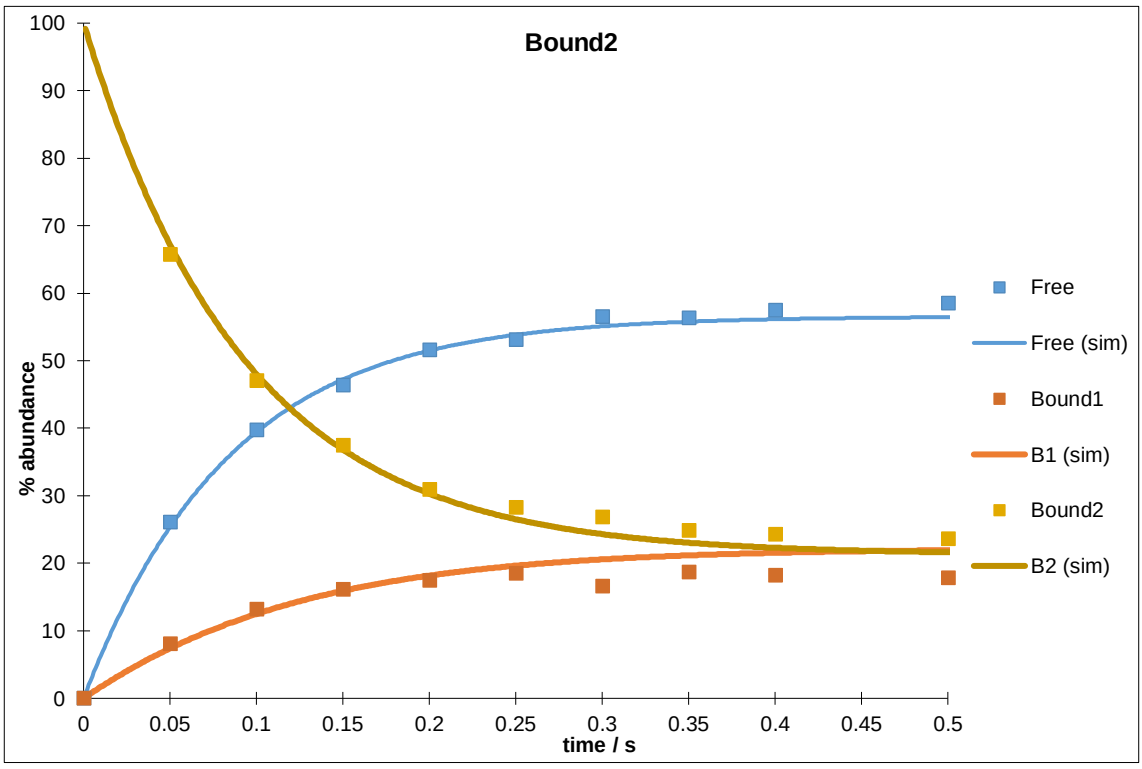

Figure 125: **'Bound 2' (F+G/2) excitation @ 303 K**

	Free	Bound1	Bound2
Free	-4.667	2.616	2.051
Bound1	5.494	-8.356	2.861
Bound2	6.673	1.752	-8.424

Table 13: Model 1 observed rate constants for (−)-nicotine *1*, IMes *18* @ 303 K. Rate constants are read as k_{XY}, *i.e.* k_{AB} is row A, column B

Excitation	Sum of least squares
Bound 1	38.871
Bound 2	46.442
Total	85.313

Table 14: sum of least squares for each plot

Eyring plots

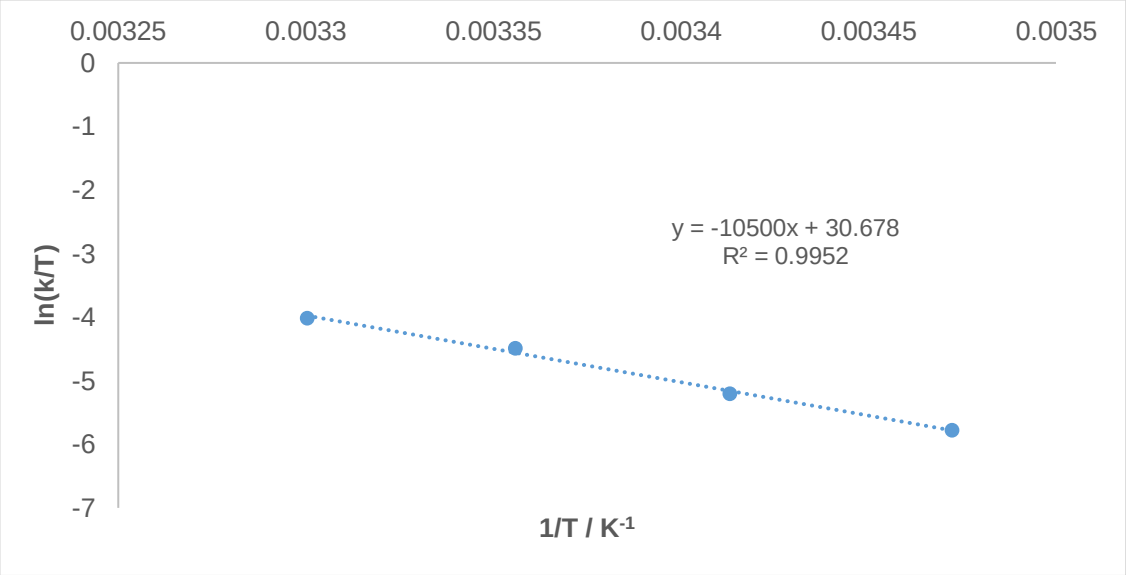

Figure 126: Eyring plot of Bound 1 for (−)-nicotine *1*, IMes *18*

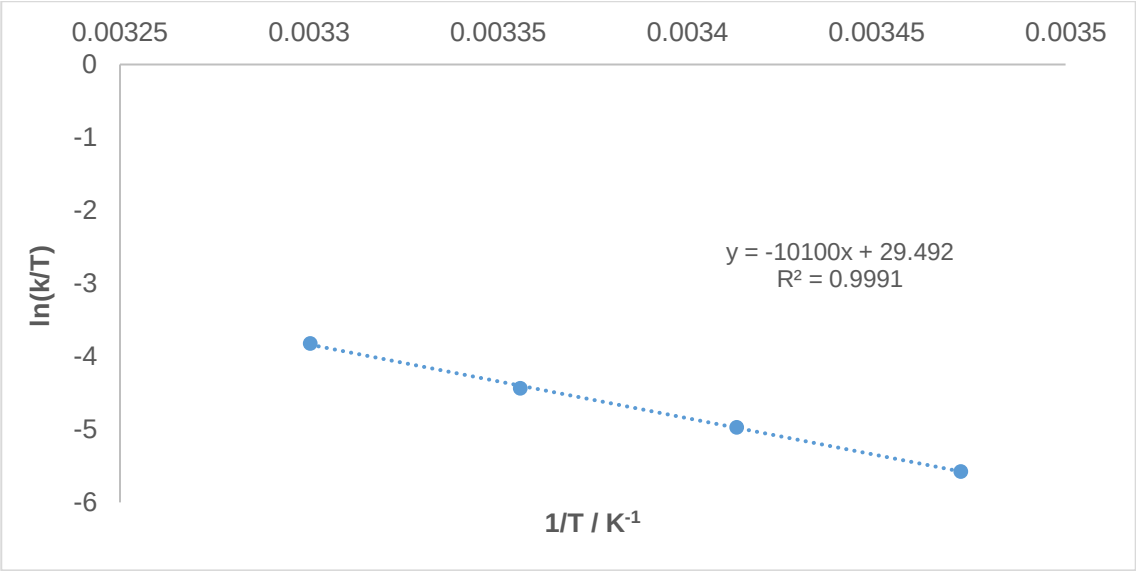

Figure 127: Eyring plot of Bound 2 for (−)-nicotine *1*, IMes *18*

Kinetic parameters

	Bound 1 -> Free	**Bound 2 -> Free**
$\Delta H‡$ / kJmol^{-1}	86.713	83.972
$\Delta S‡$ / JK^{-1}mol^{-1}	55.483	47.661
$\Delta G_{300}‡$ / kJmol^{-1}	70.066	69.672

Table 15: kinetic parameters for (−)-nicotine *1*, IMes *18*

7.1.2 Model 1 (−)-nicotine 1, d_{22}-IMes 19

288 K

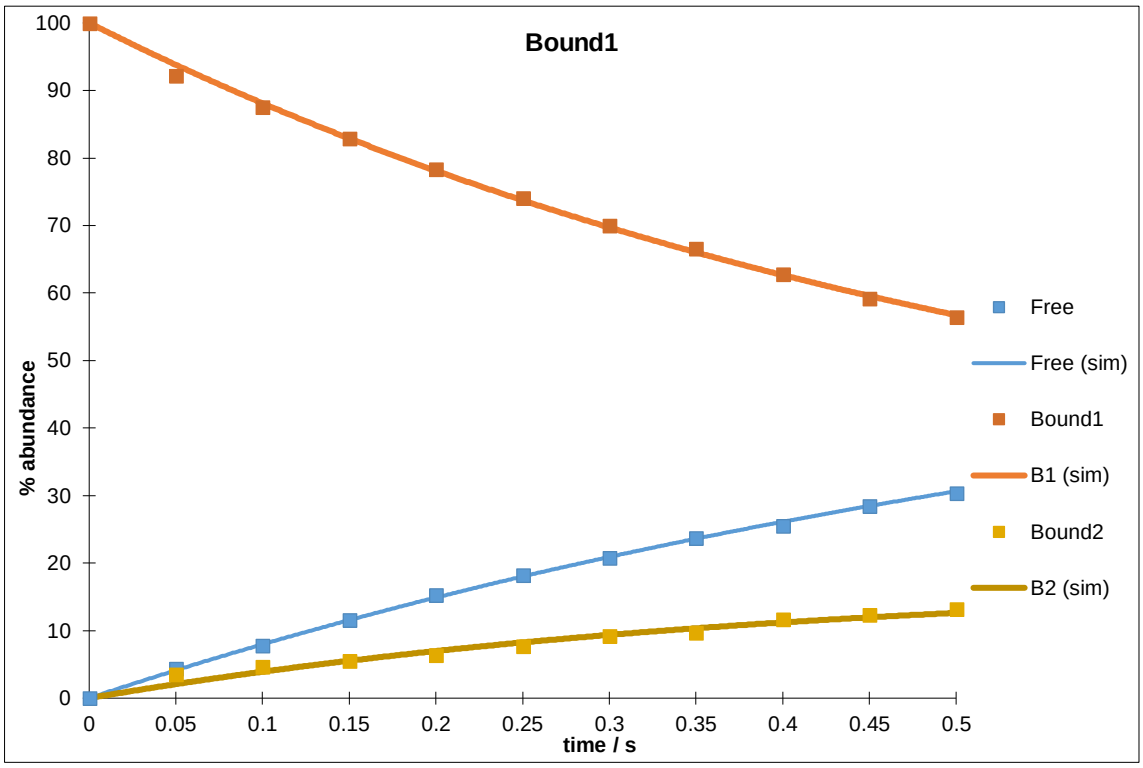

Figure 128: **'Bound 1' (A+G/2) excitation @ 288 K**

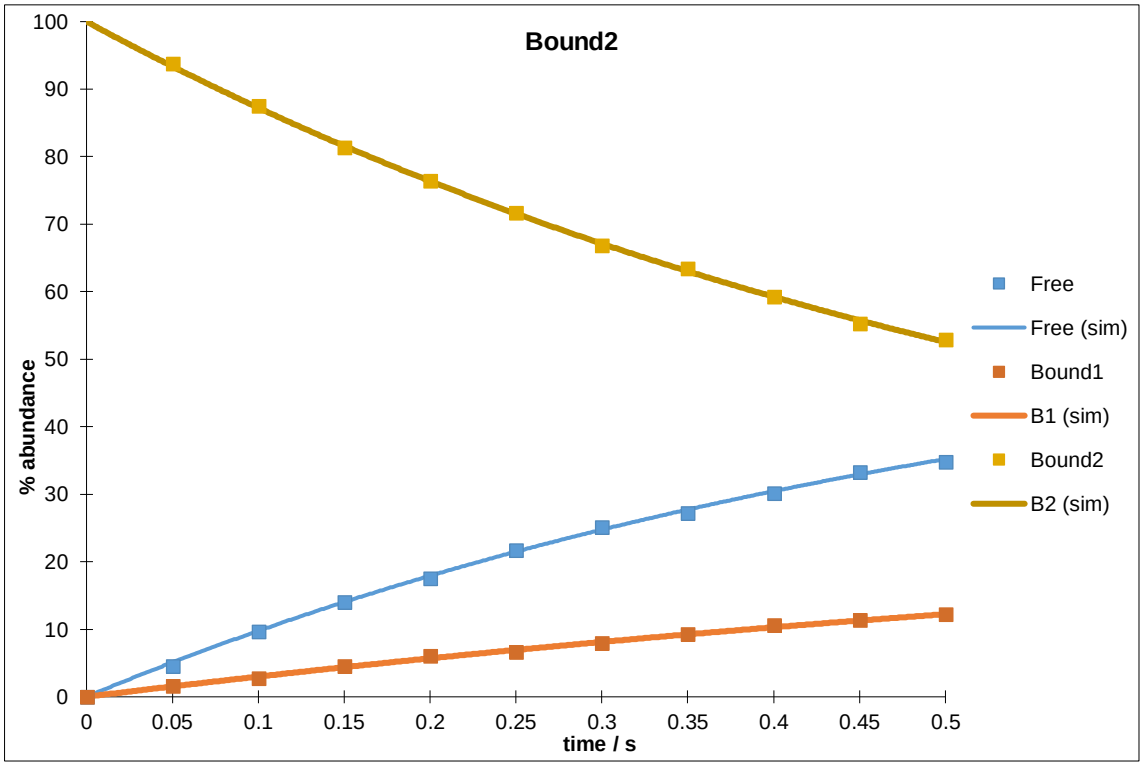

Figure 129: **'Bound 2' (F+G/2) excitation @ 288 K**

	Free	Bound1	Bound2
Free	-0.655	0.499	0.156
Bound1	0.855	-1.294	0.439
Bound2	1.065	0.315	-1.380

Table 16: **Model 1 observed rate constants for (−)-nicotine *1*, d_{22}-IMes *19* @ 288 K. Rate constants are read as k_{XY}, *i.e.* k_{AB} is row A, column B**

Excitation	Sum of least squares
Bound 1	8.388
Bound 2	2.188
Total	10.576

Table 17: sum of least squares for each plot

293 K

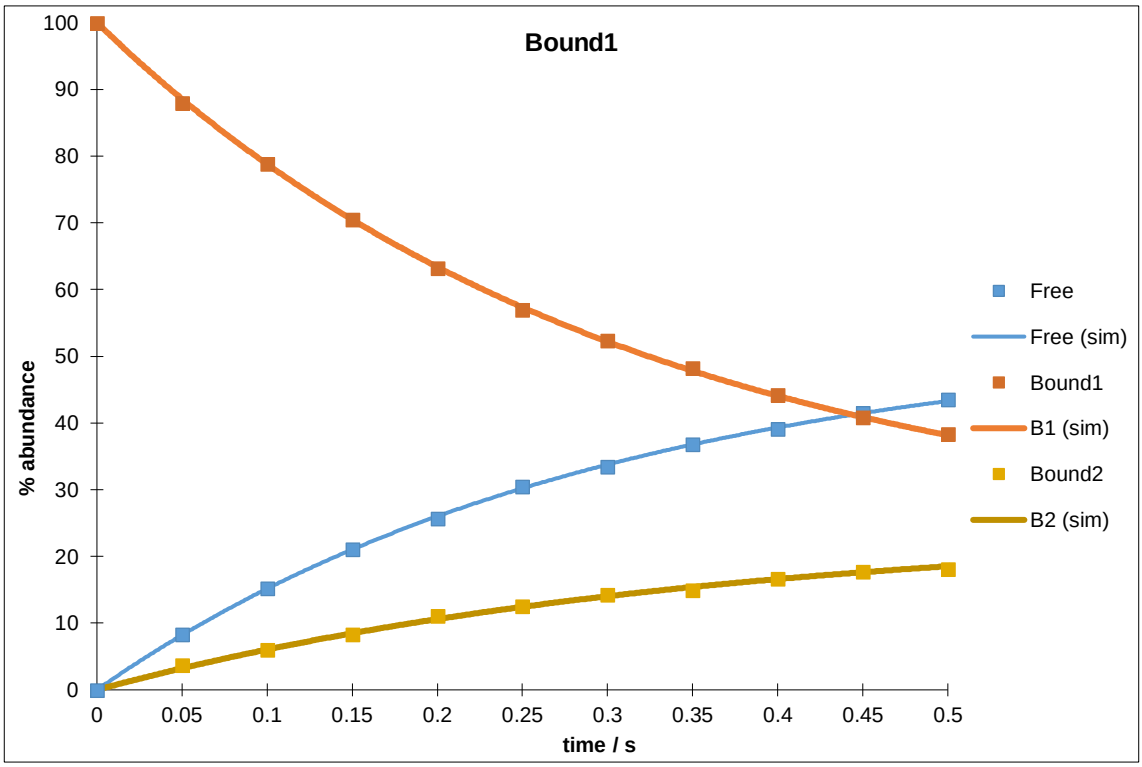

Figure 130: **'Bound 1' (A+G/2) excitation @ 293 K**

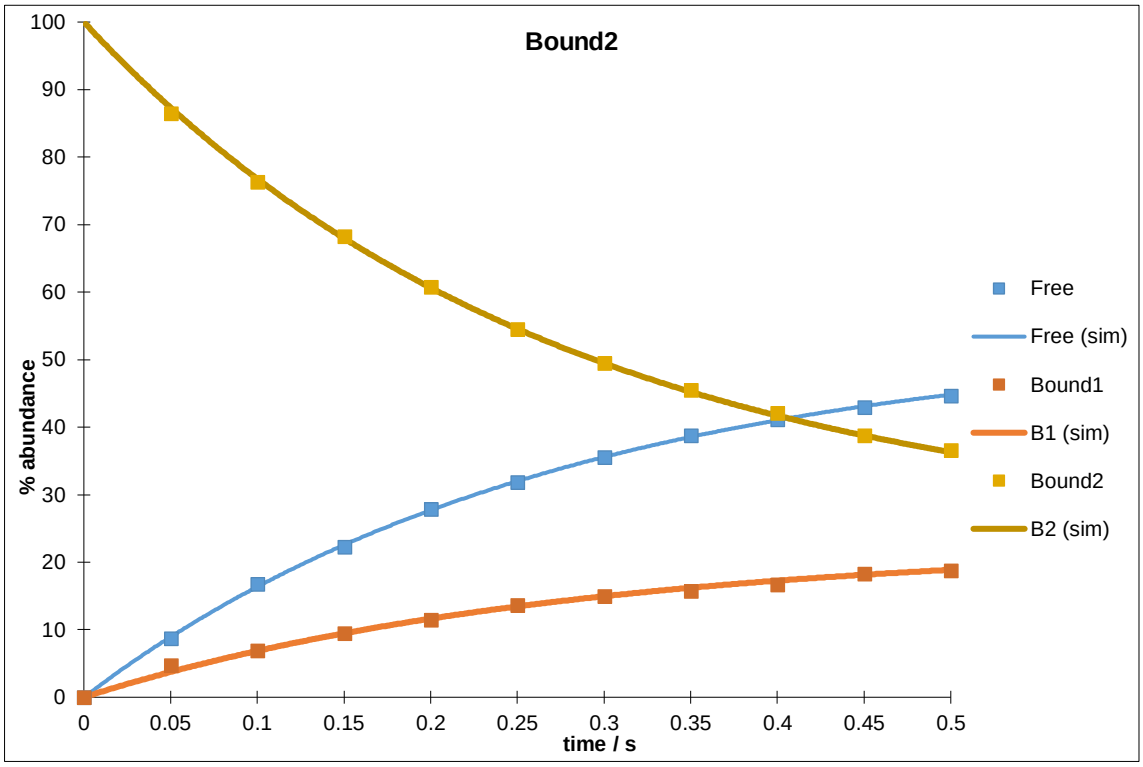

Figure 131: **'Bound 2' (F+G/2) excitation @ 293 K**

	Free	Bound1	Bound2
Free	-1.631	0.676	0.956
Bound1	1.781	-2.473	0.692
Bound2	1.950	0.817	-2.767

Table 18: **Model 1 observed rate constants for (−)-nicotine *1*, d_{22}-IMes *19* @ 293 K. Rate constants are read as k_{XY}, *i.e.* k_{AB} is row A, column B**

Excitation	Sum of least squares
Bound 1	2.056
Bound 2	3.004
Total	5.060

Table 19: sum of least squares for each plot

298 K

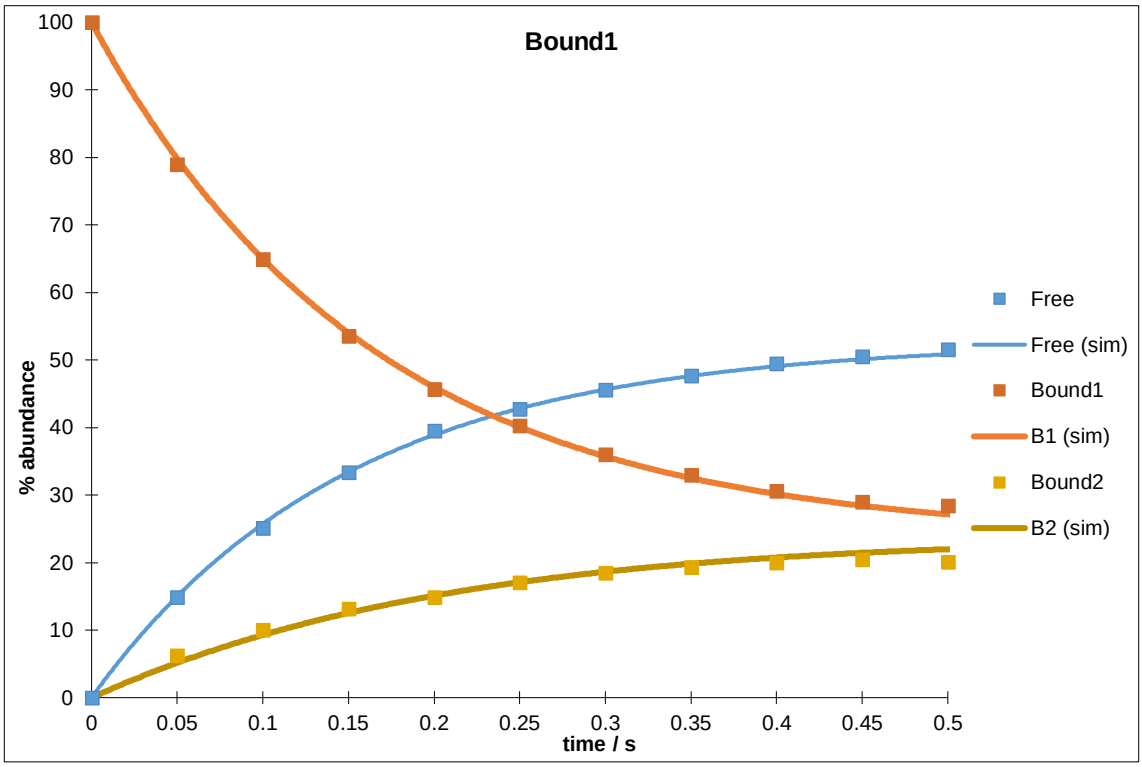

Figure 132: 'Bound 1' (A+G/2) excitation @ 298 K

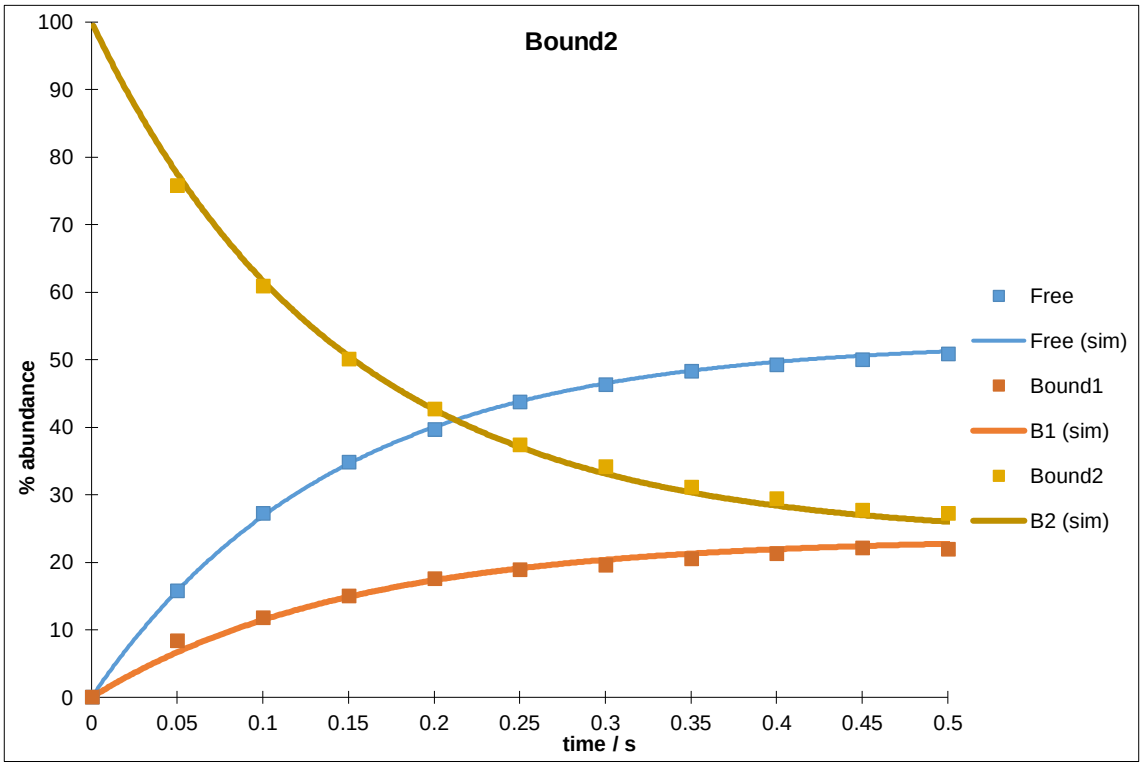

Figure 133: 'Bound 2' (F+G/2) excitation @ 298 K

	Free	Bound1	Bound2
Free	-3.249	1.389	1.861
Bound1	3.524	-4.668	1.144
Bound2	3.732	1.564	-5.296

Table 20: **Model 1 observed rate constants for (−)-nicotine *1*, d_{22}-IMes *19* @ 298 K. Rate constants are read as k_{XY}, *i.e.* k_{AB} is row A, column B**

Excitation	Sum of least squares
Bound 1	11.895
Bound 2	13.752
Total	25.647

Table 21: sum of least squares for each plot

303 K

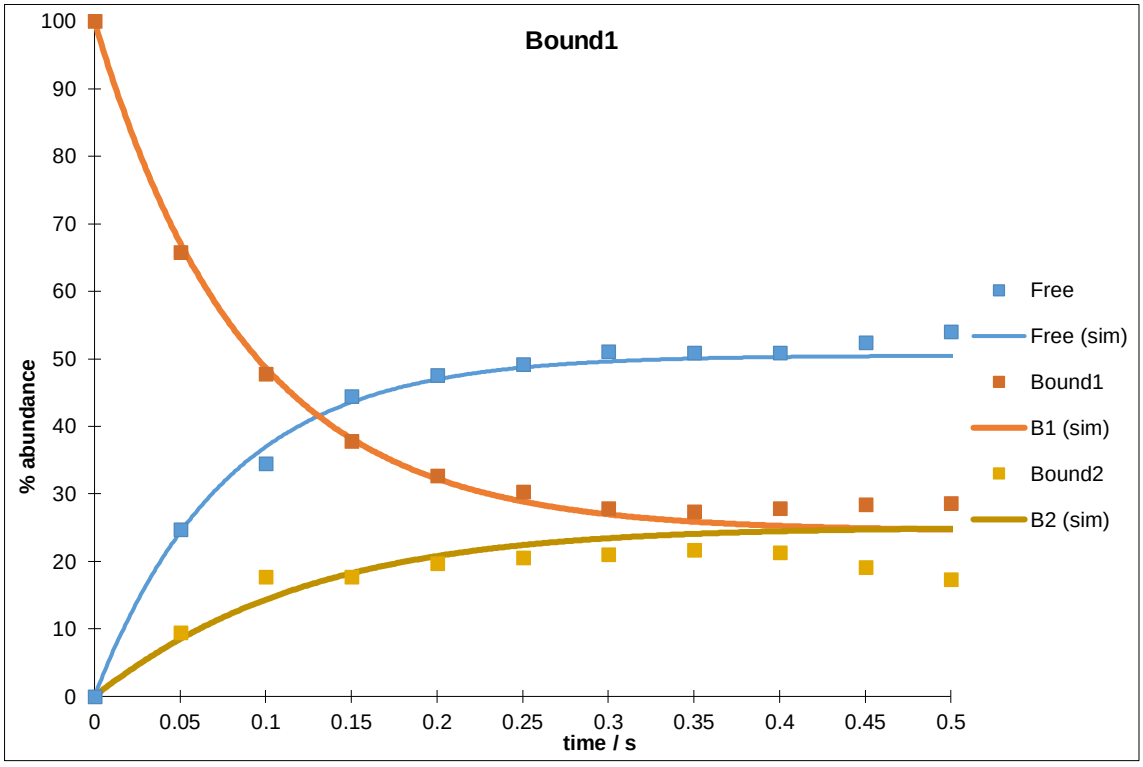

Figure 134: **'Bound 1' (A+G/2) excitation @ 303 K**

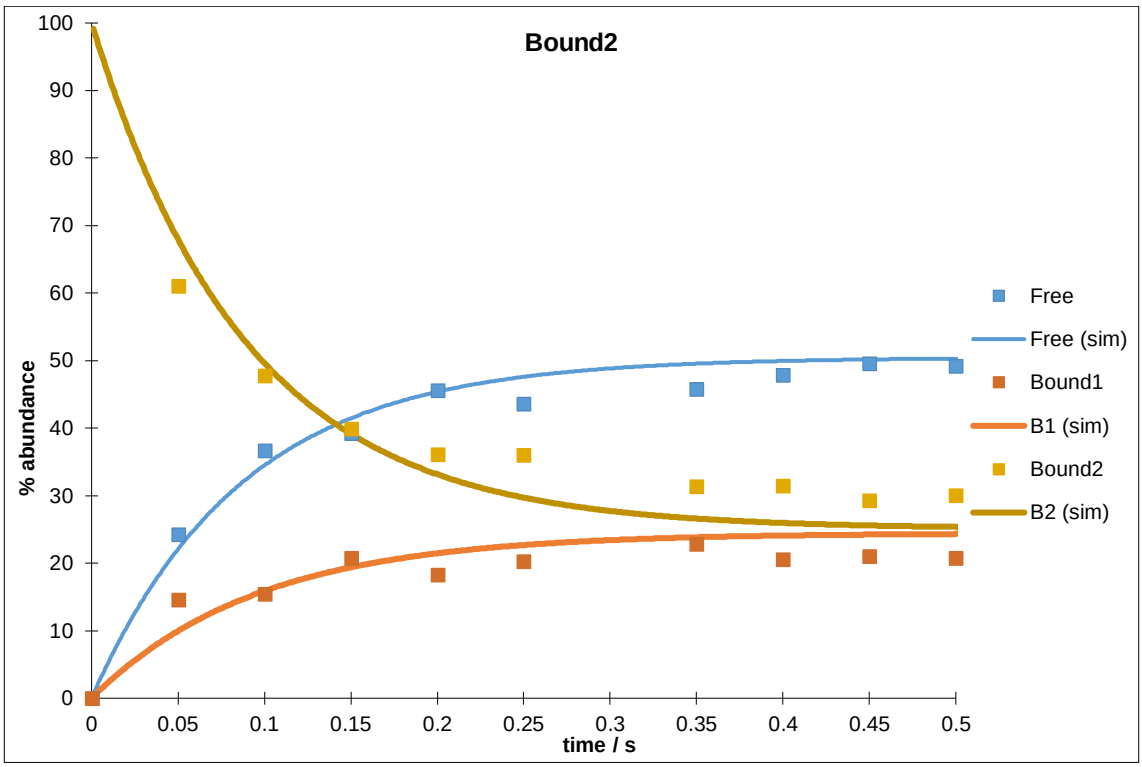

Figure 135: 'Bound 2' (F+G/2) excitation @ 303 K

	Free	Bound1	Bound2
Free	-6.049	2.883	3.167
Bound1	6.559	-8.558	1.998
Bound2	5.779	2.541	-8.320

Table 22: Model 1 observed rate constants for (−)-nicotine *1*, d_{22}-IMes *19* @ 303 K. Rate constants are read as k_{XY}, *i.e.* k_{AB} is row A, column B

Excitation	Sum of least squares
Bound 1	180.024
Bound 2	267.283
Total	447.307

Table 23: sum of least squares for each plot

Eyring plots

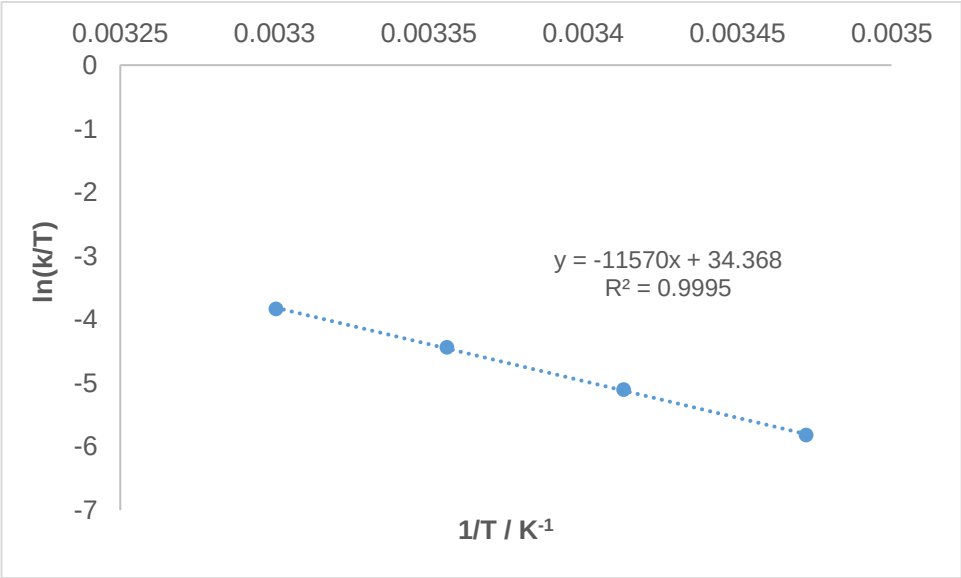

Figure 136: Eyring plot of Bound 1 for (−)-nicotine *1*, d_{22}-IMes *19*

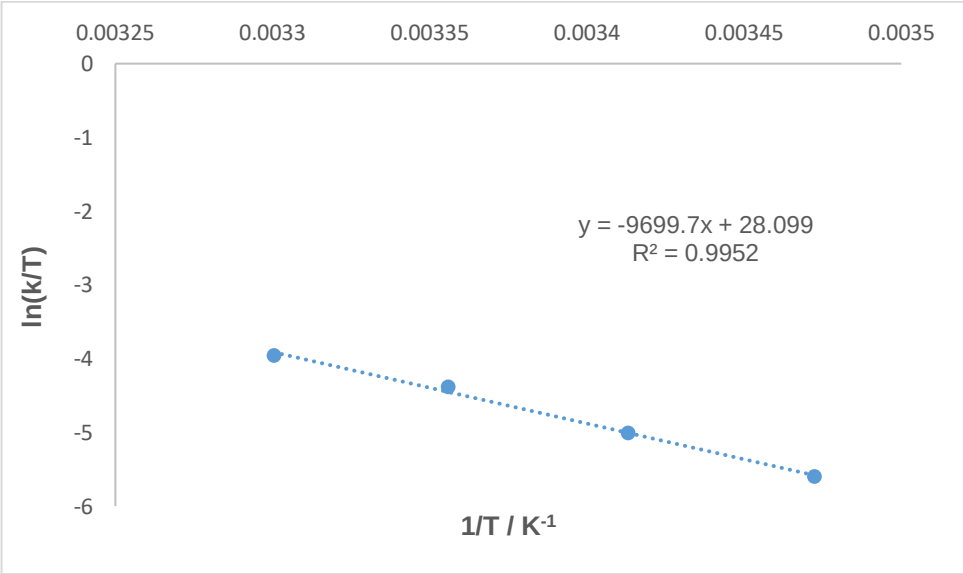

Figure 137: Eyring plot of Bound 2 for (−)-nicotine *1*, d_{22}-IMes *19*

Kinetic parameters

	Bound 1 -> Free	Bound 2 -> Free
ΔH‡ / kJmol-1	96.191	80.642
ΔS‡ / JK-1mol-1	88.201	36.081
ΔG_{300}‡ / kJmol-1	69.733	69.819

Figure 138: kinetic parameters for (−)-nicotine *1*, d_{22}-IMes *19*

7.1.3 Model 1 4,6-nicotine-d_2 9, IMes 18

288 K

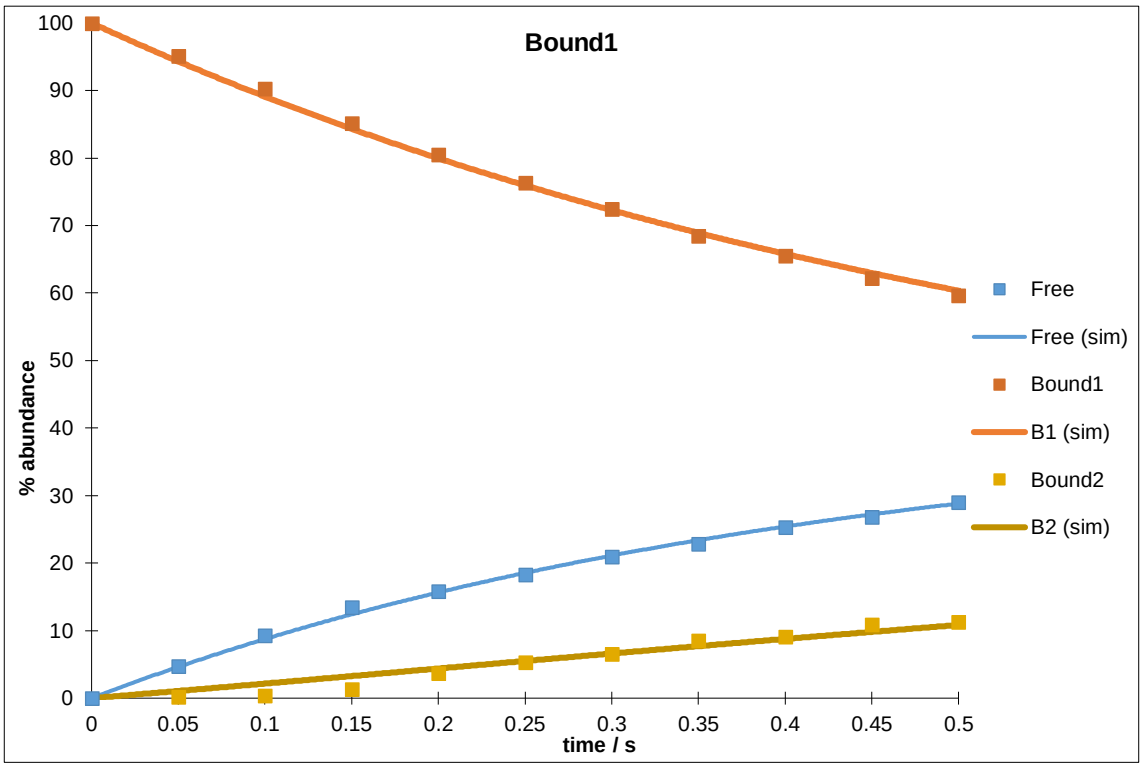

Figure 139: **'Bound 1' (A+G/2) excitation @ 288 K**

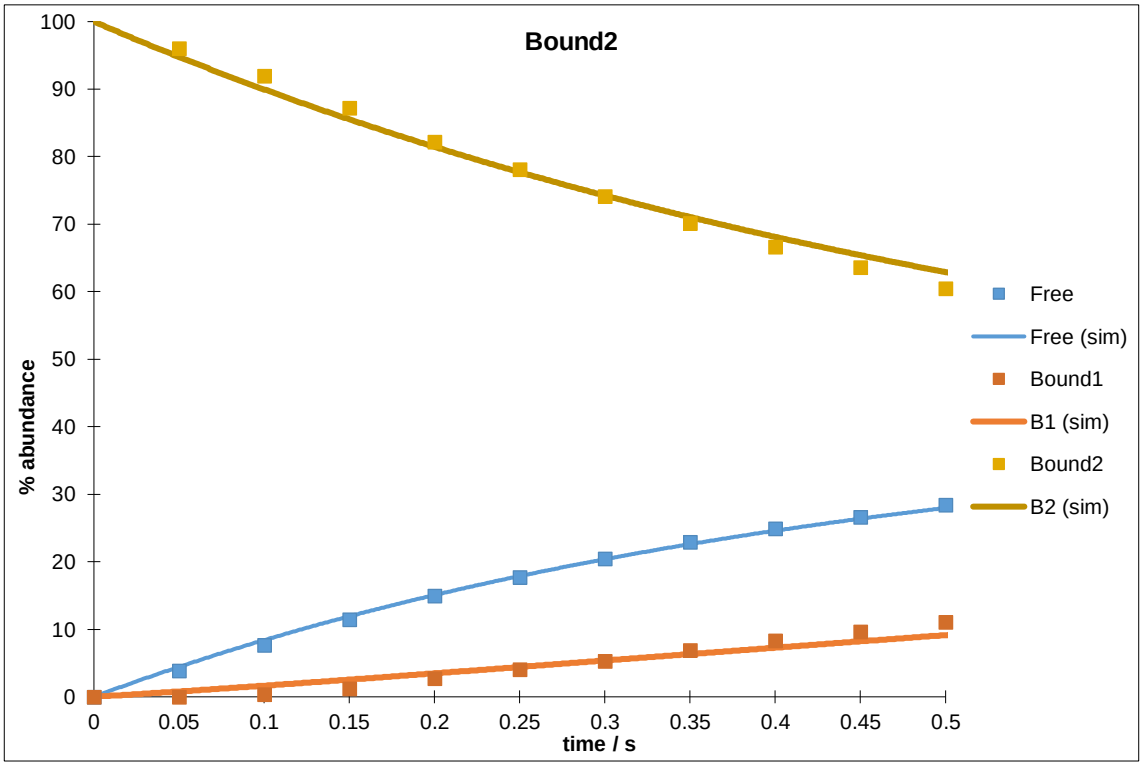

Figure 140: **'Bound 2' (F+G/2) excitation @ 288 K**

	Free	Bound1	Bound2
Free	-1.366	0.698	0.668
Bound1	0.981	-1.190	0.209
Bound2	0.939	0.152	-1.091

Table 24: Model 1 observed rate constants for 4,6-nicotine-d_2 *9*, IMes *18* @ 288 K. Rate constants are read as k_{XY}, *i.e.* k_{AB} is row A, column B

Excitation	Sum of least squares
Bound 1	16.881
Bound 2	21.742
Total	38.623

Table 25: sum of least squares for each plot and the modelled T_1 relaxation parameters (in seconds) used

293 K

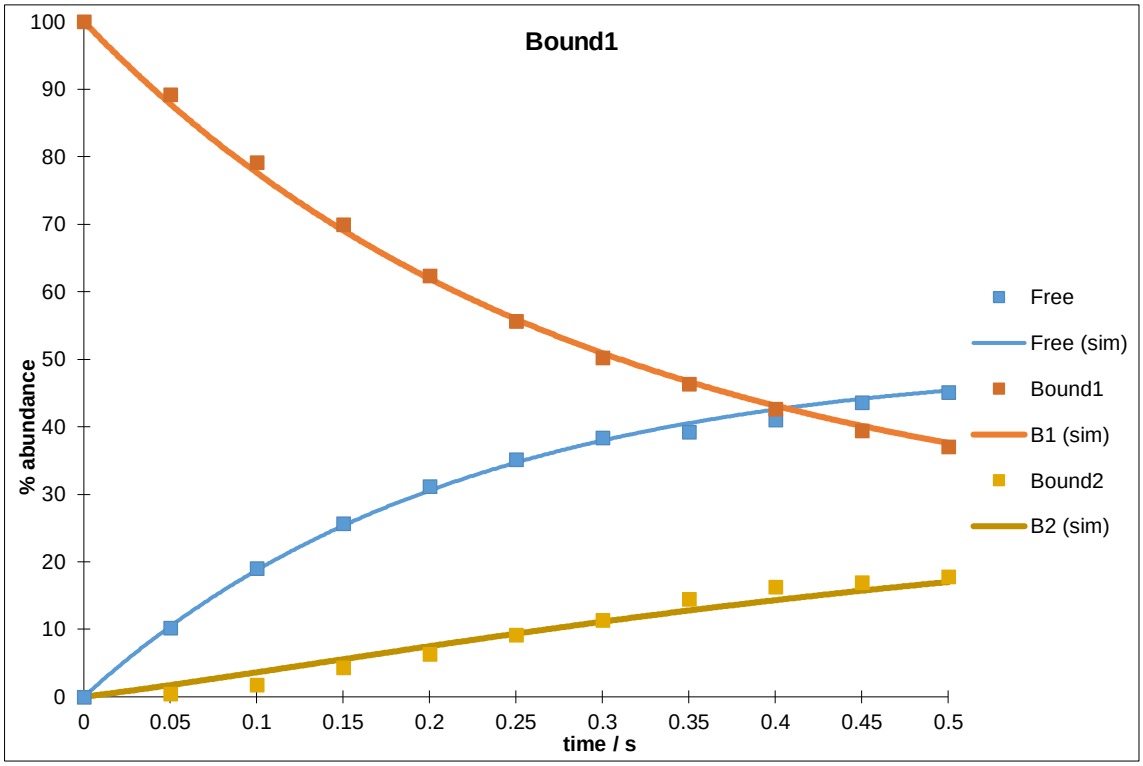

Figure 141: 'Bound 1' (A+G/2) excitation @ 293 K

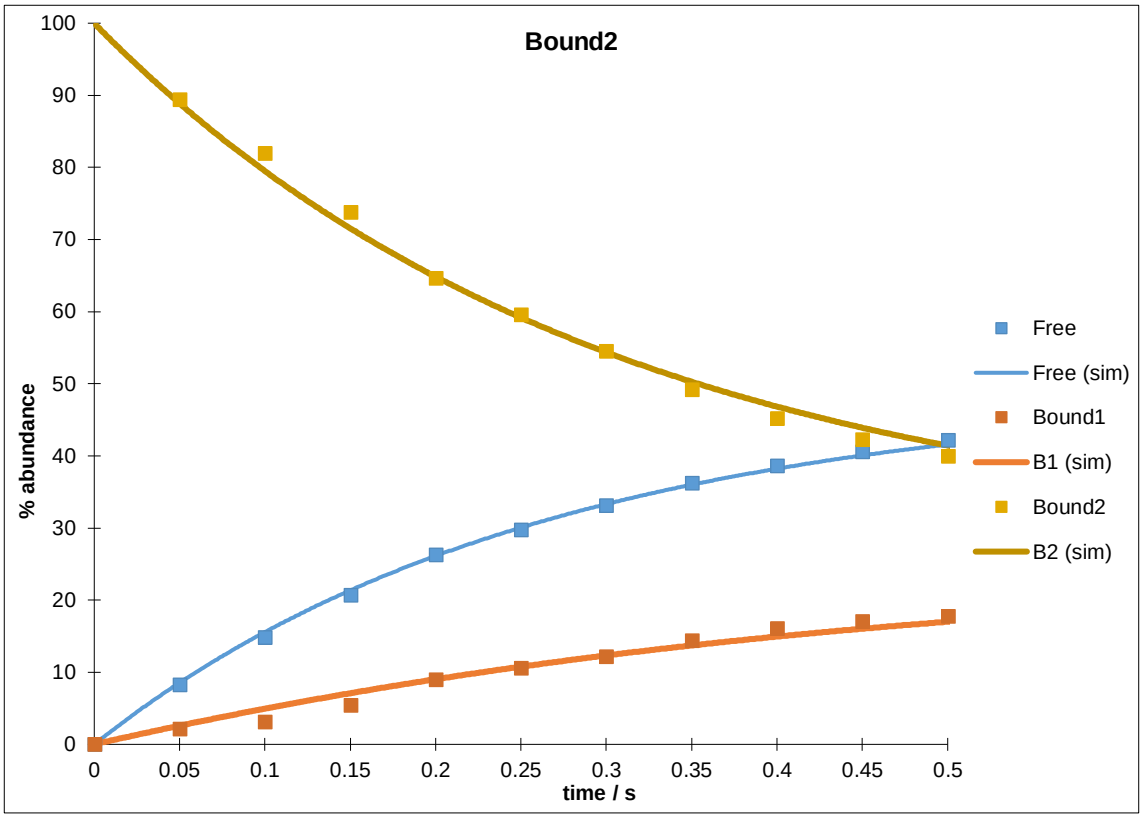

Figure 142: **'Bound 2' (F+G/2) excitation @ 293 K**

	Free	Bound1	Bound2
Free	-2.158	0.985	1.173
Bound1	2.332	-2.658	0.327
Bound2	1.877	0.539	-2.416

Table 26: **Model 1 observed rate constants for 4,6-nicotine-*d*$_2$ *9*, IMes *18* @ 293 K. Rate constants are read as k_{XY}, *i.e.* k_{AB} is row A, column B**

Excitation	Sum of least squares
Bound 1	23.041
Bound 2	28.383
Total	51.424

Table 27: sum of least squares for each plot

298 K

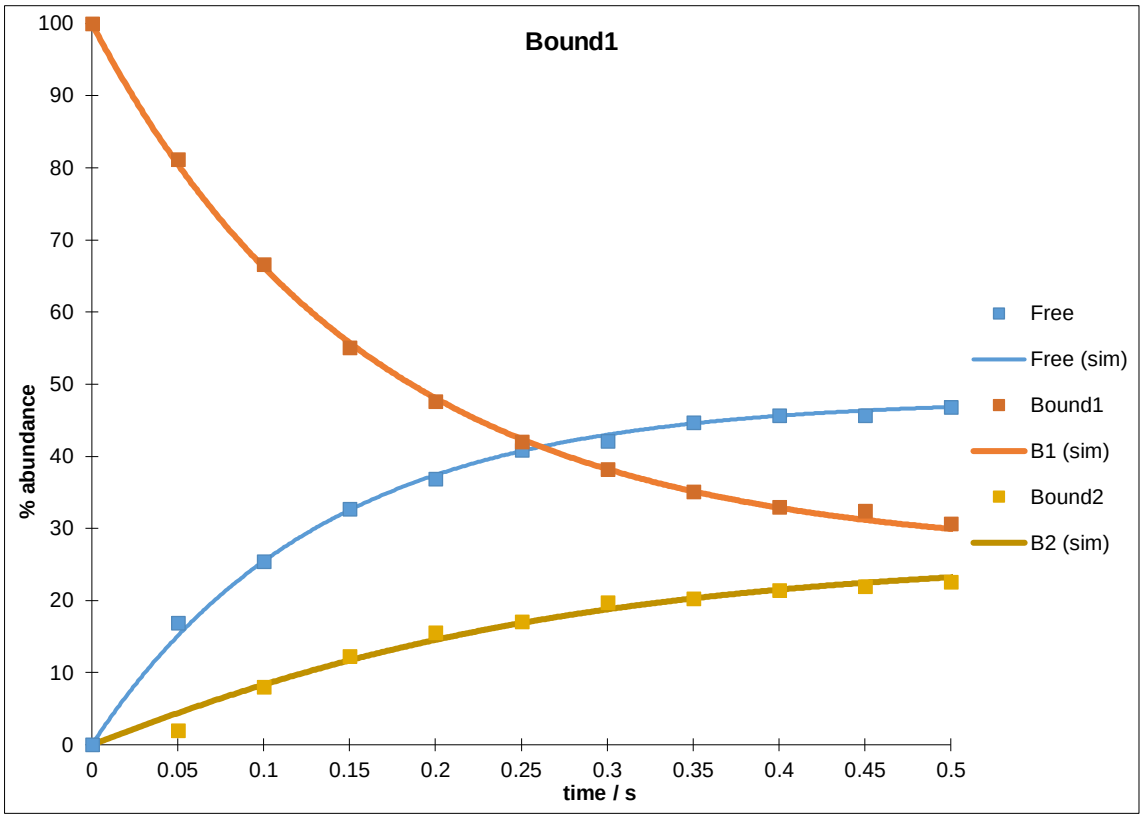

Figure 143: **'Bound 1' (A+G/2) excitation @ 298 K**

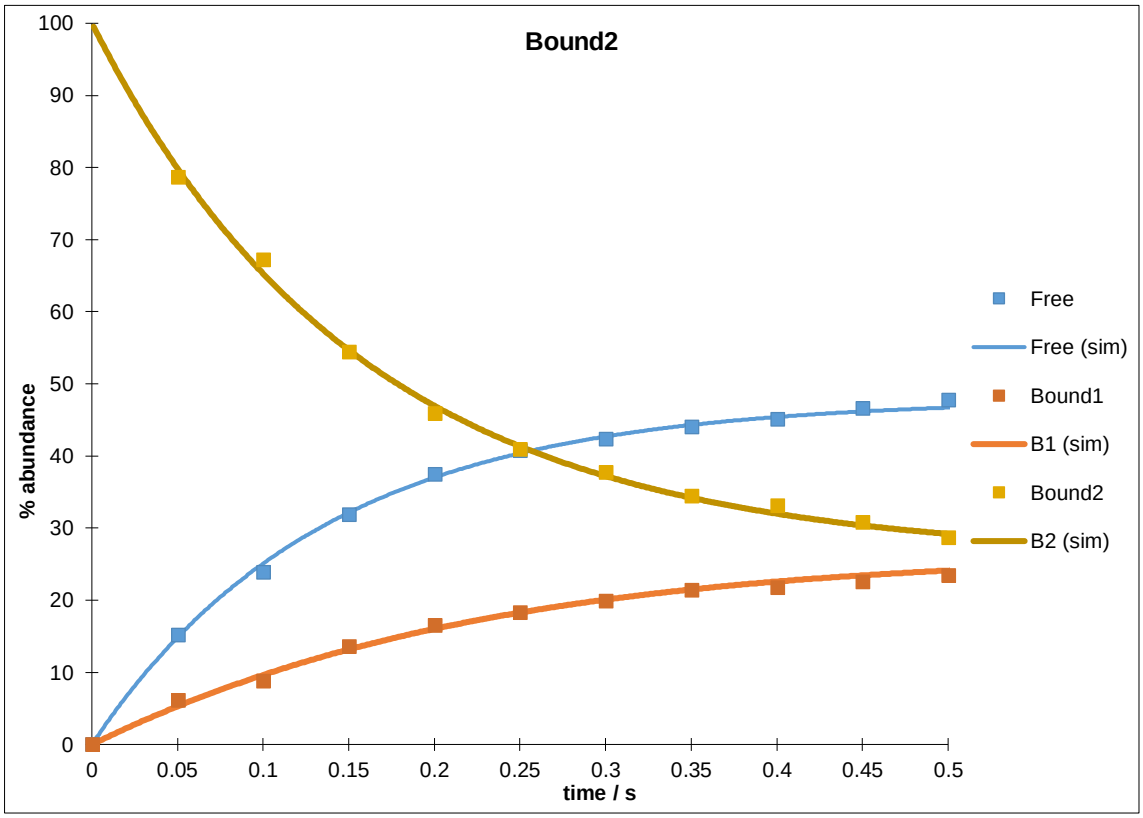

Figure 144: **'Bound 2' (F+G/2) excitation @ 298 K**

	Free	Bound1	Bound2
Free	-3.892	1.867	2.025
Bound1	3.612	-4.527	0.915
Bound2	3.543	1.152	-4.694

Table 28: **Model 1 observed rate constants for 4,6-nicotine-d_2 *9*, IMes *18* @ 298 K. Rate constants are read as k_{XY}, *i.e.* k_{AB} is row A, column B**

Excitation	Sum of least squares
Bound 1	17.252
Bound 2	13.744
Total	30.995

Table 29: sum of least squares for each plot

303 K

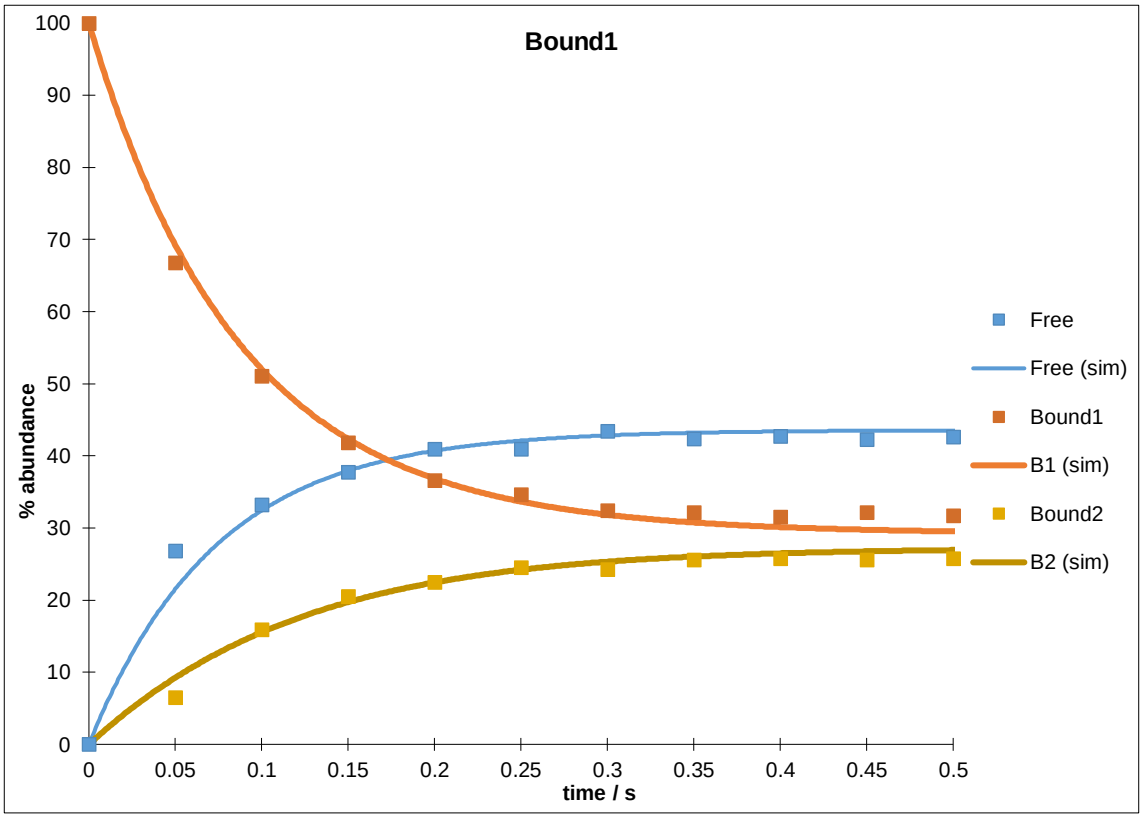

Figure 145: **'Bound 1' (A+G/2) excitation @ 303 K**

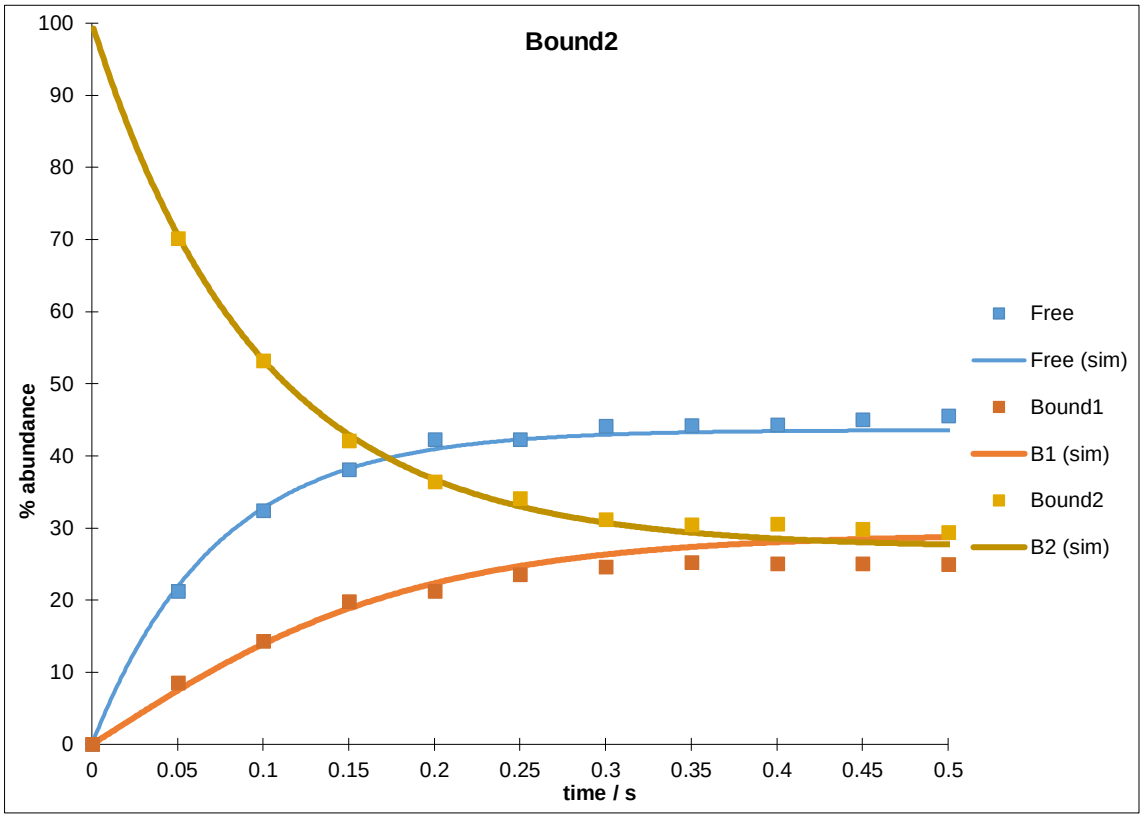

Figure 146: **'Bound 2' (F+G/2) excitation @ 303 K**

	Free	Bound1	Bound2
Free	-7.716	4.505	3.210
Bound1	5.910	-8.106	2.196
Bound2	6.015	1.479	-7.495

Table 30: **Model 1 observed rate constants for 4,6-nicotine-d_2 *9*, IMes *18* @ 303 K. Rate constants are read as k_{XY}, *i.e.* k_{AB} is row A, column B**

Excitation	Sum of least squares
Bound 1	25.419
Bound 2	33.471
Total	58.890

Table 31: sum of least squares for each plot and the modelled T_1 relaxation parameters (in seconds) used

Eyring plots

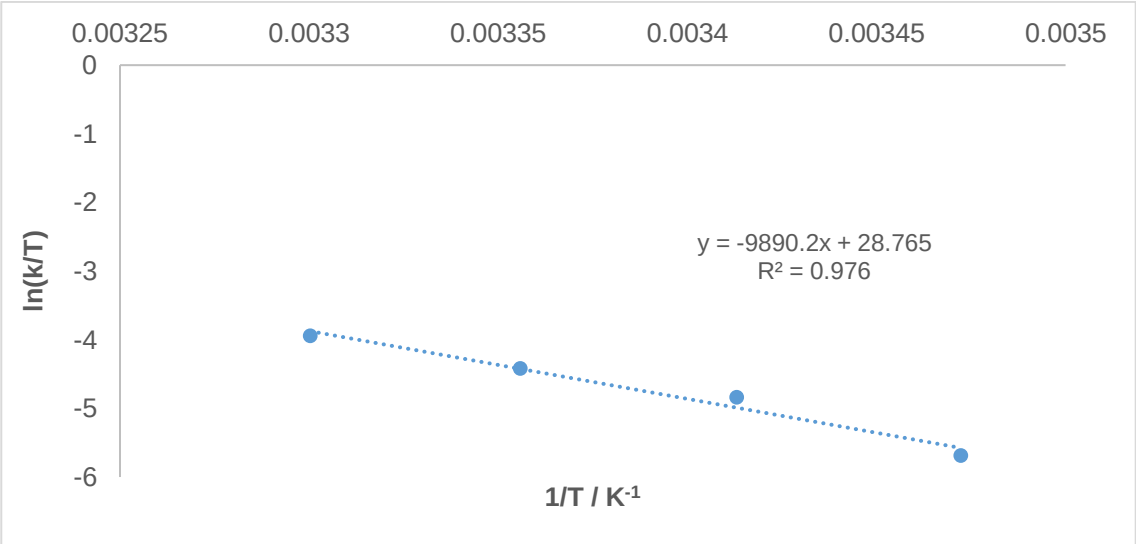

Figure 147: Eyring plot of Bound 1 for 4,6-nicotine-d_2 *9*, IMes *18*

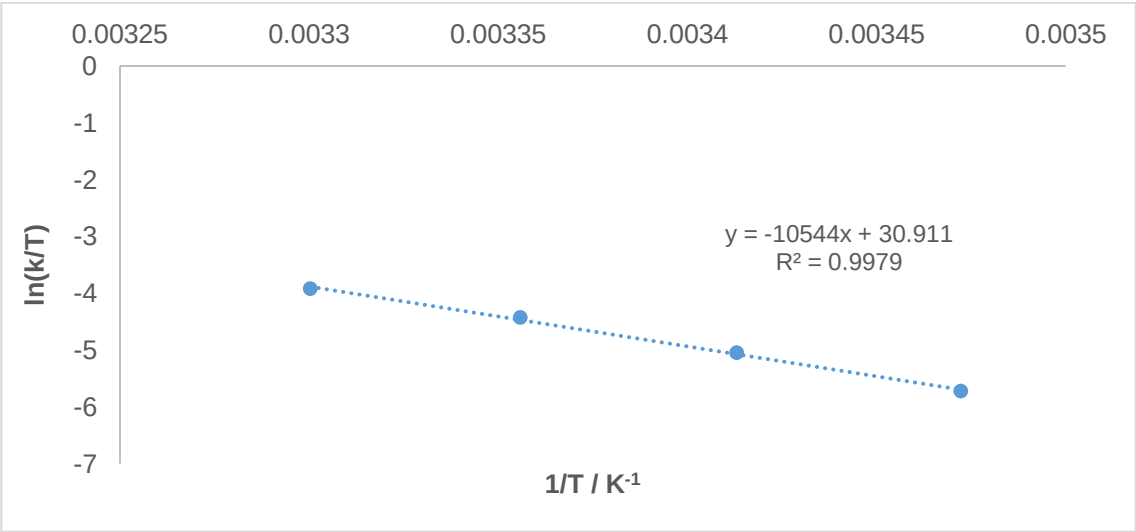

Figure 148: Eyring plot of Bound 2 for 4,6-nicotine-d_2 *9*, IMes *18*

Kinetic parameters

	Bound 1 -> Free	**Bound 2 -> Free**
ΔH‡ / kJmol-1	82.227	87.663
ΔS‡ / JK-1mol-1	41.617	59.459
ΔG‡300 / kJmol-1	69.742	69.825

Figure 149: kinetic parameters for 4,6-nicotine-d_2 *9*, IMes *18*

7.1.4 Model 1 4,6-nicotine-d_2 9, d_{22}-IMes 19

288 K

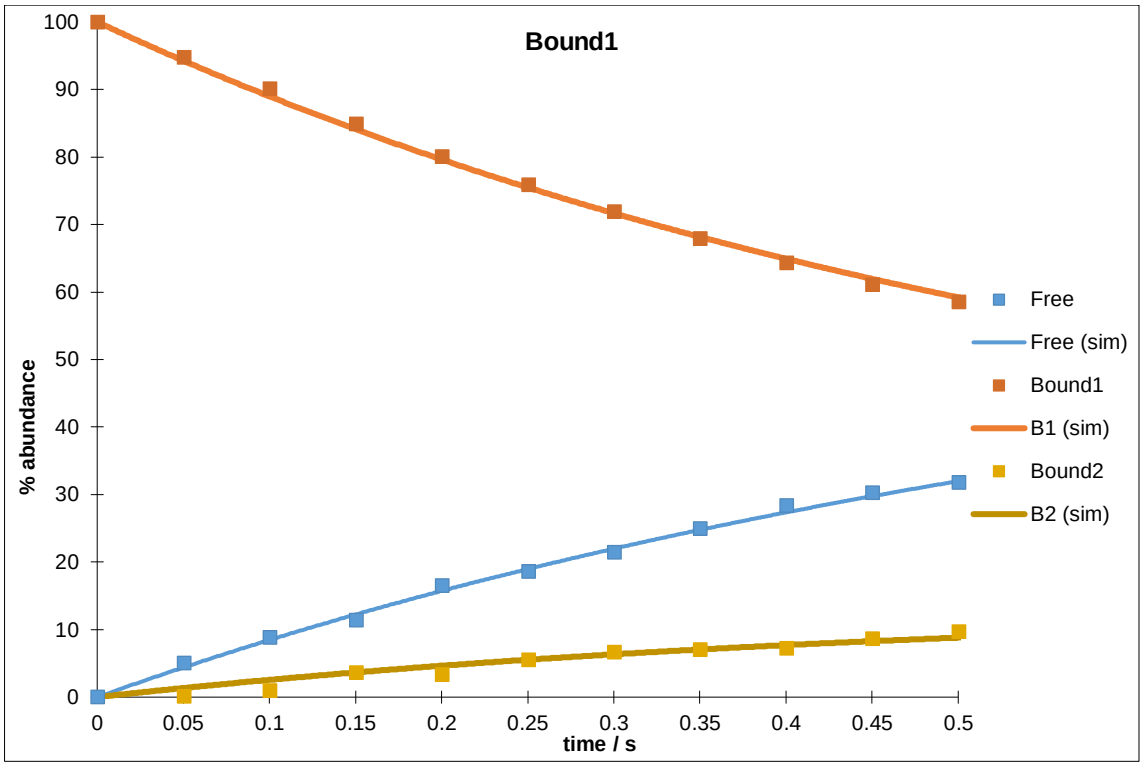

Figure 150: **'Bound 1' (A+G/2) excitation @ 288 K**

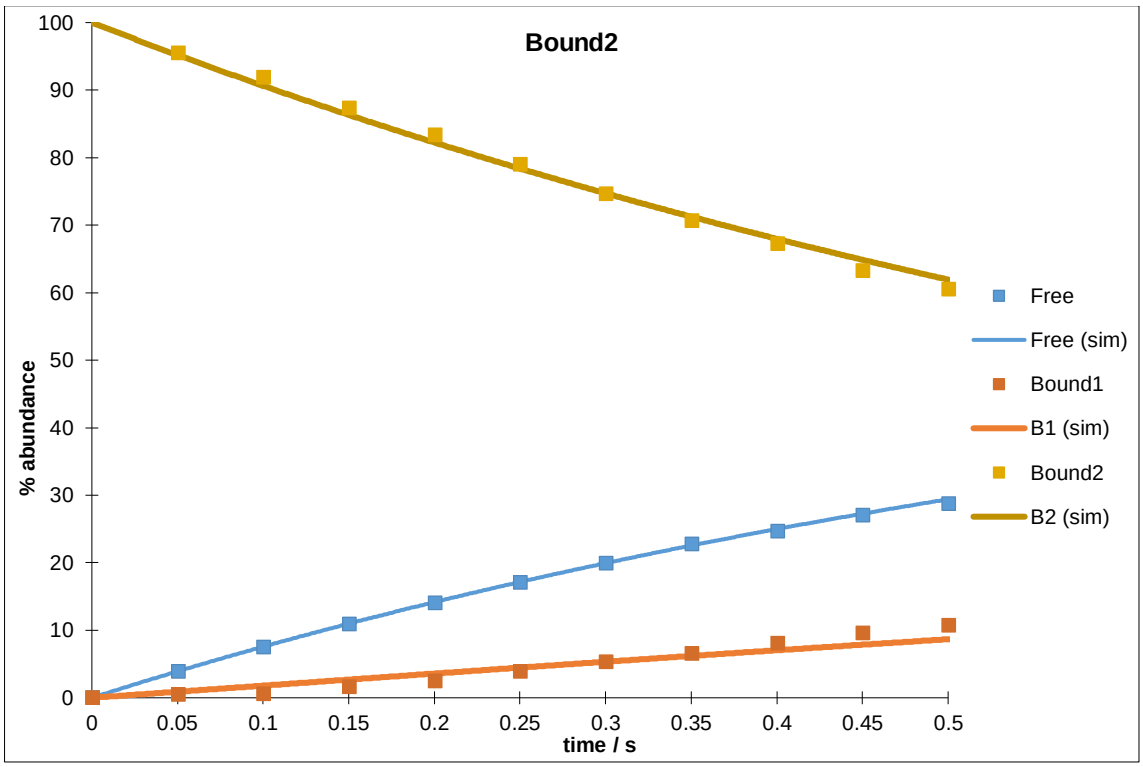

Figure 151: **'Bound 2' (F+G/2) excitation @ 288 K**

	Free	Bound1	Bound2
Free	-0.570	0.516	0.054
Bound1	0.911	-1.193	0.283
Bound2	0.808	0.179	-0.987

Table 32: Model 1 observed rate constants for 4,6-nicotine-d_2 *9*, d_{22}-IMes *19* @ 288 K. Rate constants are read as k_{XY}, *i.e.* k_{AB} is row A, column B

Excitation	Sum of least squares
Bound 1	12.975
Bound 2	15.029
Total	28.005

Table 33: sum of least squares for each plot

293 K

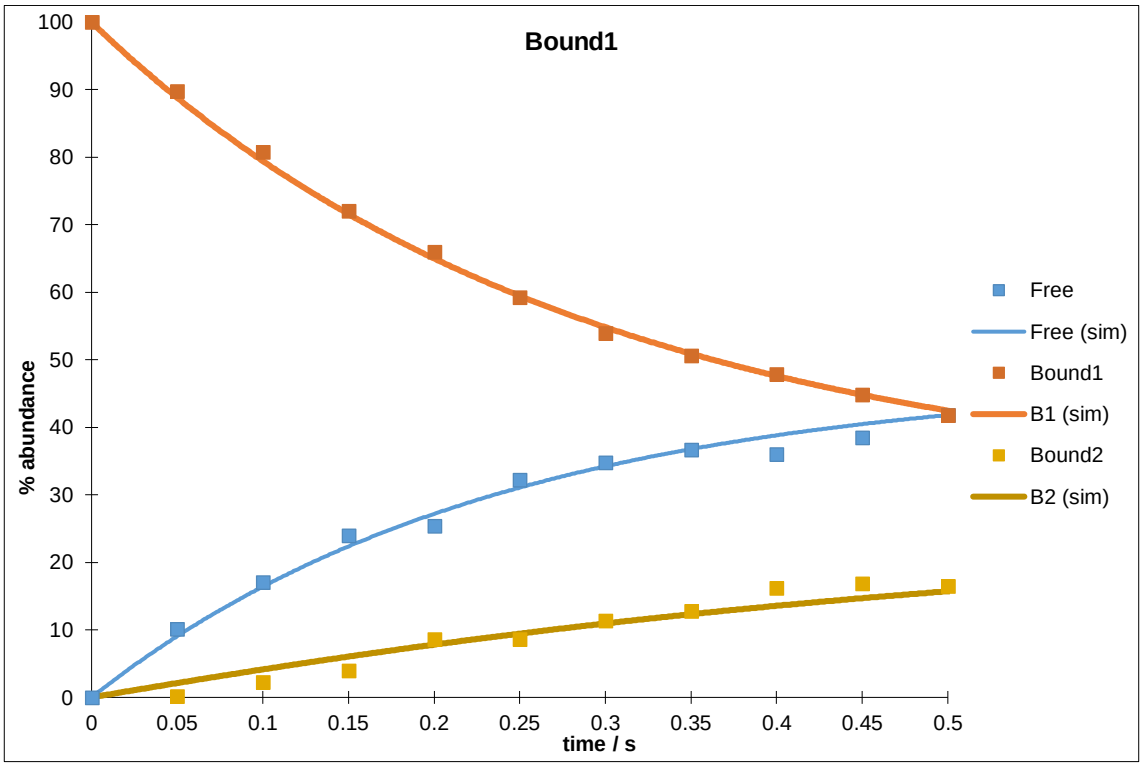

Figure 152: 'Bound 1' (A+G/2) excitation @ 293 K

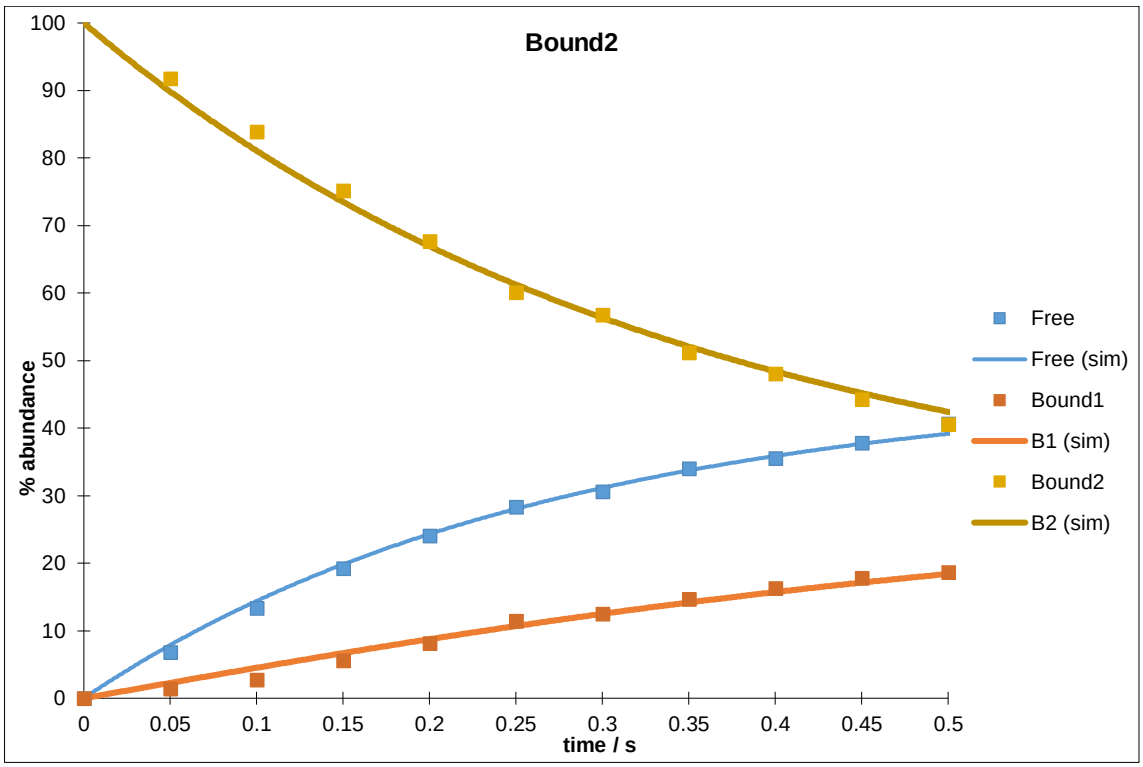

Figure 153: **'Bound 2' (F+G/2) excitation @ 293 K**

	Free	Bound1	Bound2
Free	-2.117	1.277	0.840
Bound1	2.005	-2.439	0.434
Bound2	1.726	0.454	-2.180

Table 34: **Model 1 observed rate constants for 4,6-nicotine-d_2 *9*, d_{22}-IMes *19* @ 293 K. Rate constants are read as k_{XY}, *i.e.* k_{AB} is row A, column B**

Excitation	Sum of least squares
Bound 1	37.010
Bound 2	33.872
Total	70.882

Table 35: sum of least squares for each plot

298 K

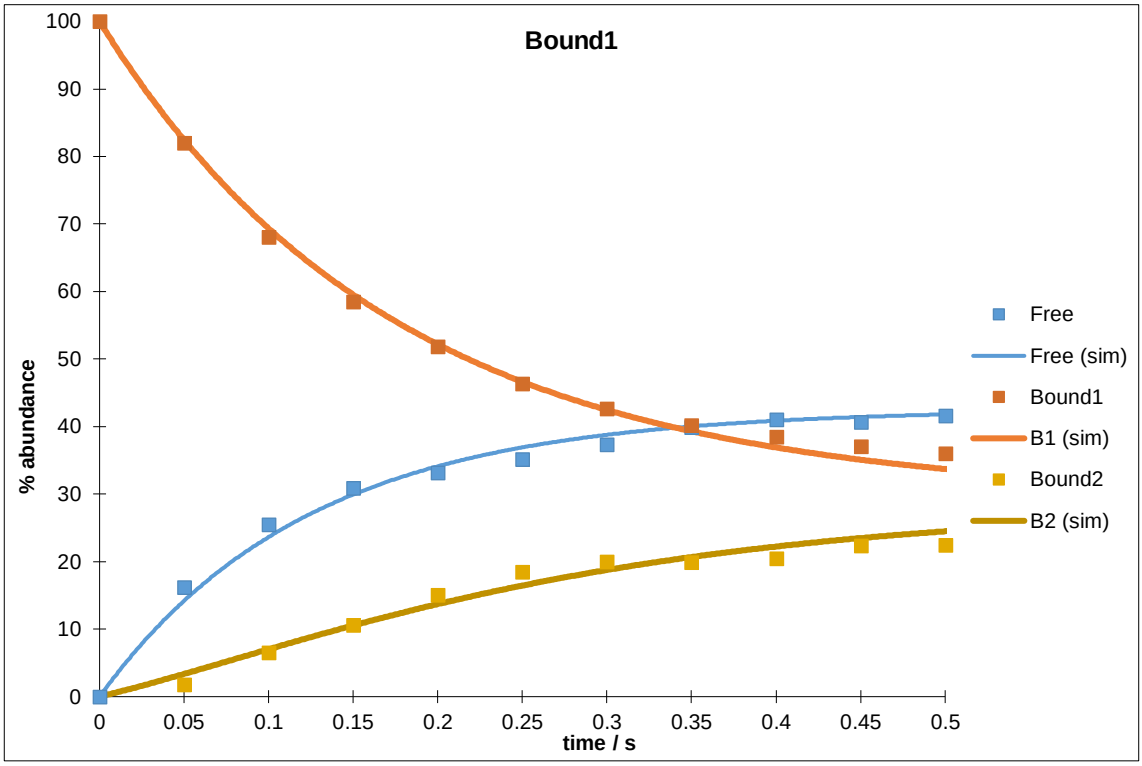

Figure 154: 'Bound 1' (A+G/2) excitation @ 298 K

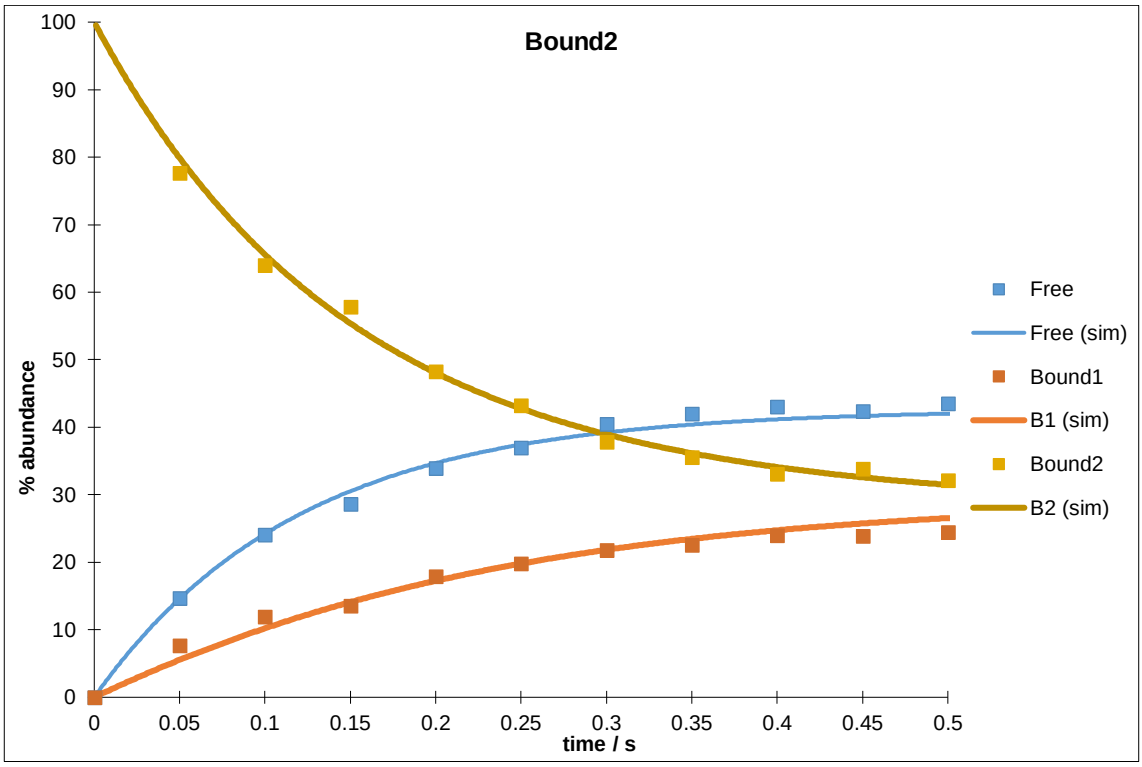

Figure 155: 'Bound 2' (F+G/2) excitation @ 298 K

	Free	Bound1	Bound2
Free	-4.714	1.994	2.721
Bound1	3.446	-4.047	0.601
Bound2	3.554	1.192	-4.746

Table 36: **Model 1 observed rate constants for 4,6-nicotine-d_2 *9*, d_{22}-IMes *19* @ 298 K. Rate constants are read as k_{XY}, *i.e.* k_{AB} is row A, column B**

Excitation	Sum of least squares
Bound 1	44.441
Bound 2	45.773
Total	90.214

Table 37: sum of least squares for each plot

303 K

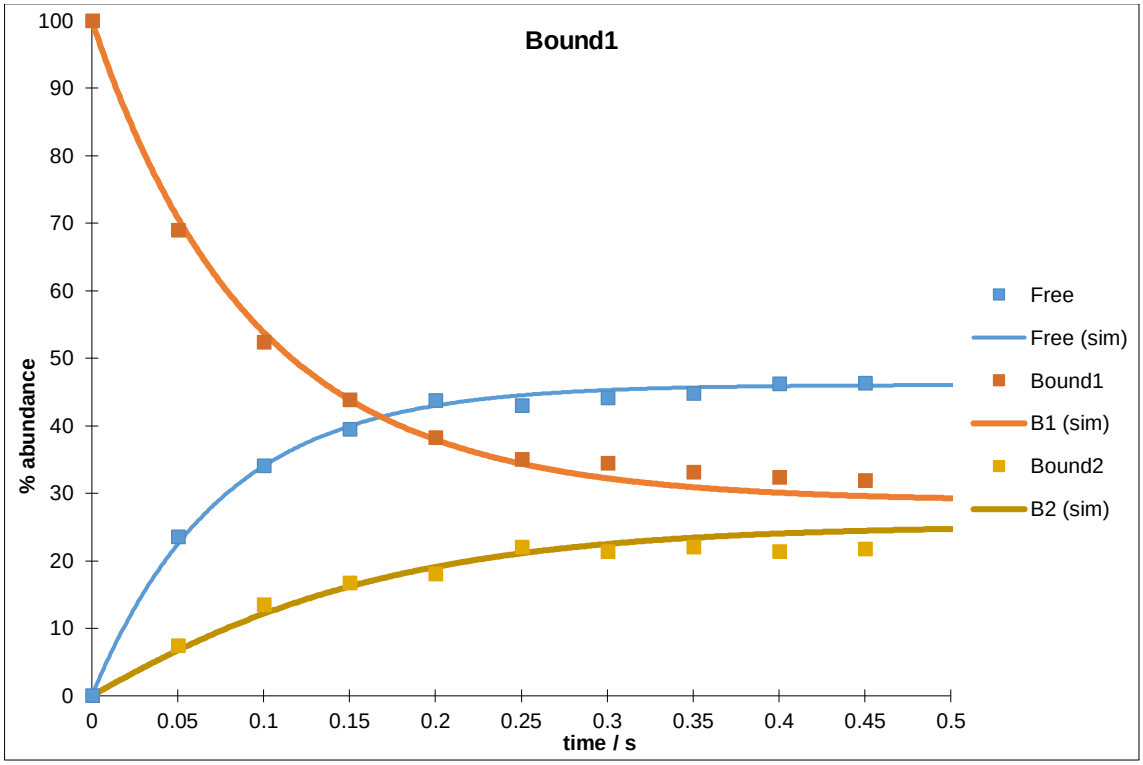

Figure 156: **'Bound 1' (A+G/2) excitation @ 303 K**

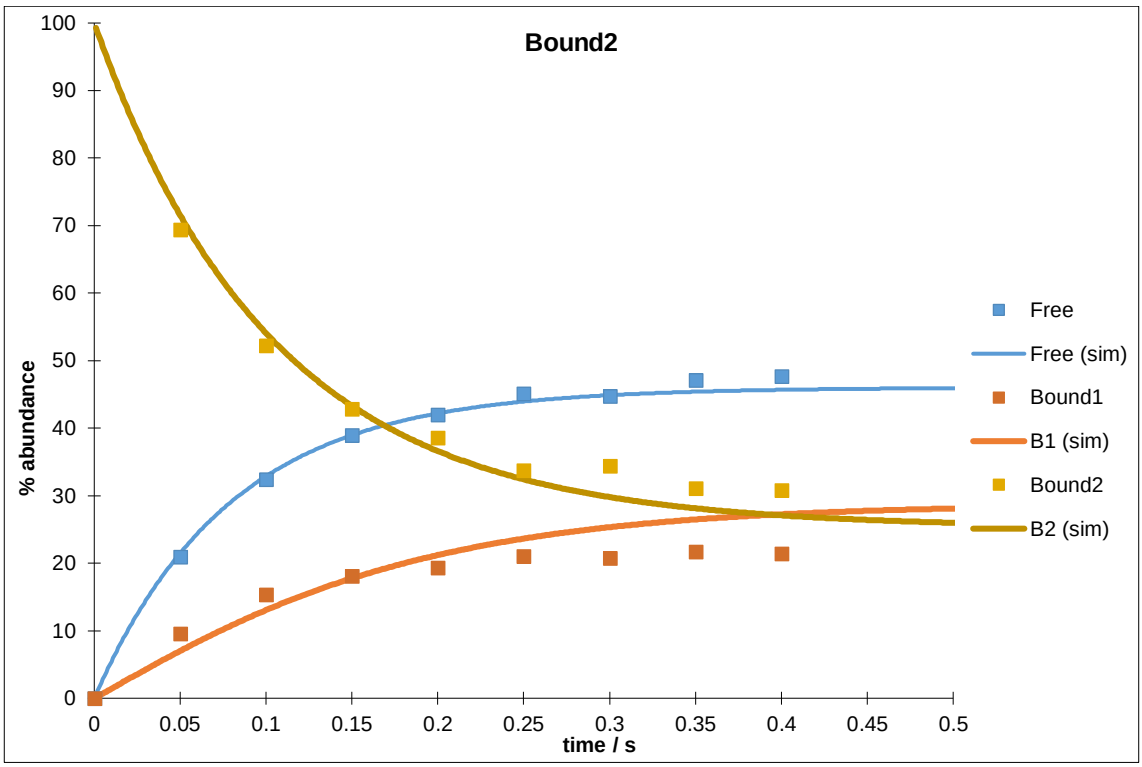

Figure 157: **'Bound 2' (F+G/2) excitation @ 303 K**

kY Y=XY	Free	Bound1	Bound2
Free	-6.972	3.935	3.037
Bound1	6.105	-7.549	1.445
Bound2	5.771	1.417	-7.188

Table 38: **Model 1 observed rate constants for 4,6-nicotine-d_2 *9*, d_{22}-IMes *19* @ 303 K. Rate constants are read as k_{XY}, *i.e.* k_{AB} is row A, column B**

Excitation	Sum of least squares
Bound 1	42.067
Bound 2	71.859
Total	113.926

Table 39: sum of least squares for each plot

Eyring plots

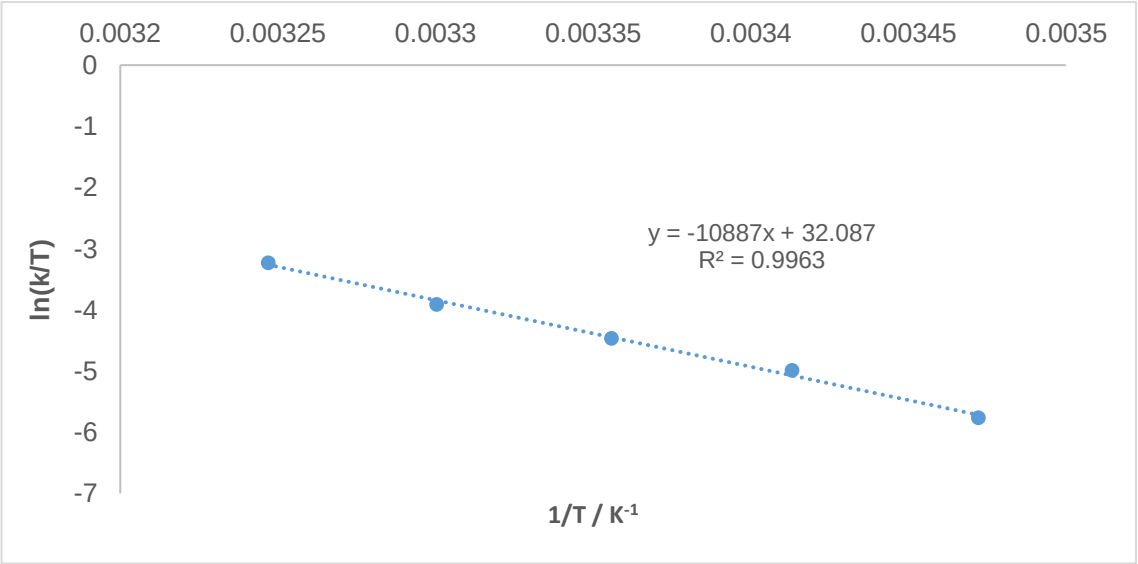

Figure 158: Eyring plot of Bound 1 for 4,6-nicotine-d_2 *9*, d_{22}-IMes *19*

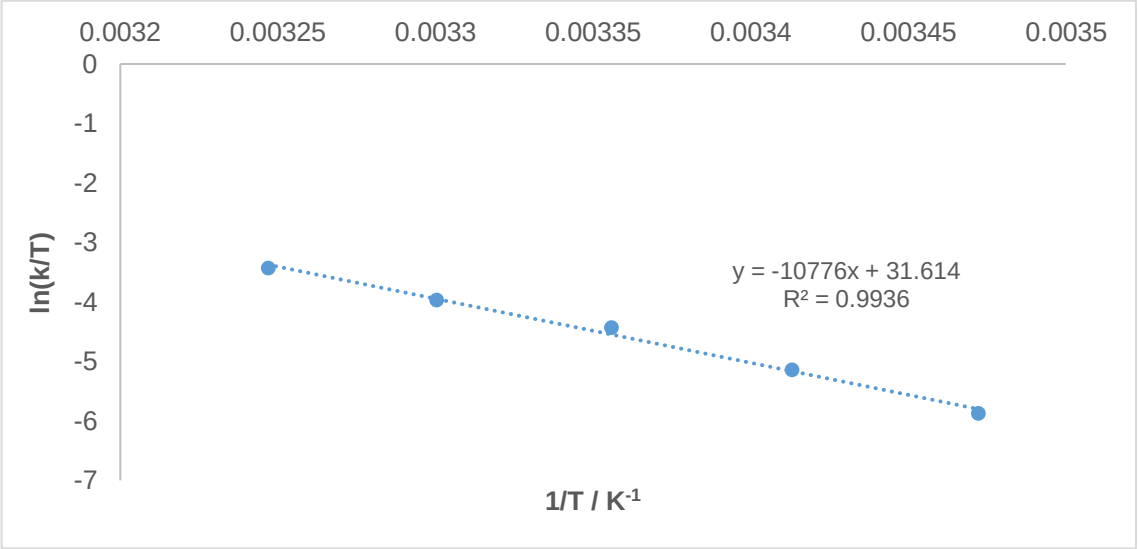

Figure 159: Eyring plot of Bound 2 for 4,6-nicotine-d_2 *9*, d_{22}-IMes *19*

Kinetic parameters

	Bound 1 -> Free	Bound 2 -> Free
ΔH‡ / kJmol-1	90.515	89.592
ΔS‡ / JK-1mol-1	69.236	65.303
ΔG_{300}‡ / kJmol-1	69.744	70.001

Figure 160: kinetic parameters for 4,6-nicotine-d_2 *9*, d_{22}-IMes *19*

7.2 Model 4 EXSY plots and rate constant tables

7.2.1 Model 4 (−)-nicotine 1, IMes 18

288 K

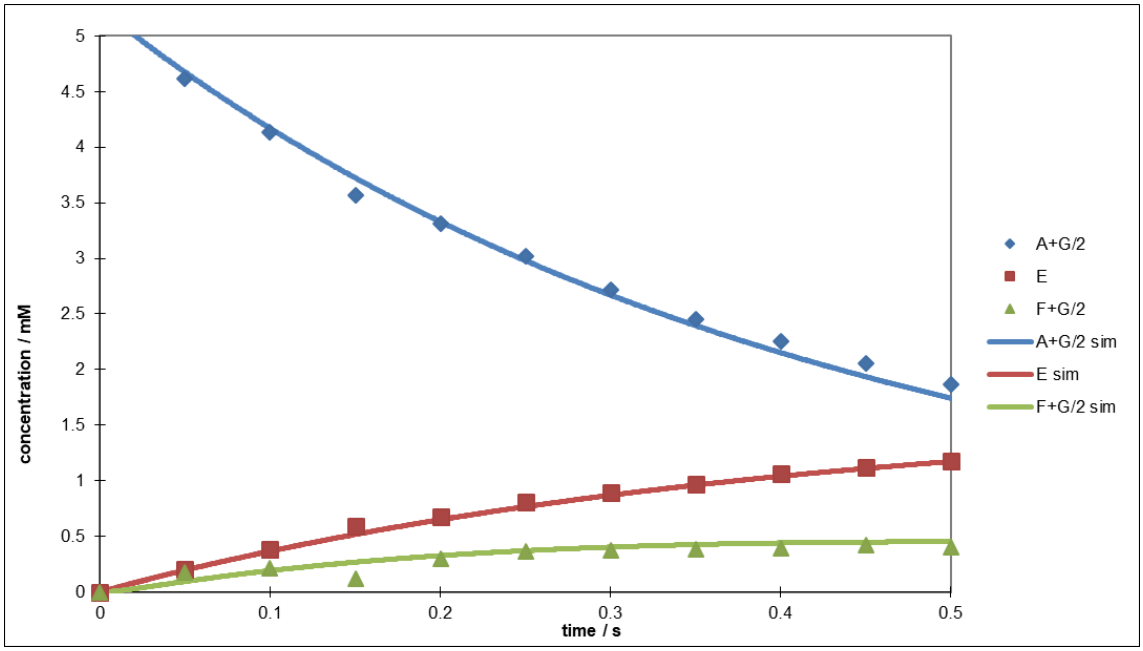

Figure 161: **'Bound 1' (A+G/2) excitation @ 288 K**

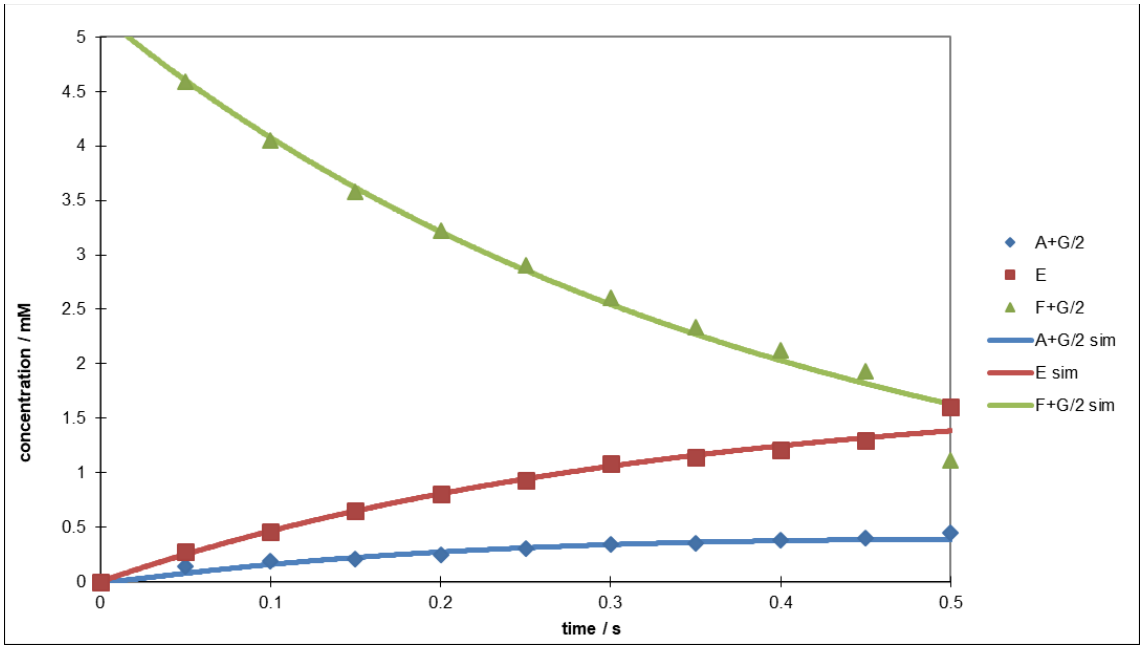

Figure 162: **'Bound 2' (F+G/2) excitation @ 288 K**

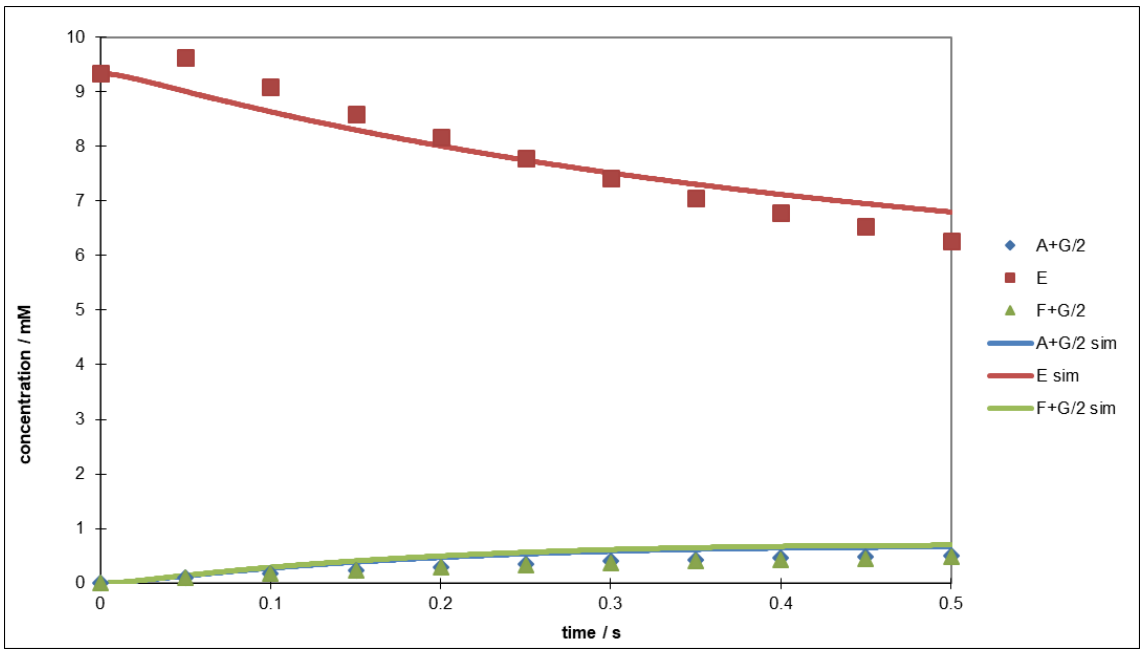

Figure 163: **'Free' (E) excitation @ 288 K**

-3.876	0.897	1.041	1.041	0.897	0	0	0	**A**
4.699	-12.864	0	0	0	5.083	0	3.082	**B**
5.083	0	-12.864	0	0	4.699	3.082	0	**C**
5.083	0	0	-12.864	0	4.699	0	3.082	**D**
4.699	0	0	0	-12.864	5.083	3.082	0	**E**
0	1.041	0.897	0.897	1.041	-3.876	0	0	**F**
0	0	11.026	0	11.026	0	-22.053	0	**G**
0	11.026	0	11.026	0	0	0	-22.053	**H**
A	**B**	**C**	**D**	**E**	**F**	**G**	**H**	

Table 40: **Model 4 observed rate constants for (−)-nicotine *1*, IMes *18* @ 288 K. Rate constants are read as k_{XY}, *i.e.* k_{AB} is row A, column B**

Excitation	Sum of least squares
Bound 1	0.233
Bound 2	0.399
Free	1.667
Total	2.299

Relax Bound	Relax Free	Relax Inter.
1.021	10.000	1.021

Table 41: sum of least squares for each plot and the modelled T_1 relaxation parameters (in seconds) used

293 K

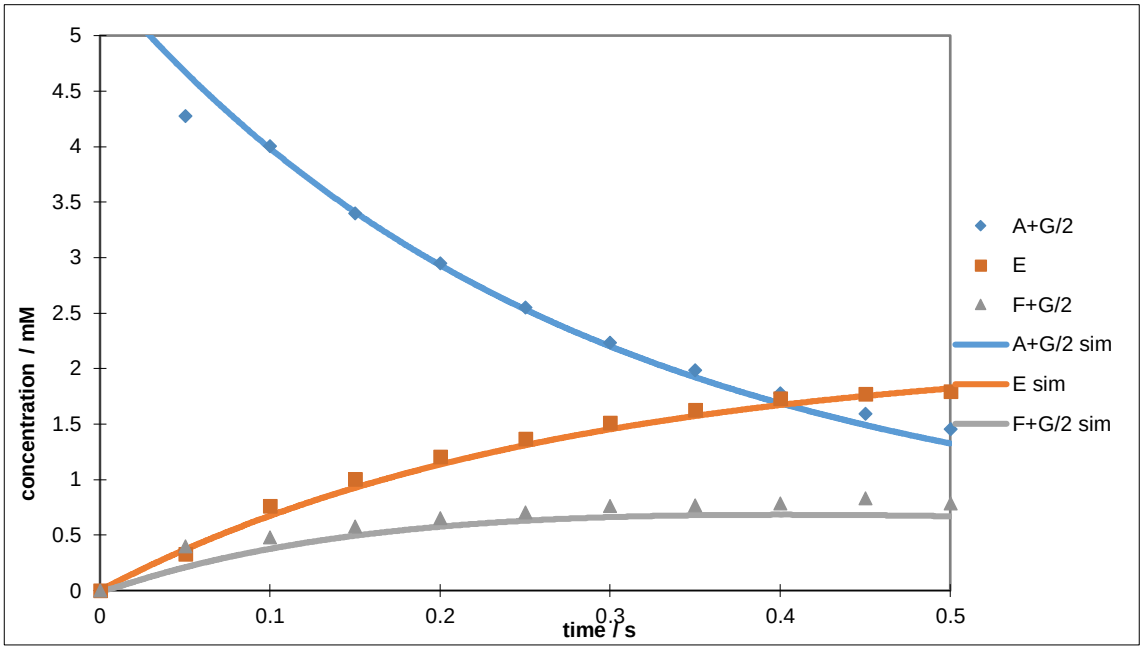

Figure 164: 'Bound 1' (A+G/2) excitation @ 293 K

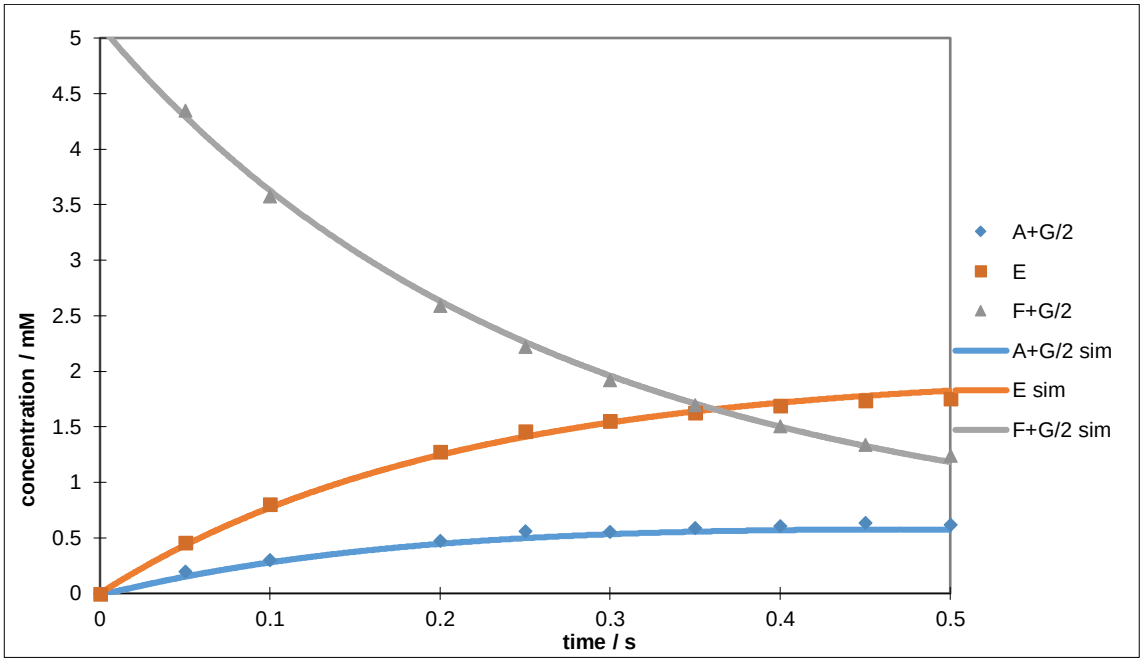

Figure 165: 'Bound 2' (F+G/2) excitation @ 293 K

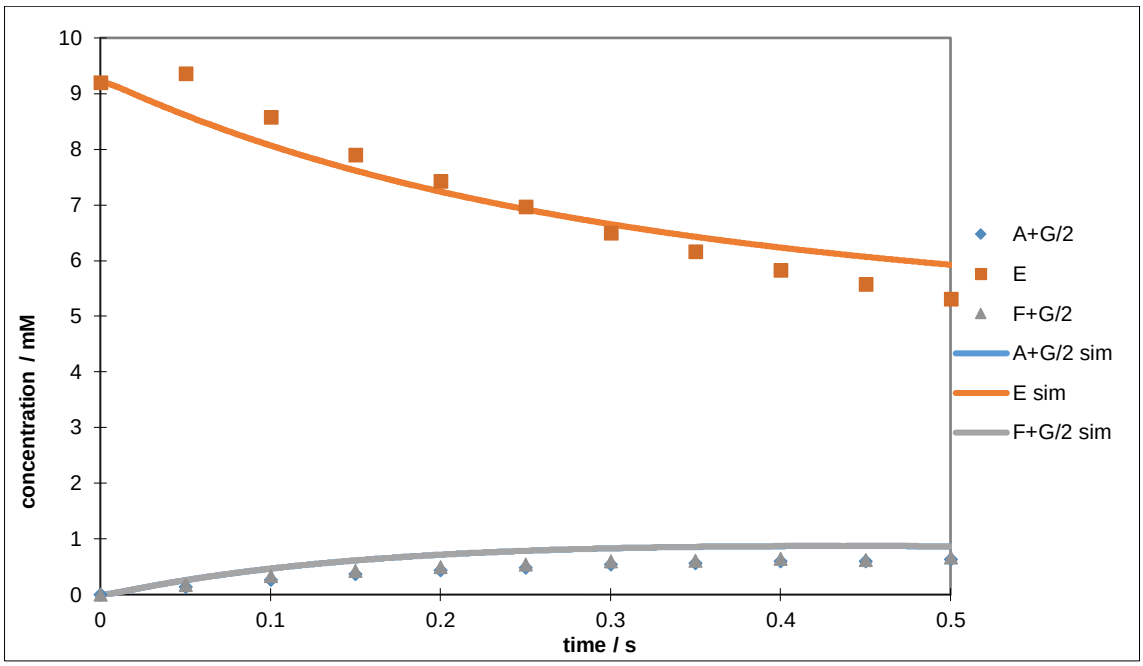

Figure 166: **'Free' (E) excitation @ 293 K**

-6.253	1.460	1.666	1.666	1.460	0	0	0	**A**
7.968	-18.972	0	0	0	7.934	0	3.070	**B**
7.934	0	-18.972	0	0	7.968	3.070	0	**C**
7.934	0	0	-18.972	0	7.968	0	3.070	**D**
7.968	0	0	0	-18.972	7.934	3.070	0	**E**
0	1.666	1.460	1.460	1.666	-6.253	0	0	**F**
0	0	15.646	0	15.646	0	-31.291	0	**G**
0	15.646	0	15.646	0	0	0	-31.291	**H**
A	**B**	**C**	**D**	**E**	**F**	**G**	**H**	

Table 42: **Model 4 observed rate constants for (−)-nicotine *1*, IMes *18* @ 293 K. Rate constants are read as k_{XY}, *i.e.* k_{AB} is row A, column B**

Excitation	Sum of least squares
Bound 1	0.380
Bound 2	0.067
Free	2.918
Total	3.365

Relax Bound	Relax Free	Relax Inter.
1.155	10.000	1.155

Table 43: sum of least squares for each plot and the modelled T_1 relaxation parameters (in seconds) used

298 K

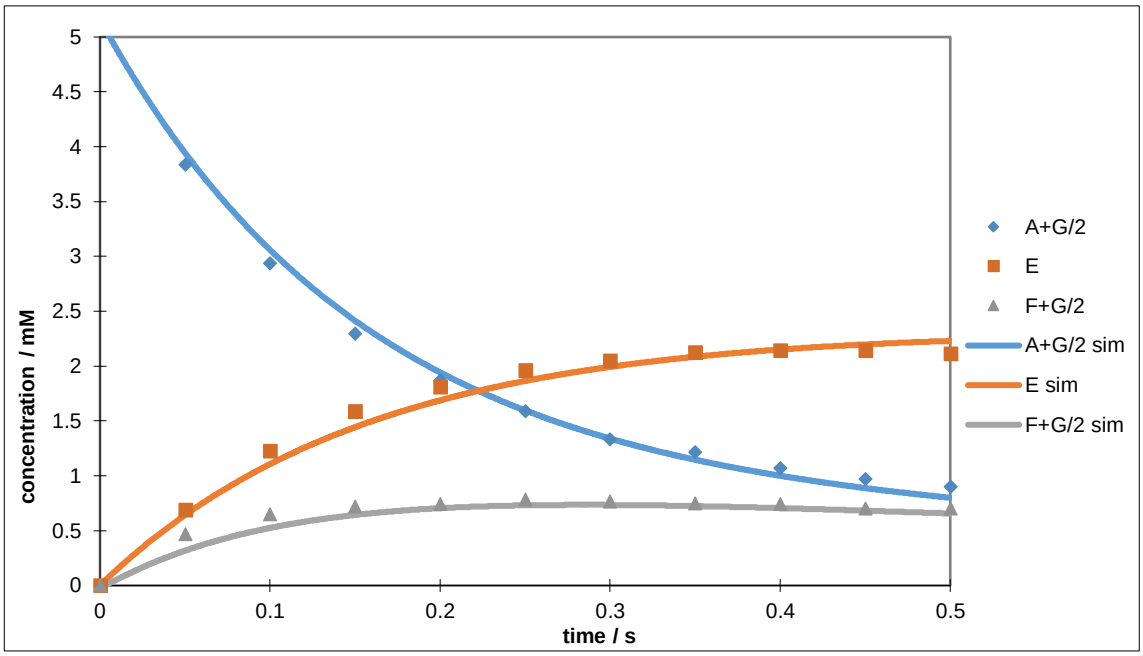

Figure 167: 'Bound 1' (A+G/2) excitation @ 298 K

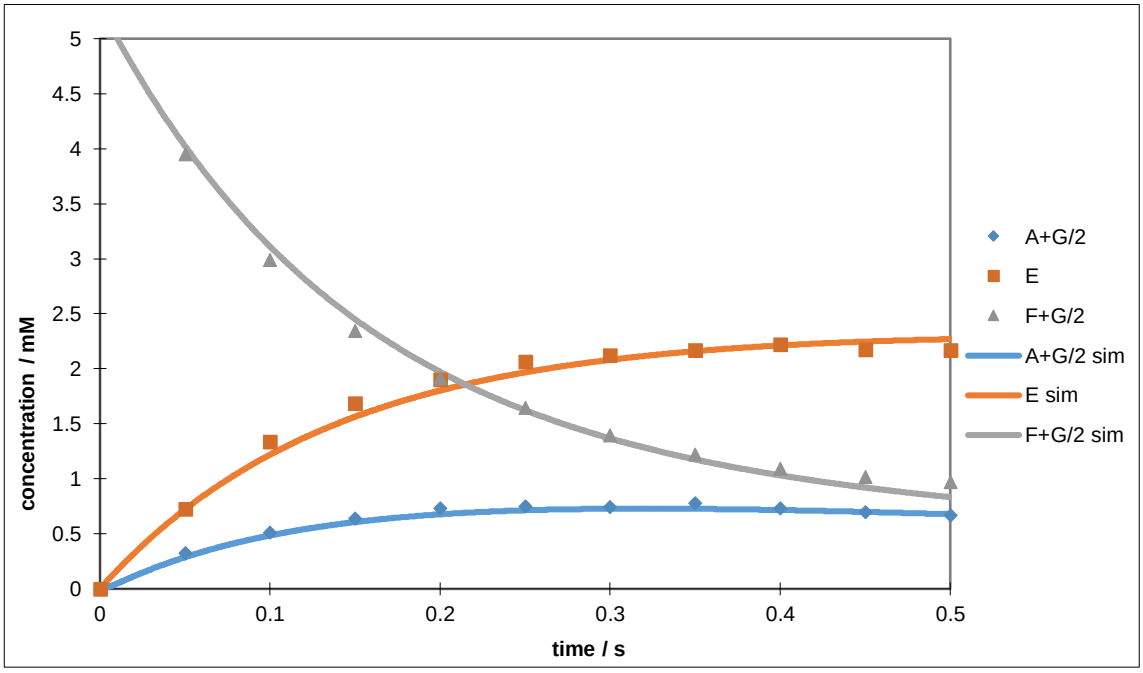

Figure 168: 'Bound 2' (A+G/2) excitation @ 298 K

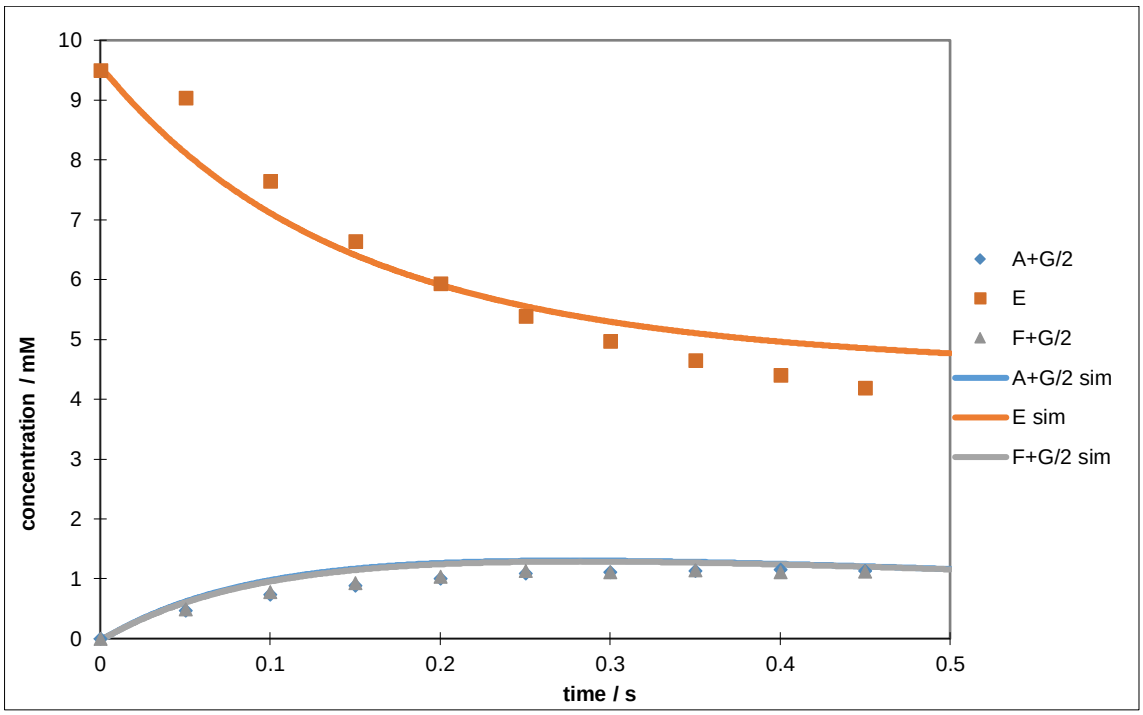

Figure 169: **'Free' (E) excitation @ 298 K**

-12.547	3.092	3.182	3.182	3.092	0	0	0	**A**
24.844	-52.084	0	0	0	24.169	0	3.071	**B**
24.169	0	-52.084	0	0	24.844	3.071	0	**C**
24.169	0	0	-52.084	0	24.844	0	3.071	**D**
24.844	0	0	0	-52.084	24.169	3.071	0	**E**
0	3.182	3.092	3.092	3.182	-12.547	0	0	**F**
0	0	45.548	0	45.548	0	-91.097	0	**G**
0	45.548	0	45.548	0	0	0	-91.097	**H**
A	**B**	**C**	**D**	**E**	**F**	**G**	**H**	

Table 44: **Model 4 observed rate constants for (−)-nicotine *1*, IMes *18* @ 298 K. Rate constants are read as k_{XY}, *i.e.* k_{AB} is row A, column B**

Excitation	Sum of least squares
Bound 1	0.208
Bound 2	0.245
Free	1.960
Total	2.413

Relax Bound	Relax Free	Relax Inter.
0.984	10.000	0.984

Table 45: sum of least squares for each plot and the modelled T_1 relaxation parameters (in seconds) used

303 K

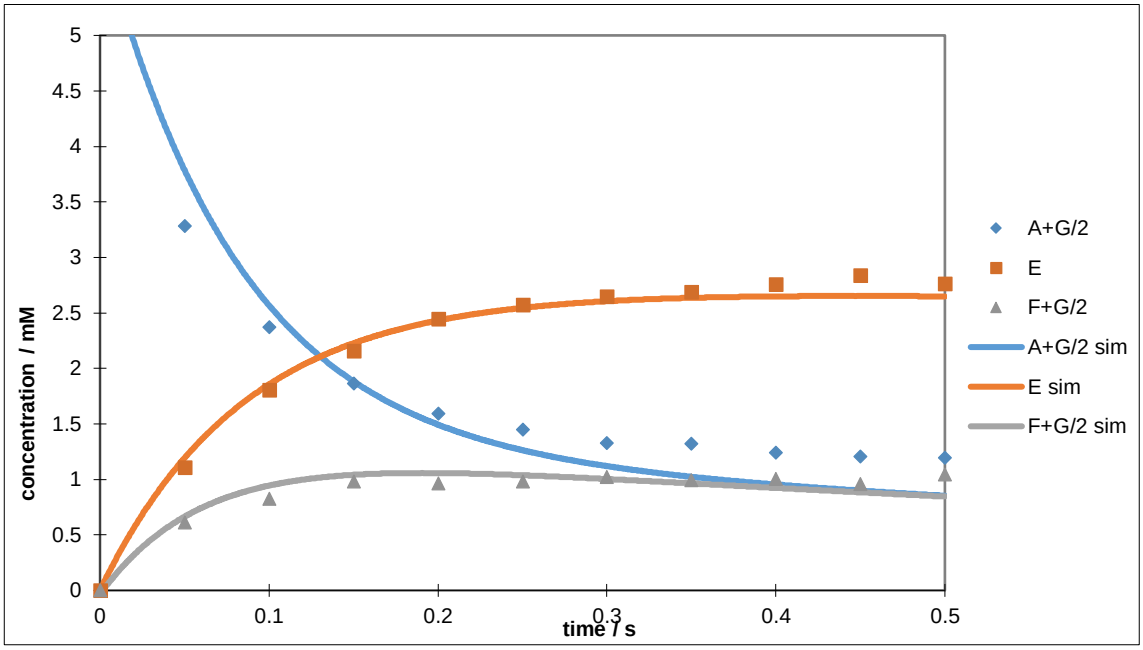

Figure 170: 'Bound 1' (A+G/2) excitation @ 303 K

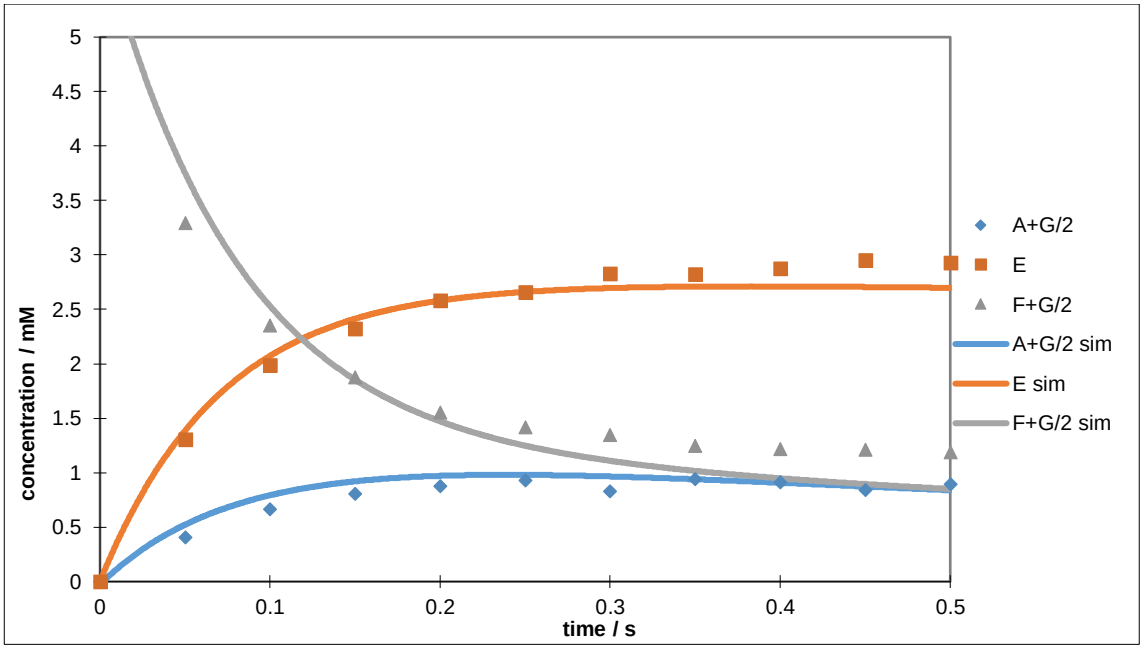

Figure 171: 'Bound 2' (F+G/2) excitation @ 303 K

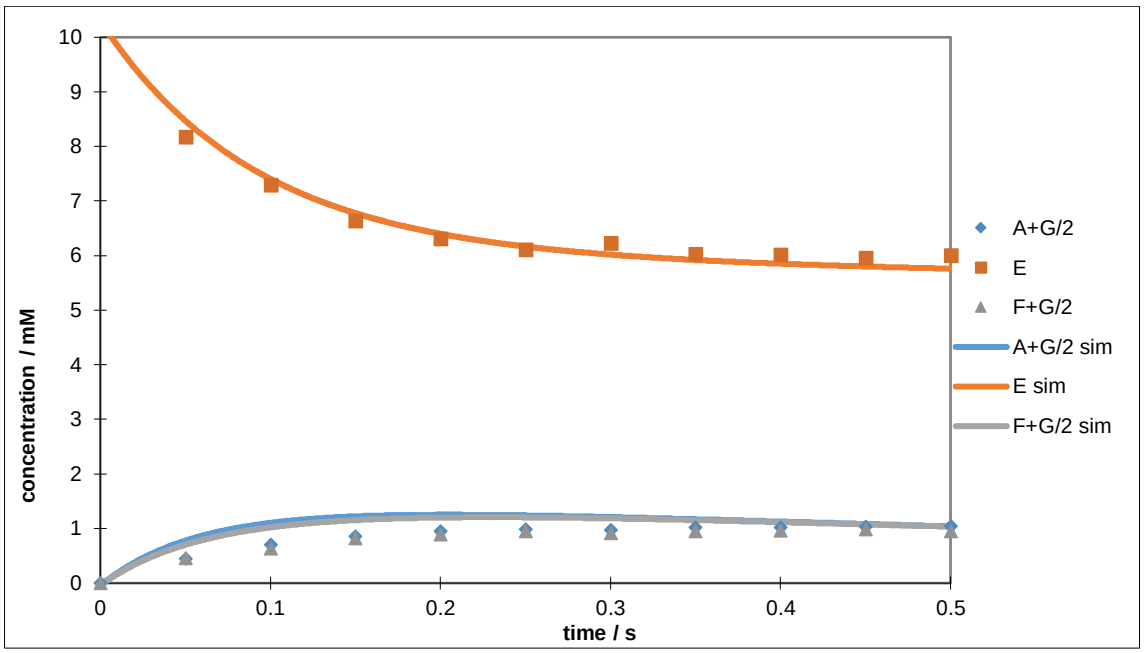

Figure 172: **'Free' (E) excitation @ 303 K**

-21.850	5.303	5.622	5.622	5.303	0	0	0	**A**
27.634	-55.320	0	0	0	24.612	0	3.075	**B**
24.612	0	-55.320	0	0	27.634	3.075	0	**C**
24.612	0	0	-55.320	0	27.634	0	3.075	**D**
27.634	0	0	0	-55.320	24.612	3.075	0	**E**
0	5.622	5.303	5.303	5.622	-21.850	0	0	**F**
0	0	43.552	0	43.552	0	-87.105	0	**G**
0	43.552	0	43.552	0	0	0	-87.105	**H**
A	**B**	**C**	**D**	**E**	**F**	**G**	**H**	

Table 46: **Model 4 observed rate constants for (−)-nicotine *1*, IMes *18* @ 303 K. Rate constants are read as k_{XY}, *i.e.* k_{AB} is row A, column B**

Excitation	Sum of least squares

Relax Bound	Relax Free	Relax Inter.

Bound 1	1.044	1.151	12.000	1.151
Bound 2	1.220			
Free	1.537			
Total	3.801			

Table 47: sum of least squares for each plot and the modelled T_1 relaxation parameters (in seconds) used

Eyring plots

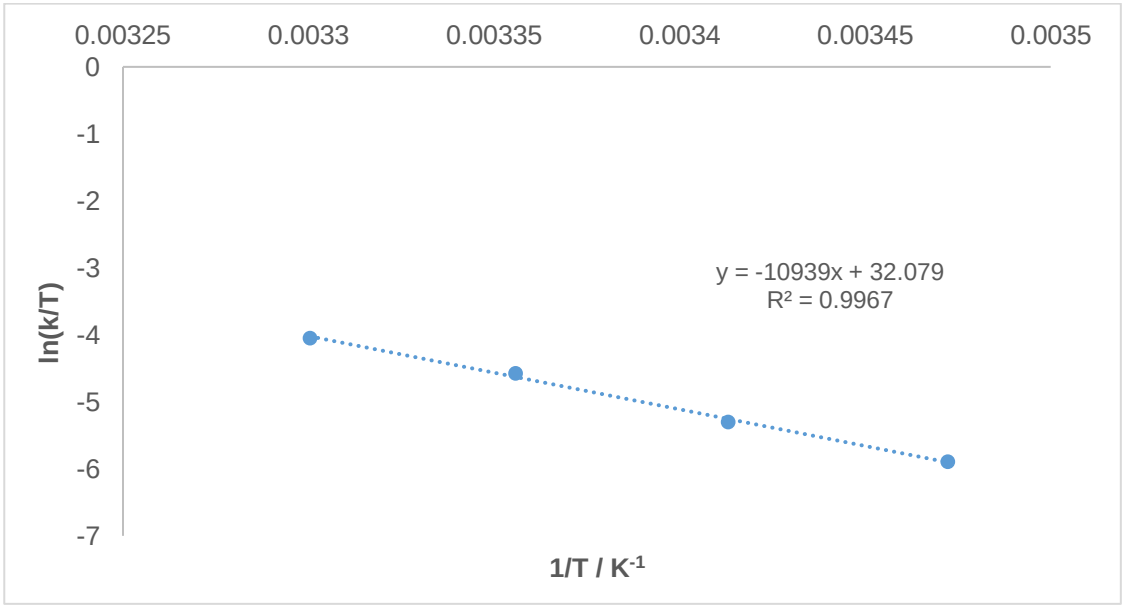

Figure 173: Eyring plot of Bound 1 for (−)-nicotine *1*, IMes *18*

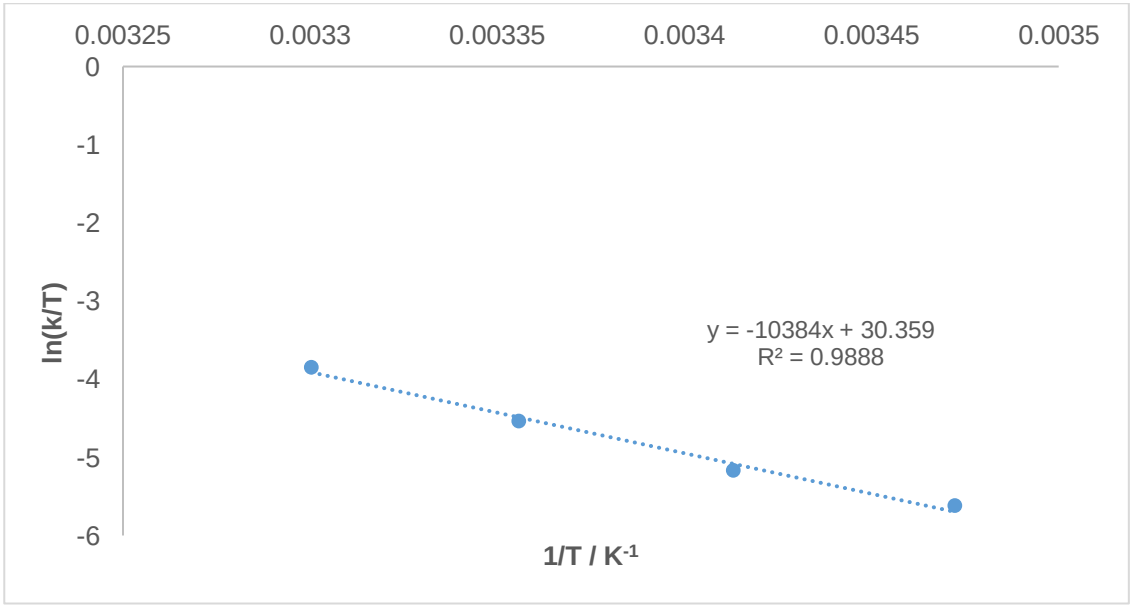

Figure 174: Eyring plot of Bound 2 for (−)-nicotine *1*, IMes *18*

Kinetic parameters

	Bound 1 -> Free	Bound 2 -> Free
$\Delta H‡$ / kJmol^{-1}	90.947	86.330
$\Delta S‡$ / JK^{-1}mol^{-1}	69.169	54.870
$\Delta G_{300}‡$ / kJmol^{-1}	70.196	69.869

Table 48: kinetic parameters for (−)-nicotine *1*, IMes *18*

7.2.2 Model 4 (−)-nicotine 1, d_{22}-IMes 19

288 K

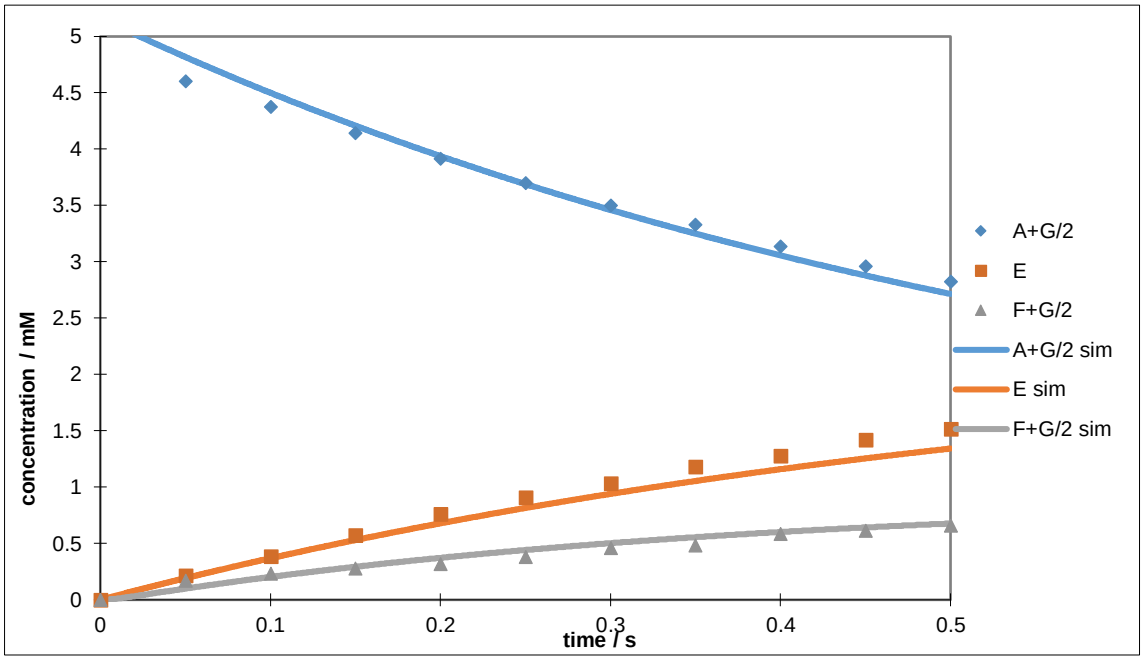

Figure 175: 'Bound 1' (A+G/2) excitation @ 288 K

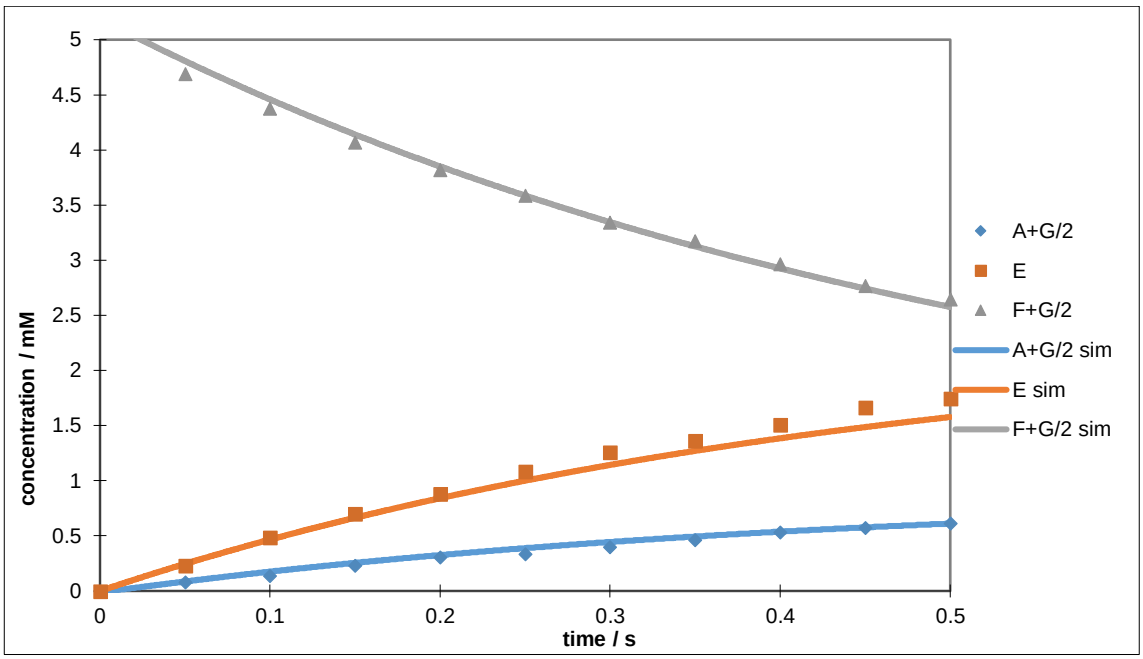

Figure 176: 'Bound 2' (F+G/2) excitation @ 288 K

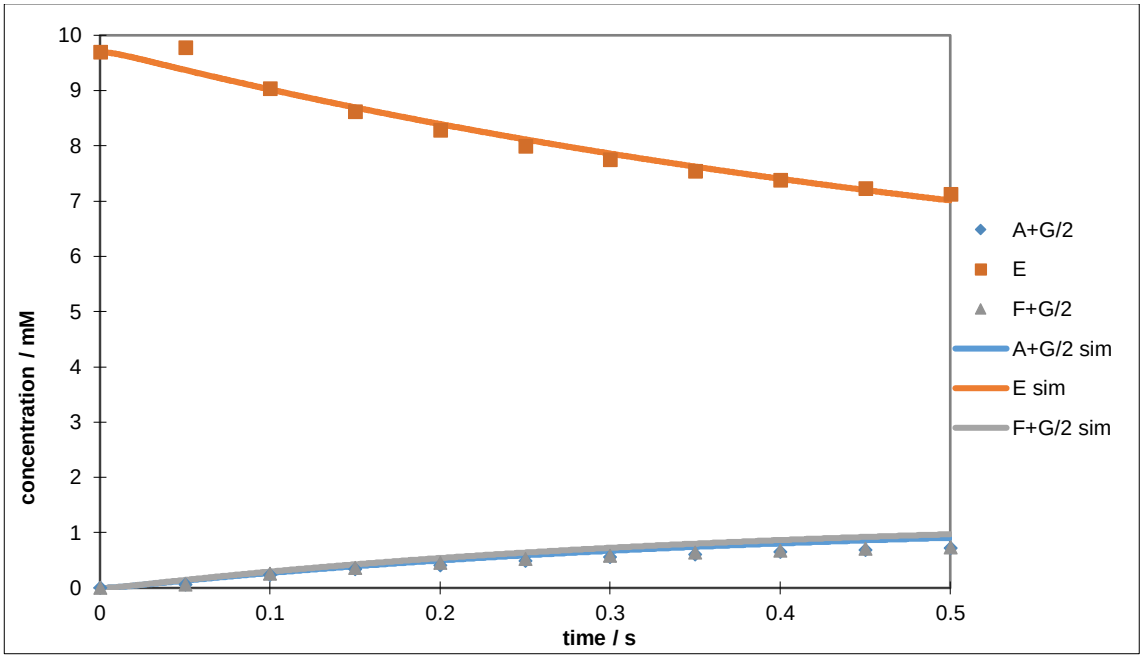

Figure 177: 'Free' (E) excitation @ 288 K

-3.556	0.778	1.000	1.000	0.778	0	0	0	**A**
6.008	-15.658	0	0	0	6.574	0	3.075	**B**
6.574	0	-15.658	0	0	6.008	3.075	0	**C**
6.574	0	0	-15.658	0	6.008	0	3.075	**D**
6.008	0	0	0	-15.658	6.574	3.075	0	**E**
0	1.000	0.778	0.778	1.000	-3.556	0	0	**F**
0	0	13.880	0	13.880	0	-27.759	0	**G**
0	13.880	0	13.880	0	0	0	-27.759	**H**
A	**B**	**C**	**D**	**E**	**F**	**G**	**H**	

Table 49: **Model 4 observed rate constants for (−)-nicotine *1*, d_{22}-IMes *19* @ 288 K. Rate constants are read as k_{XY}, *i.e.* k_{AB} is row A, column B**

Excitation	Sum of least squares
Bound 1	0.258
Bound 2	0.173
Free	0.647
Total	1.077

Relax Bound	Relax Free	Relax Inter.
7.389	10.628	7.389

Table 50: sum of least squares for each plot and the modelled T_1 relaxation parameters (in seconds) used

293 K

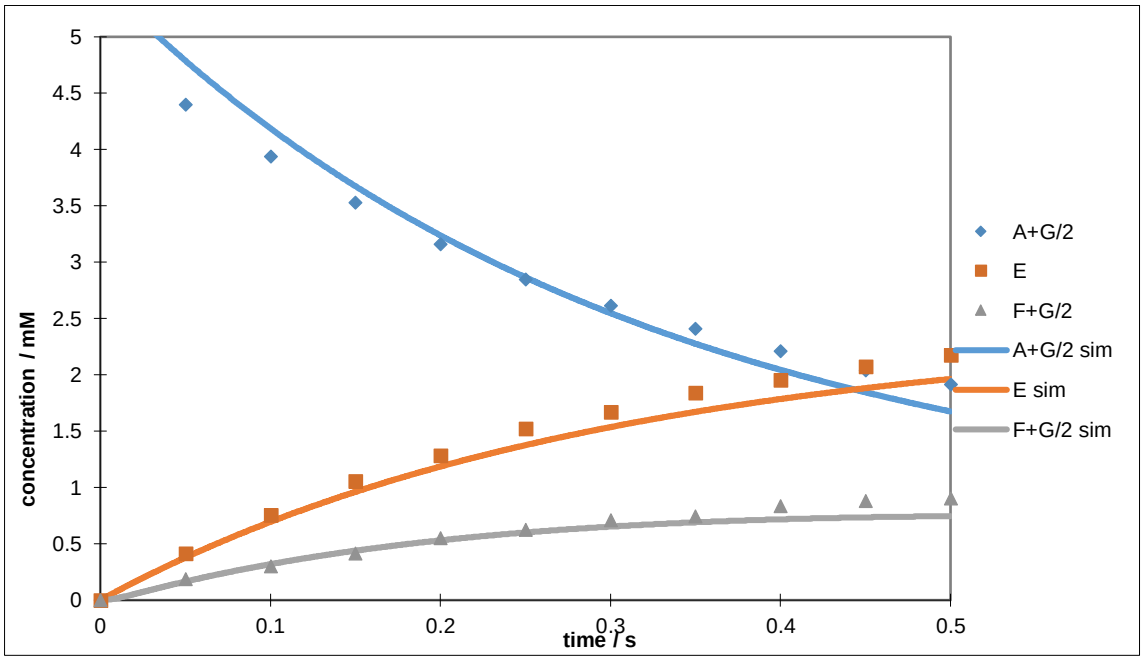

Figure 178: **'Bound 1' (A+G/2) excitation @ 293 K**

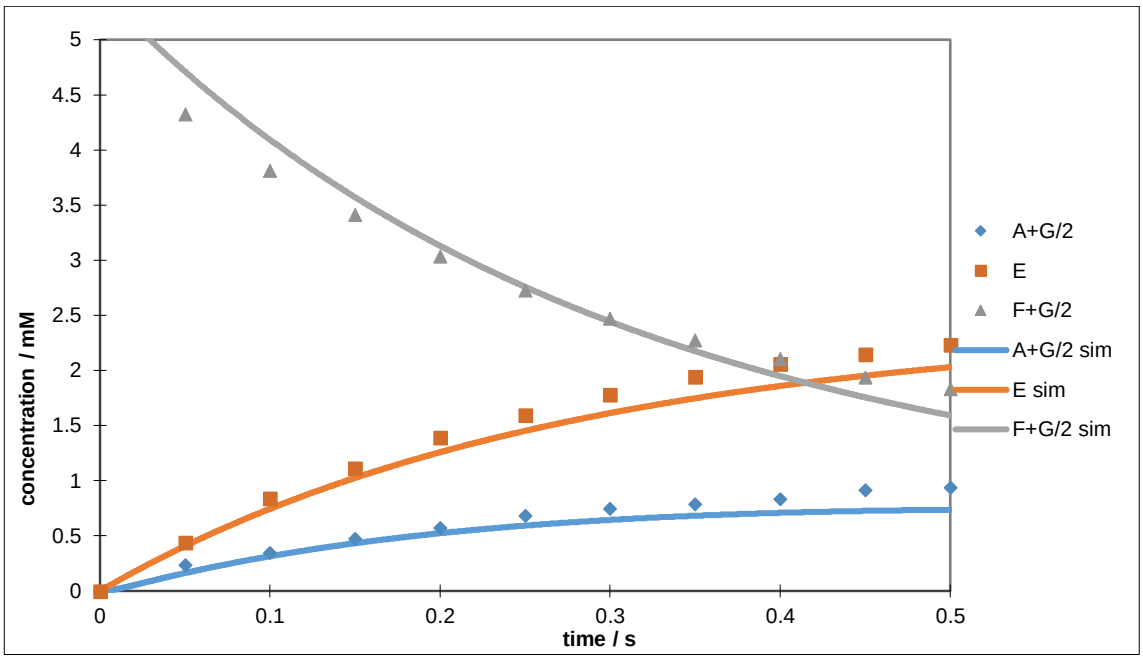

Figure 179: **'Bound 2' (F+G/2) excitation @ 293 K**

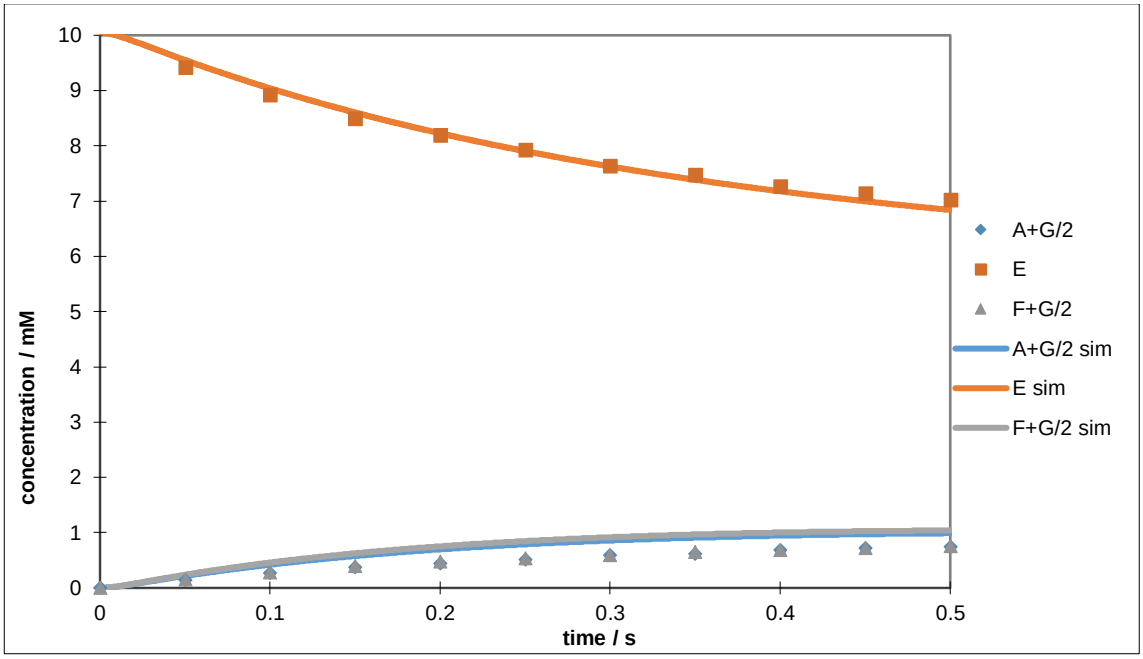

Figure 180: **'Free' (E) excitation @ 293 K**

-6.297	1.502	1.647	1.647	1.502	0	0	0	**A**
5.727	-15.062	0	0	0	6.260	0	3.075	**B**
6.260	0	-15.062	0	0	5.727	3.075	0	**C**
6.260	0	0	-15.062	0	5.727	0	3.075	**D**
5.727	0	0	0	-15.062	6.260	3.075	0	**E**
0	1.647	1.502	1.502	1.647	-6.297	0	0	**F**
0	0	11.914	0	11.914	0	-23.827	0	**G**
0	11.914	0	11.914	0	0	0	-23.827	**H**
A	**B**	**C**	**D**	**E**	**F**	**G**	**H**	

Table 51: **Model 4 observed rate constants for (−)-nicotine *1*, d_{22}-IMes *19* @ 293 K. Rate constants are read as k_{XY}, *i.e.* k_{AB} is row A, column B**

Excitation	Sum of least squares
Bound 1	0.732
Bound 2	0.826
Free	1.504
Total	3.061

Relax Bound	Relax Free	Relax Inter.
2.030	20.000	2.030

Table 52: sum of least squares for each plot and the modelled T_1 relaxation parameters (in seconds) used

298 K

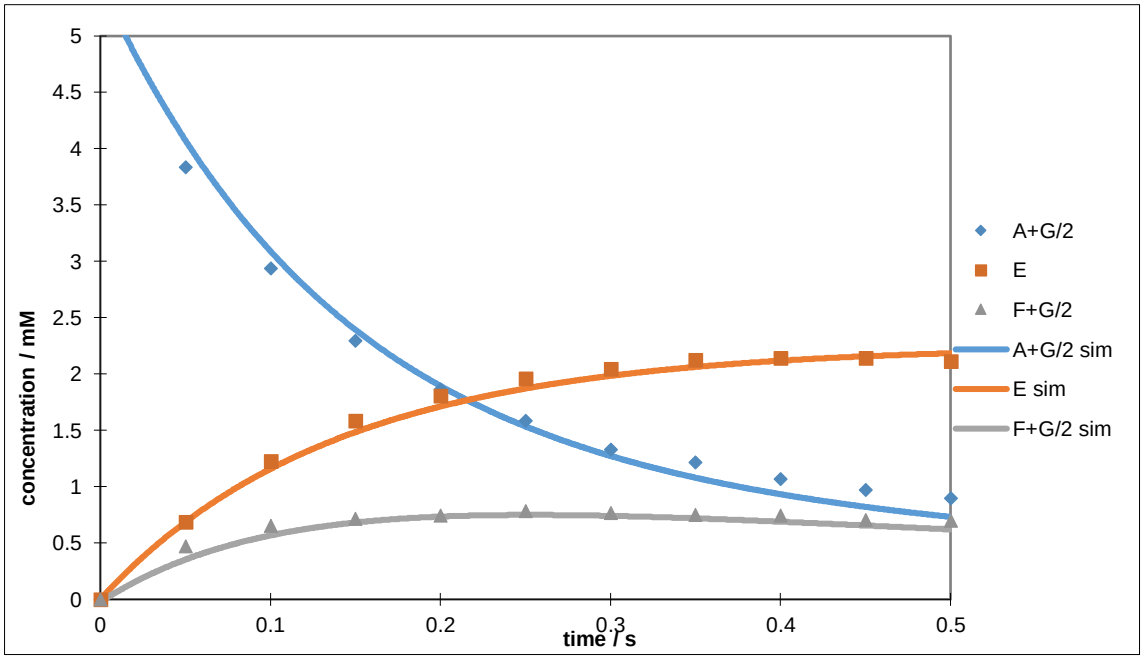

Figure 181: **'Bound 1' (A+G/2) excitation @ 298 K**

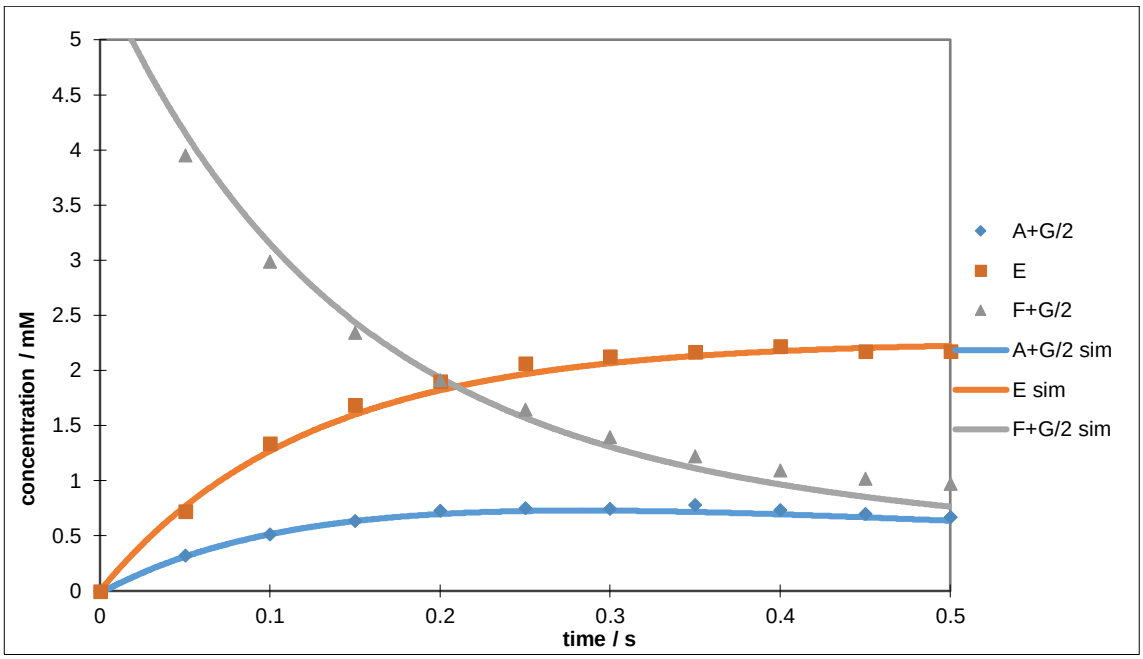

Figure 182: **'Bound 2' (F+G/2) excitation @ 298 K**

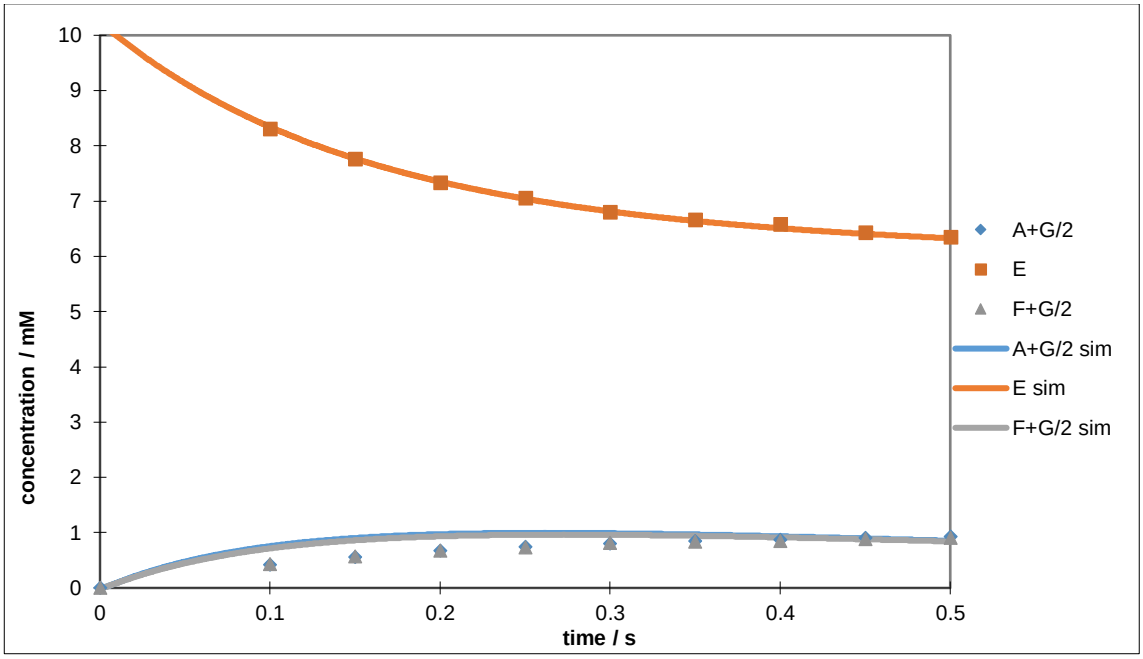

Figure 183: **'Free' (E) excitation @ 298 K**

-12.232	3.011	3.105	3.105	3.011	0	0	0	**A**
21.534	-44.807	0	0	0	20.185	0	3.088	**B**
20.185	0	-44.807	0	0	21.534	3.088	0	**C**
20.185	0	0	-44.807	0	21.534	0	3.088	**D**
21.534	0	0	0	-44.807	20.185	3.088	0	**E**
0	3.105	3.011	3.011	3.105	-12.232	0	0	**F**
0	0	38.429	0	38.429	0	-76.858	0	**G**
0	38.429	0	38.429	0	0	0	-76.858	**H**
A	**B**	**C**	**D**	**E**	**F**	**G**	**H**	

Table 53: **Model 4 observed rate constants for (−)-nicotine *1*, d_{22}-IMes *19* @ 298 K. Rate constants are read as k_{XY}, *i.e.* k_{AB} is row A, column B**

Excitation	Sum of least squares
Bound 1	0.336
Bound 2	0.408
Free	0.723
Total	1.467

Relax Bound	Relax Free	Relax Inter.
0.813	20.000	0.813

Table 54: sum of least squares for each plot and the modelled T_1 relaxation parameters (in seconds) used

303 K

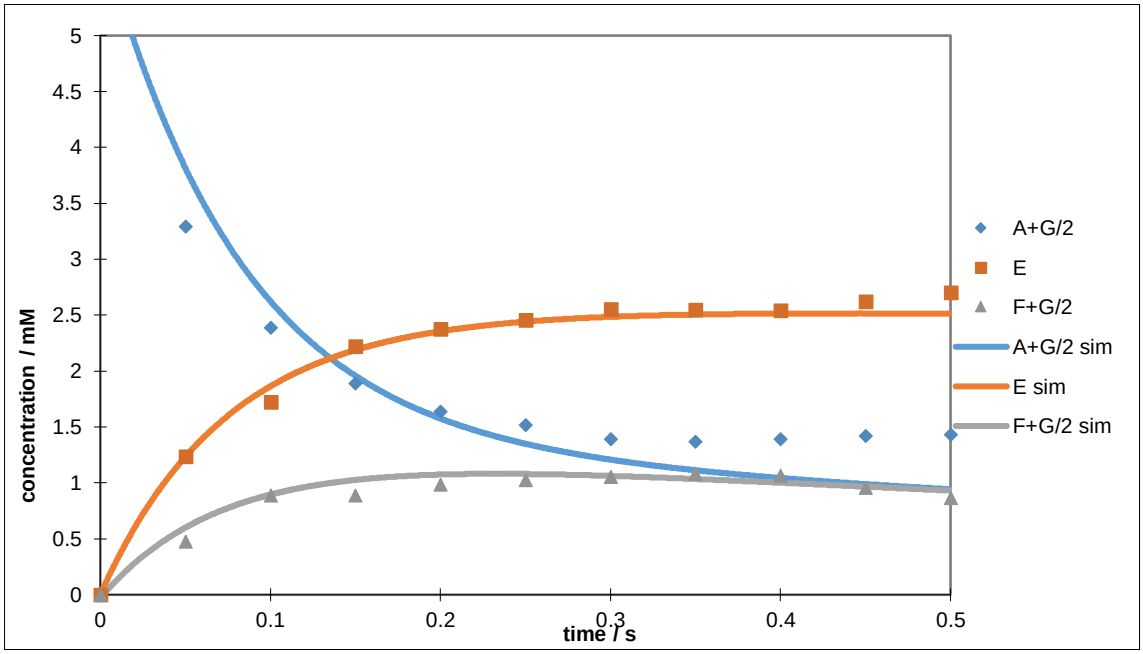

Figure 184: **'Bound 1' (A+G/2) excitation @ 303 K**

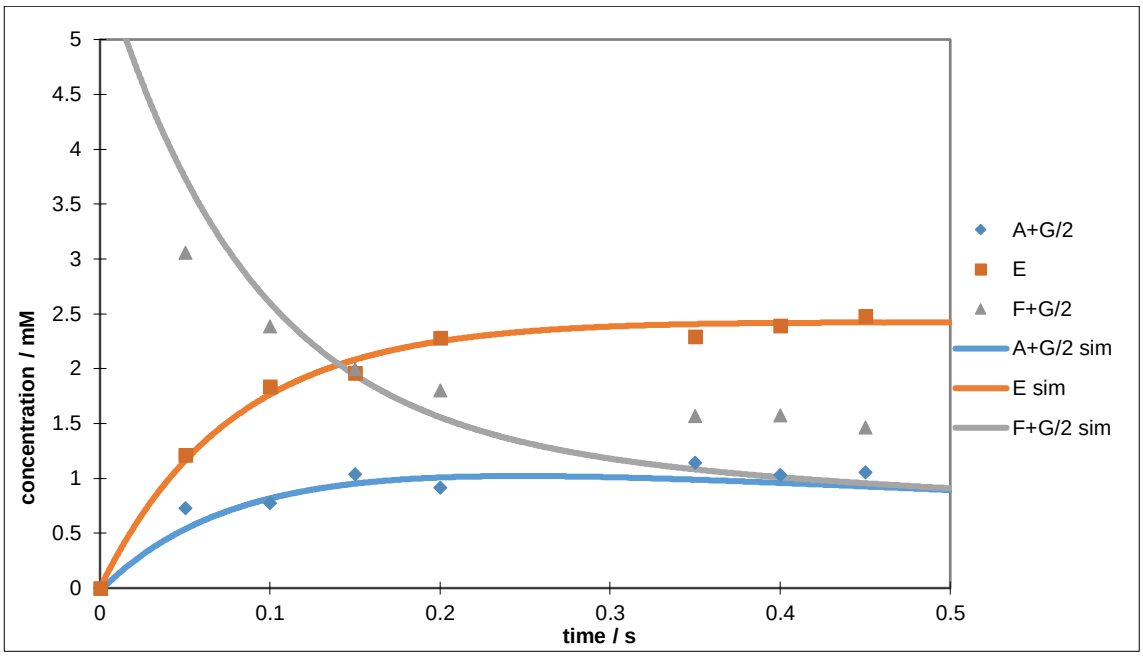

Figure 185: **'Bound 2' (F+G/2) excitation @ 303 K**

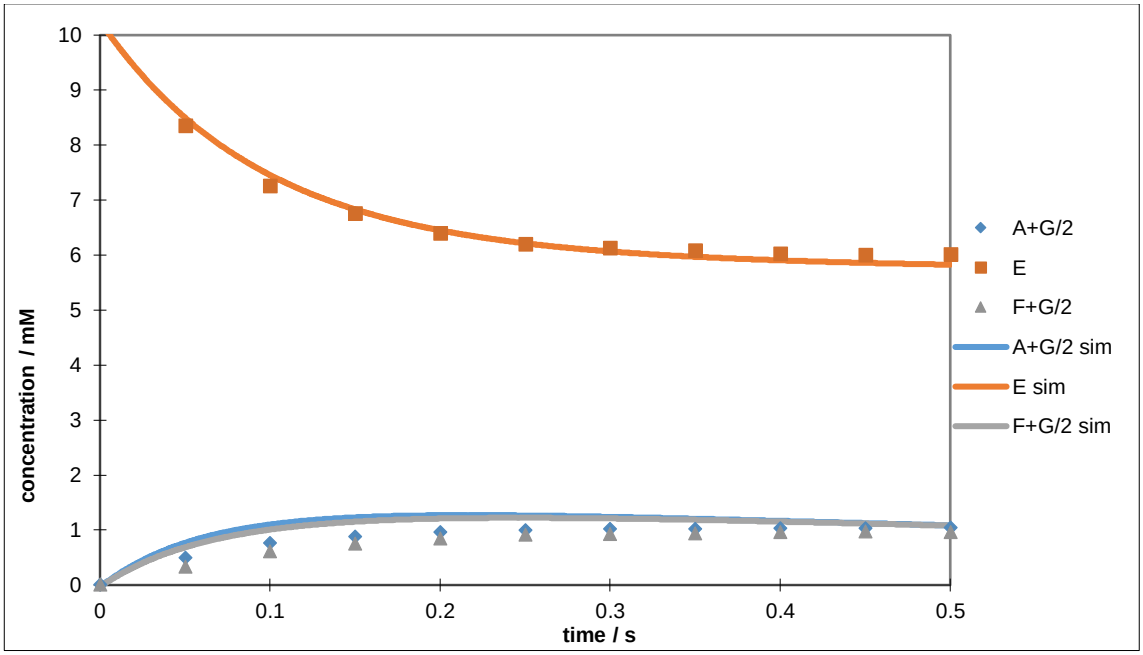

Figure 186: **'Free' (E) excitation @ 303 K**

-22.497	5.710	5.538	5.538	5.710	0	0	0	**A**
327.13	-64.622	0	0	0	28.818	0	3.091	**B**
28.818	0	-64.622	0	0	32.713	3.091	0	**C**
28.818	0	0	-64.622	0	32.713	0	3.091	**D**
32.713	0	0	0	-64.622	28.818	3.091	0	**E**
0	5.538	5.710	5.710	5.538	-22.497	0	0	**F**
0	0	53.284	0	53.284	0	-106.568	0	**G**
0	53.284	0	53.284	0	0	0	-106.568	**H**
A	**B**	**C**	**D**	**E**	**F**	**G**	**H**	

Table 55: Model 4 observed rate constants for (−)-nicotine *1*, d_{22}-IMes *19* @ 303 K. Rate constants are read as k_{XY}, *i.e.* k_{AB} is row A, column B

Excitation	Sum of least squares
Bound 1	1.195
Bound 2	1.571
Free	1.677
Total	4.444

Relax Bound	Relax Free	Relax Inter.
1.269	20.000	1.269

Table 56: sum of least squares for each plot and the modelled T_1 relaxation parameters (in seconds) used

Eyring plots

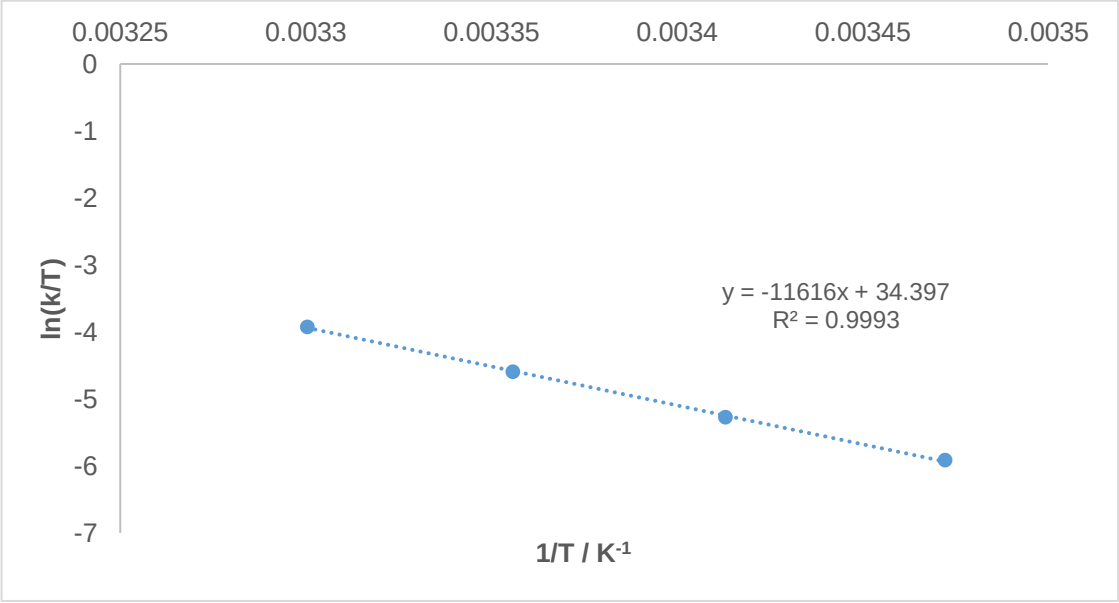

Figure 187: Eyring plot of Bound 1 for (−)-nicotine *1*, d_{22}-IMes *19*

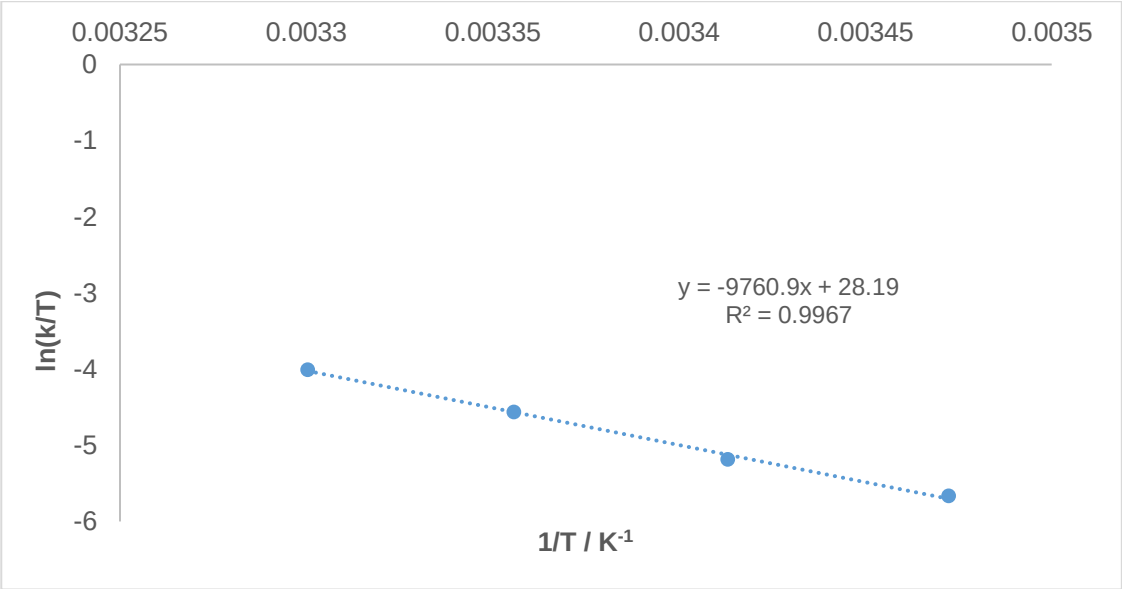

Figure 188: Eyring plot of Bound 2 for (−)-nicotine *1*, d_{22}-IMes *19*

Kinetic parameters

	Bound 1 -> Free	Bound 2 -> Free
ΔH‡ / kJmol^{-1}	94.460	82.480
ΔS‡ / JK^{-1}mol^{-1}	80.917	41.351
ΔG_{300}‡ / kJmol^{-1}	70.185	70.075

Figure 189: kinetic parameters for (−)-nicotine *1*, d_{22}-IMes *19*

7.2.3 Model 4 4,6-nicotine-d_2 9, IMes 18

288 K

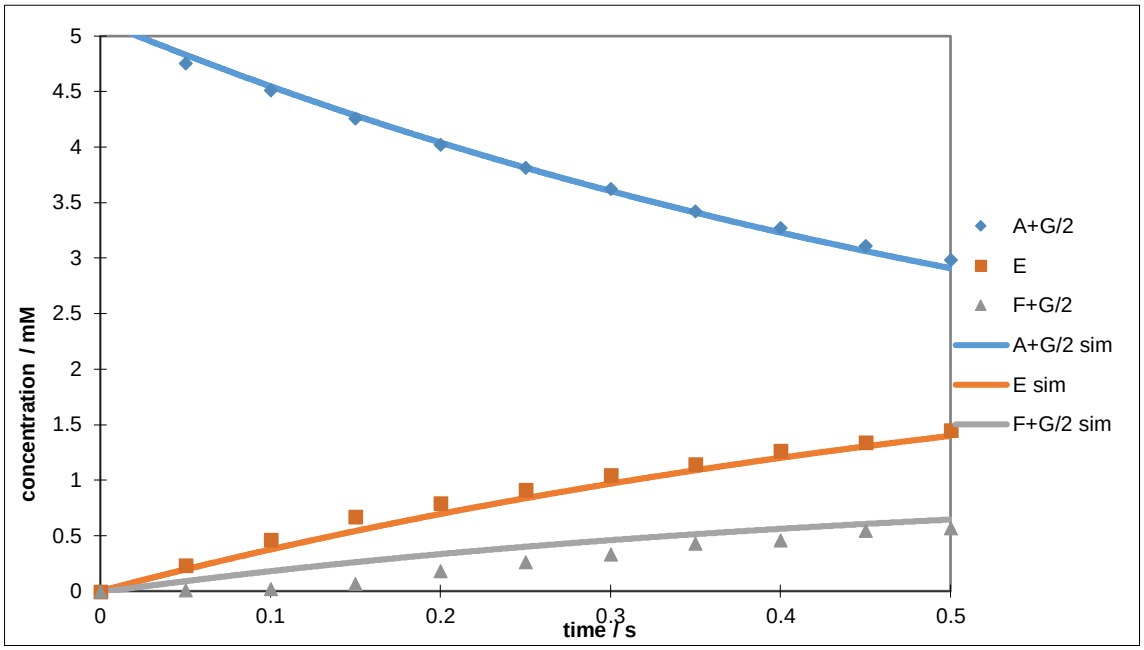

Figure 190: **'Bound 1' (A+G/2) excitation @ 288 K**

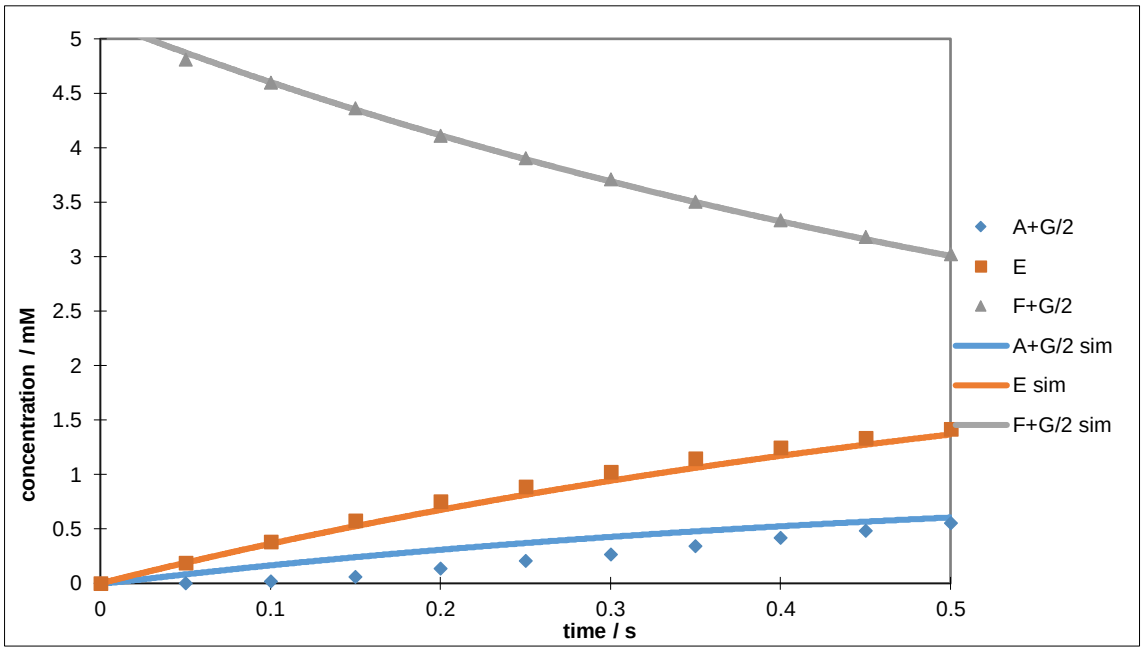

Figure 191: **'Bound 2' (F+G/2) excitation @ 288 K**

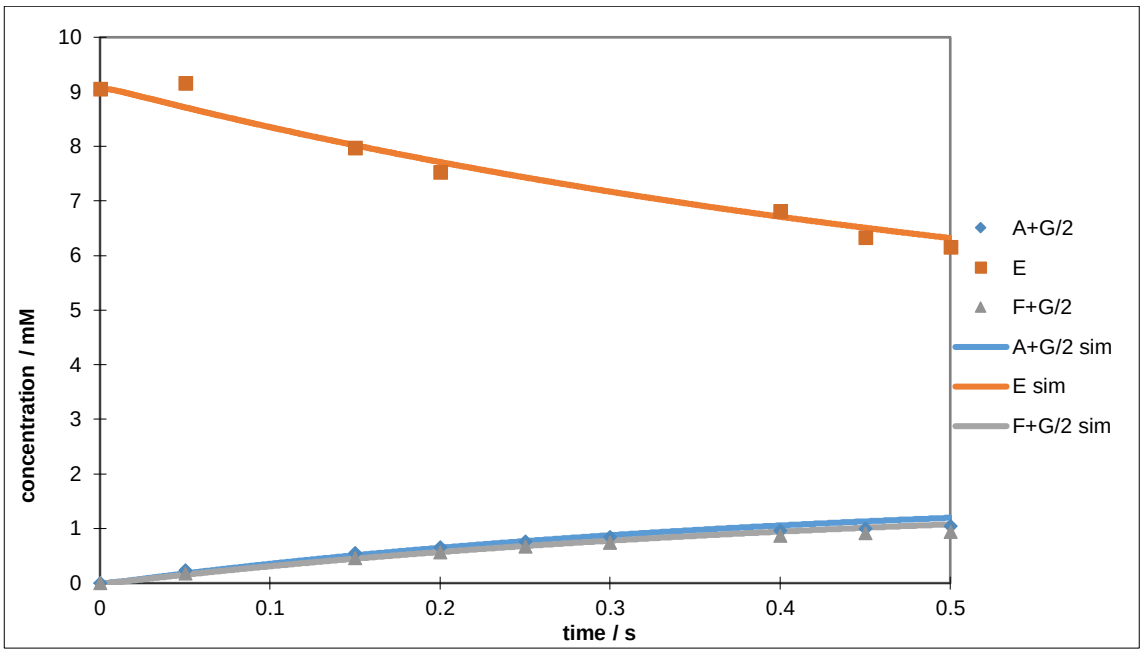

Figure 192: **'Free' (E) excitation @ 288 K**

-3.098	0.790	0.759	0.759	0.790	0	0	0	**A**
9.782	-21.385	0	0	0	8.528	0	3.075	**B**
8.528	0	-21.385	0	0	9.782	3.075	0	**C**
8.528	0	0	-21.385	0	9.782	0	3.075	**D**
9.782	0	0	0	-21.385	8.528	3.075	0	**E**
0	0.759	0.790	0.790	0.759	-3.098	0	0	**F**
0	0	19.836	0	19.836	0	-39.671	0	**G**
0	19.836	0	19.836	0	0	0	-39.671	**H**
A	**B**	**C**	**D**	**E**	**F**	**G**	**H**	

Table 57: **Model 4 observed rate constants for 4,6-nicotine-d_2 *9*, IMes *18* @ 288 K. Rate constants are read as k_{XY}, *i.e.* k_{AB} is row A, column B**

Excitation	Sum of least squares
Bound 1	0.243
Bound 2	0.236
Free	0.394
Total	0.874

Relax Bound	Relax Free	Relax Inter.
25.156	41.501	25.156

Table 58: sum of least squares for each plot and the modelled T_1 relaxation parameters (in seconds) used

293 K

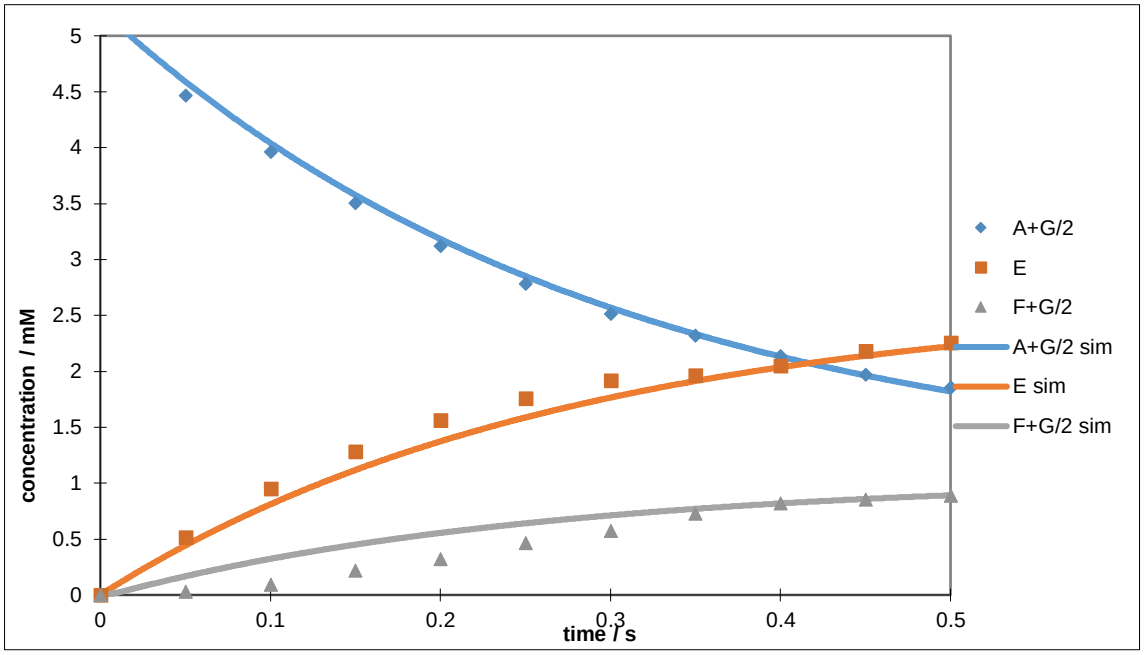

Figure 193: **'Bound 1' (A+G/2) excitation @ 293 K**

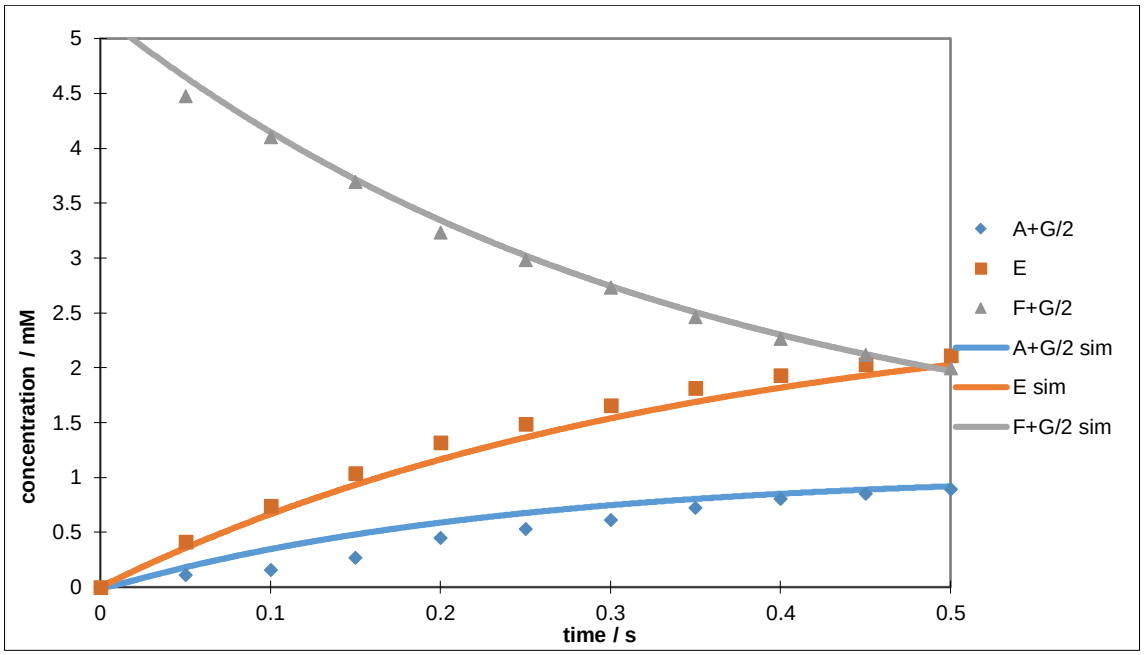

Figure 194: **'Bound 2' (F+G/2) excitation @ 293 K**

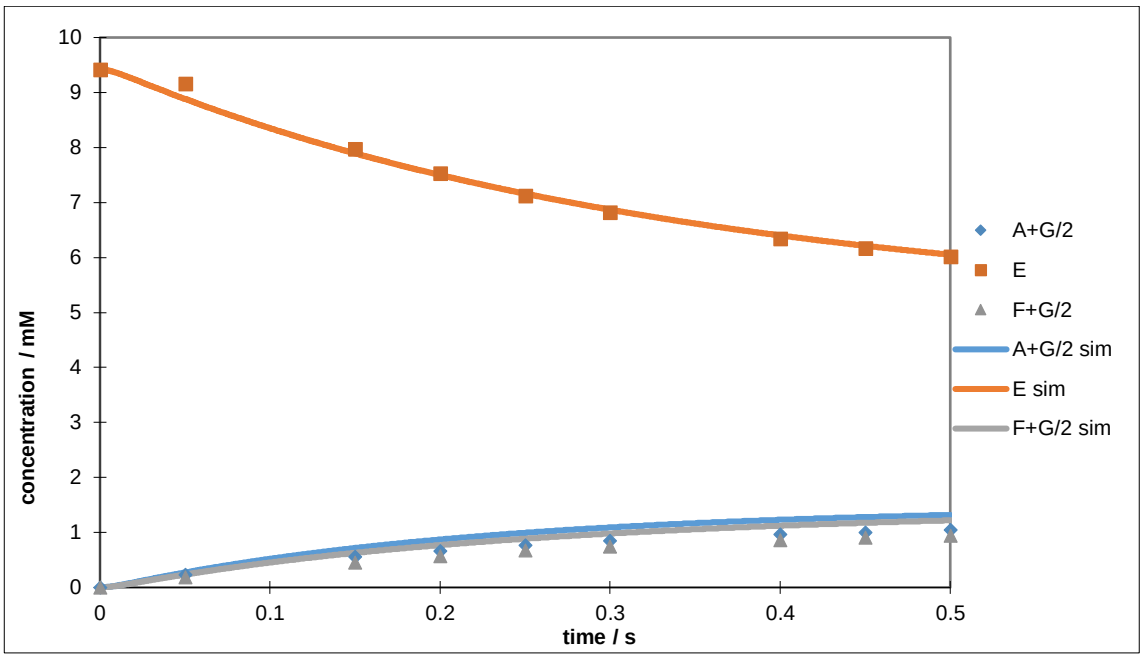

Figure 195: **'Free' (E) excitation @ 293 K**

-6.630	1.847	1.468	1.468	1.847	0	0	0	**A**
8.589	-19.066	0	0	0	7.402	0	3.075	**B**
7.402	0	-19.066	0	0	8.589	3.075	0	**C**
7.402	0	0	-19.066	0	8.589	0	3.075	**D**
8.589	0	0	0	-19.066	7.402	3.075	0	**E**
0	1.468	1.847	1.847	1.468	-6.630	0	0	**F**
0	0	15.751	0	15.751	0	-31.502	0	**G**
0	15.751	0	15.751	0	0	0	-31.502	**H**
A	**B**	**C**	**D**	**E**	**F**	**G**	**H**	

Table 59: **Model 4 observed rate constants for 4,6-nicotine-*d*$_2$ *9*, IMes *18* @ 293 K. Rate constants are read as k_{XY}, *i.e.* k_{AB} is row A, column B**

Excitation	Sum of least squares
Bound 1	0.478
Bound 2	0.375
Free	0.915
Total	1.768

Relax Bound	Relax Free	Relax Inter.
22.000	41.000	22.000

Table 60: sum of least squares for each plot and the modelled T_1 relaxation parameters (in seconds) used

298 K

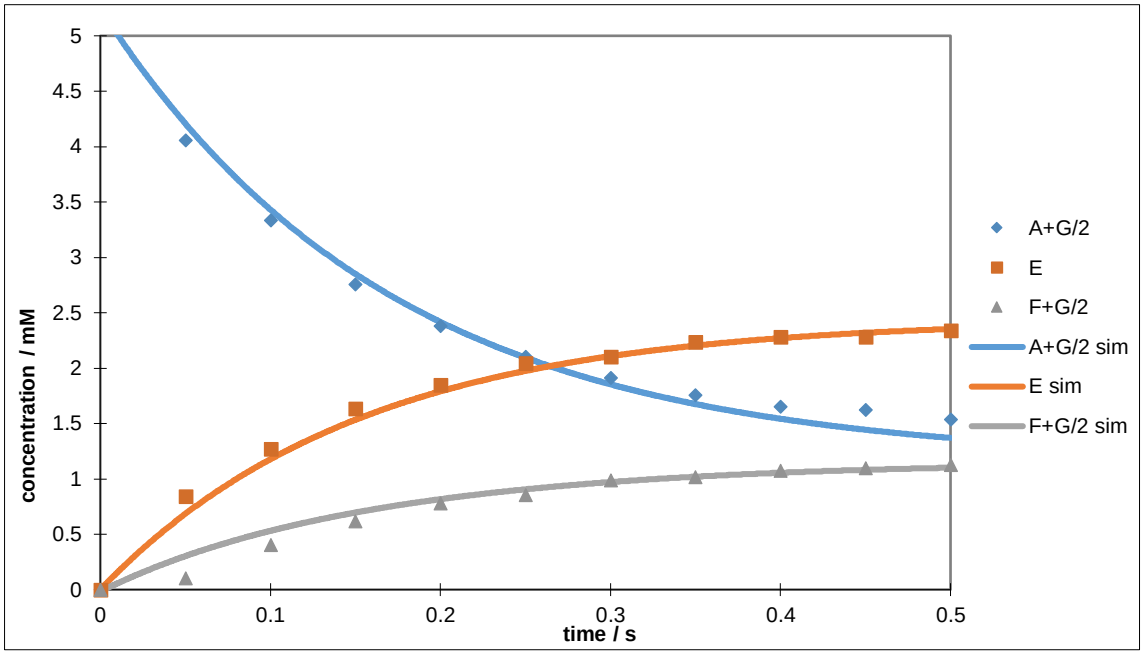

Figure 196: **'Bound 1' (A+G/2) excitation @ 298 K**

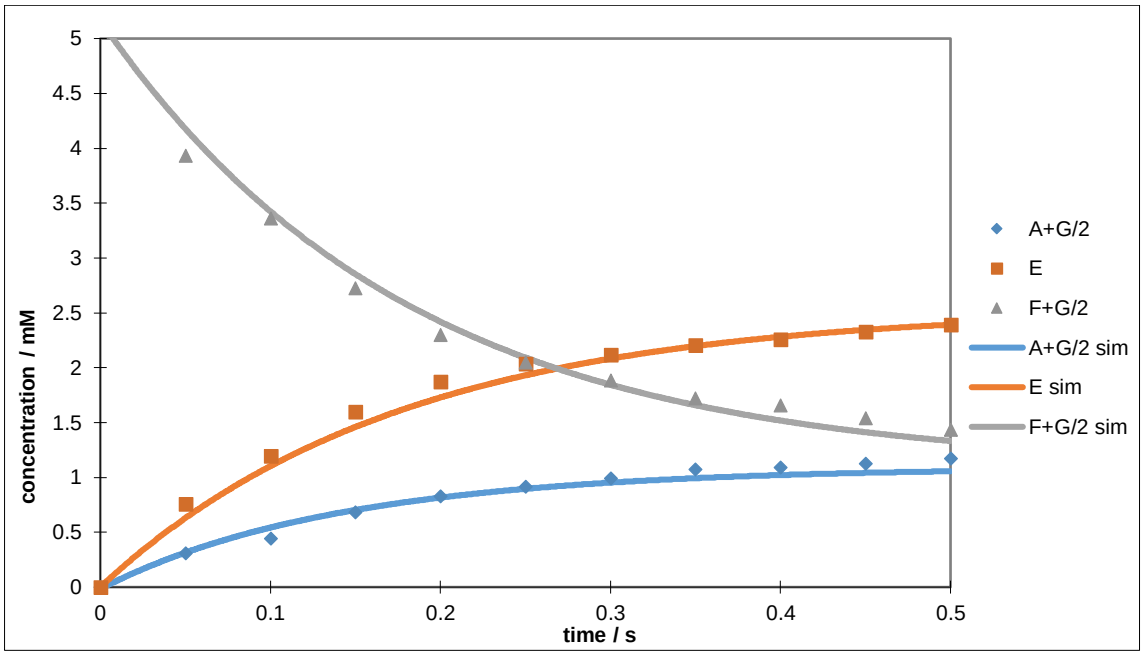

Figure 197: **'Bound 2' (F+G/2) excitation @ 298 K**

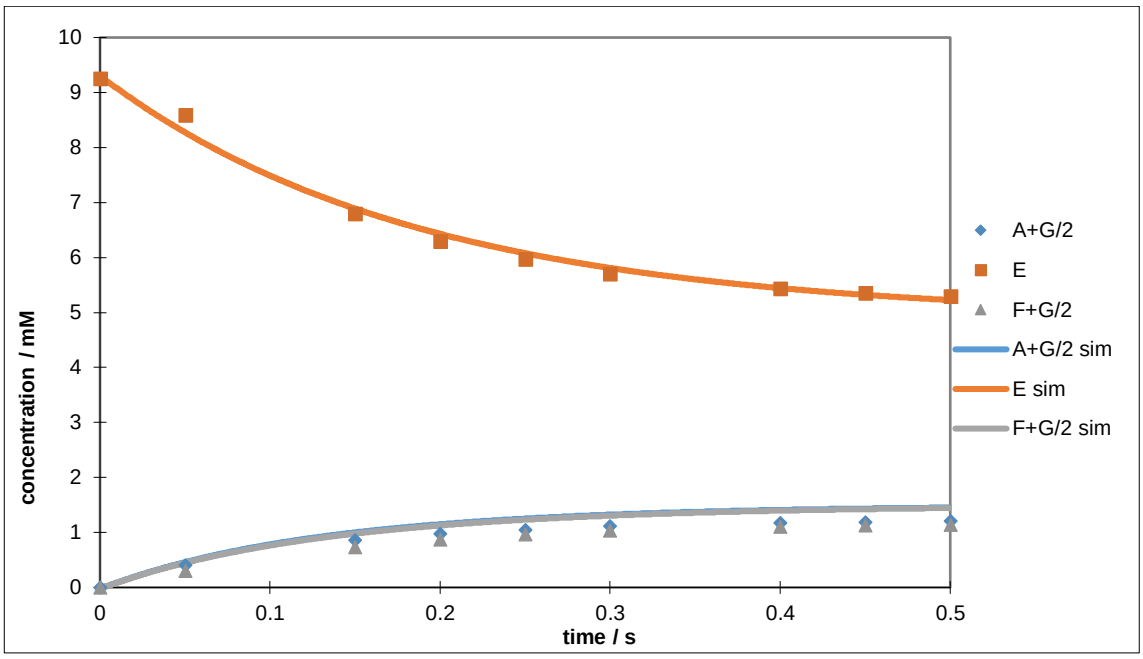

Figure 198: **'Free' (E) excitation @ 298 K**

-11.712	3.058	2.998	2.998	3.058	0	0	0	**A**
23.950	-50.273	0	0	0	23.249	0	3.075	**B**
23.249	0	-50.273	0	0	23.950	3.075	0	**C**
23.249	0	0	-50.273	0	23.950	0	3.075	**D**
23.950	0	0	0	-50.273	23.249	3.075	0	**E**
0	2.998	3.058	3.058	2.998	-11.712	0	0	**F**
0	0	44.417	0	44.417	0	-88.835	0	**G**
0	44.417	0	44.417	0	0	0	-88.835	**H**
A	**B**	**C**	**D**	**E**	**F**	**G**	**H**	

Table 61: **Model 4 observed rate constants for 4,6-nicotine-*d*$_2$ *9*, IMes *18* @ 298 K. Rate constants are read as k_{XY}, *i.e.* k_{AB} is row A, column B**

Excitation	Sum of least squares
Bound 1	0.315
Bound 2	0.250
Free	1.095
Total	1.661

Relax Bound	Relax Free	Relax Inter.
22.000	40.600	22.000

Table 62: sum of least squares for each plot and the modelled T_1 relaxation parameters (in seconds) used

303 K

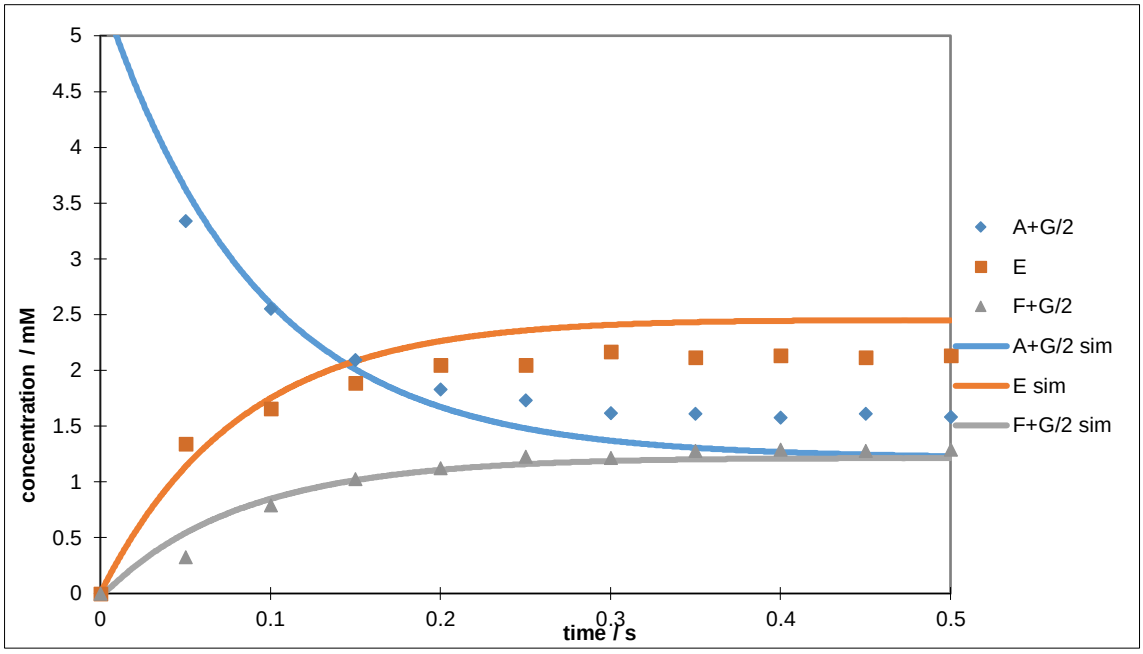

Figure 199: **'Bound 1' (A+G/2) excitation @ 303 K**

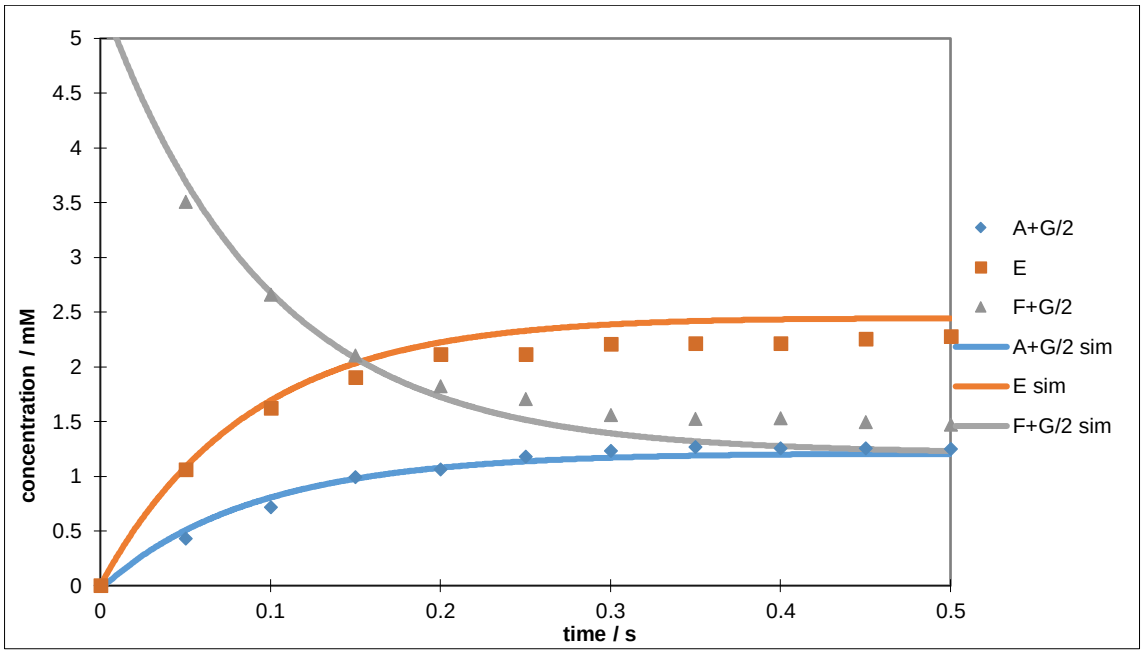

Figure 200: **'Bound 2' (F+G/2) excitation @ 303 K**

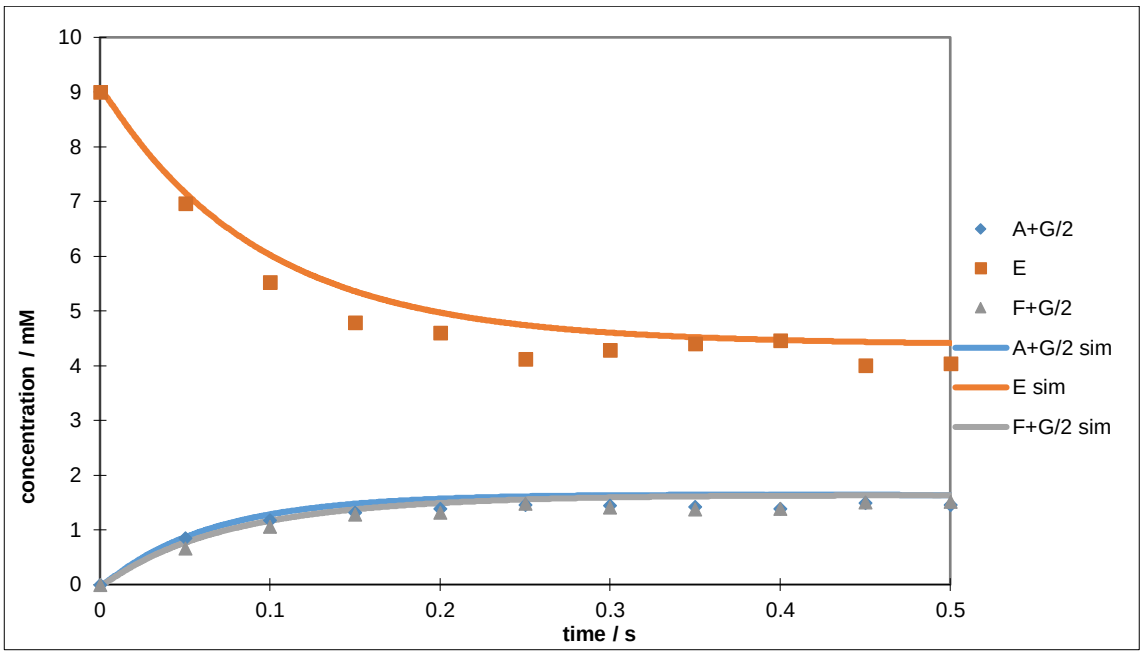

Figure 201: **'Free' (E) excitation @ 303 K**

-21.797	5.637	5.261	5.261	5.637	0	0	0	**A**
231.688	-437.563	0	0	0	202.722	0	3.153	**B**
202.722	0	-437.563	0	0	231.688	3.153	0	**C**
202.722	0	0	-437.563	0	231.688	0	3.153	**D**
231.688	0	0	0	-437.563	202.722	3.153	0	**E**
0	5.261	5.637	5.637	5.261	-21.797	0	0	**F**
0	0	426.665	0	426.665	0	-853.330	0	**G**
0	426.665	0	426.665	0	0	0	-853.330	**H**
A	**B**	**C**	**D**	**E**	**F**	**G**	**H**	

Table 63: **Model 4 observed rate constants for 4,6-nicotine-*d*$_2$ *9*, IMes *18* @ 303 K. Rate constants are read as k$_{XY}$, *i.e.* k$_{AB}$ is row A, column B**

Excitation	Sum of least squares
Bound 1	1.231
Bound 2	0.490
Free	1.577
Total	3.298

Relax Bound	Relax Free	Relax Inter.
10.7	15.0	10.7

Table 64: sum of least squares for each plot and the modelled T_1 relaxation parameters (in seconds) used

Eyring plots

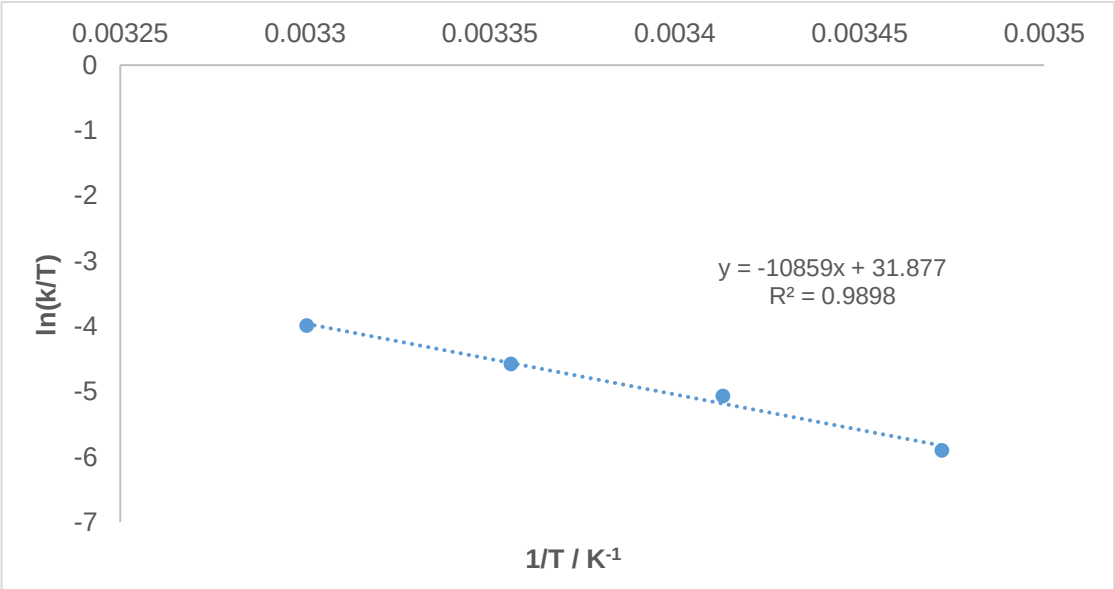

Figure 202: Eyring plot of Bound 1 for 4,6-nicotine-*d*$_2$ *9*, IMes *18*

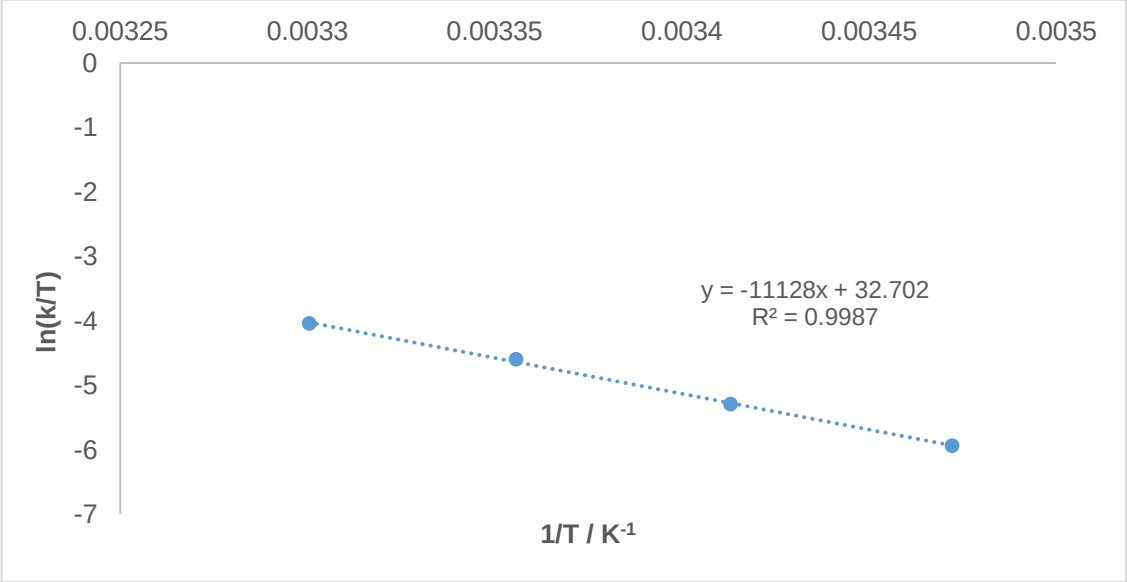

Figure 203: Eyring plot of Bound 2 for 4,6-nicotine-*d*$_2$ *9*, IMes *18*

Kinetic parameters

	Bound 1 -> Free	Bound 2 -> Free
ΔH‡ / kJmol-1	90.280	92.519
ΔS‡ / JK-1mol-1	67.490	74.349
ΔG‡300 / kJmol-1	70.033	70.214

Figure 204: kinetic parameters for 4,6-nicotine-*d*$_2$ *9*, IMes *18*

7.2.4 Model 4 4,6-nicotine-d_2 9, d_{22}-IMes 19

288 K

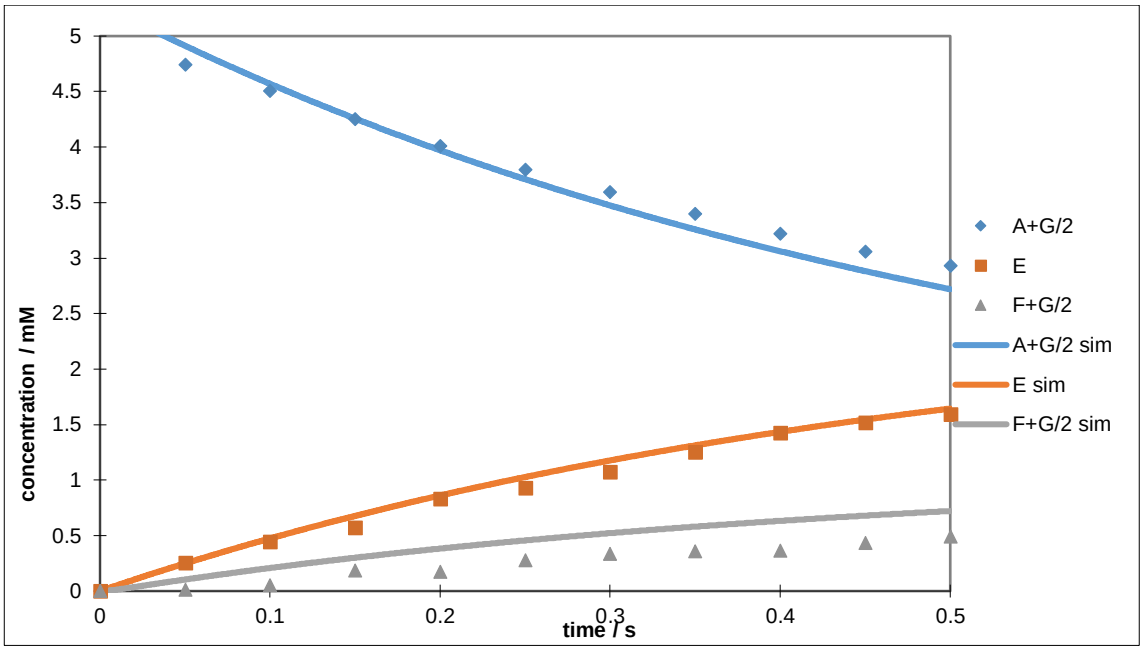

Figure 205: 'Bound 1' (A+G/2) excitation @ 288 K

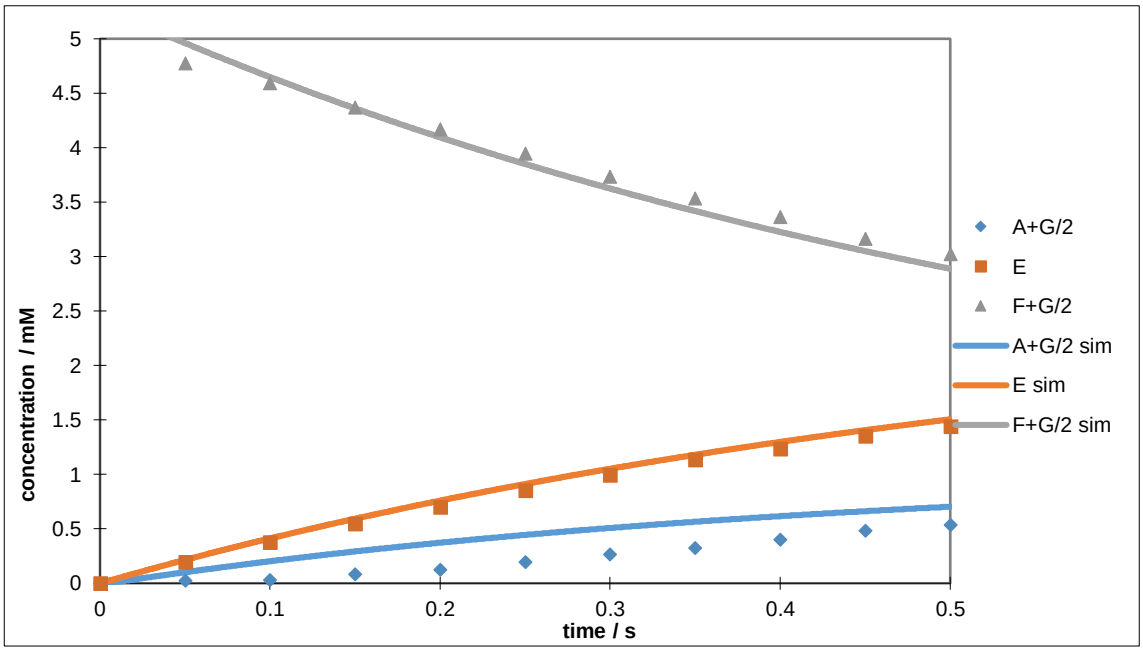

Figure 206: 'Bound 2' (F+G/2) excitation @ 288 K

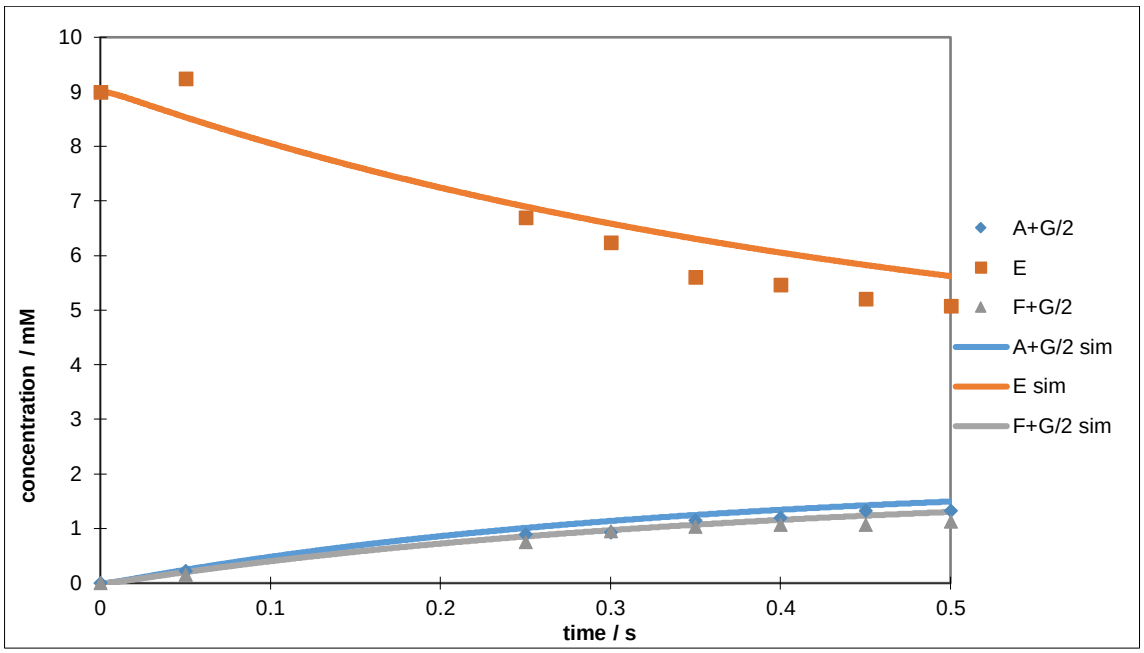

Figure 207: **'Free' (E) excitation @ 288 K**

-3.676	0.991	0.847	0.847	0.991	0	0	0	**A**
9.789	-20.931	0	0	0	8.089	0	3.053	**B**
8.089	0	-20.931	0	0	9.789	3.053	0	**C**
8.089	0	0	-20.931	0	9.789	0	3.053	**D**
9.789	0	0	0	-20.931	8.089	3.053	0	**E**
0	0.847	0.991	0.991	0.847	-3.676	0	0	**F**
0	0	19.093	0	19.093	0	-38.187	0	**G**
0	19.093	0	19.093	0	0	0	-38.187	**H**
A	**B**	**C**	**D**	**E**	**F**	**G**	**H**	

Table 65: **Model 4 observed rate constants for 4,6-nicotine-d_2 *9*, d_{22}-IMes *19* @ 288 K. Rate constants are read as k_{XY}, *i.e.* k_{AB} is row A, column B**

Excitation	Sum of least squares
Bound 1	0.632
Bound 2	0.587
Free	2.471
Total	3.690

Relax Bound	Relax Free	Relax Inter.
30.0	41.5	30.0

Table 66: sum of least squares for each plot and the modelled T_1 relaxation parameters (in seconds) used

293 K

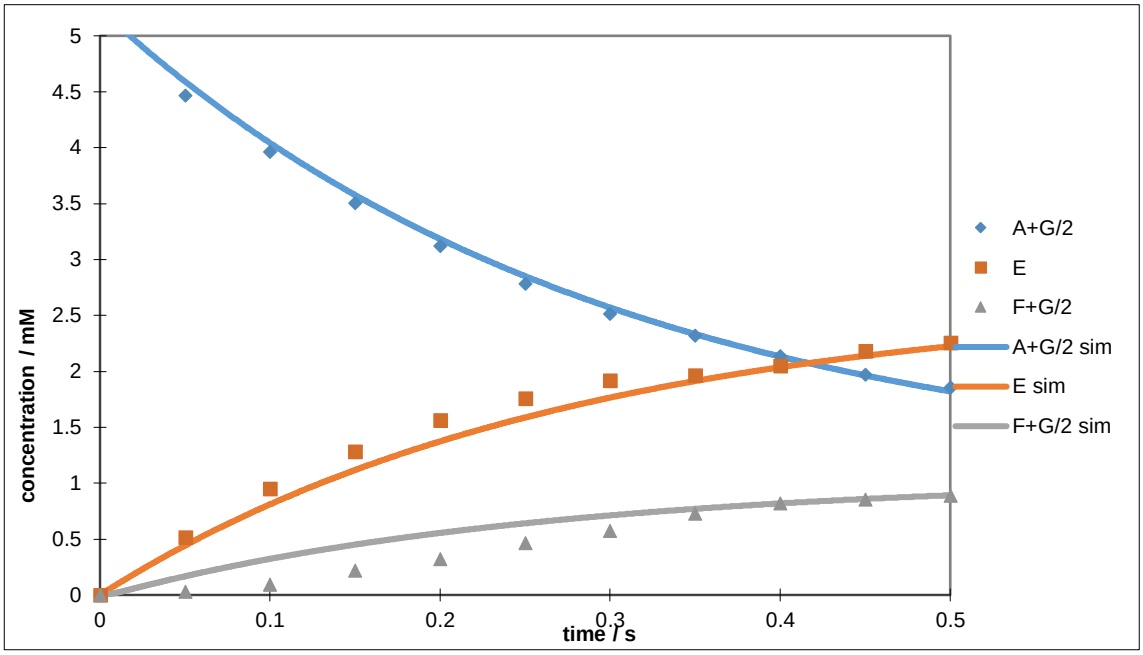

Figure 208: **'Bound 1' (A+G/2) excitation @ 293 K**

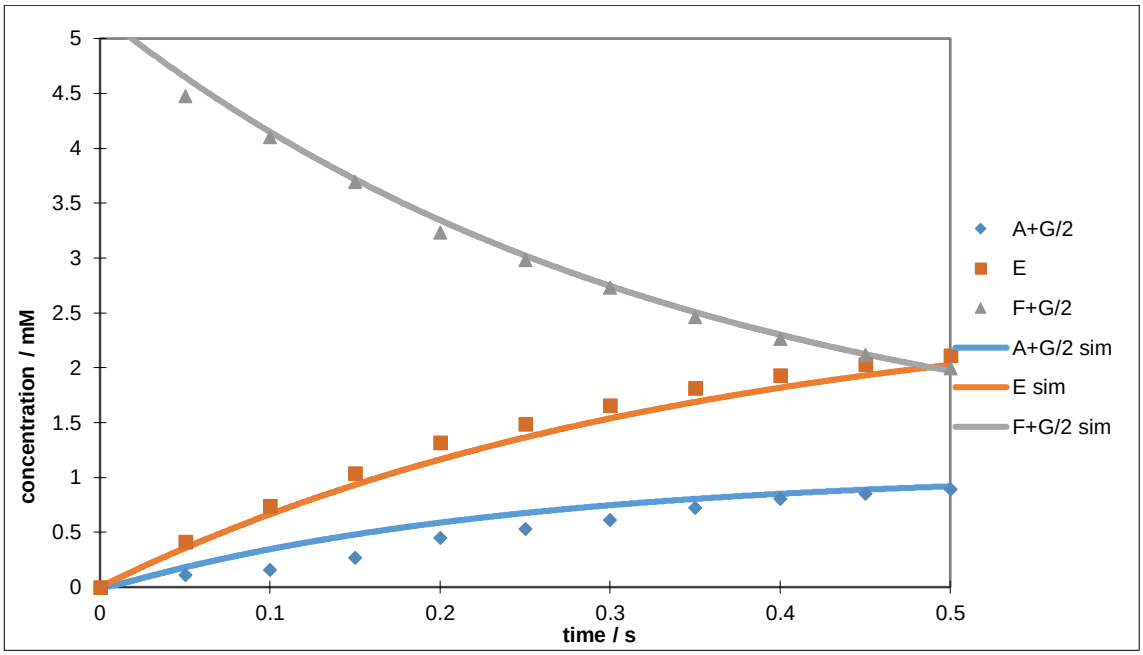

Figure 209: **'Bound 2' (F+G/2) excitation @ 293 K**

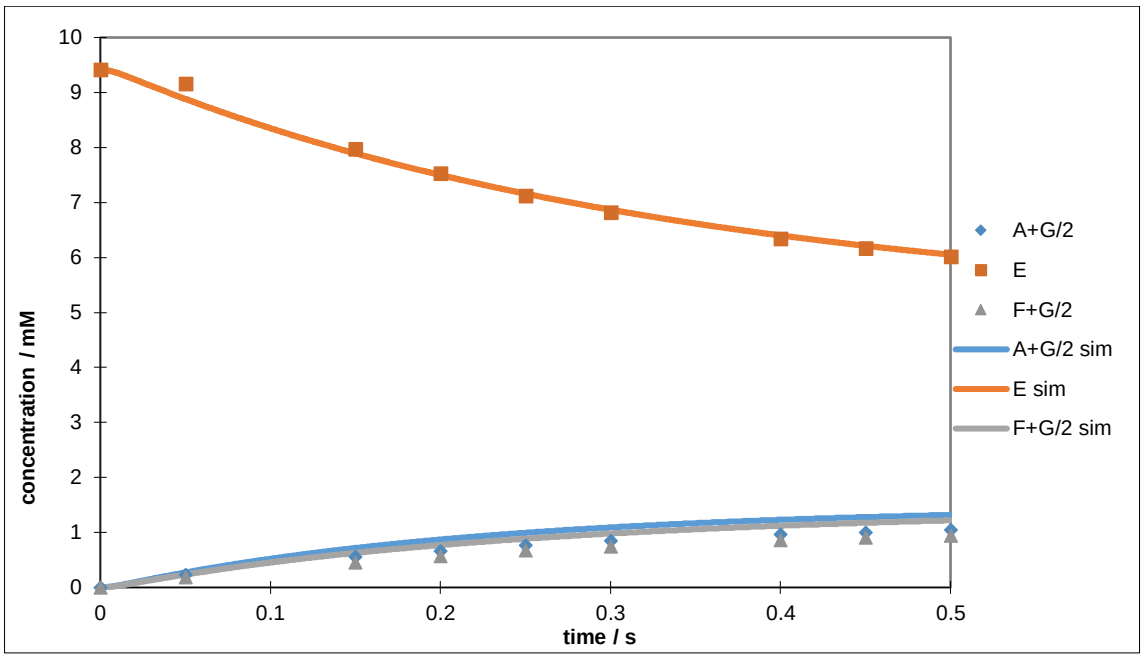

Figure 210: **'Free' (E) excitation @ 293 K**

-6.630	1.847	1.468	1.468	1.847	0	0	0	**A**
8.589	-19.066	0	0	0	7.402	0	3.075	**B**
7.402	0	-19.066	0	0	8.589	3.075	0	**C**
7.402	0	0	-19.066	0	8.589	0	3.075	**D**
8.589	0	0	0	-19.066	7.402	3.075	0	**E**
0	1.468	1.847	1.847	1.468	-6.630	0	0	**F**
0	0	15.751	0	15.751	0	-31.502	0	**G**
0	15.751	0	15.751	0	0	0	-31.502	**H**
A	**B**	**C**	**D**	**E**	**F**	**G**	**H**	

Table 67: **Model 4 observed rate constants for 4,6-nicotine-d_2 *9*, d_{22}-IMes *19* @ 293 K. Rate constants are read as k_{XY}, *i.e.* k_{AB} is row A, column B**

Excitation	Sum of least squares
Bound 1	0.47826
Bound 2	0.37528
Free	0.91485
Total	1.76839

Relax Bound	Relax Free	Relax Inter.
22	41	22

Table 68: sum of least squares for each plot and the modelled T_1 relaxation parameters (in seconds) used

298 K

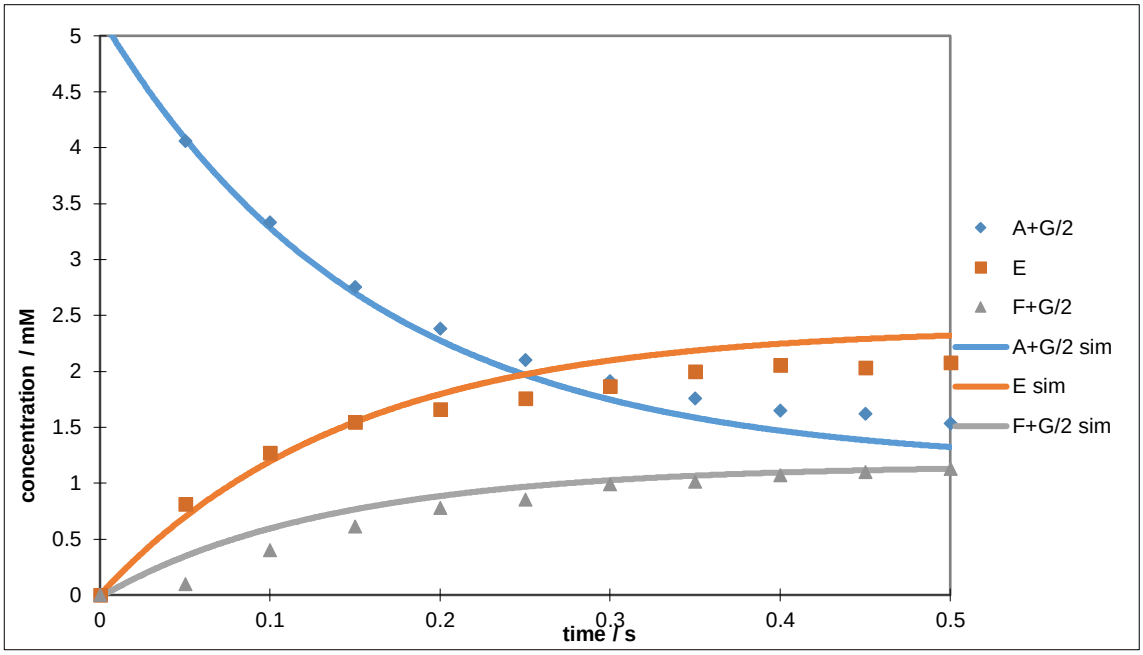

Figure 211: **'Bound 1' (A+G/2) excitation @ 298 K**

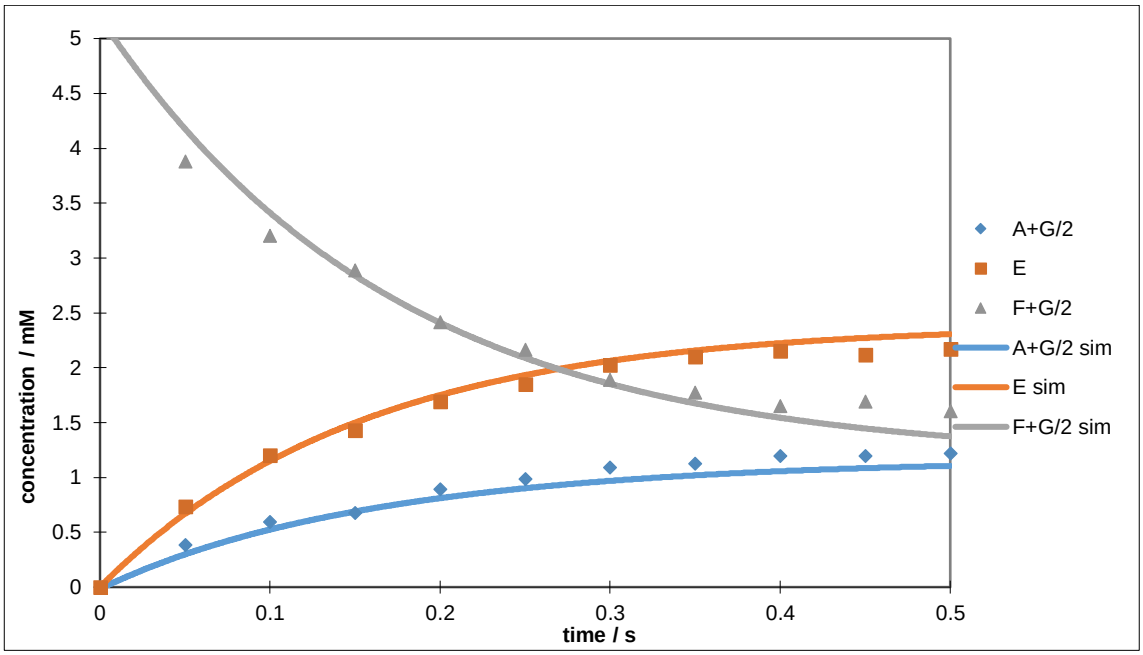

Figure 212: **'Bound 2' (F+G/2) excitation @ 298 K**

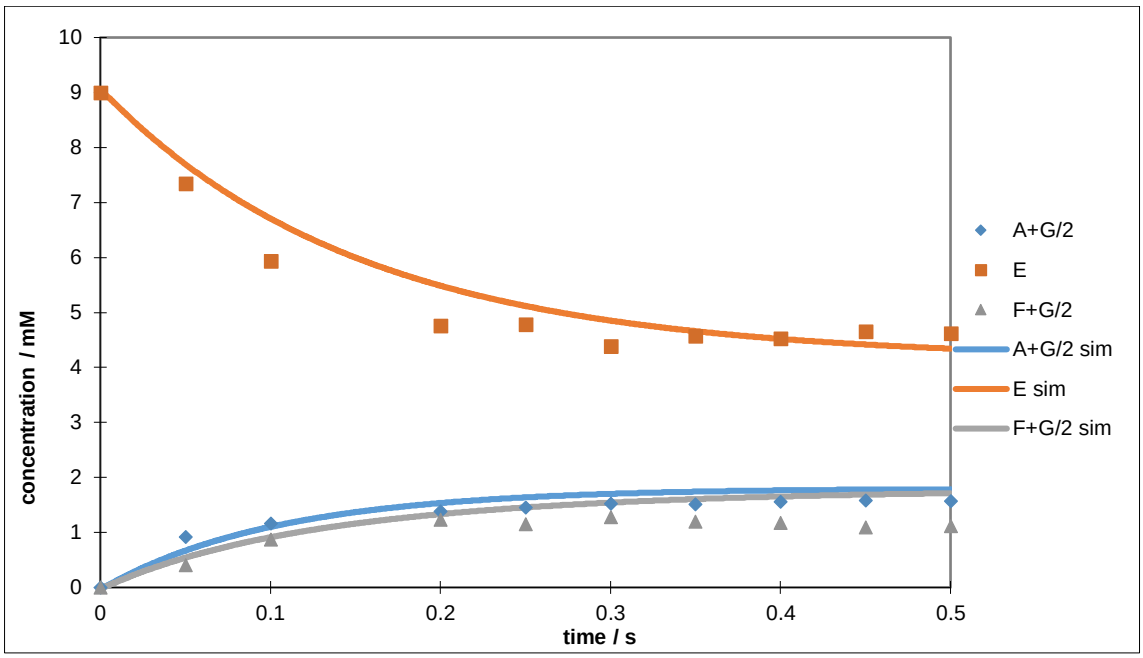

Figure 213: **'Free' (E) excitation @ 298 K**

-12.422	3.152	3.019	3.019	3.152	0	0	0	**A**
26.727	-51.062	0	0	0	21.257	0	3.079	**B**
21.257	0	-51.062	0	0	26.727	3.079	0	**C**
21.257	0	0	-51.062	0	26.727	0	3.079	**D**
26.727	0	0	0	-51.062	21.257	3.079	0	**E**
0	3.019	3.152	3.152	3.019	-12.422	0	0	**F**
0	0	44.851	0	44.851	0	-89.702	0	**G**
0	44.851	0	44.851	0	0	0	-89.702	**H**
A	**B**	**C**	**D**	**E**	**F**	**G**	**H**	

Table 69: **Model 4 observed rate constants for 4,6-nicotine-d_2 *9*, d_{22}-IMes *19* @ 298 K. Rate constants are read as k_{XY}, *i.e.* k_{AB} is row A, column B**

Excitation	Sum of least squares
Bound 1	0.704
Bound 2	0.482
Free	3.405
Total	4.591

Relax Bound	Relax Free	Relax Inter.
32.0	40.6	32.0

Table 70: sum of least squares for each plot and the modelled T_1 relaxation parameters (in seconds) used

303 K

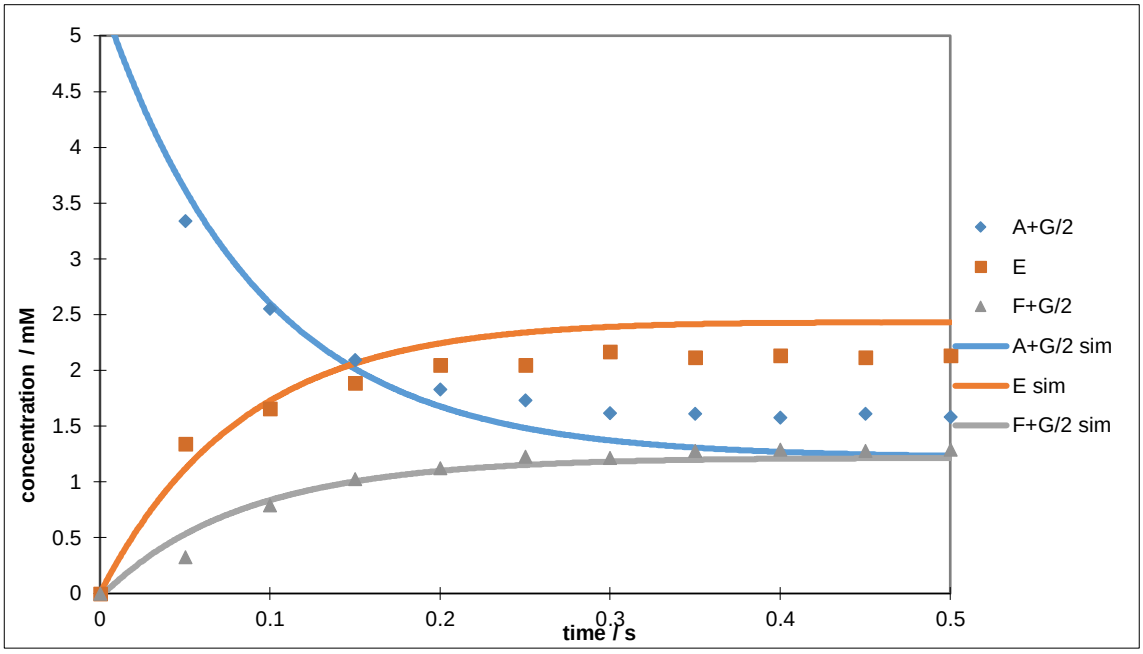

Figure 214: 'Bound 1' (A+G/2) excitation @ 303 K

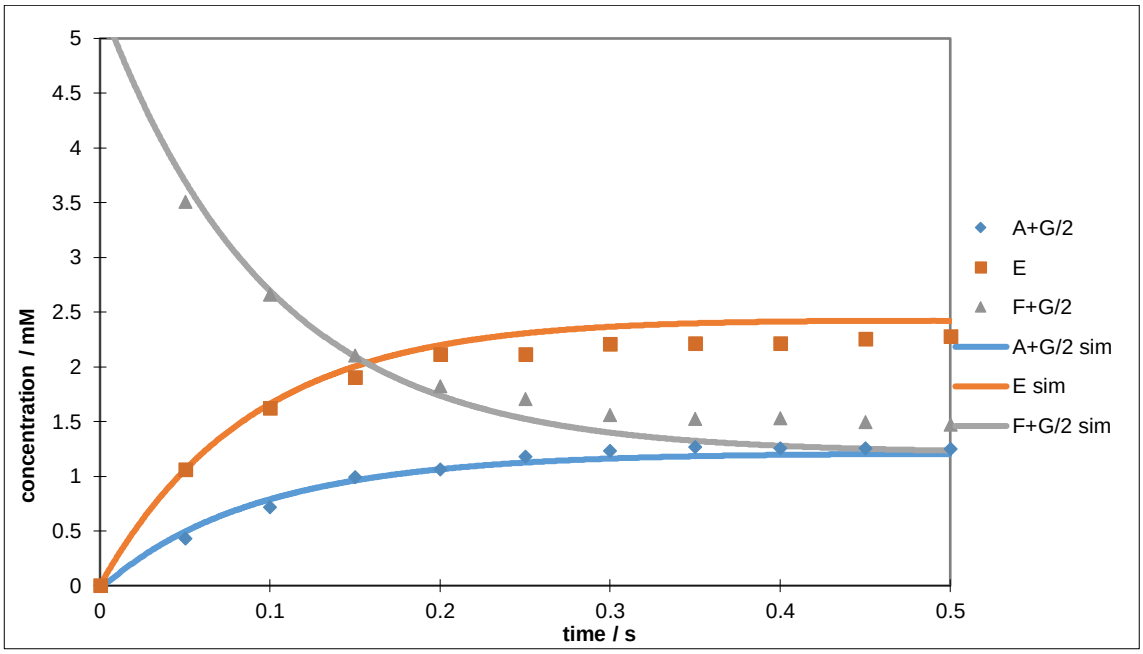

Figure 215: 'Bound 2' (F+G/2) excitation @ 303 K

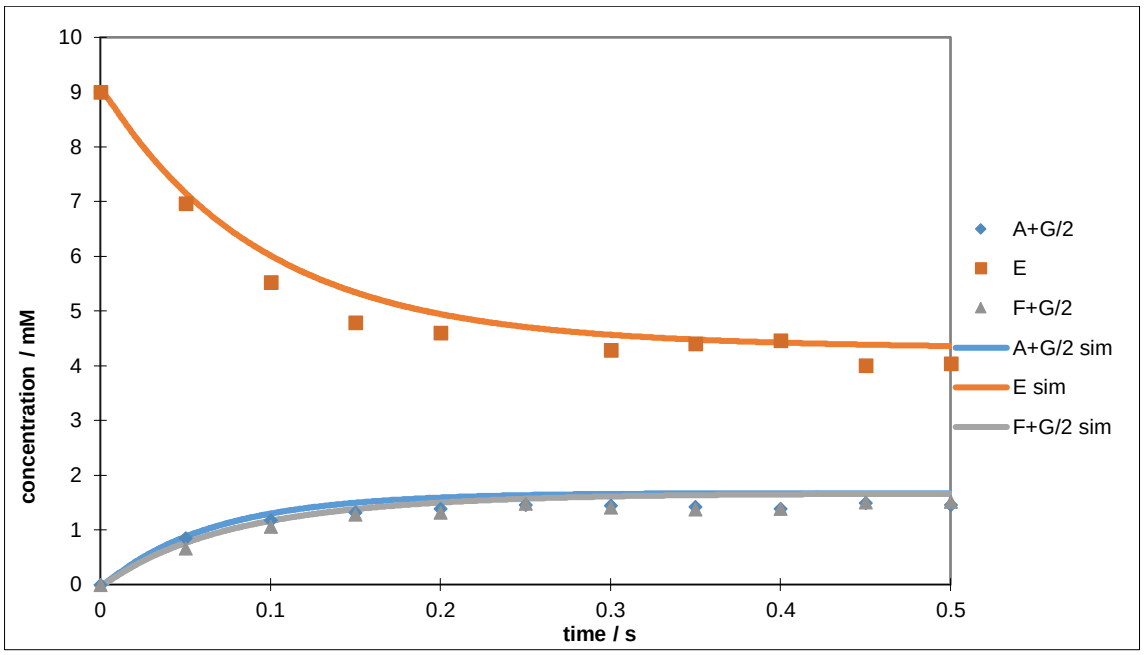

Figure 216: **'Free' (E) excitation @ 303 K**

-21.726	5.604	5.259	5.259	5.604	0	0	0	**A**
232.858	-438.222	0	0	0	202.161	0	3.203	**B**
202.161	0	-438.222	0	0	232.858	3.203	0	**C**
202.161	0	0	-438.222	0	232.858	0	3.203	**D**
232.858	0	0	0	-438.222	202.161	3.203	0	**E**
0	5.259	5.604	5.604	5.259	-21.726	0	0	**F**
0	0	427.359	0	427.359	0	-854.718	0	**G**
0	427.359	0	427.359	0	0	0	-854.718	**H**
A	**B**	**C**	**D**	**E**	**F**	**G**	**H**	

Table 71: **Model 4 observed rate constants for 4,6-nicotine-d_2 *9*, d_{22}-IMes *19* @ 303 K. Rate constants are read as k_{XY}, *i.e.* k_{AB} is row A, column B**

Excitation	Sum of least squares
Bound 1	1.48835
Bound 2	0.67089
Free	1.70689
Total	3.86613

Relax Bound	Relax Free	Relax Inter.
30	20	30

Table 72: sum of least squares for each plot and the modelled T_1 relaxation parameters (in seconds) used

Eyring plots

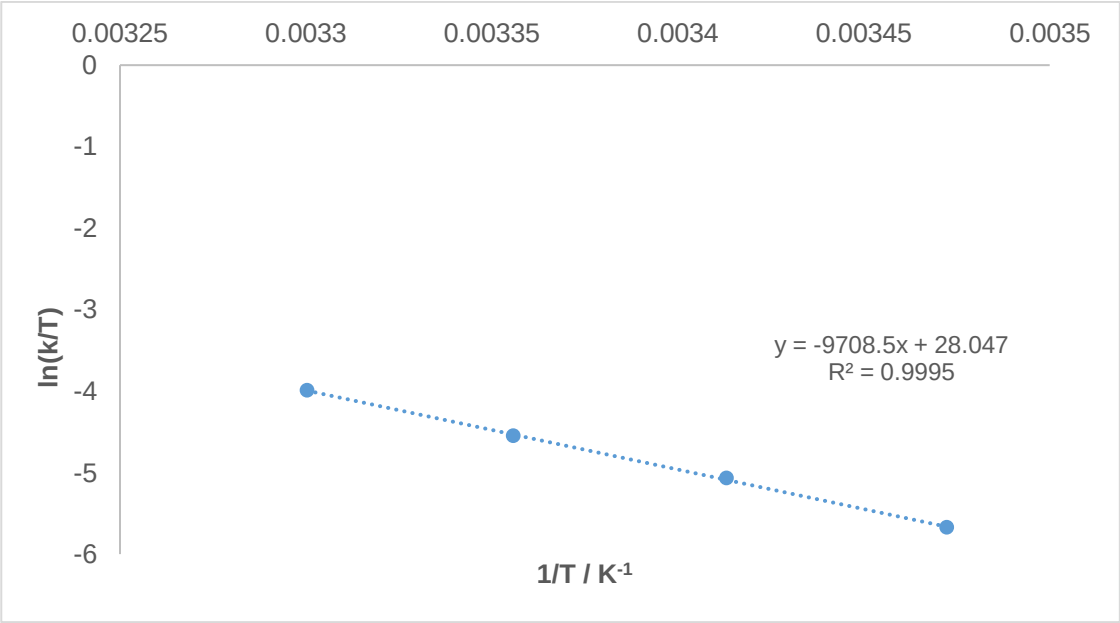

Figure 217: Eyring plot of Bound 1 for 4,6-nicotine-d_2 *9*, d_{22}-IMes *19*

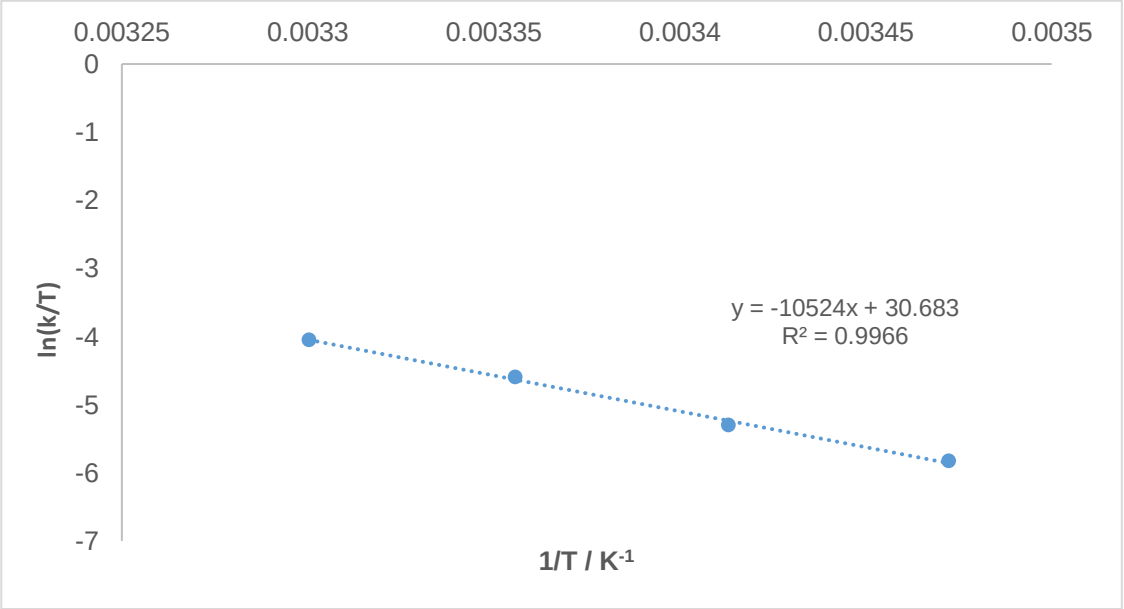

Figure 218: Eyring plot of Bound 2 for 4,6-nicotine-d_2 *9*, d_{22}-IMes *19*

Kinetic parameters

	Bound 1 -> Free	Bound 2 -> Free
ΔH‡ / kJmol-1	80.716	87.497
ΔS‡ / JK-1mol-1	35.647	57.563
ΔG_{300}‡ / kJmol-1	70.022	70.228

Figure 219: kinetic parameters for 4,6-nicotine-d_2 *9*, d_{22}-IMes *19*

7.3 EXSY Eyring error estimates

7.3.1 Model 1 errors

T / K	kobs/ s-1									
	(-)-nicotine, IMes		(-)-nicotine, d_{22}-IMes		4,6-nicotine-d2, IMes		4,6-nicotine-d2, d22-IMes			
	Bound1	Bound2	Bound1	Bound2	Bound1	Bound2	Bound1	Bound2	Avg.	S. Dev
288	0.894	1.093	0.855	1.065	0.981	0.939	0.911	0.808	0.943	0.099
293	1.608	2.044	1.781	1.950	2.332	1.877	2.005	1.726	1.915	0.223
298	3.362	3.546	3.524	3.912	3.612	3.543	3.446	3.554	3.562	0.161
303	5.594	6.673	6.559	5.779	5.910	6.015	6.105	5.771	6.051	0.384
$\Delta H^{\ddagger}$	86.710	83.970	96.193	80.643	82.227	87.663	90.515	89.592	87.189	5.017
$\Delta S^{\ddagger}$	55.480	47.660	88.200	36.080	41.617	59.459	69.236	65.303	57.879	16.715
$\Delta G_{300}^{\ddagger}$	70.034	69.672	69.733	69.819	69.742	69.825	69.744	70.001	69.821	0.131

Table 73: Model 1 EXSY data combined, with standard deviation errors. $\Delta H^{\ddagger}$ is in $kJmol^{-1}$, $\Delta S^{\ddagger}$ is in $JK^{-1}mol^{-1}$ and $\Delta G_{300}^{\ddagger}$ is in $kJmol^{-1}$

7.3.2 Model 4 errors

T / K	k_{obs}/ s^{-1}									
	(-)-nicotine, IMes		(-)-nicotine, d_{22}-IMes		4,6-nicotine-d2, IMes		4,6-nicotine-d2, d22-IMes			
	Bound1	Bound2	Bound1	Bound2	Bound1	Bound2	Bound1	Bound2	Avg.	S. Dev
288	0.797	1.040	0.778	1.000	0.790	0.759	0.991	0.847	0.875	0.115
293	1.460	1.666	1.502	1.647	1.847	1.468	1.847	1.468	1.613	0.165
298	3.092	3.181	3.026	3.105	3.058	2.998	3.152	3.019	3.079	0.065
303	5.303	6.465	5.959	5.480	5.637	5.261	5.604	5.259	5.621	0.415
$\Delta H^{\ddagger}$	90.947	86.330	94.460	82.480	90.280	92.519	80.716	87.497	88.154	4.817
$\Delta S^{\ddagger}$	69.169	54.870	80.917	41.351	74.660	74.349	35.647	57.563	61.066	16.503
$\Delta G_{300}^{\ddagger}$	70.196	69.869	70.185	70.075	70.033	70.214	70.022	70.228	70.103	0.126

Table 74: Model 4 EXSY data combined, with standard deviation errors. $\Delta H^{\ddagger}$ is in $kJmol^{-1}$, $\Delta S^{\ddagger}$ is in $JK^{-1}mol^{-1}$ and $\Delta G_{300}^{\ddagger}$ is in $kJmol^{-1}$

7.3.3 Comparison

T / K	Avg dissociation rate / s^{-1}				
	Model 1	S. dev.	Model 4	S. dev.	% change
288	0.943	0.099	0.875	0.115	-7.79%
293	1.915	0.223	1.613	0.165	-18.74%
298	3.562	0.161	3.079	0.065	-15.70%
303	6.051	0.384	5.621	0.415	-7.65%

Average $\Delta H^{\ddagger}$ / $kJmol^{-1}$				
Model 1	S. dev.	Model 4	S. dev.	% change
87.189	5.017	88.154	4.817	1.09%

Average $\Delta S^{\ddagger}$ / $JK^{-1}mol^{-1}$				
Model 1	S. dev.	Model 4	S. dev.	% change
57.879	16.715	61.066	16.503	5.22%

Average $\Delta G_{300}^{\ddagger}$ / $kJmol^{-1}$				
Model 1	S. dev.	Model 4	S. dev.	% change
69.821	0.131	70.103	0.126	0.40%

Table 75: comparison of data from Models 1 and 4, with errors

7.4 SABRE error estimates

7.4.1 Varied substrate concentration

(−)-nicotine 1, IMes 18

	Signal enhancement (relative to thermal)			
	2-proton	6-proton	4-proton	5-proton
1	301.113	370.758	338.895	74.331
2	279.931	342.551	304.695	35.087
3	327.298	299.124	316.039	18.041
Mean	302.781	337.478	319.876	42.486
SD	23.728	36.086	17.420	28.865
No. of data points (n)	3	3	3	3
Root n	1.732	1.732	1.732	1.732
Standard error	**13.699**	**20.834**	**10.058**	**16.665**
Standard error as % of mean	4.524	6.173	3.144	39.225

Table 76: 'shake and drop' errors for 4 equivalents (−)-nicotine *1* with IMes *18*, shaken in stray field. Lab book reference no. WHD/A/7/7 A

	Signal enhancement (relative to thermal)			
	2-proton	**6-proton**	**4-proton**	**5-proton**
1	238.726	311.437	208.035	36.954
2	251.515	328.240	236.929	109.909
3	221.026	321.634	199.330	3.176
Mean	237.089	320.437	214.765	50.013
SD	15.311	8.465	19.682	54.552
No. of data points (n)	3	3	3	3
Root n	1.732	1.732	1.732	1.732
Standard error	8.840	4.888	11.363	31.495
Standard error as % of mean	3.728	1.525	5.291	62.975

Table 77: 'shake and drop' errors for 5 equivalents (−)-nicotine *1* with IMes *18,* shaken in stray field. Lab book reference no. WHD/A/1/1 A

	Signal enhancement (relative to thermal)			
	2-proton	**6-proton**	**4-proton**	**5-proton**
1	222.279	252.861	224.533	74.207
2	273.112	292.850	266.680	75.249
3	216.842	222.722	206.652	61.065
Mean	237.411	256.145	232.622	70.174
SD	31.037	35.179	30.820	7.906
No. of data points (n)	3	3	3	3
Root n	1.732	1.732	1.732	1.732
Standard error	**17.919**	**20.311**	**17.794**	**4.564**
Standard error as % of mean	7.548	7.929	7.649	6.504

Table 78: 'shake and drop' errors for 6 equivalents (−)-nicotine *1* with IMes *18,* shaken in stray field. Lab book reference no. WHD/A/7/7 B

	Signal enhancement (relative to thermal)			
	2-proton	**6-proton**	**4-proton**	**5-proton**
1	214.285	234.144	195.974	91.750
2	221.078	243.101	207.362	104.656
3	215.793	234.979	196.629	88.178
Mean	217.052	237.408	199.988	94.861
SD	3.567	4.948	6.394	8.668
No. of data points (n)	3	3	3	3
Root n	1.732	1.732	1.732	1.732
Standard error	**2.060**	**2.857**	**3.692**	**5.005**
Standard error as % of mean	0.949	1.203	1.846	5.276

Table 79: 'shake and drop' errors for 10 equivalents (−)-nicotine *1* with IMes *18*, shaken in stray field. Lab book reference no. WHD/A/7/7 D

	Signal enhancement (relative to thermal)			
	2-proton	**6-proton**	**4-proton**	**5-proton**
1	177.115	190.163	158.731	71.952
2	177.483	188.775	157.969	72.341
3	142.408	156.233	125.658	52.609
Mean	165.669	178.390	147.453	65.634
SD	20.145	19.202	18.879	11.282
No. of data points (n)	3	3	3	3
Root n	1.732	1.732	1.732	1.732
Standard error	**11.631**	**11.086**	**10.900**	**6.514**
Standard error as % of mean	7.021	6.214	7.392	9.924

Table 80: 'shake and drop' errors for 15 equivalents (−)-nicotine *1* with IMes *18*, shaken in stray field. Lab book reference no. WHD/A/7/7 E

(−)-nicotine 1, d_{22}-IMes 19

	Signal enhancement (relative to thermal)			
	2-proton	**6-proton**	**4-proton**	**5-proton**
1	361.592	435.371	370.286	6.395
2	364.573	419.076	352.768	21.373
Mean	363.082	427.224	361.527	13.884
SD	2.107	11.523	12.387	10.591
No. of data points (n)	2	2	2	2
Root n	1.41421	1.41421	1.41421	1.41421
Standard error	**1.4901**	**8.1477**	**8.75915**	**7.489**
Standard error as % of mean	0.4104	1.90713	2.42282	53.9398

Table 81: 'shake and drop' errors for 4 equivalents (−)-nicotine *1* with d_{22}-IMes *19*, shaken in stray field. Lab book reference no. WHD/A/12/12 A2

	Signal enhancement (relative to thermal)			
	2-proton	**6-proton**	**4-proton**	**5-proton**
1	453.596	452.449	349.426	24.430
2	440.185	430.167	324.032	23.686
Mean	446.890	441.308	336.729	24.058
SD	9.483	15.756	17.956	0.526
No. of data points (n)	2	2	2	2
Root n	1.414	1.414	1.414	1.414
Standard error	**6.705**	**11.141**	**12.697**	**0.372**
Standard error as % of mean	1.500	2.525	3.771	1.545

Table 82: 'shake and drop' errors for 6 equivalents (−)-nicotine *1* with d_{22}-IMes *19*, shaken in stray field. Lab book reference no. WHD/A/12/12 B2

	Signal enhancement (relative to thermal)			
	2-proton	**6-proton**	**4-proton**	**5-proton**
1	331.926	383.994	269.026	68.011
2	325.827	363.146	265.861	22.398
3	316.746	372.855	269.282	47.477
Mean	324.833	373.332	268.056	45.962
SD	7.638	10.432	1.906	22.844
No. of data points (n)	3	3	3	3
Root n	1.732	1.732	1.732	1.732
Standard error	**4.410**	**6.023**	**1.100**	**13.189**
Standard error as % of mean	1.358	1.613	0.410	28.696

Table 83: 'shake and drop' errors for 8 equivalents (−)-nicotine *1* with d_{22}-IMes *19*, shaken in stray field. Lab book reference no. WHD/A/12/12 C2

	Signal enhancement (relative to thermal)			
	2-proton	**6-proton**	**4-proton**	**5-proton**
1	240.780	257.477	165.317	58.529
2	225.413	245.378	163.441	40.854
3	207.414	234.526	151.423	48.399
Mean	224.536	245.793	160.060	49.261
SD	16.700	11.481	7.539	8.869
No. of data points (n)	3	3	3	3
Root n	1.732	1.732	1.732	1.732
Standard error	**9.642**	**6.629**	**4.352**	**5.121**
Standard error as % of mean	4.294	2.697	2.719	10.395

Table 84: 'shake and drop' errors for 10 equivalents (−)-nicotine *1* with d_{22}-IMes *19*, shaken in stray field. Lab book reference no. WHD/A/12/12 D2

	2-proton	**6-proton**	**4-proton**	**5-proton**
1	144.386	119.847	88.779	12.693
2	155.132	123.528	83.687	28.231
3	146.706	113.517	82.284	33.669
Mean	148.741	118.964	84.916	24.864
SD	5.654	5.063	3.418	10.886
No. of data points (n)	3	3	3	3
Root n	1.732	1.732	1.732	1.732
Standard error	**3.265**	**2.923**	**1.973**	**6.285**
Standard error as % of mean	2.195	2.457	2.324	25.277

Table 85: 'shake and drop' errors for 15 equivalents (−)-nicotine *1* with d_{22}-IMes *19*, shaken in stray field. Lab book reference no. WHD/A/12/12 E2

4,6-nicotine-d_2 9, IMes 18

	Signal enhancement (relative to thermal)	
	2-proton	**5-proton**
1	773.628	929.595
2	762.009	967.118
3	742.312	943.710
Mean	759.316	946.808
SD	15.831	18.952
No. of data points (n)	3	3
Root n	1.732	1.732
Standard error	**9.140**	**10.942**
Standard error as % of mean	1.204	1.156

Table 86: 'shake and drop' errors for 4 equivalents 4,6-nicotine-d_2 *9* with IMes *18*, shaken in stray field. Lab book reference no. WHD/A/9/9 A

	Signal enhancement (relative to thermal)	
	2-proton	**5-proton**
1	468.113	974.633
2	490.522	1021.289
3	497.003	1034.782
Mean	485.213	1010.235
SD	30.259	23.578
No. of data points (n)	3	3
Root n	1.732	1.732
Standard error	**17.470**	**13.613**
Standard error as % of mean	3.601	1.347

Table 87: 'shake and drop' errors for 5 equivalents 4,6-nicotine-d_2 *9* with IMes *18*, shaken in stray field. Lab book reference no. WHD/A/1/1 E

	Signal enhancement (relative to thermal)	
	2-proton	**5-proton**
1	666.062	737.943
2	606.188	692.801
3	643.759	703.563
Mean	638.670	711.436
SD	30.259	23.578
No. of data points (n)	3	3
Root n	1.732	1.732
Standard error	**17.470**	**13.613**
Standard error as % of mean	2.735	1.913

Table 88: 'shake and drop' errors for 6 equivalents 4,6-nicotine-d_2 *9* with IMes *18*, shaken in stray field. Lab book reference no. WHD/A/9/9 B

	Signal enhancement (relative to thermal)	
	2-proton	**5-proton**
1	288.735	334.530
2	249.941	281.919
3	243.303	274.231
Mean	260.659	296.893
SD	24.539	32.820
No. of data points (n)	3	3
Root n	1.732	1.732
Standard error	**14.168**	**18.949**
Standard error as % of mean	5.435	6.382

Table 89: 'shake and drop' errors for 10 equivalents 4,6-nicotine-d_2 *9* with IMes *18*, shaken in stray field. Lab book reference no. WHD/A/9/9 D

	Signal enhancement (relative to thermal)	
	2-proton	**5-proton**
1	195.296	219.779
2	212.347	241.908
Mean	203.822	230.843
SD	12.056	15.647
No. of data points (n)	2	2
Root n	1.414	1.414
Standard error	**8.525**	**11.064**
Standard error as % of mean	4.183	4.793

Table 90: 'shake and drop' errors for 15 equivalents 4,6-nicotine-d_2 *9* with IMes *18*, shaken in stray field. Lab book reference no. WHD/A/9/9 E

4,6-nicotine-d_2 9, d_{22}-IMes 19

	Signal enhancement (relative to thermal)	
	2-proton	**5-proton**
1	824.355	1137.279
2	703.320	1035.748
3	754.069	1103.929
Mean	760.581	1092.319
SD	60.780	51.752
No. of data points (n)	3	3
Root n	1.732	1.732
Standard error	**35.091**	**29.879**
Standard error as % of mean	4.614	2.735

Table 91: 'shake and drop' errors for 4 equivalents 4,6-nicotine-d_2 *9* with d_{22}-IMes *19*, shaken in stray field. Lab book reference no. WHD/A/10/10 A2

	Signal enhancement (relative to thermal)	
	2-proton	**5-proton**
1	811.081	1142.324
2	711.883	1049.495
3	856.175	1087.511
Mean	793.046	1093.110
SD	73.817	46.667
No. of data points (n)	3	3
Root n	1.732	1.732
Standard error	**42.618**	**26.943**
Standard error as % of mean	5.374	2.465

Table 92: 'shake and drop' errors for 6 equivalents 4,6-nicotine-d_2 *9* with d_{22}-IMes *19*, shaken in stray field. Lab book reference no. WHD/A/10/10 B2

	Signal enhancement (relative to thermal)	
	2-proton	**5-proton**
1	580.199	732.476
2	652.263	728.973
Mean	616.231	730.724
SD	50.957	2.477
No. of data points (n)	2	2
Root n	1.414	1.414
Standard error	**36.032**	**1.752**
Standard error as % of mean	5.847	0.240

Table 93: 'shake and drop' errors for 8 equivalents 4,6-nicotine-d_2 *9* with d_{22}-IMes *19*, shaken in stray field. Lab book reference no. WHD/A/10/10 C2

	Signal enhancement (relative to thermal)	
	2-proton	**5-proton**
1	434.221	525.580
2	418.039	486.906
3	438.101	484.545
Mean	430.120	499.010
SD	10.641	23.040
No. of data points (n)	3	3
Root n	1.732	1.732
Standard error	**6.143**	**13.302**
Standard error as % of mean	1.428	2.666

Table 94: 'shake and drop' errors for 10 equivalents 4,6-nicotine-d_2 *9* with d_{22}-IMes *19*, shaken in stray field. Lab book reference no. WHD/A/10/10 D2

	Signal enhancement (relative to thermal)	
	2-proton	**5-proton**
1	289.830	323.748
2	260.698	289.764
3	276.598	298.271
4	273.938	305.409
Mean	367.022	405.731
SD	14.587	17.684
No. of data points (n)	4	4
Root n	2	2
Standard error	**7.293**	**8.842**
Standard error as % of mean	1.987	2.179

Table 95: 'shake and drop' errors for 15 equivalents 4,6-nicotine-d_2 *9* with d_{22}-IMes *19*, shaken in stray field. Lab book reference no. WHD/A/10/10 E2

7.4.2 Substrate screen

6-nicotine-d_1 4, IMes 18

	Signal enhancement (relative to thermal)		
	2-proton	**4-proton**	**5-proton**
1	427.121	391.142	35.307
2	416.886	362.634	10.286
3	399.986	328.694	40.016
Mean	414.664	360.823	28.536
SD	13.703	31.263	15.980
No. of data points (n)	3	3	3
Root n	1.732	1.732	1.732
Standard error	**7.912**	**18.050**	**9.226**
Standard error as % of mean	1.908	5.002	32.330

Table 96: 'shake and drop' errors for 5 equivalents 6-nicotine-d_1 *4* with IMes *18*, shaken in stray field. Lab book reference no. WHD/A/1/1 C

5,6-nicotine-d_2 8, IMes 18

	Signal enhancement (relative to thermal)	
	2-proton	**4-proton**
1	294.465	283.890
2	239.337	230.198
3	232.696	218.726
Mean	255.499	244.271
SD	33.908	34.787
No. of data points (n)	3	3
Root n	1.732	1.732
Standard error	**19.577**	**20.084**
Standard error as % of mean	7.662	8.222

Table 97: 'shake and drop' errors for 5 equivalents 5,6-nicotine-d_2 *8* with IMes *18*, shaken in stray field. Lab book reference no. WHD/A/1/1 D

2,6-nicotine-d_2 10, IMes 18

	Signal enhancement (relative to thermal)	
	4-proton	**5-proton**
1	336.907	232.446
2	296.303	179.767
3	329.884	189.382
Mean	321.031	200.531
SD	21.701	28.054
No. of data points (n)	3	3
Root n	1.732	1.732
Standard error	**12.529**	**16.197**
Standard error as % of mean	3.903	8.077

Table 98: 'shake and drop' errors for 5 equivalents 2,6-nicotine-*d_2 10* with IMes *18,* shaken in stray field. Lab book reference no. WHD/A/13/13 A

7.4.3 Alternative catalysts

4,6-nicotine-d_2 9, I^{t}Bu 20

	Signal enhancement (relative to thermal)	
	2-proton	**5-proton**
1	386.105	413.923
2	381.214	409.448
3	384.631	403.148
Mean	383.983	408.840
SD	2.509	5.413
No. of data points (n)	3	3
Root n	1.732	1.732
Standard error	**1.449**	**3.125**
Standard error as % of mean	0.377	0.764

Table 99: 'shake and drop' errors for 5 equivalents 4,6-nicotine-*d_2 9* with I^{t}Bu *20,* shaken in stray field. Lab book reference no. WHD/A/21/21 B

4,6-nicotine-d_2 9, ICl 21

	Signal enhancement (relative to thermal)	
	2-proton	**5-proton**
1	344.935	292.583
2	337.111	292.529
3	349.760	305.998
Mean	343.935	297.037
SD	6.384	7.761
No. of data points (n)	3	3
Root n	1.732	1.732
Standard error	**3.686**	**4.481**
Standard error as % of mean	1.072	1.509

Table 100: 'shake and drop' errors for 5 equivalents 4,6-nicotine-*d_2* *9* with ICl *21*, shaken in stray field. Lab book reference no. WHD/A/21/21 B

7.4.4 Mixing studies

(−)-nicotine 1, IMes 18 with magnetic shaker

	Signal enhancement (relative to thermal)			
	2-proton	**6-proton**	**4-proton**	**5-proton**
1	577.607	679.631	636.477	324.541
2	676.202	611.555	667.711	278.195
3	657.226	496.057	622.287	264.482
Mean	637.012	595.747	642.158	289.073
SD	52.313	92.802	23.239	31.472
No. of data points (n)	3	3	3	3
Root n	1.732	1.732	1.732	1.732
Standard error	**30.203**	**53.579**	**13.417**	**18.171**
Standard error as % of mean	4.741	8.994	2.089	6.286

Table 101: 'shake and drop' errors for 5 equivalents 6-nicotine-*d_1* *4* with IMes *18*, shaken in a 60 G magnetic shaker assembly. Lab book reference no. WHD/A/28/28 A

4,6-nicotine-d_2 9, d_{22}-IMes 19

	Signal enhancement (relative to thermal)	
	2-proton	**5-proton**
1	1492.728	2760.423
2	1764.185	2947.070
3	1619.669	2723.149
Mean	1625.527	2810.214
SD	135.823	119.977
No. of data points (n)	3	3
Root n	1.732	1.732
Standard error	**78.418**	**69.269**
Standard error as % of mean	4.824	2.465

Table 102: 'shake and drop' errors for 5 equivalents 4,6-nicotine-d_2 *9* with d_{22}-IMes *19,* shaken in a 60 G magnetic shaker assembly for six seconds. Lab book reference no. WHD/A/28/28 A

7.4.5 Co-ligand 'doping' studies

4,6-nicotine-d_2 9, pyridine-d_5 23, d_{22}-IMes 19

	Signal enhancement (relative to thermal)	
	2-proton	**5-proton**
1	2565.540	2985.735
2	2882.261	2572.397
3	2914.442	2170.771
Mean	2787.414	2576.301
SD	192.821	407.496
No. of data points (n)	3	3
Root n	1.732	1.732
Standard error	**111.325**	**235.268**
Standard error as % of mean	3.994	9.132

Table 103: 'shake and drop' errors for 2.5 equivalents 4,6-nicotine-d_2 *9* with 2.5 equivalents coligand py-d_5 23 and d_{22}-IMes *19,* shaken in a 60 G magnetic shaker assembly for six seconds. Lab book reference no. WHD/A/26/26 C

7.4.6 Variable pressure studies

(−)-nicotine 1, IMes 18

	Signal enhancement (relative to thermal)			
	2-proton	**6-proton**	**4-proton**	**5-proton**
1	301.029	414.545	379.842	20.201
2	302.959	410.413	354.783	19.899
3	307.185	391.876	353.938	32.690
Mean	303.724	405.611	362.854	24.263
SD	3.148	12.073	14.718	7.299
No. of data points (n)	3	3	3	3
Root n	1.732	1.732	1.732	1.732
Standard error	**1.818**	**6.970**	**8.497**	**4.214**
Standard error as % of mean	0.598	1.718	2.342	17.369

Table 104: 'shake and drop' errors for 5 equivalents (−)-nicotine *1* with IMes *18*, with 5 bar *p*-H_2 shaken in stray field. Lab book reference no. WHD/A/23/23 B

	Signal enhancement (relative to thermal)			
	2-proton	**6-proton**	**4-proton**	**5-proton**
1	521.466	456.189	417.485	25.580
2	554.234	434.675	445.864	23.392
3	591.065	459.542	455.583	12.882
Mean	555.589	450.135	439.644	20.618
SD	34.819	13.493	19.796	6.788
No. of data points (n)	3	3	3	3
Root n	1.732	1.732	1.732	1.732
Standard error	**20.103**	**7.790**	**11.429**	**3.919**
Standard error as % of mean	3.618	1.731	2.600	19.009

Table 105: 'shake and drop' errors for 5 equivalents (−)-nicotine *1* with IMes *18*, with 6 bar *p*-H_2 shaken in stray field. Lab book reference no. WHD/A/23/23 A

4,6-nicotine-d_2 9, IMes 18

	Signal enhancement (relative to thermal)	
	2-proton	**5-proton**
1	679.958	983.195
2	600.21	903.918
3	689.671	910.465
Mean	656.613	932.526
SD	49.0873	44.0027
No. of data points (n)	3	3
Root n	1.73205	1.73205
Standard error	**28.3406**	**25.4049**
Standard error as % of mean	4.31617	2.72432

Table 106: 'shake and drop' errors for 5 equivalents 4,6-nicotine-d_2 *1* with IMes *18*, with 5 bar *p*-H_2 shaken in stray field. Lab book reference no. WHD/A/23/23 C

	Signal enhancement (relative to thermal)	
	2-proton	**5-proton**
1	521.466	25.580
2	554.234	23.392
3	591.065	12.882
Mean	555.589	20.618
SD	34.819	6.788
No. of data points (n)	3	3
Root n	1.732	1.732
Standard error	**20.103**	**3.919**
Standard error as % of mean	3.618	19.009

Table 107: 'shake and drop' errors for 5 equivalents 4,6-nicotine-d_2 *1* with IMes *18*, with 6 bar *p*-H_2 shaken in stray field. Lab book reference no. WHD/A/23/23 D2

4,6-nicotine-d_2 9, IMes 18 with magnetic shaker

	Signal enhancement (relative to thermal)	
	2-proton	**5-proton**
1	1179.599	1826.441
2	1110.885	1737.346
Mean	1145.242	1781.894
SD	48.589	62.999
No. of data points (n)	3	3
Root n	1.732	1.732
Standard error	**28.053**	**36.373**
Standard error as % of mean	2.449	2.041

Table 108: 'shake and drop' errors for 5 equivalents 4,6-nicotine-d_2 *1* with IMes *18*, with 5 bar *p*-H_2 shaken in a 60 G magnetic shaker assembly. Lab book reference no. WHD/A/23/23 C

	Signal enhancement (relative to thermal)	
	2-proton	**5-proton**
1	1187.903	25.580
2	1235.533	23.392
Mean	1211.718	24.486
SD	33.679	1.547
No. of data points (n)	3	3
Root n	1.732	1.732
Standard error	**19.445**	**0.893**
Standard error as % of mean	1.605	3.648

Table 109: 'shake and drop' errors for 5 equivalents 4,6-nicotine-d_2 *1* with IMes *18*, with 6 bar *p*-H_2 shaken in a 60 G magnetic shaker assembly. Lab book reference no. WHD/A/23/23 D2

4,6-nicotine-d_2 9, d_{22}-IMes 19 with magnetic shaker

	Signal enhancement (relative to thermal)	
	2-proton	**5-proton**
1	1326.195	2291.781
2	1271.767	2139.874
3	1342.555	2351.567
Mean	1313.506	2261.074
SD	37.061	109.136
No. of data points (n)	3	3
Root n	1.732	1.732
Standard error	**21.397**	**63.010**
Standard error as % of mean	1.629	2.787

Table 110: 'shake and drop' errors for 5 equivalents 4,6-nicotine-d_2 *1* with d_{22}-IMes *19*, with 6 bar *p*-H_2 shaken in a 60 G magnetic shaker assembly. Lab book reference no. WHD/A/23/23 E

7.4.7 Variable temperature studies

(−)-nicotine 1, IMes 18

	Signal enhancement (relative to thermal)			
	2-proton	**6-proton**	**4-proton**	**5-proton**
1	308.301	364.235	281.798	8.018
2	355.306	265.865	312.010	4.020
Mean	331.804	315.050	296.904	6.019
SD	33.237	69.558	21.363	2.827
No. of data points (n)	2	2	2	2
Root n	1.414	1.414	1.414	1.414
Standard error	**23.502**	**49.185**	**15.106**	**1.999**
Standard error as % of mean	7.083	15.612	5.088	33.211

Table 111: 'shake and drop' errors for 4 equivalents (−)-nicotine *1* with IMes *18*, shaken in stray field at 303 K. Lab book reference no. WHD/A/18/18 B

	Signal enhancement (relative to thermal)			
	2-proton	**6-proton**	**4-proton**	**5-proton**
1	506.633	225.320	394.821	8.514
2	542.643	216.479	403.871	6.836
Mean	524.638	220.900	399.346	7.675
SD	25.463	6.252	6.399	1.187
No. of data points (n)	2	2	2	2
Root n	1.414	1.414	1.414	1.414
Standard error	**18.005**	**4.421**	**4.525**	**0.839**
Standard error as % of mean	3.432	2.001	1.133	10.932

Table 112: 'shake and drop' errors for 4 equivalents (−)-nicotine *1* with IMes *18*, shaken in stray field at 308 K. Lab book reference no. WHD/A/18/18 A

	Signal enhancement (relative to thermal)			
	2-proton	**6-proton**	**4-proton**	**5-proton**
1	406.008	265.804	327.373	12.071
2	337.129	307.133	313.459	13.012
3	408.197	252.753	352.730	14.350
Mean	383.778	275.230	331.187	13.144
SD	40.414	28.389	19.912	1.145
No. of data points (n)	3	3	3	3
Root n	1.732	1.732	1.732	1.732
Standard error	**23.333**	**16.390**	**11.496**	**0.661**
Standard error as % of mean	6.080	5.955	3.471	5.031

Table 113: 'shake and drop' errors for 4 equivalents (−)-nicotine *1* with IMes *18*, shaken in stray field at 308 K. Lab book reference no. WHD/A/18/18 C

	Signal enhancement (relative to thermal)	
	2-proton	**5-proton**
1	340.850	473.834
2	315.248	447.800
3	295.081	443.586
Mean	317.059	455.073
SD	22.938	16.384
No. of data points (n)	3	3
Root n	1.732	1.732
Standard error	**13.243**	**9.459**
Standard error as % of mean	4.177	2.079

Table 114: 'shake and drop' errors for 4 equivalents 4,6-nicotine-d_2 *9* with IMes *18*, shaken in stray field at 303 K. Lab book reference no. WHD/A/18/18 E

	Signal enhancement (relative to thermal)	
	2-proton	**5-proton**
1	280.600	400.263
2	272.422	395.864
3	265.342	375.732
Mean	272.788	390.620
SD	7.636	13.079
No. of data points (n)	3	3
Root n	1.732	1.732
Standard error	**4.408**	**7.551**
Standard error as % of mean	1.616	1.933

Table 115: 'shake and drop' errors for 4 equivalents 4,6-nicotine-d_2 *9* with IMes *18*, shaken in stray field at 308 K. Lab book reference no. WHD/A/18/18 D3

	Signal enhancement (relative to thermal)	
	2-proton	**5-proton**
1	247.715	354.717
2	272.333	349.431
3	259.020	370.905
Mean	259.689	358.351
SD	12.322	11.189
No. of data points (n)	3	3
Root n	1.732	1.732
Standard error	**7.114**	**6.460**
Standard error as % of mean	2.740	1.803

Table 116: 'shake and drop' errors for 4 equivalents 4,6-nicotine-d_2 *9* with IMes *18*, shaken in stray field at 313 K. Lab book reference no. WHD/A/18/18 F

8: Abbreviations

2D – two-dimensional

2DFT – two-dimensional Fourier transform

2-py, 4-py, 5-py etc. – 2-pyridyl, 4-pyridyl, 5-pyridyl etc.

ALTADENA - Adiabatic Longitudinal Transport After Dissociation Engenders Net Alignment

ANOVA – analysis of variance

Ar – argon

B_0 – external magnetic field

B_x, B_y, B_z – external magnetic field in *x, y, z* axis, respectively

BuLi – butyllithium

°C – Celcius

CE – cross-effect

CF – cystic fibrosis

cm - centimeter

COD – cyclooctadiene

Co-D – deuterated co-ligand

COPD – chronic obstructive pulmonary disease

cos – cosine

COSY – Correlation Spectroscopy

CPL – circularly polarised light

CSI – Chemical Shift Imaging

d – doublet

d – day(s)

dd – doublet of doublets

ddd – doublet of doublets of doublets

dm - decimeter

DMAE – dimethylaminoethanol

DMF – dimethylformamide

DNP – Dynamic Nuclear Polarisation

DoM – directed *ortho* metalation

DQ – double quantum

DS – dummy scans

e – exponential

eq. – equivalents

ESI – electrospray ionisation

ETL – echo train length

EtOAc – ethyl acetate

EXSY – Exchange Spectroscopy

FFT – fast Fourier transform

FID – free induction decay

FISP – free induction with steady-state free precession

FOV – field of view

FT-IR – Fourier-transformed infrared

G – Gauss

g – gram

GHz – gigahertz

ħ – 'h bar' reduced Planck's constant *i.e.* h/2π

h – Planck's constant

h – hour(s)

HRMS – High Resolution Mass Spectrometry

HSQC – Heteronuclear Single Quantum Coherence

Hz – hertz

I – nuclear spin quantum number

ICl (as carbene ligand) - 1,3-bis(4-chloro-2,6-dimethylphenyl)imidazole-2-ylidene

IMes (as carbene ligand) - 1,3-bis(2,4,6-trimethylphenyl)imidazole-2-ylidene

IR – infrared

I^{t}Bu (as carbene ligand) - 1,3-bis(4-*tert*-butyl-2,6-trimethylphenyl)imidazole-2-ylidene

***J* –** rotational quantum number/energy level

J – scalar coupling in Hz

K – Kelvin

k_{obs} – observed rate constant

k_B – Boltzmann constant

L – ligand

LC-MS – tandem liquid chromatography and mass spectrometry

ln – natural logarithm (base *e*)

m – multiplet

m/z – mass to charge ratio

M_0 – maximum/initial magnetisation

Mes – mesityl

mg – milligram(s)

mL – millilitre(s)

MHz – megahertz

mM – millimoles per dm^3

mm – millimetre(s)

mmol – millimole(s)

mol – mole(s)

MRI – Magnetic Resonance Imaging

$\boldsymbol{M'_{ss}}$ – steady state magnetisation

$\boldsymbol{M_x}$, $\boldsymbol{M_y}$, $\boldsymbol{M_z}$ – magnetisation in *x*, *y*, *z*

NBS – *N*-bromosuccinimide

NIC – (−)-nicotine

NMR – Nuclear Magnetic Resonance

NOESY – Nuclear Overhauser Effect Spectroscopy

NS – number of scans

OPSY – Only *para*-Hydrogen Spectroscopy

OPSY-d – double-quantum OPSY

OPSY-z – zero-quantum OPSY

P – polarisation

PASADENA - Parahydrogen And Synthesis Allow Dramatically Enhanced Nuclear Alignment

PFG – pulsed field gradient

***p*-H_2** – *para*-hydrogen

PHIP – *para*-Hydrogen Induced Polarisation

ppm – parts per million

prev. – previous

PTF – polarisation transfer field

Py – pyridine

RARE – Rapid Acquisition with Relaxation Enhancement

RF – radiofrequency

$\boldsymbol{R_F}$ – retention factor

rt – room temperature

s – second(s)

SABRE – Signal Amplification By Reversible Exchange

SE – solid effect

$\mathbf{S_{hyp}}$ – hyperpolarised signal

SINO – signal-to-noise function in Bruker TopSpin

SNR – signal-to-noise ratio

SQ – single quantum

SSFP – steady-state free precession

$\mathbf{S_{therm}}$ – thermal signal

Sub - substrate

T - temperature

T – Tesla

TD – time domain

TE – echo time

THF – tetrahydrofuran

TLC – thin-layer chromatography

TM – thermal mixing

TMP - 2,2,6,6-tetramethylpiperidine

TOF – time-of-flight

TR – repetition time

wt. – weight

ZQ – zero quantum

$\boldsymbol{\delta_C}$ **–** carbon chemical shift

$\boldsymbol{\delta_H}$ **–** hydrogen chemical shift

$\boldsymbol{\Delta G_{300}^{\ddagger}}$ - activation Gibbs' free energy at 300 K

$\boldsymbol{\Delta H^{\ddagger}}$ - activation enthalpy

$\boldsymbol{\Delta S^{\ddagger}}$ - activation entropy

$\boldsymbol{\tau_{mix}}$ – mixing time

9: References

(1) Adams, R. W.; Aguilar, J. A.; Atkinson, K. D.; Cowley, M. J.; Elliott, P. I.; Duckett, S. B.; Green, G. G.; Khazal, I. G.; Lopez-Serrano, J.; Williamson, D. C. *Science* **2009**, *323*, 1708.

(2) Nikolaou, P.; Goodson, B. M.; Chekmenev, E. Y. *Chem. Eur. J.* **2015**, *21*, 3156.

(3) Ardenkjaer-Larsen, J. H.; Fridlund, B.; Gram, A.; Hansson, G.; Hansson, L.; Lerche, M. H.; Servin, R.; Thaning, M.; Golman, K. *Proc. Natl. Acad. Sci. U.S.A.* **2003**, *100*, 10158.

(4) Penfield, J. G.; Reilly Jr, R. F. *Nat. Clin. Pract. Nephrol.* **2007**, *3*, 654.

(5) Aime, S.; Dastrù, W.; Gobetto, R.; Santelia, D.; Viale, A. In *Molecular Imaging I*; Semmler, W., Schwaiger, M., Eds.; Springer Berlin Heidelberg: 2008, p 247.

(6) Roberts, L. D.; Dabbs, J. W. T. *Annu. Rev. Nucl. Sci.* **1961**, *11*, 175.

(7) Viale, A.; Aime, S. *Curr. Opin. Chem. Biol.* **2010**, *14*, 90.

(8) Kemsley, J. *Chemical & Engineering News* **2008**, *86*, 12.

(9) Duckett, S. B.; Sleigh, C. J. *Prog. Nucl. Magn. Reson. Spectrosc.* **1999**, *34*, 71.

(10) Månsson, S.; Johansson, E.; Magnusson, P.; Chai, C.-M.; Hansson, G.; Petersson, J. S.; Ståhlberg, F.; Golman, K. *Eur. Radiol.* **2006**, *16*, 57.

(11) Owers-Bradley, J. R.; Horsewill, A. J.; Peat, D. T.; Goh, K. S.; Gadian, D. G. *Phys. Chem. Chem. Phys.* **2013**, *15*, 10413.

(12) Hirsch, M. L.; Kalechofsky, N.; Belzer, A.; Rosay, M.; Kempf, J. G. *J. Am. Chem. Soc.* **2015**, *137*, 8428.

(13) Albert, M.; Cates, G.; Driehuys, B.; Happer, W.; Saam, B.; Springer Jr, C.; Wishnia, A. *Nature* **1994**, *370*, 199.

(14) Kadlecek, S. *Am. Sci.* **2002**, *90*, 540.

(15) Roos, J. E.; McAdams, H. P.; Kaushik, S. S.; Driehuys, B. *Magn. Reson. Imaging Clin. N. Am.* **2015**, *23*, 217.

(16) Albert, M. S.; Balamore, D. *Nucl. Instrum. Methods Phys. Res., Sect. A* **1998**, *402*, 441.

(17) Driehuys, B. *Optics and Photonics News* **1995**, *6*, 38.

(18) Albert, M. S.; Tseng, C. H.; Williamson, D.; Oteiza, E. R.; Walsworth, R. L.; Kraft, B.; Kacher, D.; Holman, B. L.; Jolesz, F. A. *J Magn Reson B* **1996**, *111*, 204.

(19) Shukla, Y.; Wheatley, A.; Kirby, M.; Svenningsen, S.; Farag, A.; Santyr, G. E.; Paterson, N. A.; McCormack, D. G.; Parraga, G. *Acad. Radiol.* **2012**, *19*, 941.

(20) Lilburn, D. M.; Pavlovskaya, G. E.; Meersmann, T. *J. Magn. Reson.* **2013**, *229*, 173.

(21) Martin, C. C.; Williams, R. F.; Gao, J. H.; Nickerson, L. D.; Xiong, J.; Fox, P. T. *J. Magn. Reson. Imag.* **1997**, *7*, 848.

(22) Qing, K.; Ruppert, K.; Jiang, Y.; Mata, J. F.; Miller, G. W.; Shim, Y. M.; Wang, C.; Ruset, I. C.; Hersman, F. W.; Altes, T. A. *J. Magn. Reson. Imag.* **2014**, *39*, 346.

(23) Bartik, K.; Luhmer, M.; Dutasta, J.-P.; Collet, A.; Reisse, J. *J. Am. Chem. Soc.* **1998**, *120*, 784.

(24) Spence, M. M.; Rubin, S. M.; Dimitrov, I. E.; Ruiz, E. J.; Wemmer, D. E.; Pines, A.; Yao, S. Q.; Tian, F.; Schultz, P. G. *Proc. Natl. Acad. Sci. U.S.A.* **2001**, *98*, 10654.

(25) Mohr, P. J.; Newell, D. B.; Taylor, B. N. *J. Phys. Chem. Ref. Data* **2016**, *45*, 043102.

(26) Maly, T.; Sirigiri, J. R. *Appl. Magn. Reson.* **2012**, *43*, 181.

(27) Bridge12 Technologies: http://www.bridge12.com/what-is-dynamic-nuclear-polarization-dnp-nmr/, 2011.

(28) Maly, T.; Debelouchina, G. T.; Bajaj, V. S.; Hu, K. N.; Joo, C. G.; Mak-Jurkauskas, M. L.; Sirigiri, J. R.; van der Wel, P. C. A.; Herzfeld, J.; Temkin, R. J.; Griffin, R. G. *J. Chem. Phys.* **2008**, *128*, 02B611.

(29) Gelis, I.; Vitzthum, V.; Dhimole, N.; Caporini, M. A.; Schedlbauer, A.; Carnevale, D.; Connell, S. R.; Fucini, P.; Bodenhausen, G. *J. Biomol. NMR* **2013**, *56*, 85.

(30) Takahashi, H.; Ayala, I.; Bardet, M.; De Paepe, G.; Simorre, J. P.; Hediger, S. *J. Am. Chem. Soc.* **2013**, *135*, 5105.

(31) Leunbach, I.; Young, I.; Ehnholm, G.; Hansson, G.; Petersson, S.; Wistrand, L.-G.; Golman, K.; Google Patents: USA, 1999; Vol. 6008644.

(32) McCarney, E. R.; Armstrong, B. D.; Lingwood, M. D.; Han, S. *Proc. Natl. Acad. Sci. U.S.A.* **2007**, *104*, 1754.

(33) Ardenkjaer-Larsen, J.; Laustsen, C.; Pullinger, B.; Kadlecek, S.; Emami, K.; Rizi, R. *Proc. Int. Soc. Mag. Reson. Med.* **2011**, *19*, 3534.

(34) Lingwood, M. D.; Siaw, T. A.; Sailasuta, N.; Abulseoud, O. A.; Chan, H. R.; Ross, B. D.; Bhattacharya, P.; Han, S. *Radiology* **2012**, *265*, 418.

(35) Kurhanewicz, J.; Vigneron, D. B.; Brindle, K.; Chekmenev, E. Y.; Comment, A.; Cunningham, C. H.; Deberardinis, R. J.; Green, G. G.; Leach, M. O.; Rajan, S. S.; Rizi, R. R.; Ross, B. D.; Warren, W. S.; Malloy, C. R. *Neoplasia* **2011**, *13*, 81.

(36) Wiemer, E. A.; Ter Kuile, B. H.; Michels, P. A.; Opperdoes, F. R. *Biochem. Biophys. Res. Commun.* **1992**, *184*, 1028.

(37) McRobbie, D. W.; Moore, E. A.; Graves, M. J.; Prince, M. R. *MRI from Picture to Proton*; Cambridge University Press, 2017.

(38) Kohler, S.; Yen, Y.; Wolber, J.; Chen, A.; Albers, M.; Bok, R.; Zhang, V.; Tropp, J.; Nelson, S.; Vigneron, D. *Magn. Reson. Med.* **2007**, *58*, 65.

(39) Lau, A. Z.; Chen, A. P.; Ghugre, N. R.; Ramanan, V.; Lam, W. W.; Connelly, K. A.; Wright, G. A.; Cunningham, C. H. *Magn. Reson. Med.* **2010**, *64*, 1323.

(40) Hovav, Y.; Levinkron, O.; Feintuch, A.; Vega, S. *Appl. Magn. Reson.* **2012**, *43*, 21.

(41) Hovav, Y.; Feintuch, A.; Vega, S. *Phys. Chem. Chem. Phys.* **2013**, *15*, 188.

(42) Banerjee, D.; Shimon, D.; Feintuch, A.; Vega, S.; Goldfarb, D. *J. Magn. Reson.* **2013**, *230*, 212.

(43) Rioux, F. *The Chemical Educator* **2001**, *6*, 288.

(44) Atkins, P.; de Paula, J. *Physical Chemistry*; W. H. Freeman: Oxford University Press, 2007.

(45) Matthews, M. J.; Petitpas, G.; Aceves, S. M. *Appl. Phys. Lett.* **2011**, *99*, 3.

(46) Blazina, D.; Duckett, S. B.; Halstead, T. K.; Kozak, C. M.; Taylor, R. J.; Anwar, M. S.; Jones, J. A.; Carteret, H. A. *Magn. Reson. Chem.* **2005**, *43*, 200.

(47) Duckett, S. B.; Mewis, R. E. *Acc. Chem. Res.* **2012**, *45*, 1247.

(48) Duckett, S. B.; Wood, N. J. *Coord. Chem. Rev.* **2008**, *252*, 2278.

(49) Frydman, L. *Nat. Chem.* **2009**, *1*, 176.

(50) Atkinson, K. D.; Cowley, M. J.; Elliott, P. I.; Duckett, S. B.; Green, G. G.; Lopez-Serrano, J.; Whitwood, A. C. *J. Am. Chem. Soc.* **2009**, *131*, 13362.

(51) Duckett, S. B.; Mewis, R. E.; Highton, L. A.; John, R. O. https://www.york.ac.uk/res/sbd/parahydrogen/generating.html, 2015

(52) Bowers, C. R.; Weitekamp, D. P. *Phys. Rev. Lett.* **1986**, *57*, 2645.

(53) Bowers, C. R.; Weitekamp, D. P. *J. Am. Chem. Soc.* **1987**, *109*, 5541.

(54) Pravica, M. G.; Weitekamp, D. P. *Chem. Phys. Lett.* **1988**, *145*, 255.

(55) Natterer, J.; Bargon, J. *Prog. Nucl. Magn. Reson. Spectrosc.* **1997**, *31*, 293.

(56) Eisenberg, R. *Acc. Chem. Res.* **1991**, *24*, 110.

(57) Eguillor, B.; Caldwell, P. J.; Cockett, M. C.; Duckett, S. B.; John, R. O.; Lynam, J. M.; Sleigh, C. J.; Wilson, I. *J. Am. Chem. Soc.* **2012**, *134*, 18257.

(58) Blazina, D.; Duckett, S. B.; Dunne, J. P.; Godard, C. *Dalton Trans.* **2004**, 2601.

(59) Golman, K.; Axelsson, O.; Johannesson, H.; Mansson, S.; Olofsson, C.; Petersson, J. S. *Magn. Reson. Med.* **2001**, *46*, 1.

(60) Atkinson, K. D.; Cowley, M. J.; Duckett, S. B.; Elliott, P. I.; Green, G. G.; López-Serrano, J.; Khazal, I. G.; Whitwood, A. C. *Inorg. Chem.* **2008**, *48*, 663.

(61) Aguilar, J. A.; Adams, R. W.; Duckett, S. B.; Green, G. G.; Kandiah, R. *J. Magn. Reson.* **2011**, *208*, 49.

(62) van Weerdenburg, B. J.; Gloggler, S.; Eshuis, N.; Engwerda, A. H.; Smits, J. M.; de Gelder, R.; Appelt, S.; Wymenga, S. S.; Tessari, M.; Feiters, M. C.; Blumich, B.; Rutjes, F. P. *Chem. Commun.* **2013**, *49*, 7388.

(63) Hovener, J. B.; Schwaderlapp, N.; Borowiak, R.; Lickert, T.; Duckett, S. B.; Mewis, R. E.; Adams, R. W.; Burns, M. J.; Highton, L. A.; Green, G. G.; Olaru, A.; Hennig, J.; von Elverfeldt, D. *Anal. Chem.* **2014**, *86*, 1767.

(64) Cowley, M. J.; Adams, R. W.; Atkinson, K. D.; Cockett, M. C.; Duckett, S. B.; Green, G. G.; Lohman, J. A.; Kerssebaum, R.; Kilgour, D.; Mewis, R. E. *J. Am. Chem. Soc.* **2011**, *133*, 6134.

(65) Rayner, P. J.; Burns, M. J.; Olaru, A. M.; Norcott, P.; Fekete, M.; Green, G. G. R.; Highton, L. A. R.; Mewis, R. E.; Duckett, S. B. *Proc. Natl. Acad. Sci. U.S.A.* **2017**, *114*, E3188.

(66) Rayner, P. J.; Duckett, S. B. *Angew. Chem. Int. Ed. Engl.* **2018**, *57*, 6742.

(67) Allouche-Arnon, H.; Lerche, M. H.; Karlsson, M.; Lenkinski, R. E.; Katz-Brull, R. *Contrast Media Mol. Imaging* **2011**, *6*, 499.

(68) Holmes, A. J.; Rayner, P. J.; Cowley, M. J.; Green, G. G.; Whitwood, A. C.; Duckett, S. B. *Dalton Trans.* **2015**, *44*, 1077.

(69) Norcott, P.; Burns, M. J.; Rayner, P. J.; Mewis, R. E.; Duckett, S. B. *Magn. Reson. Chem.* **2018**, *56*, 663.

(70) Norcott, P.; Rayner, P. J.; Green, G. G.; Duckett, S. B. *Chem. Eur. J.* **2017**, *23*, 16990.

(71) Carravetta, M.; Levitt, M. H. *J. Am. Chem. Soc.* **2004**, *126*, 6228.

(72) Levitt, M. H. In *Annual Review of Physical Chemistry, Vol 63*; Johnson, M. A., Martinez, T. J., Eds.; Annual Reviews: Palo Alto, 2012; Vol. 63, p 89.

(73) Roy, S. S.; Rayner, P. J.; Norcott, P.; Green, G. G. R.; Duckett, S. B. *Phys. Chem. Chem. Phys.* **2016**, *18*, 24905.

(74) Levitt, M. H. *eMagRes* **2007**.

(75) Olaru, A. M.; Roy, S. S.; Lloyd, L. S.; Coombes, S.; Green, G. G.; Duckett, S. B. *Chem. Commun.* **2016**, *52*, 7842.

(76) Roy, S. S.; Norcott, P.; Rayner, P. J.; Green, G. G.; Duckett, S. B. *Angew. Chem. Int. Ed. Engl.* **2016**, *55*, 15642.

(77) Diler, A.; Üzüm, G.; Lefauconnier, J.; Ziylan, Y. In *Biology and Physiology of the Blood-Brain Barrier*; Springer: 1996, p 333.

(78) Mayer, B. *Arch. Toxicol.* **2014**, *88*, 5.

(79) Fevrier, F. C.; Smith, E. D.; Comins, D. L. *Org. Lett.* **2005**, *7*, 5457.

(80) Wagner, F. F.; Comins, D. L. *Eur. J. Org. Chem.* **2006**, 3562.

(81) Wagner, F. F.; Comins, D. L. *Tetrahedron* **2007**, *63*, 8065.

(82) Wagner, F. F.; Comins, D. L. *Org. Lett.* **2006**, *8*, 3549.

(83) Beak, P.; Brown, R. A. *J. Org. Chem.* **1982**, *47*, 34.

(84) Snieckus, V. *Chem. Rev.* **1990**, *90*, 879.

(85) Beak, P.; Meyers, A. I. *Acc. Chem. Res.* **1986**, *19*, 356.

(86) Gros, P.; Fort, Y.; Caubère, P. *J. Chem. Soc., Perkin Trans. 1* **1997**, 3071.

(87) Gros, P.; Fort, Y.; Caubère, P. *J. Chem. Soc., Perkin Trans. 1* **1997**, 3597.

(88) Gros, P.; Choppin, S.; Mathieu, J.; Fort, Y. *J. Org. Chem.* **2002**, *67*, 234.

(89) Schlosser, M. *Angew. Chem. Int. Ed. Engl.* **2005**, *44*, 376.

(90) Pavlik, J. W.; Laohhasurayotin, S. *J. Heterocycl. Chem.* **2007**, *44*, 1485.

(91) Marques, C. A.; Selva, M.; Tundo, P. *J. Org. Chem.* **1993**, *58*, 5256.

(92) *IUPAC Solubility Data Series*; Pergamon Press: Oxford, 1981; Vol. 5/6.

(93) Pandey, P. N.; Purkayastha, M. L. *Synthesis-Stuttgart* **1982**, 876.

(94) Mewis, R. E.; Atkinson, K. D.; Cowley, M. J.; Duckett, S. B.; Green, G. G.; Green, R. A.; Highton, L. A.; Kilgour, D.; Lloyd, L. S.; Lohman, J. A.; Williamson, D. C. *Magn. Reson. Chem.* **2014**, *52*, 358.

(95) Mewis, R. E.; Green, R. A.; Cockett, M. C.; Cowley, M. J.; Duckett, S. B.; Green, G. G.; John, R. O.; Rayner, P. J.; Williamson, D. C. *J. Phys. Chem. B* **2015**, *119*, 1416.

(96) Ruddlesden, A. J.; Mewis, R. E.; Green, G. G.; Whitwood, A. C.; Duckett, S. B. *Organometallics* **2015**, *34*, 2997.

(97) Zeng, H.; Xu, J.; Gillen, J.; McMahon, M. T.; Artemov, D.; Tyburn, J. M.; Lohman, J. A.; Mewis, R. E.; Atkinson, K. D.; Green, G. G.; Duckett, S. B.; van Zijl, P. C. *J. Magn. Reson.* **2013**, *237*, 73.

(98) Bakhmutov, V. I. *Practical NMR Relaxation For Chemists*; Wiley Online Library, 2004.

(99) Bloch, F. *Phys. Rev.* **1946**, *70*, 460.

(100) Goldman, M. *J. Magn. Reson.* **2001**, *149*, 160.

(101) Fekete, M.; Bayfield, O.; Duckett, S. B.; Hart, S.; Mewis, R. E.; Pridmore, N.; Rayner, P. J.; Whitwood, A. *Inorg. Chem.* **2013**, *52*, 13453.

(102) Rayner, P. J.; Burns, M. J. Unpublished Results.

(103) Iali, W.; Olaru, A. M.; Green, G. G. R.; Duckett, S. B. *Chemistry* **2017**, *23*, 10491.

(104) Aguilar, J. A.; Elliott, P. I.; Lopez-Serrano, J.; Adams, R. W.; Duckett, S. B. *Chem Commun (Camb)* **2007**, *11*, 1183.

(105) Lloyd, L. S.; Asghar, A.; Burns, M. J.; Charlton, A.; Coombes, S.; Cowley, M. J.; Dear, G. J.; Duckett, S. B.; Genov, G. R.; Green, G. G. R.; Highton, L. A. R.; Hooper, A. J. J.; Khan, M.; Khazal, I. G.; Lewis, R. J.; Mewis, R. E.; Roberts, A. D.; Ruddlesden, A. J. *Cat. Sci. Tech.* **2014**, *4*, 3544.

(106) Appleby, K. M.; Mewis, R. E.; Olaru, A. M.; Green, G. G. R.; Fairlamb, I. J. S.; Duckett, S. B. *Chem. Sci.* **2015**, *6*, 3981.

(107) Truong, M. L.; Theis, T.; Coffey, A. M.; Shchepin, R. V.; Waddell, K. W.; Shi, F.; Goodson, B. M.; Warren, W. S.; Chekmenev, E. Y. *J. Phys. Chem.* **2015**, *119*, 8786.

(108) d'Angelo, J. V. H.; Francesconi, A. *Z. J. Chem. Eng. Data* **2001**, *46*, 671.

(109) Rayner, P. J.; Norcott, P.; Appleby, K. M.; Iali, W.; John, R. O.; Hart, S. J.; Whitwood, A. C.; Duckett, S. B. *Nat. Commun.* **2018**, *9*, 4251.

(110) van Weerdenburg, B. J.; Eshuis, N.; Tessari, M.; Rutjes, F. P.; Feiters, M. C. *Dalton Trans.* **2015**, *44*, 15387.

(111) Highton, L. A. PhD Thesis, University of York, 2013.

(112) Richardson, P. M.; Jackson, S.; Parrott, A. J.; Nordon, A.; Duckett, S. B.; Halse, M. E. *Magn. Reson. Chem.* **2018**, *56*, 641.

(113) Hennig, J.; Nauerth, A.; Friedburg, H. *Magn. Reson. Med.* **1986**, *3*, 823.

(114) Chavhan, G. B.; Babyn, P. S.; Jankharia, B. G.; Cheng, H. L.; Shroff, M. M. *Radiographics* **2008**, *28*, 1147.

(115) Mezrich, R. *Radiology* **1995**, *195*, 297.

(116) Ridgway, J. P. In *Cardiovascular MR Manual*; Plein, S., Greenwood, J., Ridgway, J. P., Eds.; Springer International Publishing: Cham, 2015, p 57.

(117) Jellinger, K. A. *European Journal of Neurology* **2001**, *8*, 96.

(118) Gaillard, F. https://radiopaedia.org/cases/mri-physics-diagrams, 2013.

(119) Gyngell, M. L.; Frahm, J.; Merboldt, K. D.; Hanicke, W.; Bruhn, H. *J. Magn. Reson.* **1988**, *77*, 596.

(120) Scheffler, K.; Lehnhardt, S. *Eur. Radiol.* **2003**, *13*, 2409.

(121) Frank, A., Duke University, 2008.

(122) Jeener, J.; Meier, B. H.; Bachmann, P.; Ernst, R. R. *J. Chem. Phys.* **1979**, *71*, 4546.

(123) Stott, K.; Keeler, J.; Van, Q. N.; Shaka, A. J. *J. Magn. Reson.* **1997**, *125*, 302.

(124) Kessler, H.; Oschkinat, H.; Griesinger, C. *J. Magn. Reson.* **1986**, *70*, 106.

(125) Stonehouse, J.; Adell, P.; Keeler, J.; Shaka, A. J. *J. Am. Chem. Soc.* **1994**, *116*, 6037.

(126) Eberhardt, F.; Glymour, C.; Scheines, R. In *Innovations in Machine Learning*; Springer: Carnegie Mellon University, 2006, p 97.